ADVANCED ENERGY MATERIALS
www.advenergymat.de

Challenges in Developing Electrodes, Electrolytes, and Diagnostics Tools to Understand and Advance Sodium-Ion Batteries

*Gui-Liang Xu, Rachid Amine, Ali Abouimrane, Haiying Che, Mouad Dahbi, Zi-Feng Ma, Ismael Saadoune, Jones Alami, Wenjuan Liu Mattis, Feng Pan, Zonghai Chen, and Khalil Amine**

Considering the natural abundance and low cost of sodium resources, sodium-ion batteries (SIBs) have received much attention for large-scale electrochemical energy storage. However, smart structure design strategies and good mechanistic understanding are required to enable advanced SIBs with high energy density. In recent years, the exploration of advanced cathode, anode, and electrolyte materials, as well as advanced diagnostics have been extensively carried out. This review mainly focuses on the challenging problems for the attractive battery materials (i.e., cathode, anode, and electrolytes) and summarizes the latest strategies to improve their electrochemical performance as well as presenting recent progress in operando diagnostics to disclose the physics behind the electrochemical performance and to provide guidance and approaches to design and synthesize advanced battery materials. Outlook and perspectives on the future research to build better SIBs are also provided.

1. Introduction

The consumption of fossil fuel and emisssion of CO_2 have caused serious environmental issues, giving rise to growing demand for clean and sustainable energy.[1] Therefore, significant attempts have been made to pursue high-power and high-energy power source devices in the past decades. Among them, lithium-ion batteries (LIBs) have been considered as one of the most appealing candidates because of their outstanding merits such as high energy densities, long calendar life, lack of memory effect, and so forth.[2] Since first commercialization by Sony Corporation in the 1990s, LIBs have become the main power source for the portable electronics markets and are now showing great potential use for automobile market. However, because lithium is a rare metal element, the feasibility of its widely use in grid-scale energy storage has become a serious concern.[3] As shown in **Figure 1**a, the limited abudance of lithium is not enough to meet the increasing energy demands powered by LIBs technologies.[4] Moreover, lithium resources are nonuniformly distributed in the world (≈40% in South America) and are mainly monopolized by four companies, which will lead to sustained price increase in the near future (Figure 1b).[5]

For the above reasons and given the natural abundance of sodium resource, room-temperature sodium-ion batteries (SIBs) are viewed as a potential alternative to state-of-the-art

Dr. G.-L. Xu, Z. H. Chen, Dr. K. Amine
Chemical Sciences and Engineering Division
Argonne National Laboratory
Lemont, IL 60439, USA
E-mail: amine@anl.gov
R. Amine
Materials Science Division
Argonne National Laboratory
Lemont, IL 60439, USA
Dr. A. Abouimrane
Qatar Environment and Energy Research Institute
Hamad Bin Khalifa University
Qatar Foundation
P.O. Box 5825, 34110, Doha, Qatar
H. Y. Che, Prof. Z.-F. Ma
Chemical Engineering Division
Shanghai Jiaotong University
Shanghai 200240, China
The ORCID identification number(s) for the author(s) of this article can be found under https://doi.org/10.1002/aenm.201702403.

DOI: 10.1002/aenm.201702403

Dr. M. Dahbi, Prof. I. Saadoune, Prof. J. Alami
Materials Science and Nano-engineering Department
Mohammed VI Polytechnic University
Ben Guerir 43150, Morocco
Prof. I. Saadoune
LCME
FST Marrakesh
University Cadi Ayyad
Av. A. Khattabi, BP 549, 40000 Marrakech, Morocco
Dr. W. Mattis
12603 Southwest Freeway, Suite 210 Stafford
Texas 77477, USA
Prof. F. Pan
School of Advanced Materials
Peking University
Shenzhen Graduate School
Shenzhen 518055, China
Dr. K. Amine
IRMC
Imam Abdulrahman Bin Faisal University
Dammam 34212, Saudi Arabia

LIBs.[6] The components and working mechanisms of SIBs are basically similar to the rock-chair type LIBs, which relys on the shuttle of lithium ions between the cathode and the anode (Figure 1c). After the exploration of the Li/TiS_2 system by Whittingham in 1976,[7] Newman and Kelmann reported that TiS_2 can also host Na^+ at room temperature in 1980.[8] However, because of the rapid advances and commercialization of LIB technologies, the exploration of SIBs has been minimal in the past decades. Another important reason is because SIBs present lower energy density than LIBs, making Na less attractive for automotive applications.[9] This is resulted from the larger atomic weight (23 for Na vs 7 for Li) and the lower standard electrochemical potential of Na (2.71 V for Na vs 3.04 V for Li). Moreover, the larger ionic radius of Na^+ (1.02 Å) than Li^+ (0.67 Å) also brings more challenges on the development of good Na-host materials with optimal electrochemical properties.[10] Despite these challenges, academic research activities on SIBs over the past few years have intensified due to the rapid development of novel synthetic methods and advanced characterization techniques (Figure 1d). Significant successes have been achieved in the development of advanced cathode materials,[11,12] anode materials,[13] and electrolytes[14] as well as the understanding of Na^+ intercalation chemistry as determined by advanced diagnostic tools.[15,16] These successes are offering new opportunities to increase further the energy density of SIBs.

Cathode materials largely determine the energy density, lifespan and abuse tolerance of SIBs.[17] **Figure 2**a shows the specific capacities, working voltages, and energy densities of various reported cathode materials, which mainly incudes layered- and tunnel-structured sodium metal oxides; polyanion cathodes including pyrophosphates, phosphates, sodium (Na) super ionic conductor (NASICON) types and fluorophosphates; organic compounds; and hexacyanometalates such as prussian blue and prussian white.[12] Similar to LIBs chemistry, layered-structured sodium metal oxides and polyanion cathodes have attracted the most attention. Despite most SIBs cathode materials are either imitating or duplicating from lithium analogues, there is a significant difference in the intercalation chemisties between sodiation and lithiation. For example, Okada et al. revealed that α-$NaFeO_2$ could undergo reversible Fe^{4+}/Fe^{3+} redox reaction.[18] However, the lithium analogue $LiFeO_2$ was shown to be inactive.[19] Therefore, smart structure design strategies and good mechanistic understanding are required to develop advanced SIB cathode materials.

For some time, the absence of suitable anode materials has obstructed progress in the development of SIBs.[20] Graphite, the anode material of choice in state-of-the-art LIBs, can only store a small amount of sodium due to the insufficient interlayer distance and stretched C—C bonds induced by sodiation, which makes the Na–graphite intercalation compound thermodynamically unstable.[21] The discovery of hard carbon as an SIB anode material by Stevens and Dahn in 2000 encouraged the development of advanced Na-based anode materials.[22] As shown in Figure 2b, carbon-based, Titanium (Ti)-based, NASICON-type, and alloy-based materials as well as conversion reaction-based materials such as metal oxides/sulfides/selenides, have been extensively explored.[13,20] Among them, carbon-based materials such as expanded graphite[23] and organic carboxylate[24] are still considered as promising anode materials owing to their moderate working voltage and considerable specific capacities. Ti-based materials usually present high rate capability and ultralong cycle life, showing great potential use for high-power SIBs.[25] Despite the reasonable capacities of most metal oxides/sulfides/selenides and NASICON-type materials, their average working voltages are too high, making them less attractive as the SIB anode.[26–29] Alloy-based materials, especially phosphorus-based anode materials, are considered as the most appealing candidate because of their attractive theoretical capacities of up to 2596 mA h g^{-1}.[30] However, stable host materials are usually required to overcome the large volume changes induced during repeated charge/discharge to achieve long-term cycle stability.[31]

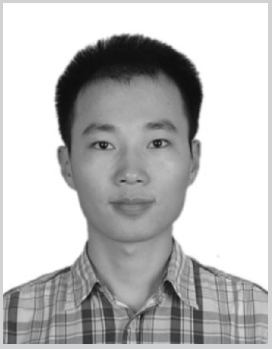

Gui-Liang Xu is an assistant chemist at Argonne National Laboratory. His research focuses on both fundamental understanding by operando synchrotron X-ray techniques and materials development relating to electrochemical energy storage systems, including lithium-ion, sodium-ion, lithium–sulfur and lithium–selenium batteries.

Rachid Amine is an assistant chemist at Argonne National Laboratory (ANL) since 2013. He is also a Ph.D. candidate in Chemical Engineering Department at the University of Illinois at Chicago. His research efforts have focused on development of high energy materials and beyond lithium ion technologies.

Khalil Amine is an Argonne Distinguished Fellow and Manager of the Advanced Battery Technology programs at Argonne National Laboratory, where he is responsible for directing the research and development of advanced materials and battery systems for HEV, PHEV, EV, satellite, military, and medical applications. Dr. Amine currently serves a committee member of the U.S. National Research Consul, U.S. Academy of Sciences, on battery-related technologies. He is also the president of IMLB LLC, an international automotive battery conference.

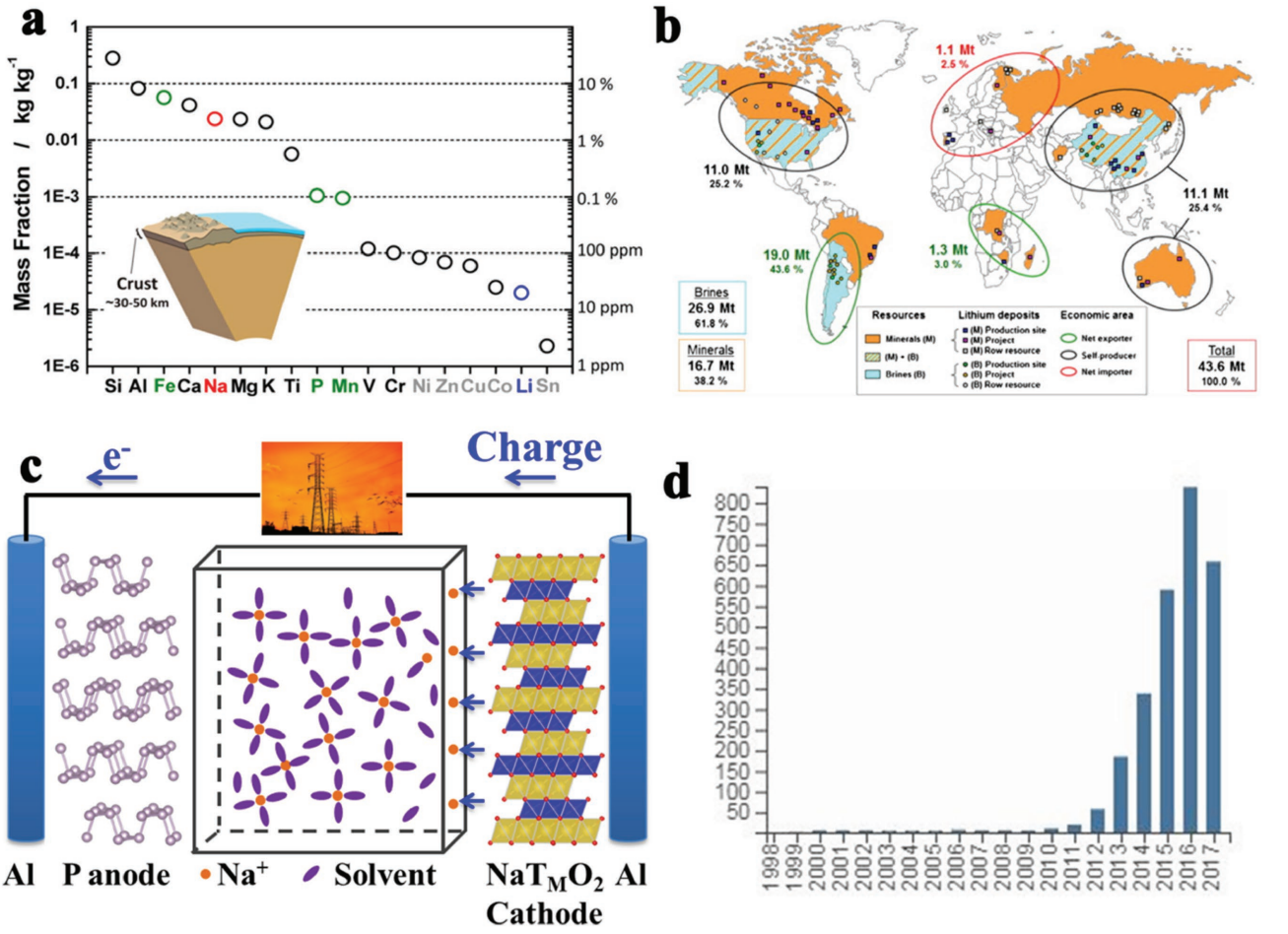

Figure 1. a) Elemental abundance in the Earth's crust.[4] b) Map of lithium resource availability and geostrategic impacts.[5] c) Schematic illustration of Na-ion batteries. d) Number of publications related to the sodium-ion batteries in the past decades. Data was derived from Web of Science using "sodium-ion batteries" as key word. Panel (a) reproduced with permission.[4] Copyright 2014, American Chemical Society. Panel (b) reproduced with permission.[5] Copyright 2012, Elsevier.

Electrolytes play a critical role on the safety, cycle life, and battery performance of SIBs. The interaction between electrodes and electrolytes significantly affects the solid–electrolyte interphase (SEI) layer and the internal structure of active materials. As shown in Figure 2c, the electrolytes can be mainly categorized into aqueous, organic liquid, and solid state.[14] The average working voltages of SIBs based on aqueous electrolytes are in the range of 1.0–1.5 V, and the corresponding cell energy densities are less than 100 Wh kg^{-1}, making them less attractive. Organic electrolytes have a higher stability window, i.e., 1.5–4.25 V, leading to energy densities of between 150 and 300 Wh kg^{-1}. Compared with the organic liquid electrolyte, a solid-state electrolyte has a more stable electrochemical window and higher safety, which enables high-voltage cathode materials and the use of Na metal as the anode; the resulting cell offers energy density of 500 Wh kg^{-1} or even higher.[14] However, challenges related to the ionic conductivity and interfacial problems between electrodes and electrolytes need to be addressed.

The development of advanced SIBs requires an in-depth understanding of the science behind their electrochemical performance. Rechargeable batteries are very complex systems, which involve amorphous and crystalline structure evolution, which is sometimes accompanied by large volumetric changes during charge/discharge.[32] Also, the synthesis of battery materials greatly affected the chemical composition, morphology, and phase structures of battery materials and, thus, the electrochemical performance.[33] Advanced diagnostic tools, especially operando based, are critical to elucidate the interplay between electrodes, electrolytes and interface. Recently, nuclear magnetic resonance (NMR) spectroscopy, transmission electron microscopy (TEM), and synchrotron-based techniques such as X-ray diffraction (XRD), pair distribution function (PDF) analysis, X-ray absorption spectroscopy (XAS), and transmission X-ray microscopy (TXM) have been widely used in SIB studies, which have advanced the development of this system (Figure 2d).[15,16,34]

Review articles related to sodium-ion batteries,[4,6,10,35–37] cathode materials,[11,17,38] anode materials,[13,37,39] and electrolytes[14,40] have been recently published by different groups; in this review article, we will focus on the most challenging problems for the most attractive SIB materials (i.e., cathode, anode, and electrolyte) and summarize the latest strategies to improve their electrochemical performance. We also present

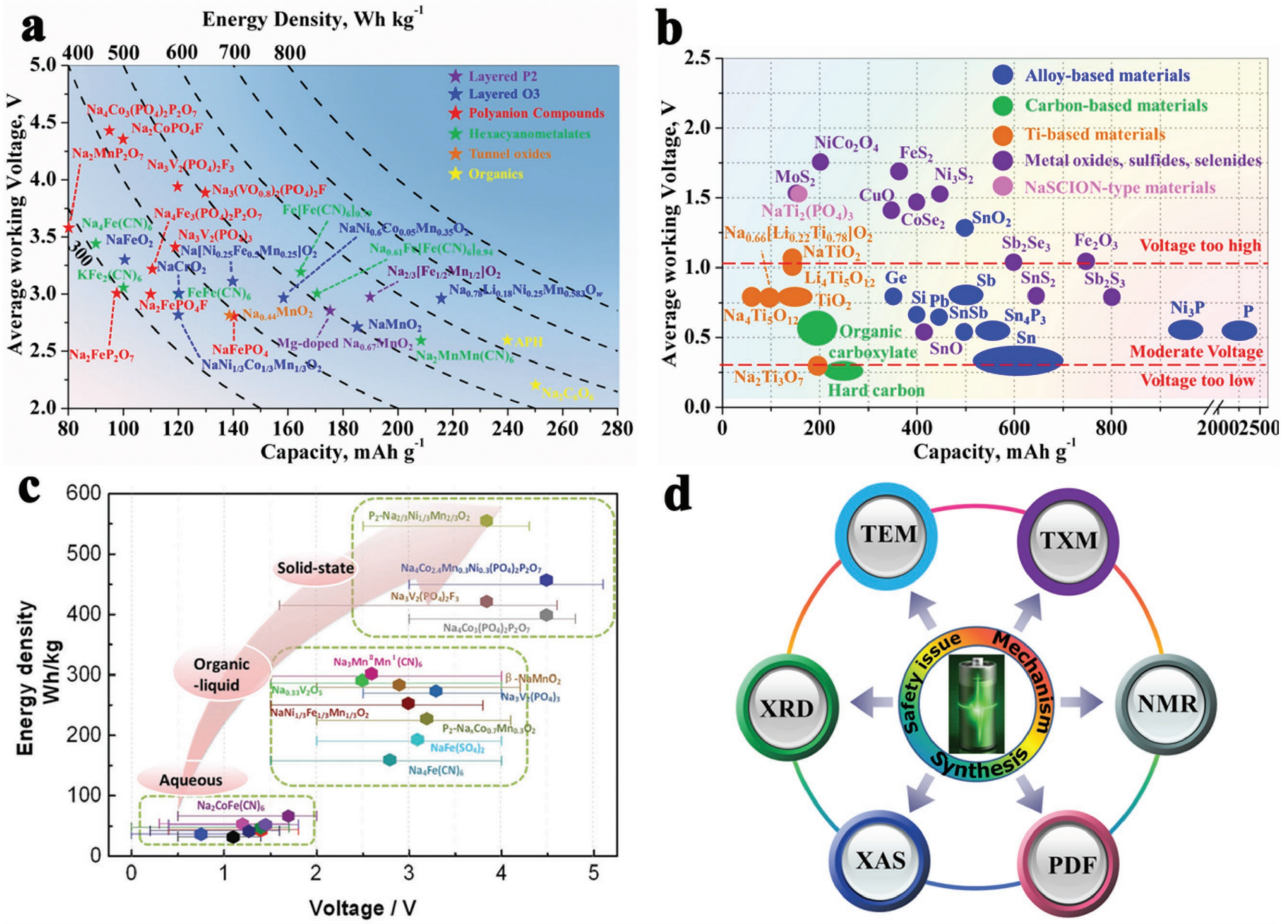

Figure 2. Performance data for SIB a) cathode materials, b) anode materials, and c) electrolytes [14]; d) diagnostic techniques for SIBs. Panel (c) reproduced with permission.[14] Copyright 2017, Royal Society of Chemistry.

recent progress of operando diagnostics to understand the relationship between structure and performance, and to provide guidance and approaches to design and synthesize better battery materials. For the cathode materials, we are particularly interested in the high-voltage cycling stability challenges for layered-structured transtion metal oxide materials on account of the higher energy densities achieved by pushing up the working voltage range. The capacity fading mechanism and the corresponding optimization approaches such as surface coating, cation and anion doping, and intergrated structures will be discussed. We will also focus on the polyanion cathodes for SIBs owing to their stability, safety, and suitable operating voltages. Structural effects on the electrochemical properties of $NaFePO_4$, $Na_3V_2(PO_4)_3$, fluorophosphates, and Co-based pyrophosphates that have an energy density above 400 Wh kg^{-1} will be summarized. For the anode materials, we will include recent progress of carbon-based, Ti-based, and phosphorus-based anode materials. We will also introduce the application of advanced diagnostic techniques to investigate thermal stability and synthetic studies of battery materials as well as widely reported battery cycling studies. Finally, we will provide an outlook and perspectives on the major challenges in using SIBs for larger-scale electrochemical energy storage applications.

2. Cathode Materials

2.1. Layered-Structured Sodium Metal Oxide Cathodes

Layered sodium metal oxides ($Na_xT_MO_2$, T_M = Ni, Co, Mn, Fe, Cr, V, Cu, etc.) with their analogues have received much attention because of their high theoretical capacities (for instance, 235 mA h g^{-1} for O3-$NaNiO_2$).[17] Typically, they consist of repeating T_MO_6 layers along the *c*-axis direction with Na^+ being sandwiched in between the oxide layers. According to the definition by Delmas et al.,[41] the crystal structures of layered sodium metal oxides can be categorized into O3-(ABCABC), O′3-, P2-(ABBA), P3-(ABBCCA), and P′3-type (**Figure 3**a). O indicates that sodium occupies the octahedral site of sodium layers, P represents prismatic site, while prime (′) symbol indicates a monoclinic distorted phase.[4,17,36]

For the O3-type cathodes, the *x* value representing the Na amount is very close to 1, offering higher initial capacities. Similar to O3-type $Li_xT_MO_2$, Na ions usually migrate through interstitial tetrahedral sites to avoid the high activation energy barriers by hopping directly from one octahedral site to an adjacent octahedral site (Figure 3b).[42,43] The *x* values for P2- and P3-type are usually in the range of 0.6–0.7. Contrary to O3-type, they present a much lower diffusion barrier because of their

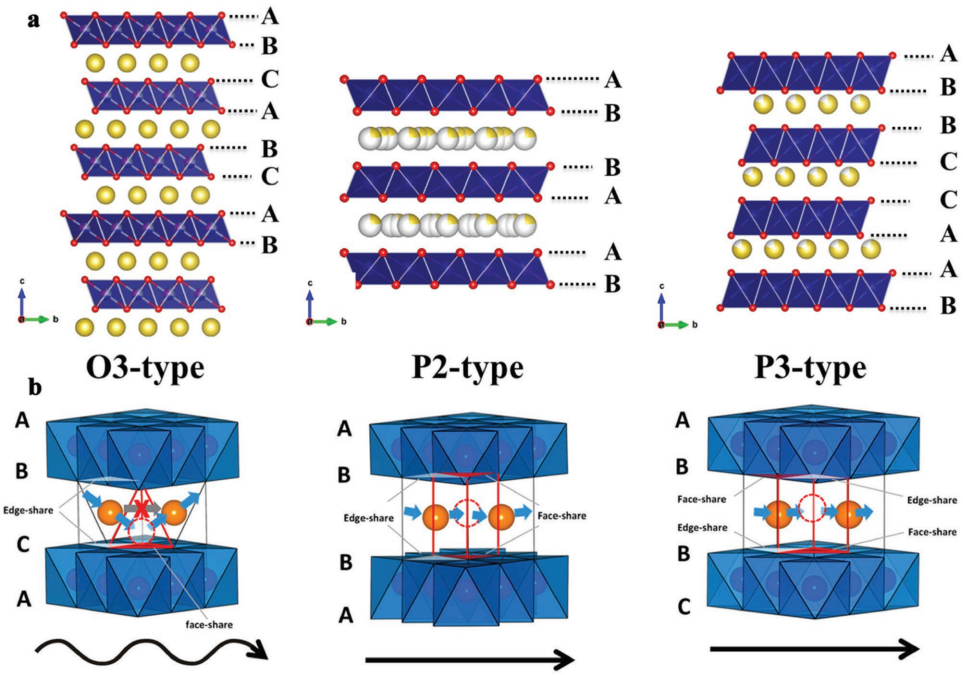

Figure 3. a) Crystal structure and b) sodium-ion migration path[4] for O3, P2, and P3-type cathode materials for SIBs. Panel (b) reproduced with permission.[4] Copyright 2014, American Chemical Society.

open diffusion path in *ab* direction (Figure 3b).[4] It has been found that the electrochemical performance of the P2- and O3-type material are heavily affected by the their phase structures. In this section, we will discuss recent development of P2- and O3-type layered transition metal oxide cathodes, in particular their high voltage cycle stability.

2.1.1. P2-Type Layered Sodium Metal Oxide Cathodes

Early studies by Delmas et al. revealed that P2-Na_xCoO_2 phase could be stable when the Na content is in the range of 0.46–0.83.[44] Since then, various P2-type cathode materials such as Na_xMnO_2,[45–47] $Na_{2/3}Fe_xMn_{1-x}O_2$,[48–52] $Na_xCo_yMn_{1-y}O_2$,[53–56] $Na_{2/3}Ni_xMn_{1-x}O_2$,[57–61] $Na_{2/3}Mn_xFe_yCo_{1-x-y}O_2$,[62] and $Na_{2/3}Ni_xCo_yMn_{1-x-y}O_2$[63–65] have been reported by examining the role of different transition metals. It has been found that Ni can increase the average discharge potential and thus energy density of the materials because of its high redox potential, Co can improve the structure stability, and Mn can contribute to an increase in the thermal stability, while Fe can suppress minor structural transition during cycling and concomitant Na^+ ordering processes and thus increases capacity retention.[55] Yamada and co-workers reported that by increasing y in P2-$Na_{2/3}Mn_yCo_{1-y}O_2$, the initial specific capacity increases while the cycle stability degrades (**Figure 4**a).[53]

The morphological effect on the sodium storage performance of P2-type cathode materials was also explored. Through a two-step self-templating method, as shown in Figure 4b, Lou and co-workers reported that compared to irregular P2-$Na_{0.7}CoO_2$, uniform P2-$Na_{0.7}CoO_2$ microspheres could demonstrate higher reversible capacity, improved cycle stability and rate capability.[66] Furthermore, Srinivasan and co-workers reported that P2-$Na_xCo_{0.1}Mn_{0.9}O_2$ spheres can combine the advantages of both Co doping and morphological effects and thus exhibit the best cycle stability (Figure 4c).[55] Operando XRD during charging revealed that P2-Na_xMnO_2 flakes undergo partial phase transition toward an orthorhombic crystal system during the sodiation process, while Co doping can prevent these structural transformations (Figure 4d).

Note that the electrochemical results discussed above are all within a relatively low voltage range, in which the P2 structure is relatively stable. Achieving reversible Na^+ extraction at high operating voltages could further increase the energy density of SIB cathodes. However, the irreversible P2-O2 transition and the associate large volume change of the O2 phase (more than 20%) would raise a serious concern on the cycle stability.[60] Komaba and co-workers have reported a P2-$Na_{2/3}[Fe_{1/2}Mn_{1/2}]O_2$ cathode, which can exhibit 190 mA h g^{-1} based on the reversible Fe^{4+}/Fe^{3+} redox couple within 1.5–4.3 V (**Figure 5**a).[48] As a result, it can offer an energy density of ≈520 Wh kg^{-1}, which is higher than previous reported SIBs and is comparable to that of $LiFePO_4$ and spinel $LiMn_2O_4$ (Figure 5b). The authors claimed that the P2-OP4 instead of P2-O2 transition was involved and was highly reversible during charge/discharge, and the OP4 was claimed to reduce the structural damage by gliding of layers, however, the observed rapid capacity fade (from 190 to 150 mA h g^{-1} in only 30 cycles) does not support their claim.[46] Guo and co-workers further demonstrated that P2-$Na_{2/3}[Fe_{1/2}Mn_{1/2}]O_2$ can only maintain half of the initial capacity after 80 cycles within 1.5–4.2 V,[51] which presents almost the same fading rate as the results reported by Komaba and co-workers (Figure 5c). By using operando synchrotron X-ray powder diffraction, Guo and co-workers

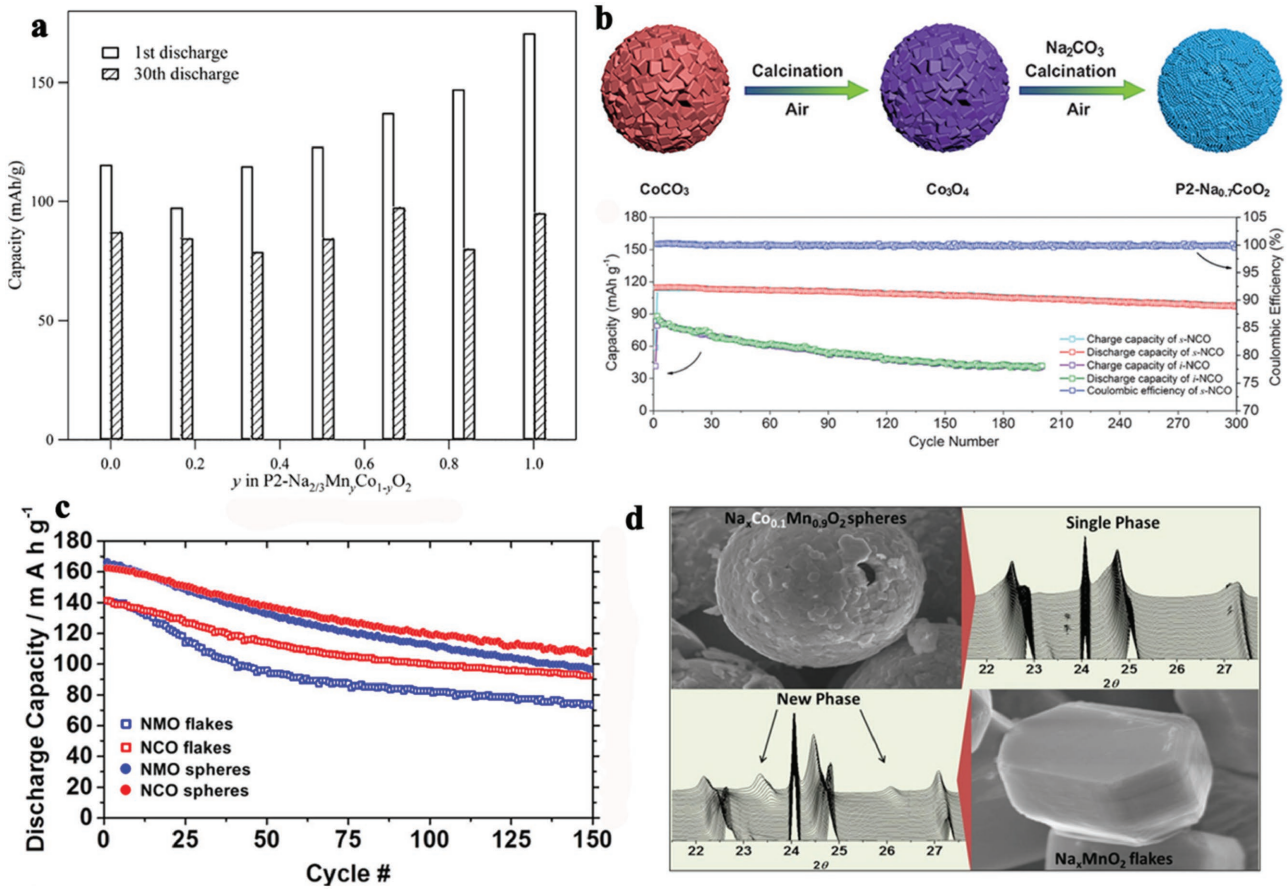

Figure 4. a)Specific capacity at the 1st and 30th discharge for P2-$Na_{2/3}Mn_yCo_{1-y}O_2$.[53] b)Schematic illustration of the two-step synthesis of P2-$Na_{0.7}CoO_2$ (NCO) microspheres and cycling performance of sphere $Na_{0.7}CoO_2$ and irregular $Na_{0.7}CoO_2$ at a current rate of 0.4 C.[66] c)Cycling stability of NMO flakes and spheres and NCO flakes and spheres at 50 mA g^{-1}.[55] d)Morphologies and the corresponding structure evolution of NCO spheres and NMO flakes during charge by synchrotron X-ray diffraction.[55] Reproduced with permission.[53,55,66] Panel (a) reproduced with permission.[53] Copyright 2013, American Chemical Society. Panel (b) reproduced with permission.[66] Copyright 2017, Wiley-VCH. Panels (c,d) reproduced with permission.[55] Copyright 2016, American Chemical Society.

found that the P2-$Na_{2/3}[Fe_{1/2}Mn_{1/2}]O_2$ was transformed to OP4 phase when charged to 4.2 V, and further returned into a P2-type orthorhombic phase with a *Cmcm* space group when discharged to 1.5 V (Figure 5d).[51] The rapid capacity fading mainly comes from the associated large cell volume changes with the multiple two-phase reactions. Moreover, Yang and co-workers reported that the transition metal cations migration into the tetrahedral sites in the sodium layers would also deteriorate the cycling stability, which is because it would increase the occupancy energy and inhibit the migration of Na^+ to the neighboring octahedral sites, thus leading to the gradual destruction of layer structures.[67] In addition, the oxygen activity is another possible reason for this capacity fading. Similar capacity fade during high-voltage cycling for P2-type cathodes was also reported in the case of $Na_{2/3}(Mn_{1/2}Fe_{1/4}Co_{1/4})O_2$,[62] $Na_{0.67}Mn_{0.67}Ni_{0.33}O_2$,[68] $Na_{2/3}[Ni_xMn_{1-x}]O_2$,[60,69] and $Na_{0.67}Mn_{0.72}Ni_{0.14}Co_{0.14}O_2$.[63]

Another challenging problem for P2-type cathodes is their sodium deficiency.[70] In a real SIB, the amount of sodium ion needed for charge storage would solely rely on the sodium reservoir on the cathode side. The lack of a sodium reservoir in P2-type cathodes creates a technological barrier to use an anode material without sodium, such as hard carbon. Some researchers have performed the pre-sodiation of the carbon using a half-cell configuration, then dismantled the cell and used the carbon anode against the sodiated cathode to overcome the irreversibility of the anode.[71] However, this method cannot be scaled up for commercialization. Tarascon and co-workers reported that Na_3P can be used as the sacrificial salt to generate higher reversible capacity and to compensate for the sodium deficiency of P2-type cathode materials.[72] However, Na_3P cannot be handled in air or a dry atmosphere. Singh and co-workers found that the sodium deficiency issue of the P2-$Na_{0.67}[Fe_{0.5}Mn_{0.5}]O_2$ cathode can be overcome by the addition of NaN_3.[73] However, the generation of N_2 gas during the nonreversible electrochemically driven decomposition of NaN_3 upon oxidation is detrimental to the battery, causing N_2 overpressure that can lead to cell venting. Moreover, the low Na content in NaN_3 (only 35% Na by weight) imposes a penalty on the energy density. Hence, the search for an optimum Na compensation approach for P2-type cathodes remains a challenge.

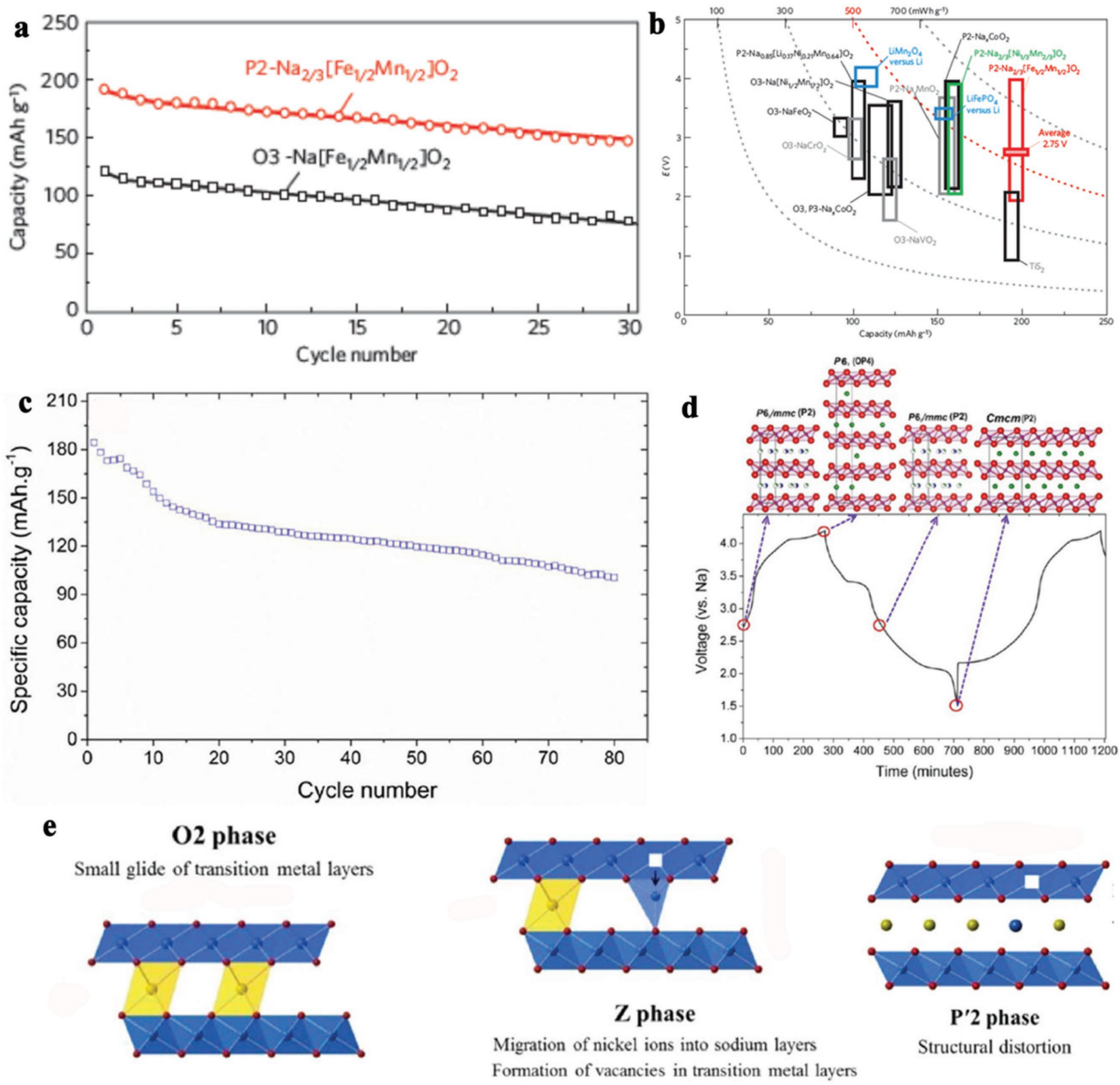

Figure 5. a) Comparison of the discharge capacity retention of P2- and O3-$Na_{2/3}[Fe_{1/2}Mn_{1/2}]O_2$ (NFMO) in sodium cells within 1.5–4.3 V at 12 mA g^{-1}.[48] b) A comparison of reversible capacity and operating voltage ranges of the layered sodium insertion materials.[48] c) Cycle stability of a typical NFMO-containing coin cell within 1.5–4.2 V at 0.1 C.[51] d) Phase evolution of the NFMO cathode during de-sodiation and sodiation.[51] e) Schematic diagram showing the structural transformation of $Na_{0.66}Ni_{0.33}Mn_{0.67}O_2$ observed experimentally.[67] Panel (a,b) reproduced with permission.[48] Copyright 2012, Nature Publishing Group. Panel (c,d) reproduced with permission.[51] Copyright 2015, American Chemical Society. Panel (e) reproduced with permission.[67] Copyright 2016, American Chemical Society.

2.1.2. O3-Type Layered Sodium Metal Oxide Cathodes

Unlike P2-type cathodes, O3-type cathodes possess higher Na content (very close to 1) and are hence more promising for practical application. The reversible sodium cycling from O3 α-$NaFeO_2$ in sodium-ion cells was first reported by Okada et al.[18] Komaba and co-workers further studied the cut-off voltage dependency on the structure and performance of the α-$NaFeO_2$ cathode.[74] Since then, layered Fe-based cathode materials such as $NaFe_{0.5}Co_{0.5}O_2$,[75] $Na_xMn_{1/3}Fe_{2/3}O_2$,[76] $NaFeO_2$-$Na[Ni_{1/2}Mn_{1/2}O_2]$,[77] $Na[Ni_{1/3}Fe_{1/3}Mn_{1/3}]O_2$,[78] $Na[Ni_{1/3}Fe_{1/3}Co_{1/3}]O_2$,[79] $Na[Ni_{0.25}Fe_{0.5}Mn_{0.25}]O_2$,[80] and $Na(NiCoFeTi)_{1/4}O_2$[81] have been thoroughly examined within a cut-off voltage of 4.0 V or lower. It was found that moderate capacities in the range of ≈100–140 mA h g^{-1} can be obtained but at the expense of use of toxic Co.[74–76] It should be also noted that adding Co could increase the cost of the cathode material. To address this problem, Hu's group reported a O_3-$Na_{0.9}[Cu_{0.22}Fe_{0.30}Mn_{0.48}]O_2$

cathode based on Cu, Fe, and Mn elements.[82] This cathode could deliver ≈100 mA h g^{-1} with stable cycle life up to 100 cycles. Moreover, an O_3-$Na_{0.9}[Cu_{0.22}Fe_{0.30}Mn_{0.48}]O_2$/hard carbon prototype SIB was demonstrated, which can provide an energy density of 210 Wh kg^{-1} within 100 cycles. In another study, Lee et al. reported that more than 20% of the Fe^{4+} species that was generated in the de-sodiated $Na_{1-x}FeO_2$ electrode was spontaneously reduced back to Fe^{3+} during open circuit storage of a charged cell.[83] They further found that part of iron ions would migrate to neighboring tetrahedral sites in sodium layers and subsequently result in pinning the original O3 phase down and blocking sodium diffusion pathways. Therefore, the chemical and structural instabilities related to the Fe^{4+}/Fe^{3+} species require more attention for the future development of stable layered Fe-based cathode.

O3-$NaCrO_2$ material has also attracted considerable interest as an SIB cathode. Hagenmuller and co-workers reported that $NaCrO_2$ can accommodate reversible de-intercalation/intercalation of Na^+ in the early 1980s.[84] Later, Komaba et al. also revealed that a reversible Cr^{4+}/Cr^{3+} redox reaction can take place during the electrochemical reaction of O3-$NaCrO_2$ because of its large interslab distance.[85] Moreover, good thermal stability of de-sodiated O3-$NaCrO_2$ was confirmed by Xia and Dahn.[86] In addition, carbon coating can effectively increase cycle stability, rate performance and heat generation onset temperature of the $NaCrO_2$ cathode.[87] The electrode performance of O3-$NaCrO_2$ at elevated temperature (80 °C) has been recently reported in pure ionic liquid–alkali metal ions (Na^+ and K^+) as cations, and bis(fluorosulfonyl)amide (FSA) as an anion, excellent cyclability, and rate capability have been demonstrated.[88] Recently, Fu and co-workers further demonstrated the feasibility of utilizing the reversible Cr^{6+}/Cr^{3+} redox couple during the charge/discharge process in O3-type layered $NaFe_{1/3}Cr_{1/3}Mn_{1/3}O_2$ cathode.[89] They found that Fe^{3+} and Mn^{4+} doping can prevent the disproportionation reaction of Cr^{4+}. Therefore, this O3-type $NaFe_{1/3}Cr_{1/3}Mn_{1/3}O_2$ can deliver 186 mA h g^{-1} together with good Coulombic efficiency (CE) for room-temperature SIBs. However, due to the harmful effect of Cr^{6+} to the environment and human body, it needs to be carefully handled.

Considering the success of the Li[NiCoMn]O_2 family as the cathode in LIBs, Prakash and co-workers revisited the Na-based layered oxides with special attention to $NaNi_{1/3}Mn_{1/3}Co_{1/3}O_2$.[65] Recently, Sun and co-workers conducted a systematic study on layered $Na[Ni_xCo_yMn_z]O_2$ cathodes to investigate the role of transition metal on their specific capacities, cycle stability, and abuse tolerance.[90] It can be concluded that increasing the content of Ni in the material can have higher specific capacity but at the expense of decreased cycle stability; Co is mainly used to stabilize the crystal structure and can thus improve the cycle stability; while Mn is related to the safety issue of the cathode materials, i.e., higher Mn, better thermal stability. Sun and co-workers further explored the morphological effects on the electrochemical performance of $Na[Ni_xCo_yMn_z]O_2$.[91] They proposed a full concentration gradient layered $Na[Ni_{0.60}Co_{0.05}Mn_{0.35}]O_2$ cathode (**Figure 6**a,b), which demonstrated much better electrochemical performance than bulk sample without concentration gradient distribution.[91] The hierarchical columnar $Na[Ni_{0.60}Co_{0.05}Mn_{0.35}]O_2$ can maintain a reversible capacity of above 120 mA h g^{-1} after 100 cycles at 15 mA g^{-1}. Furthermore, a $Na[Ni_{0.60}Co_{0.05}Mn_{0.35}]O_2$/hard carbon prototype cell that can deliver 143 mA h g^{-1} with a stable cycle life up to 300 cycles in 1.5–2.9 V was demonstrated (Figure 6c).

Similar to P2-type cathode materials, the stable cycle performance of the above-mentioned O3 cathode materials is usually obtained within a relatively low voltage range. The stabilities of cathode structures and electrolytes remain a serious concern during high-voltage cycling. For example, O3-$NaNi_{0.5}Mn_{0.5}O_2$ electrodes can deliver ≈125 mA h g^{-1} based on the Ni^{3+}/Ni^{2+} redox couple (Mn^{4+} is inactive) with stable cycle life at 4.8 mA g^{-1} in 2.2–3.8 V. However, when the voltage is increased to 4.5 V, despite a higher initial charge capacity up to 250 mA h g^{-1}, a large initial irreversible capacity loss together with poor cycle stability was observed (**Figure 7**a,b).[92] It has been also found that O3-$NaNi_{0.5}Mn_{0.5}O_2$ undergoes complicated structure evolution of $O3_{hex}$-$O3'_{mon}$-$P3_{hex}$-$P3'_{mon}$-$P3''_{hex}$ upon charging (Figure 7c). The formation of $P3''_{hex}$ phase is highly related to the incorporation of intercalation of electrolyte solvents considering the anomalously large interslab distances (≈7.0 Å), which would deteriorate the structure reversibility and further cycle stability. Sathiya et al. also reported that the $NaNi_{1/3}Co_{1/3}Mn_{1/3}O_2$ cathode can deliver higher capacity when raised the charge voltage to 4.2 V, but at the expense of intense capacity loss during the first few cycles in the case of O3-$NaNi_{1/3}Mn_{1/3}Co_{1/3}O_2$.[65] Using synchrotron-based operando high-energy XRD combined with electrochemical measurements, Wang et al. reported the dissymmetric phase transformation and structure evolution mechanism of layered O3-$NaNiO_2$ material during the initial charge/discharge process.[93] Phase transformation and deformation of O3-$NaNiO_2$ below 3.0 and over 4.0 V were attributed to the irreversible capacity loss in the initial cycle.

2.1.3. Strategies to Improve High-Voltage Cycling Stability

In the above section, we discussed the electrochemical behaviors of P2- and O3-type cathode materials at different voltage ranges. **Figure 8** compares the specific capacity, capacity retention, and cycle life of bare P2- and O3-type cathode materials reported in the literature. The star means lower voltage range (<4.1 V), while the circle represents high voltage range (>4.1 V). It can be found that most P2 and O3 cathodes present moderate capacities of around 120–150 mA h g^{-1} with a capacity retention of above 80% for up to 100 cycles. However, when cycled in the high-voltage range, the capacity retention was dramatically decreased to only 40% in some cases. Irreversible structure evolution such as P2-O2 (OP4) and O3-P3″ transformation, transition cation migration, stacking faults, oxygen activity and electrolyte decomposition are the main cause for the observed capacity fading. It is encouraging to see that significant improvements have been achieved in the past few years by using smart structure design approaches, which mainly include surface modification, cation and/or anion doping, and integrated structures.

Surface Modification: Surface modification has been frequently applied to enhance the cycle stability and rate capability of electrode materials for LIBs.[94] The coating materials include

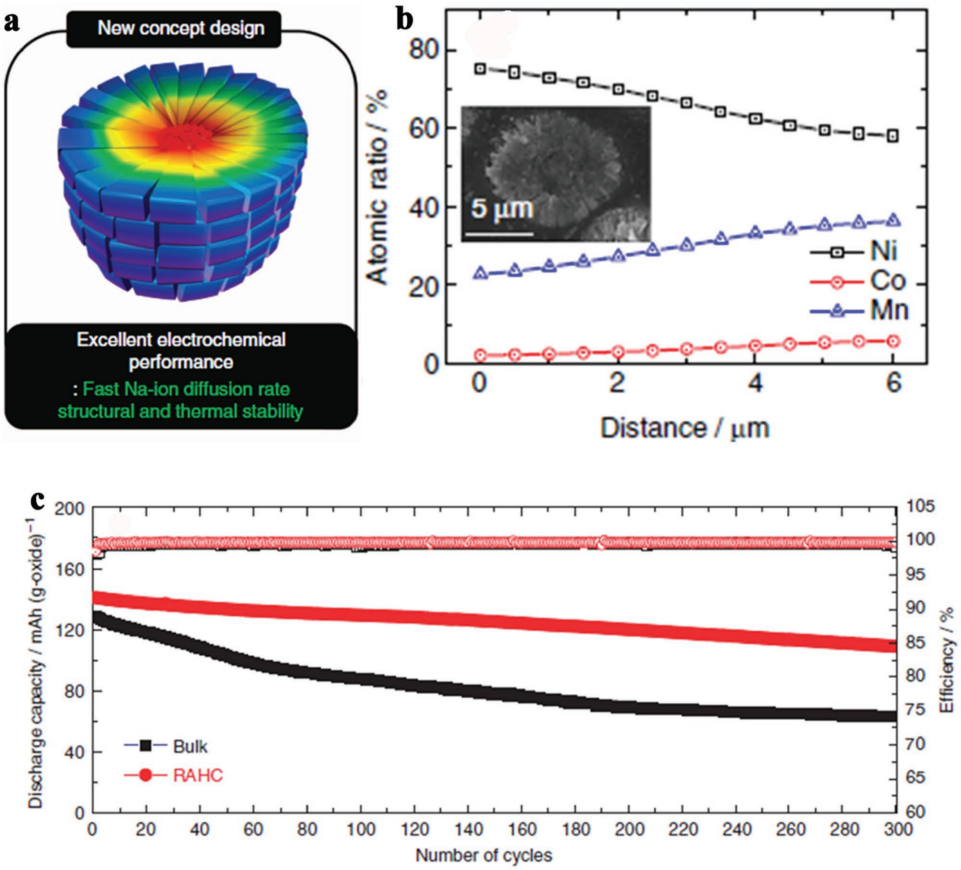

Figure 6. a) Representative hemisphere image of new concept design for the RAHC cathode materials. b) Electron probe microanalyzer results (inset: cross-sectional SEM image) of sodiated $Na[Ni_{0.60}Co_{0.05}Mn_{0.35}]O_2$. c) Long-term cycle retention of C/$Na[Ni_{0.60}Co_{0.05}Mn_{0.35}]O_2$ RAHC and C/bulk full cells (cutoff: 1.5–3.9 V, current density: 75 mA g^{-1}). Panel (a–c) reproduced with permission.[91] Copyright 2015, Nature Publishing Group.

mainly conductive carbon materials, metal oxides, metal fluorides and so forth.[95] The main function of surface modification is to suppress the side reactions between electrode materials and electrolytes. In the case of O3-type cathode materials, surface coating study to improve their cycle stability during high-voltage cycling has yet to be reported. So far, there are only a few reports on P2-type layered-structured cathode materials.

Park et al. reported a P2-$Na_{2/3}Fe_{1/2}Mn_{1/2}O_2$ cathode with a thin and uniform amorphous surface carbon coating layer by using 2, 3-dihydroxynaphthalene (DN) as a carbon source (**Figure 9**a).[96] It was reported that the 0.2 wt% DN-coated $Na_{2/3}Fe_{1/2}Mn_{1/2}O_2$ sample deliver 20% higher capacity than an uncoated sample within 2.0–4.2 V. Nevertheless, the capacity retention between the DN-coated and bare samples was almost the same (77.7% vs 77.8%), indicating that the increased capacity may mainly come from the increased electronic conductivity, while the phase instability during high-voltage cycling has not been well addressed. Sun's group claimed that, compared to carbon coating, metal oxide coatings can well maintain the electrode structure integrity, and could thus lead to better cycle stability.[97] Based on atomic layer deposition (ALD), they reported on an Al_2O_3-coated P2-type $Na_{2/3}(Mn_{0.54}Ni_{0.13}Co_{0.13})O_2$ (denoted as "MNC") cathode.[98] They found that an ultrathin Al_2O_3 layer (≈0.3 nm) on the MNC electrode can inhibit the side reactions between MNC particles and electrolytes. Therefore, it can effectively suppress the dissolution of the ion-conductive SEI, and minimize the dissolution of active materials into the electrolyte as well as increase the discharge capacity and cyclic stability of the pristine material, especially at high working voltage (2.0–4.5 V). Very recently, Meng and co-workers also reported on an Al_2O_3-coated P2-$Na_{2/3}Ni_{1/3}Mn_{2/3}O_2$ cathode with a coating thickness of 1 nm that was prepared using ALD (Figure 9b).[99] Although the capacity retention was not dramatically improved because of the severe phase transformation that occurs above 4.2 V (Figure 9c), the Al_2O_3 coating indeed improved the CE of the cathode material during cycling. The efficiency was 91.6% in the first cycle and quickly reached 99% in the fifth cycle in the case of ALD-coated sample. For comparison, an uncoated electrode exhibited an efficiency of 83.8% in the first cycle and 95.2% by the fifth cycle, indicating an irreversible reaction. Liu et al. recently reported that by using a wet-chemistry method, P2-$Na_{2/3}Ni_{1/3}Mn_{2/3}O_2$ with a thicker Al_2O_3 surface coating layer (≈12 nm) indeed demonstrated much better cycle stability than bare P2-$Na_{2/3}Ni_{1/3}Mn_{2/3}O_2$ within 2.5–4.3 V (71.8% vs 26.8% in 300 cycles).[60] Although surface modification can somehow enhance the cycle stability, unfortunately, it helps very little in the lattice electronic conductivity or chemical diffusion coefficient of Na ions within the crystal, which may play a more critical role on their capacity fading during high-voltage cycling.

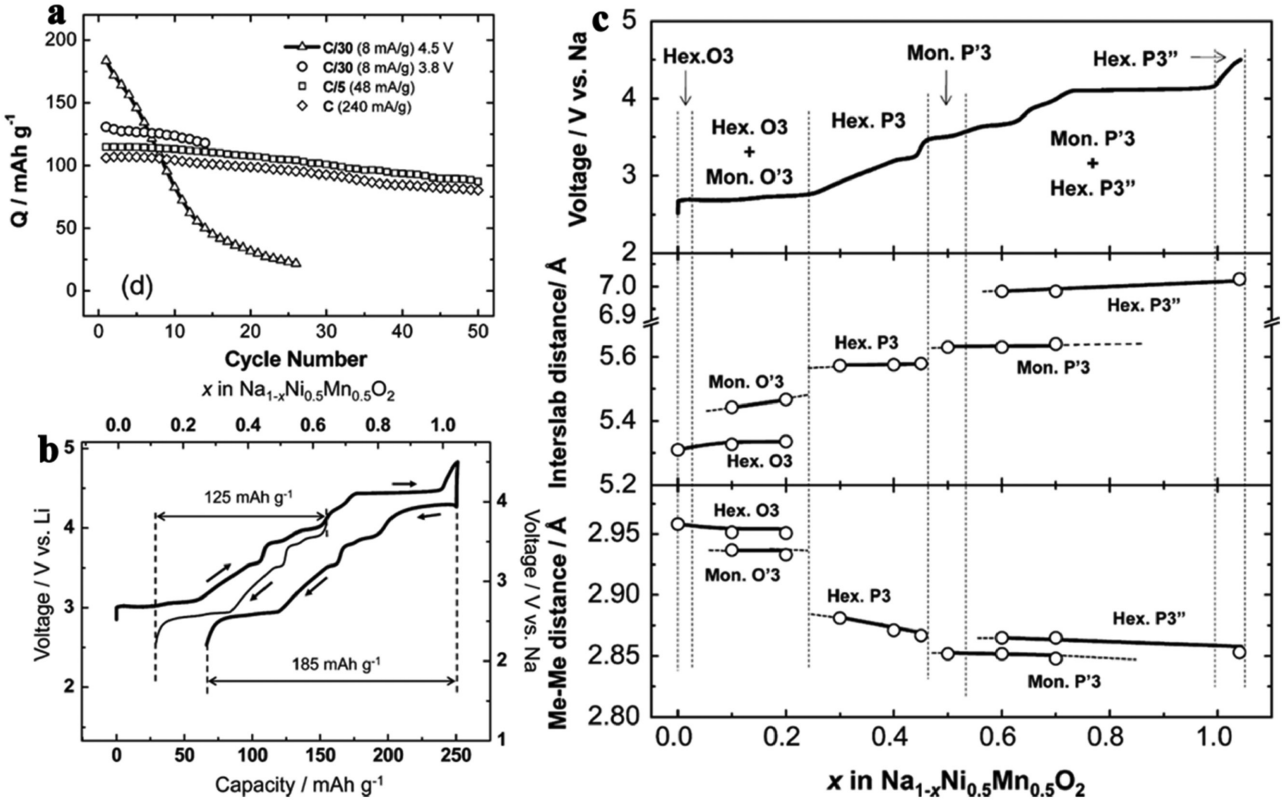

Figure 7. a) Discharge capacity retention of sodium/$NaNi_{0.5}Mn_{0.5}O_2$ cells under different experimental conditions. b) Initial charge and discharge curves of the sodium/$NaNi_{0.5}Mn_{0.5}O_2$ cell at a rate of 1/50 C (4.8 mA g^{-1}) in the voltage ranges of 2.2–3.8 and 2.2–4.5 V versus sodium metal. c) Change in the crystallographic parameters and phase evolution of $Na_{1-x}Ni_{0.5}Mn_{0.5}O_2$ as a function of the x value: averaged metal–metal interatomic distances (bottom) and interslab distances (middle). The first charge curve of the sodium/$NaNi_{0.5}Mn_{0.5}O_2$ cell is shown for comparison (top). Panel (a–c) reproduced with permission.[92] Copyright 2012, American Chemical Society.

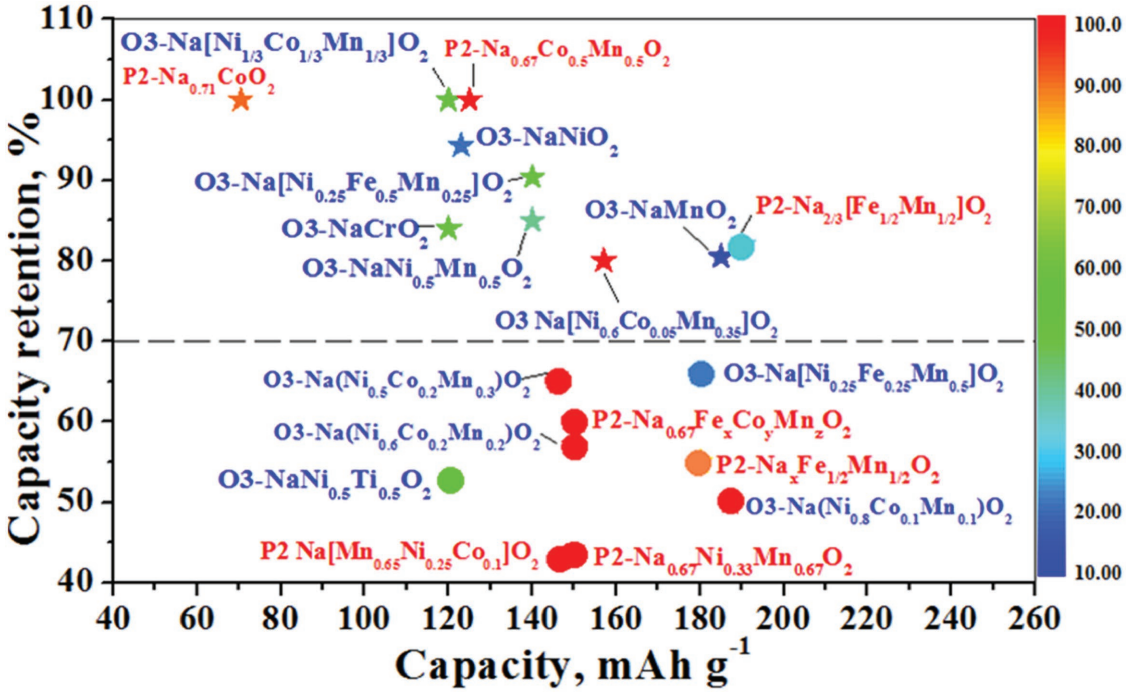

Figure 8. Plot of the capacity retention, specific capacity, and cycle life of some reported P2 and O3-type cathode materials for SIBs.

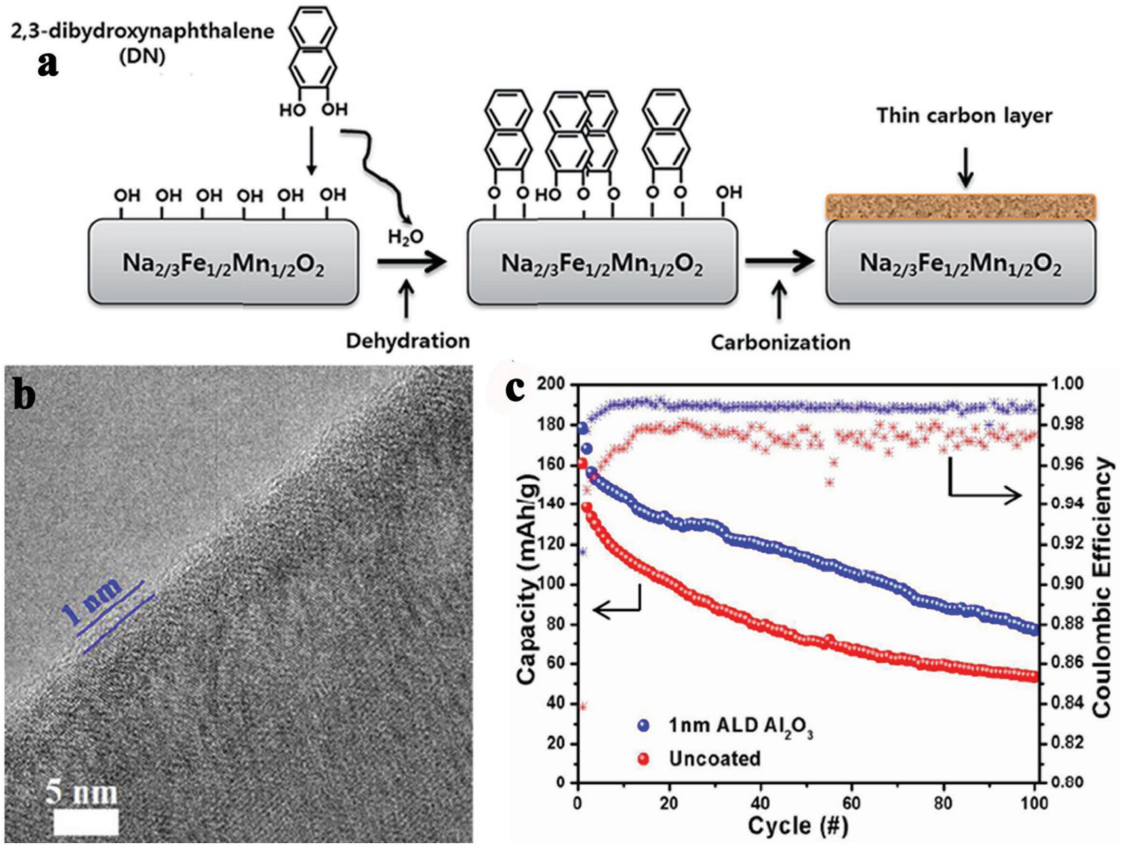

Figure 9. a) Schematic for the uniform carbon-coating process on P2-$Na_{2/3}Fe_{1/2}Mn_{1/2}O_2$.[96] b) TEM image of the uncycled Al_2O_3-coated $Na_{2/3}Ni_{1/3}Mn_{2/3}O_2$ composite electrode prepared by ALD.[99] c) Galvanostatically cycled electrodes demonstrating specific capacity versus cycle at C/20 rate and Coulombic efficiency as a function of cycle number.[99] Panel (a) reproduced with permission.[96] Copyright 2015, Royal Society of Chemistry. Panel (b,c) reproduced with permission.[99] Copyright 2017, American Chemical Society.

Cation and Anion Doping: Substitution of a small amount of Na^+, transition metal ions, and O^{2-} in NaT_MO_2 by other cations and anions has proved to effectively enhance the cycle stability of P2- and O3-type cathode materials during high-voltage cycling. Note that doping in the Na^+ site usually results in the formation of integrated structures, which will be introduced in the next section. Here we focus on the doping in the T_M sites and O sites for P2- and O3-type cathodes.

Cation Doping in T_M Sites: Monovalent doping. Li^+ doping on the T_M sites is an effective way to improve the structure stability of layered cathode materials during high-voltage cycling. Kim et al. for the first time reported that substitution of Ni and Mn in $Na[Ni_{0.25}Mn_{0.75}]O_\delta$ with a small amount of Li could stabilize the layered structure.[100] The Li-substituted $Na_{0.85}Li_{0.17}Ni_{0.21}Mn_{0.64}O_2$ presented smooth voltage profile within 2.0–4.2 V, indicating a single-phase sodium intercalation mechanism. After that, Meng and co-workers reported a Li-substituted layered P2-$Na_{0.80}[Li_{0.12}Ni_{0.22}Mn_{0.66}]O_2$ cathode also with smooth voltage profile (**Figure 10**a). They found that this material bypassed the irreversible P2-O2 phase transformation and well maintained the P2 structure even at the deep charge state (4.4 V), which is dramatically different from bare P2-type cathodes.[101] Using NMR, Meng and co-workers further found that part of Li ions migrate from the transition metal layer to the Na layer in the high-voltage region, and yet this process is highly reversible (Figure 10b). They further reported a Li-substituted O3-structured $NaLi_{0.07}Ni_{0.26}Mn_{0.4}Co_{0.26}O_2$ layered oxides, which had an initial high capacity of 147 mA h g^{-1} and stable cycle life within 1.5–4.5 V.[102] Sun and co-workers also reported a Li-substituted O3-type $Na[Li_{0.05}(Ni_{0.25}Fe_{0.25}Mn_{0.5})_{0.95}]O_2$, which can deliver 180.1 mA h g^{-1} together with good cycle stability during high-voltage cycling, showing much better electrochemical performance than bare $Na[Ni_{0.25}Fe_{0.25}Mn_{0.5}]O_2$ cathode.[103] It was found that the incorporation of Li into T_M layer improves the structural integrity because of stronger Li—O bond than Ni—O, and Mn—O bonds. As a result, the migration of Fe could be suppressed by the presence of Li in the crystal structure. Meng et al. further reported a Li-substituted O3-$Na_{0.78}Li_{0.18}Ni_{0.25}Mn_{0.583}O_w$ cathode, which shows exceptionally high discharge capacity of 240 mA h g^{-1} within 1.5–4.5 V (Figure 10c), leading to an ultra-high energy density of 675 Wh kg^{-1} (Figure 10d).[104]

Divalent Doping (Mg^{2+}, Zn^{2+}, and Cu^{2+}): Mg^{2+} doping is another popular way to enhance the cycle stability of high-voltage layered cathodes.[47,69,105–107] First-principles study has revealed that a small amount of Mg^{2+} doping in $NaCoO_2$ will improve the average intercalation potential as well as electronic conductivity and enhance the Na diffusion rate, which makes Mg-doped $NaCoO_2$ more attractive for cathode materials.[108] Bruce and co-workers reported that substitution of Mn^{3+} with Mg^{2+} can effectively suppress the Jahn–Teller effect of Mn^{3+} in

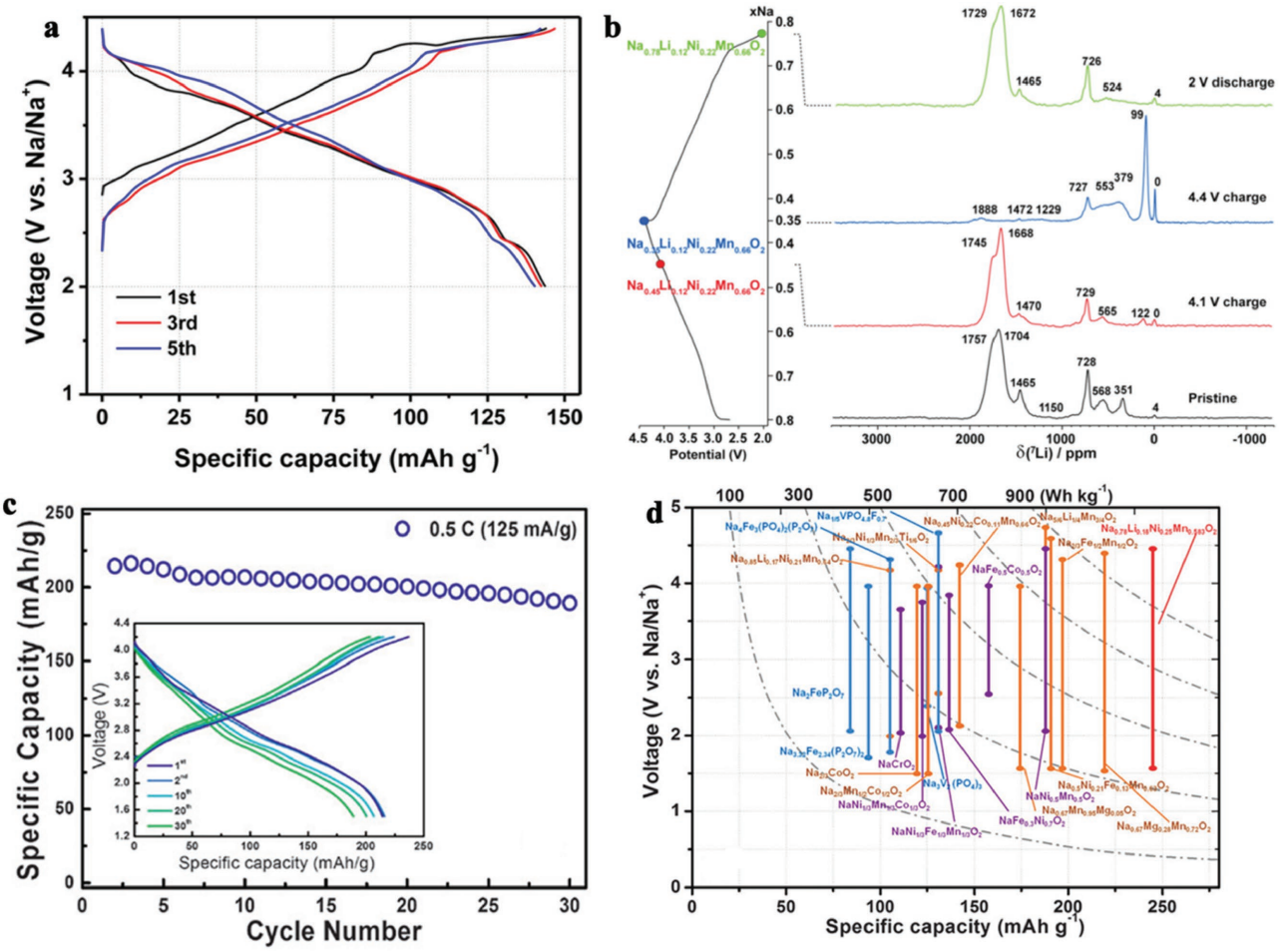

Figure 10. a) Electrochemical voltage profiles of $Na_{0.80}[Li_{0.12}Ni_{0.22}Mn_{0.66}]O_2$.[101] b) Isotropic slices of ^7Li *pj*-MATPASS NMR spectra acquired at 200 MHz on as-synthesized P2-$Na_{0.8}[Li_{0.12}Ni_{0.22}Mn_{0.66}]O_2$ and at three different stages along the first electrochemical cycle. *pj*-MATPASS experiments were performed by using a train of five nonselective $\pi/2$ pulses. The spectra have not been scaled to represent the total Li content in the sample at each stage of the cycle.[101] c) Cycling performance of $Na_{0.78}Li_{0.18}Ni_{0.25}Mn_{0.583}O_w$ with 125 mA g^{-1} current density. The inset is the corresponding electrochemical voltage profile.[104] d) Comparison of reversible capacities for the intercalation-based Na cathodes.[104] Reproduced with permission.[101,104] Panels (a,b) reproduced with permission.[101] Copyright 2014, American Chemical Society. Panels (c,d) reproduced with permission.[104] Copyright 2015, Royal Society of Chemistry.

P2-$Na_{0.67}MnO_2$.[105] Guo and co-workers also reported that substitution of Ni with Mg in P2-$Na_{0.67}Mn_{0.67}Ni_{0.33}O_2$ could prevent the irreversible P2-O2 phase transition, and could thus improve the capacity retention.[107] As shown in Figure 11a, with an optimum content of 5% Mg, the P2-$Na_{0.67}Mn_{0.67}Ni_{0.28}Mg_{0.05}O_2$ cathode can deliver 123 mA h g^{-1} with no sign of capacity fading in the initial cycles. Using solid-state NMR, synchrotron X-ray and neutron diffraction, Grey and co-workers performed a comprehensive study on the sodium storage performance and structural changes of P2-type $Na_xMn_{1-y}Mg_yO_2$ (y = 0.0, 0.05, 0.1) materials during electrochemical cycling. As shown in **Figure 11**b, in the bare P2-type Na_xMnO_2, complete phase transformation of P2-OP4 phase occurs by 3.6 V, when $x < 0.24$. In the 5% and 10% Mg-doped compounds, with an end-of-charge Na content of 0.28 and 0.32, respectively, the frequency of layer shearing events is reduced, and partial P2-to-OP4 phase transition takes place at a higher potential.[47] Yang and co-workers reported that Zn doping in the T_M layers can have similar benefits on the structure stability, leading to smoother voltage profiles and improved capacity retention (Figure 11c).[68] The Zn-substituted sample $Na_{0.66}Ni_{0.26}Zn_{0.07}Mn_{0.67}O_2$ delivers higher reversible capacity of 118 mA g^{-1} after 30 cycles than Zn-free samples. Kang et al. further compared the effect of Cu^{2+}, Mg^{2+}, and Zn^{2+} doping on the $Na_{0.67}MnO_2$.[109] In these cases, Mg and Zn are inactive, while Cu^{3+}/Cu^{2+} redox reaction took place during the electrochemical reaction. Figure 11d compares the voltage profiles of the samples with Mg^{2+}, Zn^{2+}, and Cu^{2+} doping. Among them, $Na_{0.67}Cu_{0.2}Mn_{0.8}O_2$ show higher average working voltage, which can lead to higher energy density. Figure 11e further revealed that Cu^{2+} doping can also significantly enhance the rate capability, while the improvements by Zn^{2+} and Mg^{2+} are minimal.

Trivalent (Al^{3+}) Doping: Ceder et al. reported that Al substitution in $LiCoO_2$ could increase the intercalation potential using first principles calculations.[110] Since that time, Al doping has been widely used in cathode materials of LIBs to

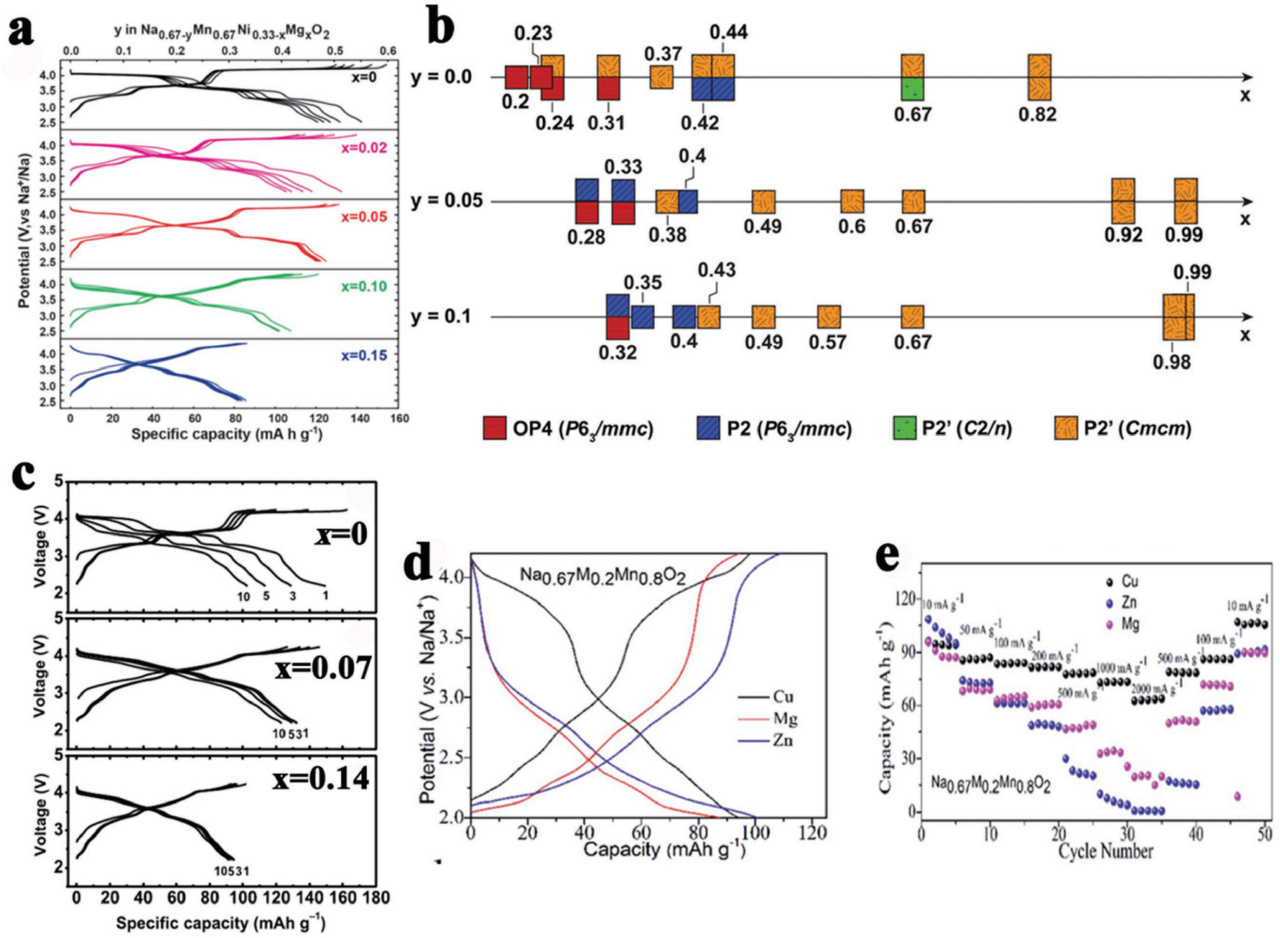

Figure 11. a) Galvanostatic charge/discharge voltage profiles of various P2-type $Na_{0.67}Mn_{0.67}Ni_{0.33-x}Mg_xO_2$ electrodes ($x = 0$, 0.02, 0.05, 0.10, and 0.15) at 0.1C (1C = 173 mA g^{-1}).[107] b) Ranges of P2, P2′, and OP4 phase stability for $Na_xMn_{1-y}MgyO_2$ ($y = 0.0$, 0.05, 0.1) upon electrochemical Na removal and reinsertion, obtained from Rietveld refinements of diffraction data.[47] c) Charge/discharge curves of $Na_{0.66}Ni_{0.33-x}Zn_xMn_{0.67}O_2$ ($x = 0$, 0.07, and 0.14) at a current density of 12 mA g^{-1}.[68] d) The comparison of representative charge/discharge curves at 10 mA g^{-1} and e) the rate capabilities of $Na_{0.67}M_{0.20}Mn_{0.80}O_2$ (M = Cu, Zn and Mg) electrodes.[109] Panel (a) reproduced with permission.[107] Copyright 2016, Wiley-VCH. Panel (b) reproduced with permission.[47] Copyright 2016, Royal Society of Chemistry. Panel (c) reproduced with permission.[68] Copyright 2015, Elsevier. Panel (d,e) reproduced with permission.[109] Copyright 2015, Royal Society of Chemistry.

improve their structure stability. It has been found that Al stabilizing effect mainly comes from the strong Al—O iono-covalent bonding via Al(s)-O(p) overlap with a high degree of charge transfer from Al to oxygen.[111] In 2013, Yuan et al. firstly investigated the impact of Al doping on the layered cathode materials for SIBs.[112] As shown in **Figure 12**a, the $Na_{0.67}[Mn_{0.65}Ni_{0.15}Co_{0.15}Al_{0.05}]O_2$ cathode presented stable voltage profiles in 50 cycles, while the Al-free sample exhibited a noticeable voltage decrease at the high voltage region, indicating that Al doping significantly improved the structural stability during high-voltage charging. Therefore, the cycle stability of Al-doped cathode was improved (Figure 12b). Hassoun and co-workers also reported that the Al-doped P2-type $Na_{0.6}Ni_{0.22}Al_{0.11}Mn_{0.66}O_2$ can attain stable and high reversible capacity of over 200 mA h g^{-1} in 50 cycles within 1.5–4.6 V (Figure 12c).[113] Using operando scanning electron microscopy (SEM) and XRD, they found that the low conductivity of the high-voltage phase may be related to the appearance of O stacking within the P-type structure (Figure 12d).

Quadrivalent Doping (Ti^{4+} and Zr^{4+}): There is also considerable interest in Ti^{4+} doping to stabilize the crystal structure of P2- and O3-type cathodes for SIBs. Komaba and co-workers reported with 1/6 Ti^{4+} substitution for Mn, the $Na_{2/3}Ni_{1/3}Mn_{1/2}Ti_{1/6}O_2$ can deliver 127 mA h g^{-1} with stable cycle life (**Figure 13**a).[114] For O3-type cathode material, Guo and co-workers recently reported a Ti-substituted $NaNi_{0.5}Mn_{0.5-x}Ti_xO_2$ with reversible O3-P3 phase transition upon Na^+ de-intercalation/intercalation, which delivered an initial discharge capacity of 135 mA h g^{-1} with 85% capacity retention after 200 cycles at 1C based on the Ni^{3+}/Ni^{2+} redox couple.[115] They further reported the co-doping of Cu/Ti in $NaNi_{0.45}Cu_{0.05}Mn_{0.4}Ti_{0.1}O_2$ can significantly extend the cycle life up to 500 cycles and enhanced structure stability toward moisture.[116] Unfortunately, the Komaba et al. and Guo et al. groups tested the Ti^{4+}-doped materials only within 2.0–4.0 V; their electrochemical behavior in the high-voltage region was not explored. Indeed, Chen and co-workers reported a Ti-substituted O3 $Na[Ni_{0.4}Fe_{0.2}Mn_{0.4-x}Ti_x]O_2$ cathode, which displays

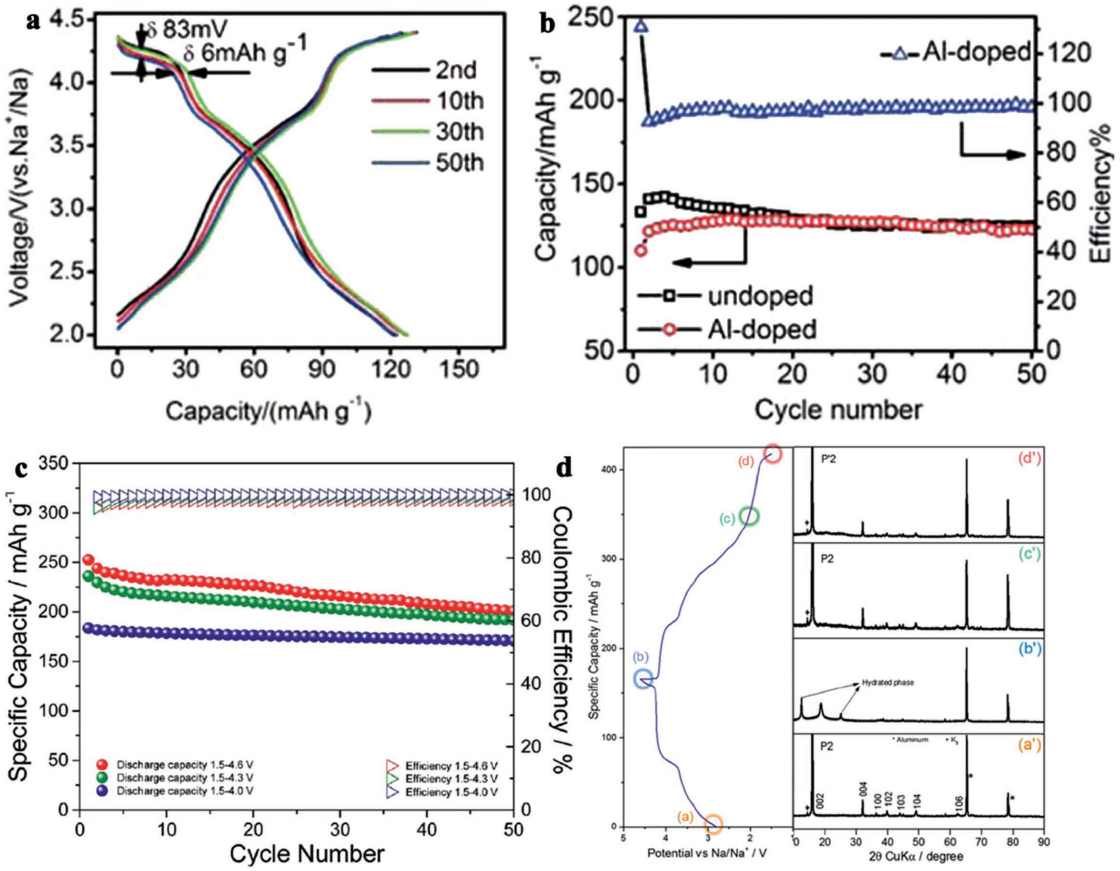

Figure 12. a) Charge/discharge curves of Al-doped $Na_{0.67}[Mn_{0.65}Ni_{0.15}Co_{0.15}Al_{0.05}]O_2$ (NaMNC) at 20 mA g^{-1}.[112] b) Comparison on the cycling performance of undoped and Al-doped NaMNC cathodes at 20 mA g^{-1}.[112] c) Cycling behavior of Na/P2-$Na_{0.6}Ni_{0.22}Al_{0.11}Mn_{0.66}O_2$ cells performed at 20 mA g^{-1} within various voltage ranges.[113] d) SEM micrographs of the P2-$Na_{0.6}Ni_{0.22}Al_{0.11}Mn_{0.66}O_2$ electrode at different charge/discharge states.[113] Panels a,b) reproduced with permission.[112] Copyright 2013, Royal Society of Chemistry. Panels c,d) reproduced with permission.[113] Copyright 2017, Royal Society of Chemistry.

much better electrochemical properties than previously reported $NaFe_y[Ni_{1/2}Mn_{1/2}]_{1-y}O_2$, which can maintain a reversible capacity of above 120 mA h g^{-1} in 200 cycles at 14 mA g^{-1} within 2.0–4.2 V (Figure 13b).[117]

Because of the larger ion radius and the stronger bond energy of Zr—O than Ni—O, Co—O, or Mn—O, Zr^{4+} doping has been also applied to enhance the cycling properties of layered cathode materials for SIBs.[118] The substitution of Zr^{4+} for Fe^{3+} can notably improve the cycle stability and rate performance. As shown in Figure 13c,d, the Zr-substituted P2-type $Na_{0.75}Mn_{0.55}Ni_{0.25}Co_{0.05}Fe_{0.15}O_2$ cathode showed better rate capability and cycle stability than the un-doped sample.

Doping in O Sites: Compared to cation doping, anion doping on the O sites has been much less reported. Very recently, Huang's group investigated the effect of F^- doping on the O3-type $NaNi_{1/3}Fe_{1/3}Mn_{1/3}O_2$.[119] The results indicate that the binding energy of oxygen changes as a result of F^- doping. In addition, F^- doping results in changes to the stoichiometry of Mn^{4+}/Mn^{3+}, which stabilizes the O3-type layered structure, thus improving cycling performance. Unfortunately, Huang et al. did not explore the effect of F^- doping on the cycle performance in high-voltage region. However, based on the significant improvements on the cycle stability of the high-voltage $Li[Ni_{1/3}Co_{1/3}Mn_{1/3}]O_2$ cathode and 5 V-$LiNi_{0.5}Mn_{1.5}O_4$ cathode by fluorine doping, anion doping on the layered cathodes of SIBs should attract more attention in the future. The improved reaction mechanism by anion doping should be also explored to find out the best chemical composition.

Integrated Structures: Integrated structures have been recently proposed to integrate the advantages of P-type and O-type cathode materials. The intergrowth structures are composed of topotactic layers with nanometer thickness. Thus, these nanodomains will affect the crystal structure evolution of their adjacent layers. There are two reported approaches to form the intergrowth structures: one is to substitute Na with Li^+ or K^+; the other is to control the synthesis conditions.

The earlier intergrowth work related to layered cathode materials for SIBs was reported by Lee et al.[120] As shown in **Figure 14**a, Li substitution for Na in $Na_{1-x}Li_xNi_{0.5}Mn_{0.5}O_2$ undergo a Na-O3, Na-P2, and Li-O3 phase transition along with increasing Li content. With an optimal Li content of 0.3, an O3-majority P2/O3 intergrowth structure was formed, which was confirmed by high-resolution TEM (HRTEM) (Figure 14b). As shown, the topotactic intergrowth of P2 and O3 at an atomic scale can be clearly observed. The rate performance comparison in Figure 14c showed that Li substitution can significantly enhance the rate performance of $Na_{1-x}Li_xNi_{0.5}Mn_{0.5}O_2$. The O3-dominated $Na_{0.7}Li_{0.3}Ni_{0.5}Mn_{0.5}O_{2+d}$ can maintain

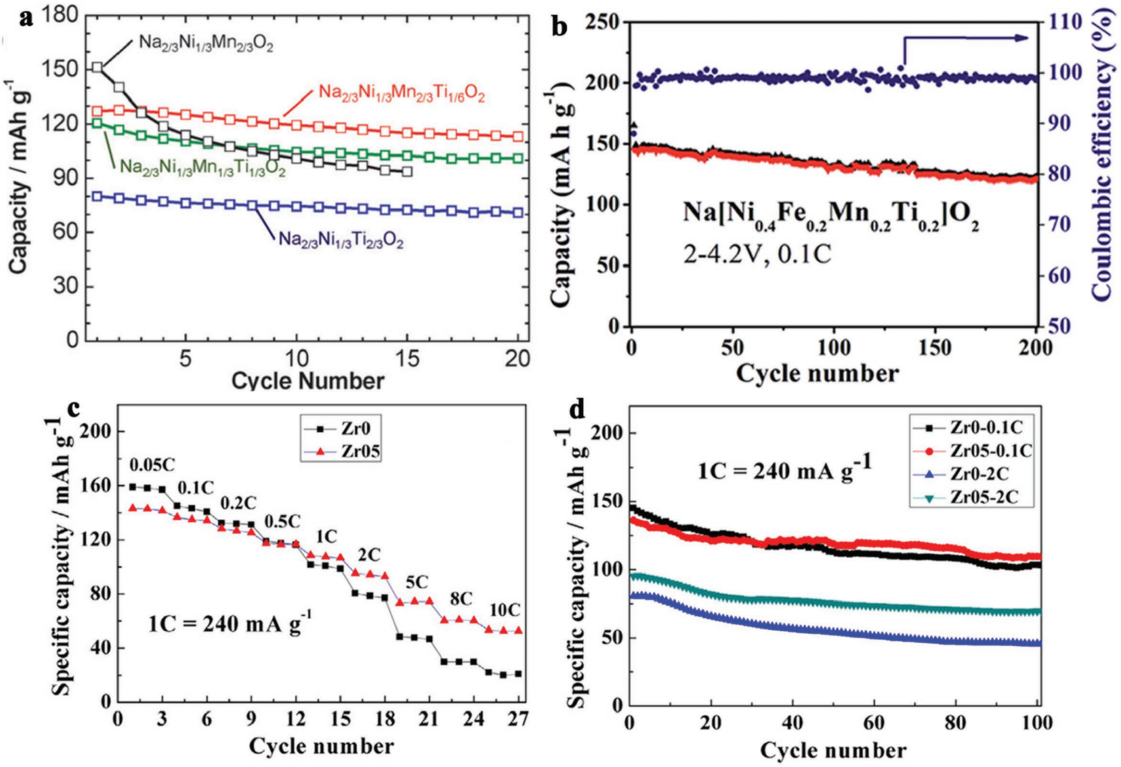

Figure 13. a) Capacity retention of Na//$Na_{2/3}Ni_{1/3}Mn_{2/3-x}Ti_xO_2$ ($0 \le x \le 2/3$) cells.[114] b) The cycling performance and the Coulombic efficiency of Na/$Na[Ni_{0.4}Fe_{0.2}Mn_{0.2}Ti_{0.2}]O_2$ at 0.1 C rate in the voltage range of 2–4.2 V. Reproduced with permission.[117] c) Rate capability and d) cycle performance at high rates for bare and Zr-doped $Na_{0.75}Mn_{0.55}Ni_{0.25}Co_{0.05}Fe_{0.15}O_2$.[118] Reproduced with permission.[114,117,118] Panel (a) reproduced with permission.[114] Copyright 2014, Royal Society of Chemistry. Panel (b) reproduced with permission.[117] Copyright 2014, Royal Society of Chemistry. Panels c,d) reproduced with permission.[118] Copyright 2017, Elsevier.

almost 95% of its initial capacity when the current density is increased from 15 to 150 mA g^{-1}, much higher than Li-free $NaNi_{0.5}Mn_{0.5}O_2$ (40%). However, the cycle life is limited to only 20 cycles as the O3-P3 phase transition dominated during the cycling process. For this reason, Zhou and co-workers reported a P2+O3 $Na_{0.66}Li_{0.18}Mn_{0.71}Ni_{0.21}Co_{0.08}O_{2+d}$ layered oxide composite by integrating minor O3 into lithium-substituted P2-majority layered material.[121] The scanning TEM for the nearby interface of P2- and O3-type phases indicates the coherent orientation relationship by intergrowth of nanoscale domains (Figure 14d). The electrochemical test showed that the P2+O3 $Na_{0.66}Li_{0.18}Mn_{0.71}Ni_{0.21}Co_{0.08}O_{2+d}$ can deliver 112.5 mA h g^{-1} after 150 cycles at 0.5 C within 1.5–4.5 V. (Figure 14e). However, the interplay mechanism between O3 and P2 in the composite is not reported. Besides Li^+ doping, Wang et al. further investigated the effects of K^+ doping on P2-type $Na_{0.67}Mn_{0.72}Ni_{0.14}Co_{0.14}O_2$ materials.[63] They found that along with increasing K^+ content, P3-type phase emerged. This may be due to the large ionic radius of K^+, which will expand the interlayer d-spacing to form P3 phase. Therefore, the P2/P3 $Na_{0.66}K_{0.01}Mn_{0.72}Ni_{0.14}Co_{0.14}O_2$ showed very good rate performance. A reversible capacity of 112.0 mA h g^{-1} after 100 cycles was retained when cycled within 1.5–4.3 V at 2.0 C.

The above studies mainly focused on Li^+ or K^+ substitution on the Na sites to form layered NaT_MO_2 with integrated structures. Keller et al. reported that the phase structures of cathode materials can be tuning by controlling the synthetic conditions. P2, O3, and mixed P3/P2/O3-type cathodes can be prepared by controlling the sintering temperature and cooling process (**Figure 15**a).[122] Among them, P3/P2/O3 $Na_{0.76}Mn_{0.5}Ni_{0.3}Fe_{0.1}Mg_{0.1}O_2$ is able to deliver the highest reversible capacity within 2.0–4.3 V (Figure 15b). This result indicated that by optimizing the synthetic condition to formulate new mixtures with optimal P/O ratios, further improvements can be achieved. Using operando HEXRD, Xu et al. were able to track the phase structural transformation of layered cathode materials during their formation process.[123] It can be clearly seen in Figure 15c that triple-phase co-existence (P2/O3/O1) occurred along with increasing the calcination temperature. However, it was found that the P2/O3/O1 intergrowth structure gradually disappeared during the cooling process (Figure 15d). Based on this finding, Xu et al. prepared three layered cathode materials with P2/O3/O1, P2/O3, and P2/P3 structure (Figure 15e). The electrochemical testing showed that the reversible capacity and cycle stability of P2/O3/O1 cathode material was significantly improved compared to the other two kinds of cathode materials within 2.0–4.4 V (Figure 15f). This is because the unique intergrowth region formed in the P2/O3/O1 cathode material can help to stabilize the crystal structure and thus lead to an improved cycle performance.

Besides intergrowth P/O cathode materials, Zheng et al. reported a spinel-integrated P2-type layered cathode for high-power SIBs.[124] Compared to the bare P2-type cathode, the spinel-integrated $Na_{0.50}Ni_{1/6}Co_{1/6}Mn_{2/3}O_2$ demonstrates

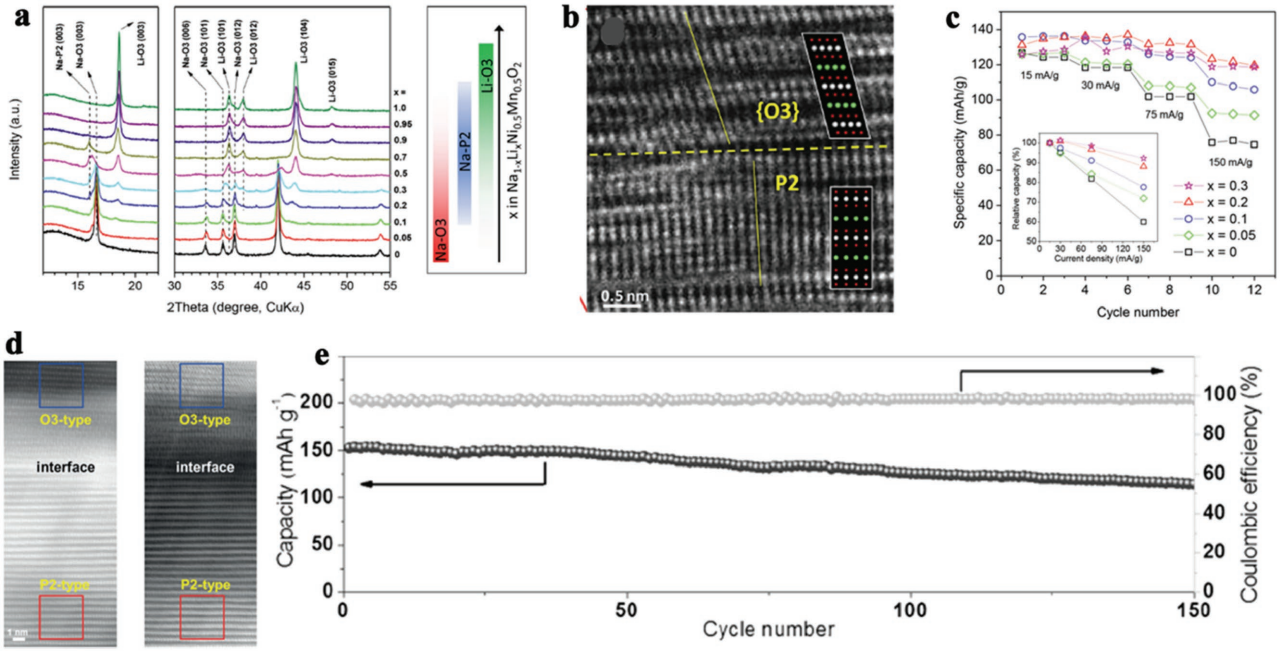

Figure 14. a) XRD patterns of $Na_{1-x}Li_xNi_{0.5}Mn_{0.5}O_{2+d}$ with different Li content, x ($0 \le x \le 1$) showing phase evolution of $Na_{1-x}Li_xNi_{0.5}Mn_{0.5}O_{2+d}$ as a function of Li content. The evolution of major phases is summarized by color switches in the right-side panel.[120] b) High-resolution TEM images directly showing the intergrowth stacking of the P2 and O3 lattices.[120] c) Rate performance of $Na_{1-x}Li_xNi_{0.5}Mn_{0.5}O_{2+d}$ ($0 \le x \le 0.3$).[120] d) High angle annular dark field and annular bright field images of P2+O3 $Na_{0.66}Li_{0.18}Mn_{0.71}Ni_{0.21}Co_{0.08}O_{2+d}$ (NaLiMNC) composite; the blue and red rectangles represent O3 structure and P2 structure areas.[121] e) The cycling performance with Coulombic efficiency of P2+O3 NaLiMNC composite at 0.5C rate. Panels (a–c) reproduced with permission.[120] Copyright 2014, Wiley-VCH. Panel (d,e) reproduced with permission.[121] Copyright 2015, Wiley-VCH.

significantly improved electrochemical performance. This finding was attributed to the improved electron transport in the integrated-spinel phase.

The intergrowth structures have opened up new opportunities for the development of high-performance SIBs. The optimal ratio amongst different phase structures is still unknown and deserves further investigation to achieve better electrochemical performance. In addition, the detailed functions of different phase structures are not very clear and may be related to their cycle stability and rate capability. Operando advanced diagnostic tools and computational modeling are needed to better explain the synergistic effect of intergrowth structures.

2.2. Polyanion Cathodes for SIBs

Polyanion-type cathodes have also received much attention as promising cathodes for future Na-ion batteries on account of their structural stability, safety, and appropriate operating potential,[125] which is owing to the strong inductive effect originating from the large high electronegativity anion groups.[4,11,12,36] In this section, we will discuss recent progress on the Polyanion cathode materials with energy density of ≈400 Wh kg^{-1} or higher, which would be $NaFePO_4$, $Na_3V_2(PO_4)_3$, fluorophosphates, and Co-based pyrophosphates.

2.2.1. $NaFePO_4$

The extensive studies of olivine $LiFePO_4$ as cathode of LIBs has stimulated the development of $NaFePO_4$ in SIBs.[126] As a counterpart of olivine $LiFePO_4$, $NaFePO_4$ has three kinds of crystal structures, i.e., olivine, maricite, and amorphous.[4,12,36] Crystal structures of both olivine and maricite consist of slightly distorted FeO_6 octahedra and PO_4 tetrahedra. The difference between these two polymorphs is the corner-sharing and edge-sharing FeO_6 chains for olivine and maricite, respectively (**Figure 16**a).[127] A 1D Na^+ diffusion channel is clearly seen along the *b*-axis in the olivine crystal structure. In contrast, the maricite $NaFePO_4$ has edge-sharing FeO_6 units that share corners with neighboring PO_4, showing no cationic channels for Na^+ movement (Figure 16b).[128] Thus, maricite $NaFePO_4$ is generally considered as electrochemical inactive. However, Kim et al. demonstrated that nanosized maricite $NaFePO_4$ could be electrochemically active.[129] Maricite $NaFePO_4$ with a particle size of 50 nm can deliver an initial capacity of 142 mA h g^{-1} and maintain ≈135 mA h g^{-1} after 200 cycles within 1.5–4.5 V (Figure 16c). It was confirmed by XRD and extended X-ray absorption fine structure (EXAFS) that maricite $NaFePO_4$ was transformed into amorphous $FePO_4$ after initial charge process, which substantially decreased the Na migration barriers, as confirmed by quantum mechanics calculations. This conclusion is further confirmed by the superior electrochemical performance of amorphous $NaFePO_4$. Li et al. reported hollow amorphous $NaFePO_4$ nanospheres on a large scale by a simple hard template process, with which the hollow nanospheres can deliver 152 mA h g^{-1} with 95% capacity retention after 300 cycles at 0.1 C (Figure 16d).[130]

Olivine $NaFePO_4$ cathode that has similar crystal structure to olivine $LiFePO_4$ has received more attention. However, the thermodynamically favored phase is maricite rather than olivine.

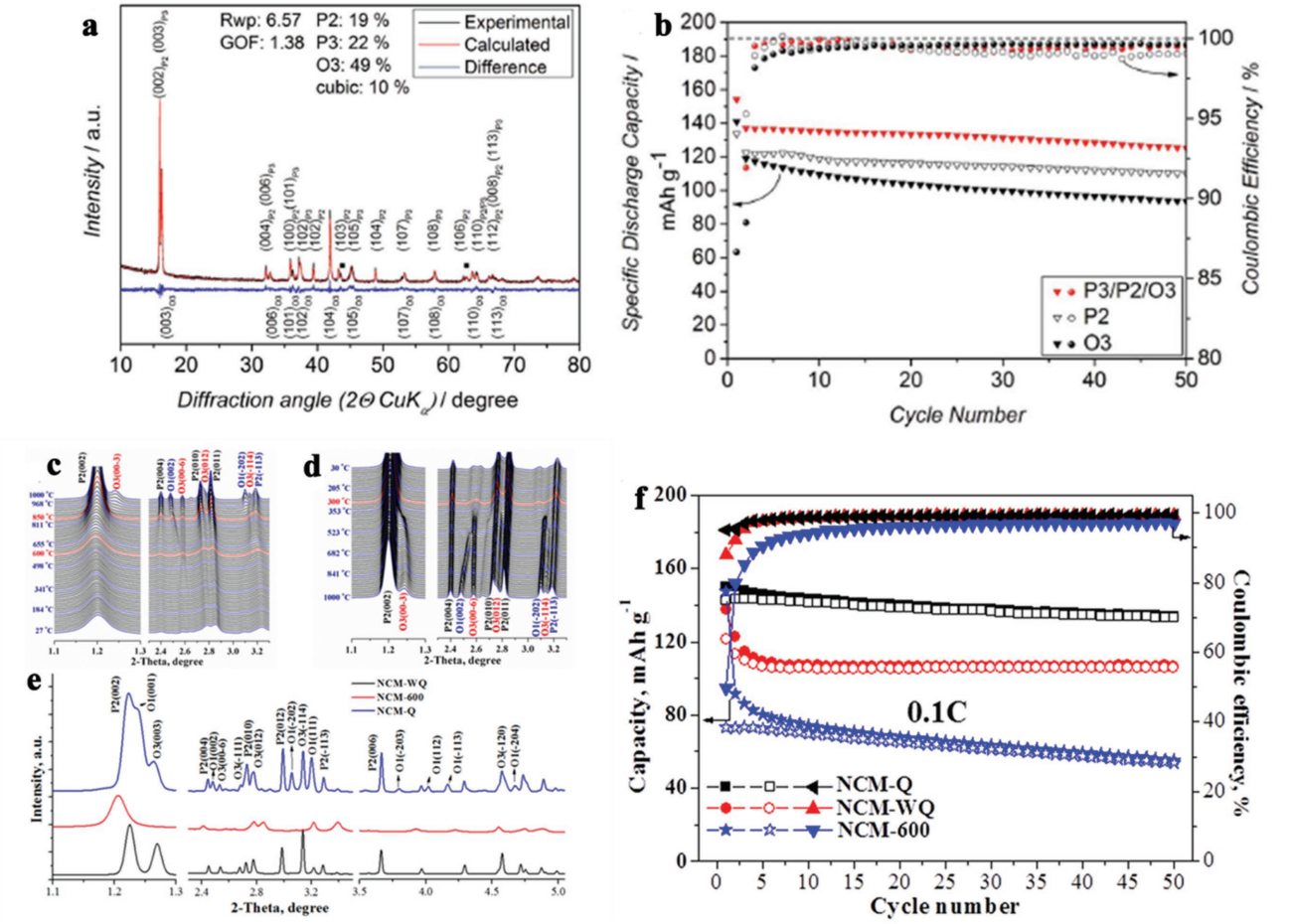

Figure 15. a) X-ray diffraction pattern and Rietveld refinement of P3/P2/O3-material.[122] b) Specific discharge capacities and Coulombic efficiencies versus cycle number for 50 cycles. Potential range: 2.0–4.3 V versus Na/Na^+.[122] In operando HEXRD patterns of the precalcined oxalate precursor during c) the heating process and d) the cooling process.[123] e) HEXRD patterns and f) cycle performance within 2.0–4.4 V for NCM-Q, NCM-WQ, and NCM-600.[123] Panels (a,b) reproduced with permission.[122] Copyright 2016, Wiley-VCH. Panels cf) reproduced with permission.[123] Copyright 2017, Royal Society of Chemistry.

Moreau et al. demonstrated that chemically sodiated olivine $NaFePO_4$ exhibits an irreversible phase transition from olivine to maricite $NaFePO_4$ at around 480 °C, resulting in significant volume shrinkage (Figure 16e).[131] Therefore, direct synthesis of olivine $NaFePO_4$ by conventional solid-state reactions at high temperature is very challenging. Olivine-type $NaFePO_4$ is usually prepared by an ion-exchange method from $LiFePO_4$ in either organic or aqueous solution.[132–134] Similar to $LiFePO_4$, the low electronic conductivity is the main challenge to attain $NaFePO_4$ cathode with outstanding electrochemical performance. Incorporating $NaFePO_4$ with highly conductive host materials is an effective way to overcome this drawback. Ali et al. reported that polythiophene-wrapped olivine $NaFePO_4$ exhibits superior performance compared with an uncoated electrode,[132] which can deliver an initial capacity of 142 mA h g^{-1} and still attain ≈132 mA h g^{-1} after 100 cycle at 10 mA g^{-1}. Also interesting is this material's sodiation/de-sodiation mechanism. Using in situ XRD, Galceran et al. reported that the charge and discharge reaction mechanisms are different.[135] The olivine $NaFePO_4$ undergoes a nonreversible charge/discharge process via an intermediate phase due to a large cell mismatch between the $NaFePO_4$ and the $FePO_4$. Three phases, $FePO_4$, $Na_{0.7}FePO_4$, and $NaFePO_4$, appear simultaneously on discharge, while they are separated into two first-order phase transitions on charge (Figure 16f). The notable differences in the reaction mechanism between $LiFePO_4$ and $NaFePO_4$ are reminders that the simple transfer of Li-ion technology to Na-ion systems is an oversimplification. Indeed, Zhu et al. reported that, C-$NaFePO_4$ shows much more inferior rate capability than C-$LiFePO_4$ that prepared by the same starting C-$FePO_4$.[134] Therefore, smart structure design is still required to address these problems and further improve the electrochemical performance of olivine $NaFePO_4$.

2.2.2. $Na_3V_2(PO_4)_3$

NASCION-type $Na_3V_2(PO_4)_3$ is a fast ion conductor with open 3D ion transport channels.[136] It mainly involves a reversible V^{4+}/V^{3+} redox couple occurring at 3.4 V during the electrochemical reaction.[137] In $Na_3V_2(PO_4)_3$, a 3D $[V_2P_3O_{12}]$ skeleton that is composed of VO_6 octahedra and PO_4 tetrahedra can be observed

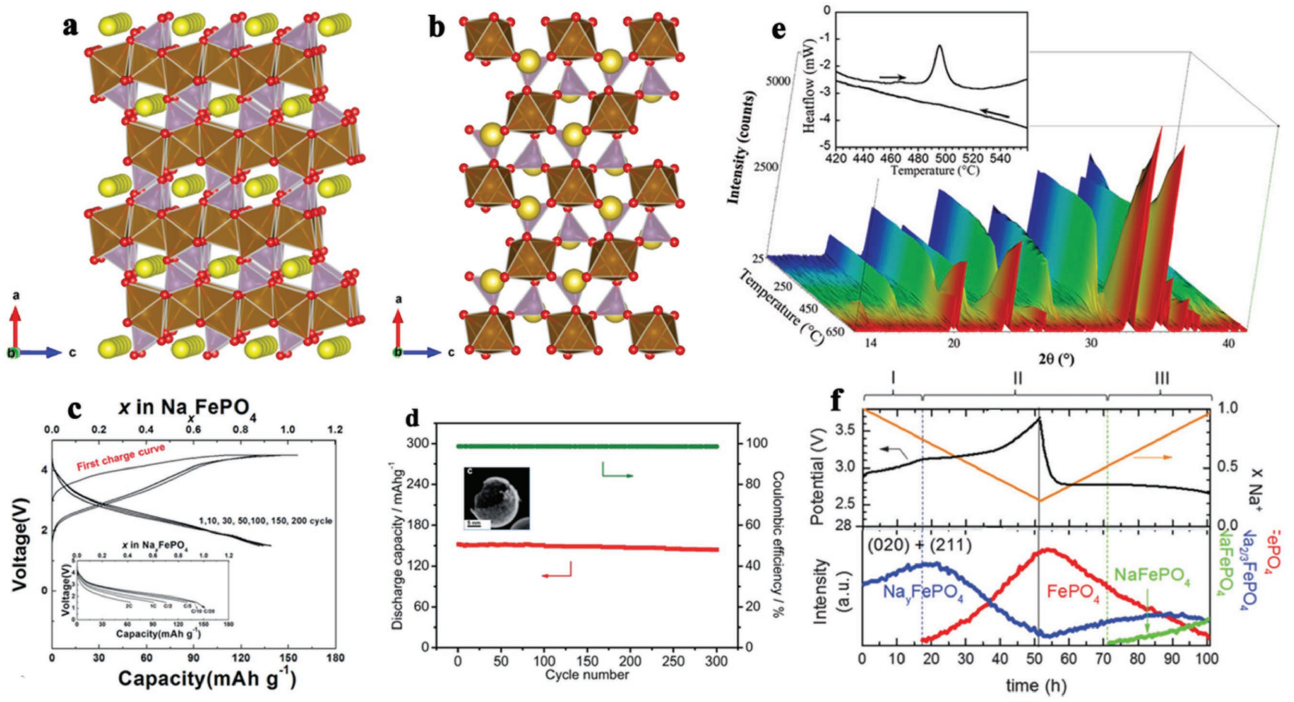

Figure 16. Crystal structure of a) olivine and b) maricite $NaFePO_4$. c) Galvanostatic curves of maricite $NaFePO_4$ over 200 cycles at C/20 in Na cell. Inset: discharge curves of maricite $NaFePO_4$ as a function of the rate from C/20 to 3C.[129] d) Cycling performance of amorphous $NaFePO_4$ cathode at 0.1C.[130] e) In situ XRD patterns of the olivine $NaFePO_4$ phase for increasing temperature from 25 to 650 °C. Inset: thermal differential analysis of the $NaFePO_4$ olivine phase. Reproduced with permission.[131] f) Voltage versus time curves of the in situ XRD experiment and sum of the integrated intensity of the (020) and (211) reflections for each of the phases involved versus time.[135] Panel (c) reproduced with permission.[129] Copyright 2015, Royal Society of Chemistry. Panel (d) reproduced with permission.[130] Copyright 2015, Royal Society of Chemistry. Panel (e) reproduced with permission.[131] Copyright 2010, American Chemical Society. Panel (f) reproduced with permission.[135] Copyright 2014, Royal Society of Chemistry.

(**Figure 17**a). The activation energies toward $Na_3V_2(PO_4)_3$ was investigated by Song et al. using first-principles calculations.[138] They found that two pathways along the *x*- and *y*-directions and one possible curved route for ion migration are favored with 3D transport characteristics (Figure 17b–d).[138] Despite the many advantages as cathodes of SIBs, $Na_3V_2(PO_4)_3$ still has low electron conductivity, which is the main barrier to achieve excellent electrochemical performance. In the past decades, carbon modification[139–167] and element doping[106,168–173] have proven to be effective ways to overcome this problem.

Carbon Modification: In the past few years, carbon coating, embedding, and supporting techniques have been widely employed to enhance the electrochemical performance of $Na_3V_2(PO_4)_3$. Jian et al. for the first time reported that $Na_3V_2(PO_4)_3$/C composite with a 6 nm carbon layer exhibits significantly improved Na storage performance.[154] This result has stimulated extensive researches to further optimize the performance of $Na_3V_2(PO_4)_3$ by particle downsizing or surface coating of conductive carbon. However, the surface carbon coating layer by decomposition of organic carbon precursor are usually amorphous, which has relatively low electric conductivity. For this reason, Fang et al. reported a facile chemical vapor deposition method to prepare a hierarchical carbon framework wrapped sub-micrometer $Na_3V_2(PO_4)_3$ (denoted as HCF-NVP), in which graphene-like coating layers are interconnected via graphited carbon nanofibers (Figure 17e).[146] The obtained HCF-NVP composite demonstrates outstanding electrochemical performance, which can maintain 54% of its initial capacity after 20 000 cycles at 30 C and can still deliver 38 mA h g^{-1} at extremely high rate of 500 C. Besides, Balaya and co-workers also reported a porous $Na_3V_2(PO_4)_3$/C cathode, which displayed exceptional long-term cycle stability up to 30 000 cycles at 40 C.[167]

There is also considerable effort on the fabrication of $Na_3V_2(PO_4)_3$/C composite by encapsulating $Na_3V_2(PO_4)_3$ in a unique carbon matrix. For example, Yu and co-workers embedded carbon-coated nanosized $Na_3V_2(PO_4)_3$ in a porous carbon matrix, which not only matches but even outshines sodium cathodes under high rate conditions (Figure 17f).[164] This material can be (dis)charged in 6 s at an extremely high rate of 22 A g^{-1} (200 C), still delivering 44 mA h g^{-1}. Yu and co-workers further replaced the porous carbon with highly ordered mesoporous carbon (CMK-3) owing to its unique pore structure (Figure 17g).[144] As a result, it exhibits superior rate capability and ultralong cyclability (78 mA h g^{-1} at 5 C after 2000 cycles) compared to carbon-coated NVP and pure NVP cathodes. However, the ordered mesoporous carbon presented inferior electrochemical performance compared with porous carbon, a finding that is not explained by the authors. On the other hand, Mai's group reported a novel layer-by-layer $Na_3V_2(PO_4)_3$@reduced graphene oxide (rGO) nanocomposite through modifying the surface charge of $Na_3V_2(PO_4)_3$ gel precursor (Figure 17h).[145] The well-confined $Na_3V_2(PO_4)_3$ nanocrystals in between rGO layers significantly facilitate the electron and Na^+ diffusion as

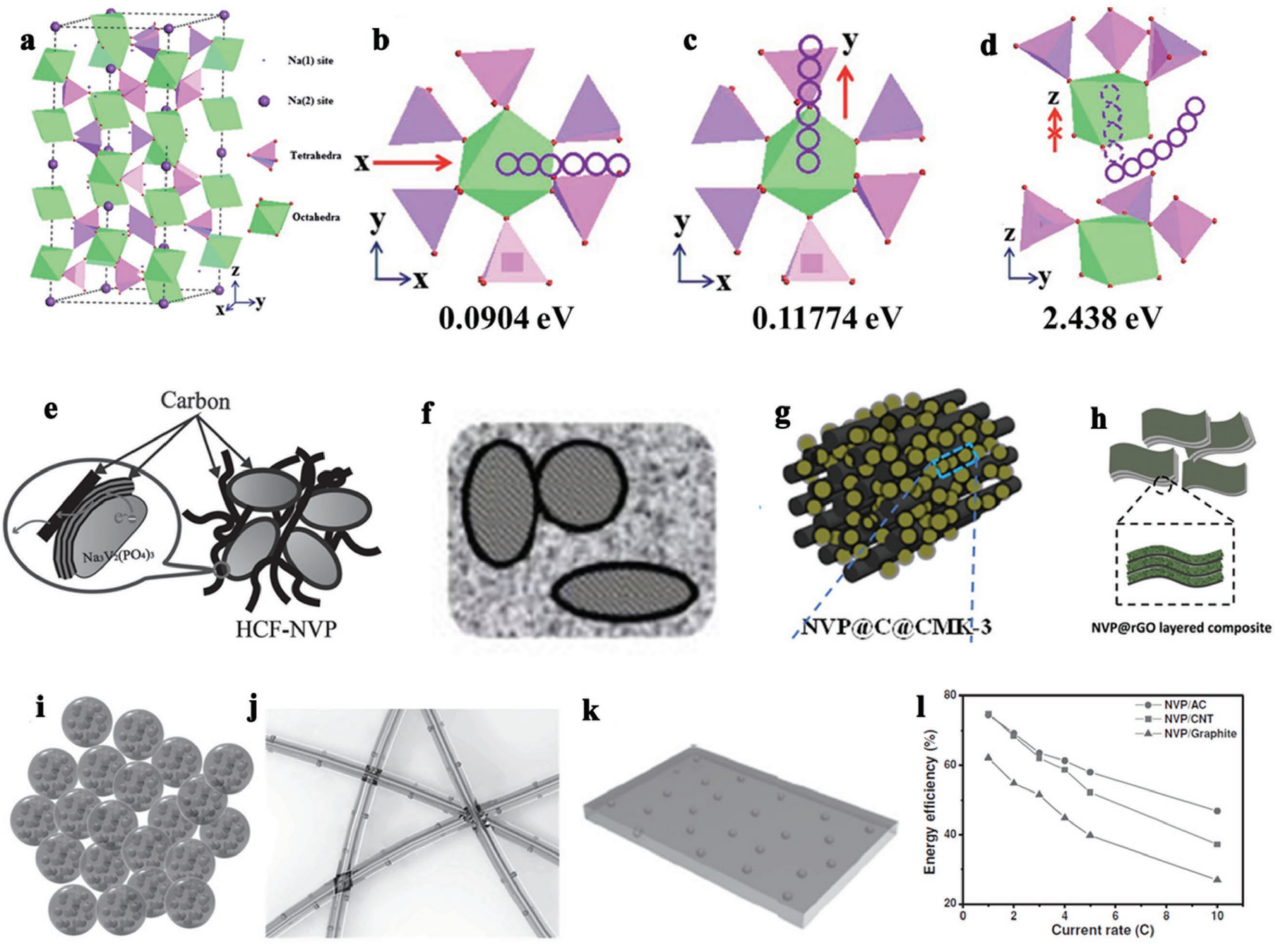

Figure 17. a) Schematic representation of $Na_3V_2(PO_4)_3$ structure.[138] Possible Na-ion migration paths in $Na_3V_2(PO_4)_3$ along b) *x*-, c) *y*-, and d) curved *z*-directions.[138] Schematic illustration of e) HCF-NVP,[146] f) C@NVP@porous carbon,[164] g) NVP@C@CMK-3,[144] and h) NVP@rGO layered composite.[145] Schematic illustration of i) NVP/AC, j) NVP/CNT, and k) NVP/graphite.[147] l) Rate capability of NVP/AC, NVP/CNT, and NVP/graphite.[147] Panel (a–d) reproduced with permission.[138] Copyright 2014, Royal Society of Chemistry. Panel (e) reproduced with permission.[146] Copyright 2015, Wiley-VCH. Panel (f) reproduced with permission.[164] Copyright 2014, American Chemical Society. Panel (g) reproduced with permission.[144] Copyright 2015, Wiley-VCH. Panel (h) reproduced with permission.[145] Copyright 2016, Wiley-VCH. Panels (i–l) reproduced with permission.[147] Copyright 2014, Wiley-VCH.

well as increase structure integrity, thus leading to superior cycle stability up to 15 000 cycles and excellent rate capability up to 200 C.

In addition, carbon-supporting $Na_3V_2(PO_4)_3$ composites are also a good way to attain better electrochemical properties.[147,160] Kim and co-workers reported a graphene-supported $Na_3V_2(PO_4)_3$ with excellent rate performance, which can significantly enhance the electronic conductivity.[160] With this material, 82% of initial 0.2 C discharge capacity can be still maintained even when the rate of increased to a 100-fold, 20 C. Li et al. further investigated the effect of supporting carbon matrix dimension on the performance of $Na_3V_2(PO_4)_3$/C, and found that the $Na_3V_2(PO_4)_3$ nanograins dispersed on 0D acetylene carbon nanospheres demonstrates the best rate performance because of the best electron and Na^+ transport (Figure 17i–l).[147]

Element Doping: Like in most cathode materials for rechargeable batteries, element doping is also an effective approaches to attain $Na_3V_2(PO_4)_3$ with significantly improved electrochemical performance. Lim et al. have investigated the impact of K^+ doping on Na sites of $Na_3V_2(PO_4)_3$ (**Figure 18**a).[171] The large ionic radius of K^+ can enlarge the d-spacing of $Na_3V_2(PO_4)_3$ along *c*-direction, which can facilitate the diffusion of Na^+, and thus improve the rate performance (Figure 18b,c). Furthermore, the K^+ can help to stabilize the crystal structure of $Na_3V_2(PO_4)_3$. On the other hand, Hu et al. reported a series of boron-substituted $Na_3V_2(P_{1-x}B_xO_4)_3$ cathodes in which B is doped on the P sites (Figure 18d).[174] The optimal composition of $Na_3V_2P_{3-1/6}B_{1/6}O_{12}$ exhibits the best cycling stability and rate capability among all the samples (Figure 18e). This improvement was attributed to the decrease of Na^+ diffusion energy barriers as confirmed by density functional theory (DFT) calculations (Figure 18f).

In fact, most of efforts have been devoted to cation doping on V sites, such as Mn^{2+},[173] Mg^{2+},[106,168] Al^{3+},[172] Fe^{3+}[175], and Cr^{4+},[169] to maintain the crystal structure and increase the electronic conductivity (Figure 18g). In addition to these effects, cation doping can remarkably improve the activity of V^{5+}/V^{4+}. For example, Lalere et al. reported that Al-doped $Na_3Al_{0.5}V_{1.5}(PO_4)_3$ can increase the energy density to above

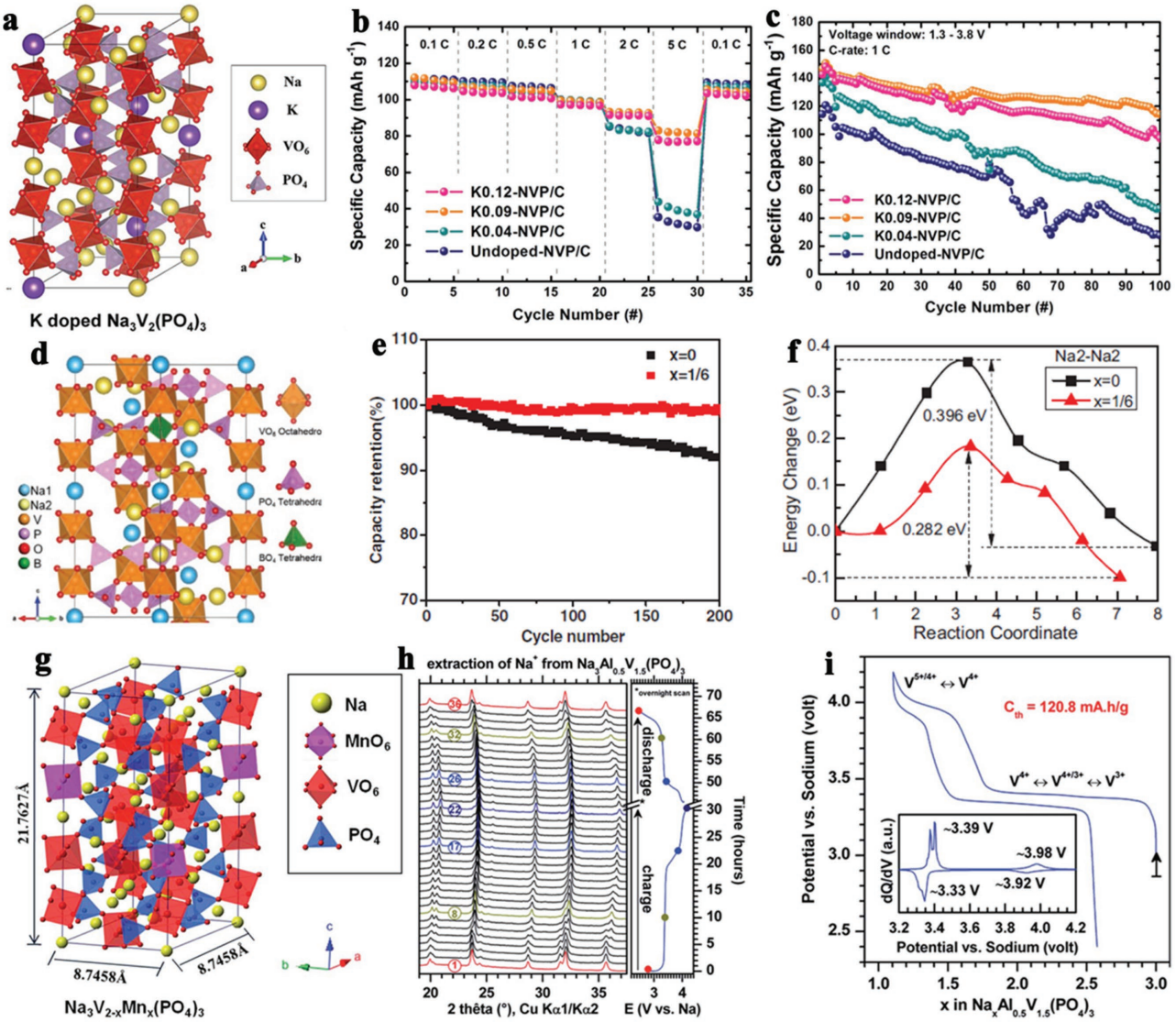

Figure 18. a) Schematic representation of K-doped $Na_3V_2(PO_4)_3$ structure.[171] b) Rate capabilities and c) cycle performance of $Na_{3-x}K_xV_2(PO_4)_3/C$.[171] d) Crystal structure of $Na_3V_2P_{3-x}B_xO_{12}$ ($x = 1/6$).[174] e) Cycling stability of the samples at 5 C.[174] f) The corresponding diffusion energy barriers along conduction path in $Na_3V_2P_{3-x}B_xO_{12}$ ($x = 0$ and $x = 1/6$).[174] g) The schematic illustration of $Na_3V_{2-x}Mn_x(PO_4)_3/C$ by Mn^{2+} partially replacing V^{3+} sites.[173] h) XRD patterns recorded operando for $Na_3Al_{0.25}V_{1.75}(PO_4)_3$ electrodes upon charge (operating on the V^{3+}/V^{2+} couple) at a current rate corresponding to 1 Na^+/30 h.[170] i) Electrochemical signatures of $Na_3Al_{0.5}V_{1.5}(PO_4)_3$ electrodes upon Na^+ extraction/insertion. Galvanostatic data were recorded for a current rate corresponding to 1 Na^+/20 h.[170] Panels (a–c) reproduced with permission.[171] Copyright 2014, Royal Society of Chemistry. Panels (d–f) reproduced with permission.[174] Copyright 2016, Wiley-VCH. Panel (g) reproduced with permission.[173] Copyright 2016, Royal Society of Chemistry. Panels (h,i) reproduced with permission.[170] Copyright 2015, Royal Society of Chemistry.

400 Wh kg^{-1}, which may because it could enable the reaction of V^{5+}/V^{4+} at 3.95 V (Figure 18h,i).[170]

Novel Cell Configuration: Very recently, Hu and co-workers reported an interesting flexible SIB using the $Na_3V_2(PO_4)_3$/rGO composite and Sb/rGO composite as the cathode and anode, respectively.[176] However, the reported flexible SIB may still suffer from the safety issue regarding metallic sodium formation during the overcharge process, because of the low Na storage potential of the Sb anode. It was reported that the $Na_3V_2(PO_4)_3$ electrode presents two voltage plateaus (3.4 V with a V^{4+}/V^{3+} redox reaction and 1.6 V with a V^{3+}/V^{2+} redox reaction) (**Figure 19**a).[177] Therefore, a symmetric $Na_3V_2(PO_4)_3//Na_3V_2(PO_4)_3$ full cell by employing $Na_3V_2(PO_4)_3$ as a bipolar electrode material was reported (Figure 19b). Zhang et al. further reported a free-standing $Na_3V_2(PO_4)_3//Na_3V_2(PO_4)_3$ symmetric full cell, which can deliver ≈100 mA h g^{-1} at 0.25 C and long cycle life up to 280 cycles at 2C.[177] Using a simple vacuum filtration method, Wang et al. can successfully prepared self-supported carbon-coated $Na_3V_2(PO_4)_3$/rGO electrodes (Figure 19c).[178] The symmetric full cell constructed with $Na_3V_2(PO_4)_3$@C@rGO//$Na_3V_2(PO_4)_3$@C@rGO presented a considerable capacity of ≈75 mA h g^{-1} and average working voltage of 1.7 V at 0.5 C. More importantly, under arbitrary bending conditions, this flexible full cell can still exhibit

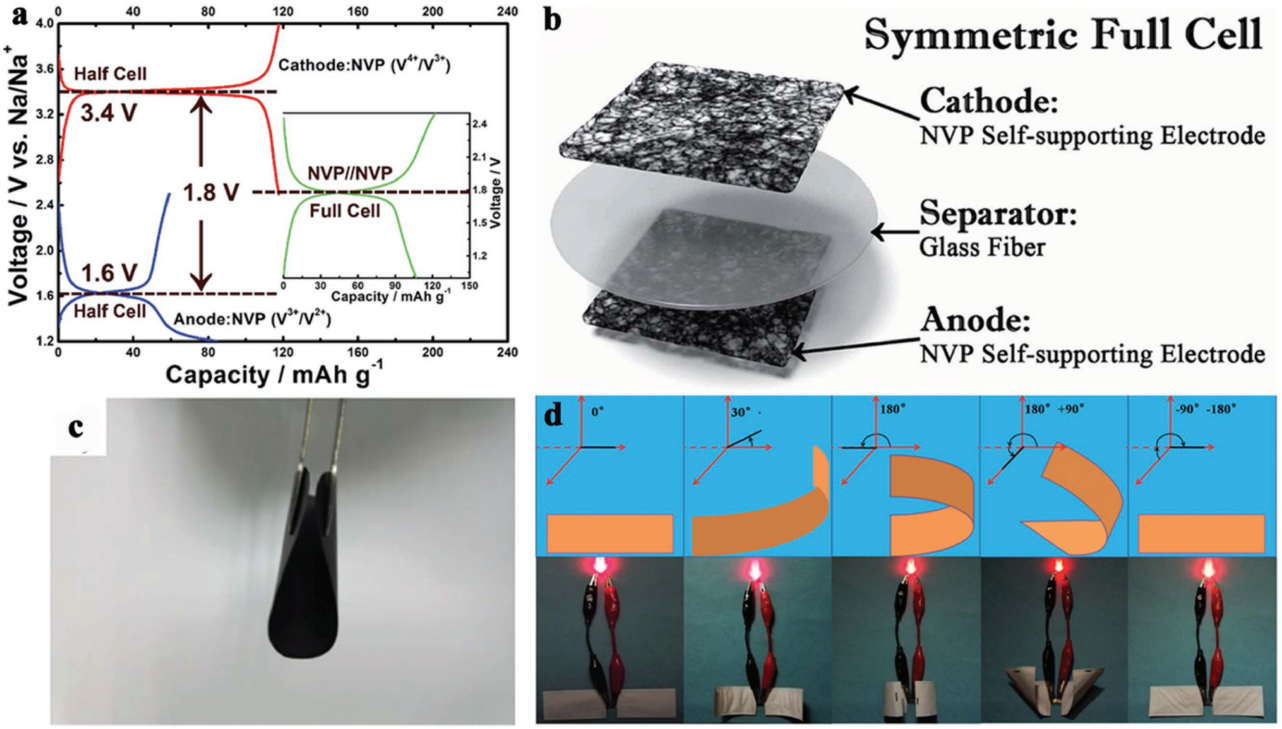

Figure 19. a) Charge/discharge voltage plateaus of the NVP self-supporting electrode: the left side shows the V^{4+}/V^{3+} (red) and V^{3+}/V^{2+} (blue) charge/discharge plateaus in a half-cell test. The right side exhibits an average charge/discharge voltage plateau of 1.8 V (green) in a NVP//NVP symmetric cell test.[177] b) Schematic illustration of the NVP symmetric full cell system.[177] c) Digital photographs of the bendable as-synthesized NVP@C@rGO membrane.[178] d) The electrochemical performance of the NVP//NVP full cell: digital pictures of the sodium-ion full cell lighting a LED under various states.[178] Panels (a,b) reproduced with permission.[177] Copyright 2016, Royal Society of Chemistry. Panels (c,d) reproduced with permission.[178] Copyright 2017, Royal Society of Chemistry.

a stable and safe electrochemical performance (Figure 19d). These results suggest a promising, low-cost sodium full cell strategy for next-generation flexible energy storage devices.

2.2.3. Fluorophosphates

It was reported that fluorine substitution can increase the working voltage and enable additional Na intercalation, and could thus increase the energy density of SIBs.[179–186] Recently, orthorhombic Na_2MPO_4F (M = Fe and Co)[186–194] and monoclinic Na_2MnPO_4F[195–197] have attracted considerable attention. The average working voltage of Na_2FePO_4F and Na_2MnPO_4F is limited to below 4.0 V, which significantly lowers their energy densities. In contrast, Na_2CoPO_4F has a very high working voltage, up to 4.3 V, and a discharge capacity of 107 mA h g^{-1}, resulting in a high energy density of around 430 Wh kg^{-1}.[188] However, compared to Na_2FePO_4F and Na_2MnPO_4F, Na_2CoPO_4F has not been widely investigated.

Vanadium-based fluorophosphates are also very appealing cathodes because of their much higher energy density.[198–204] As first reported by Barker et al. in 2003, $NaVPO_4F$/hard carbon full cell showed a high average discharge voltage of ≈3.7 V.[204] In fact, $NaVPO_4F$ exists in two different crystal structures, i.e., tetragonal structures with the *I4/mmm* space group[204] and monoclinic structure of the *C2/c* space group.[201] To improve the cyclability and rate performance, many strategies, including coating with conductive materials,[198,201,203,205] porous structures,[200] and cation doping,[206] have been attempted. For example, It was reported by Ruan et al. that the electrochemical performance of $NaVPO_4F$ can be significantly improved by graphene modification, which can deliver ≈120 mA h g^{-1} in 50 cycles (**Figure 20**a).[207] Jiao and co-workers further reported a free-standing $NaVPO_4F$/C nanofibers cathode for SIBs, which illustrate an extraordinary long-term cycle stability (up to 1000 cycles) with a stable capacity of ≈100 mA h g^{-1} at 2C (Figure 20b).[201] It is believed that the 1D $NaVPO_4F$/C nanofibers that interlink into 3D conductive network not only facilitate the electronic transport of $NaVPO_4F$ but even prevent the aggregation of $NaVPO_4F$ particles during charge/discharge, thus leading to the higher performance.

Le Meins et al. investigated $Na_3V_2(PO_4)_2F_3$, in which they found that its crystal structure is built on $V_2O_8F_3$ bioctahedra bridged by PO_4 tetrahedra (Figure 20c).[208] The structure was initially solved in the tetragonal space group *P42/mnm*,[209] but Bianchini et al. demonstrated that the strong sodium interactions can induce an orthorhombic distortion.[179] Starting in 2006, Barker et al. showed the promising capacity of this cathode when used versus lithium, sodium, and carbon anodes.[210] Since then, various $Na_3V_2(PO_4)_2F_3$ cathodes with different structures have been synthesized by different appro aches.[180,185,211–215] However, it was found that the reversible capacity is generally limited to below 128 mA h g^{-1}, which is mainly because only two Na^+ ions can be de-intercalated in

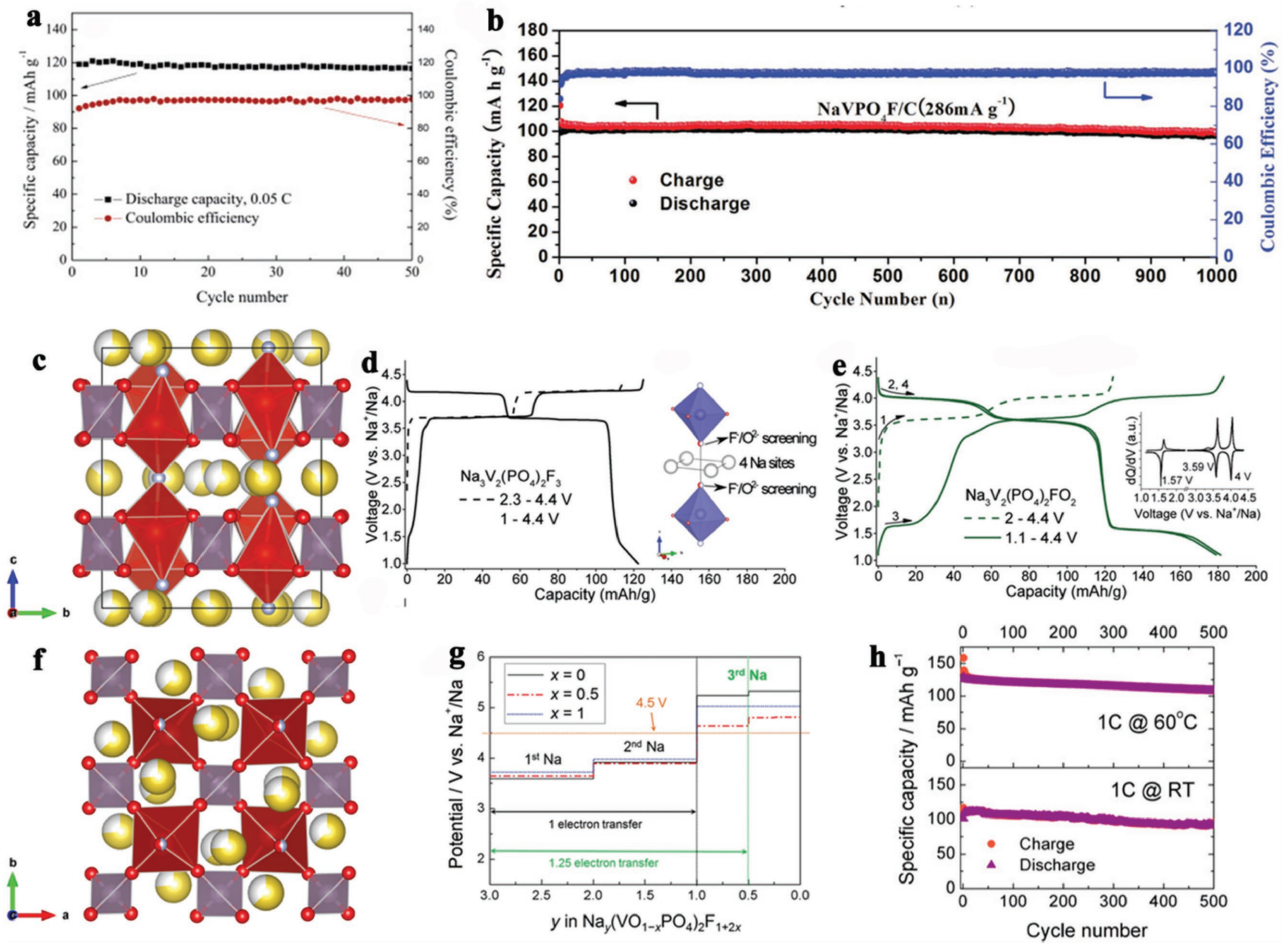

Figure 20. a) Specific capacity and Coulombic efficiency for $NaVPO_4F$/graphene during cycling at rate of 0.05 C.[207] b) Long-term cycling performance of $NaVPO_4F$/C nanofibers at 286 mA g^{-1}.[201] c) Crystal structure of $Na_3V_2(PO_4)_2F_3$. d) The electrochemical charge and discharge curve of $Na_3V_2(PO_4)_2F_3$ cycled between 1 and 4.4 V at C/20.[217] e) Electrochemical charge and discharge curve of $Na_3V_2(PO_4)_2FO_2$.[217] f) Crystal structure of $Na_3(VO_{1-x}PO_4)_2F_{1+2x}$. g) Voltage-composition curves for the $Na_y(VO_{1-y}PO_4)2F_{1+2x}$ electrodes from first-principles calculations.[218] h) Cycle life of the $Na_{1.5}VPO_{4.8}F_{0.7}$ at room and high temperatures.[219] Panel (a) reproduced with permission.[207] Copyright 2015, Elsevier. Panel (b) reproduced with permission.[201] Copyright 2017, Wiley-VCH. Panels (d,e) reproduced with permission.[217] Copyright 2017, Wiley-VCH. Panel (g) reproduced with permission.[218] Copyright 2014, Wiley-VCH. Panel (h) reproduced with permission.[219] Copyright 2013, American Chemical Society.

$Na_3V_2(PO_4)_2F_3$.[212] $Na_3V_2(PO_4)_2F_3$ is actually the end member of a complete solid solution $Na_3V_2(PO_4)_2F_{3-2y}O_{2y}$, where oxygen substitutes for fluorine in the vanadium-centered bioctahedra $V_2O_{8+2y}F_{3-2y}$ and creates vanadium of a higher average oxidation state ($V^{(3+y)+}$).[216] Ceder and co-workers further observed a significant increase in specific energy by enabling sodium insertion into $Na_3V_2(PO_4)_2FO_2$ to reach $Na_4V_2(PO_4)_2FO_2$ upon discharge.[217] This occurs at ≈1.6 V and increases the theoretical specific energy to 600 Wh kg^{-1}, rivaling that of several Li-ion battery cathodes (Figure 20d,e). This improvement is achieved by the judicious modification of the composition as O for F substitution, which disrupted Na-ion ordering and thereby enabled insertion of the fourth Na ion. In addition, $Na_3(VO_{1-x})_2(PO_4)_2F_{1+2x}$ ($0 \le x \le 1$) by substitution of V with O has also attracted the intention of researchers (Figure 20f). Kang's group for the first time reported $Na_3(VO_{0.8})_2(PO_4)_2F_{1.4}$ cathode that involves 1.2-electron transfer, which could thus attain an energy density of ≈600 Wh kg^{-1} (Figure 20g).[218] Moreover, it presents a very good cycle stability up to 500 cycles at room temperature and also high temperature (Figure 20h).[219]

2.2.4. Pyrophosphates

Pyrophosphates such as $Na_2MP_2O_7$ (M = Fe, Mn, Co)[220–227] and $Na_4M_3(PO_4)_2P_2O_7$ (M = Fe, Co)[228,229] are also a class of promising cathode materials of SIBs because of their structure deversity. However, $Na_2MP_2O_7$ shows relatively lower energy density, making them less attractive.

$Na_4Co_3(PO_4)_2P_2O_7$ crystallizes in the orthorhombic noncentrosymmetric with space group *Pn21a*.[228] Its crystal structure is shown in **Figure 21**a, which is composed of PO_4 and P_2O_7 groups. Nose et al. reported that $Na_4Co_3(PO_4)_2P_2O_7$ could deliver 95 mA h g^{-1} with an average working voltage of 4.4 V and stable cycle life (up to 100 cycles), leading to a high energy density of over 400 Wh kg^{-1} (Figure 21b).[229] The reversible capacity of $Na_4Co_3(PO_4)_2P_2O_7$ reported here is only half of its

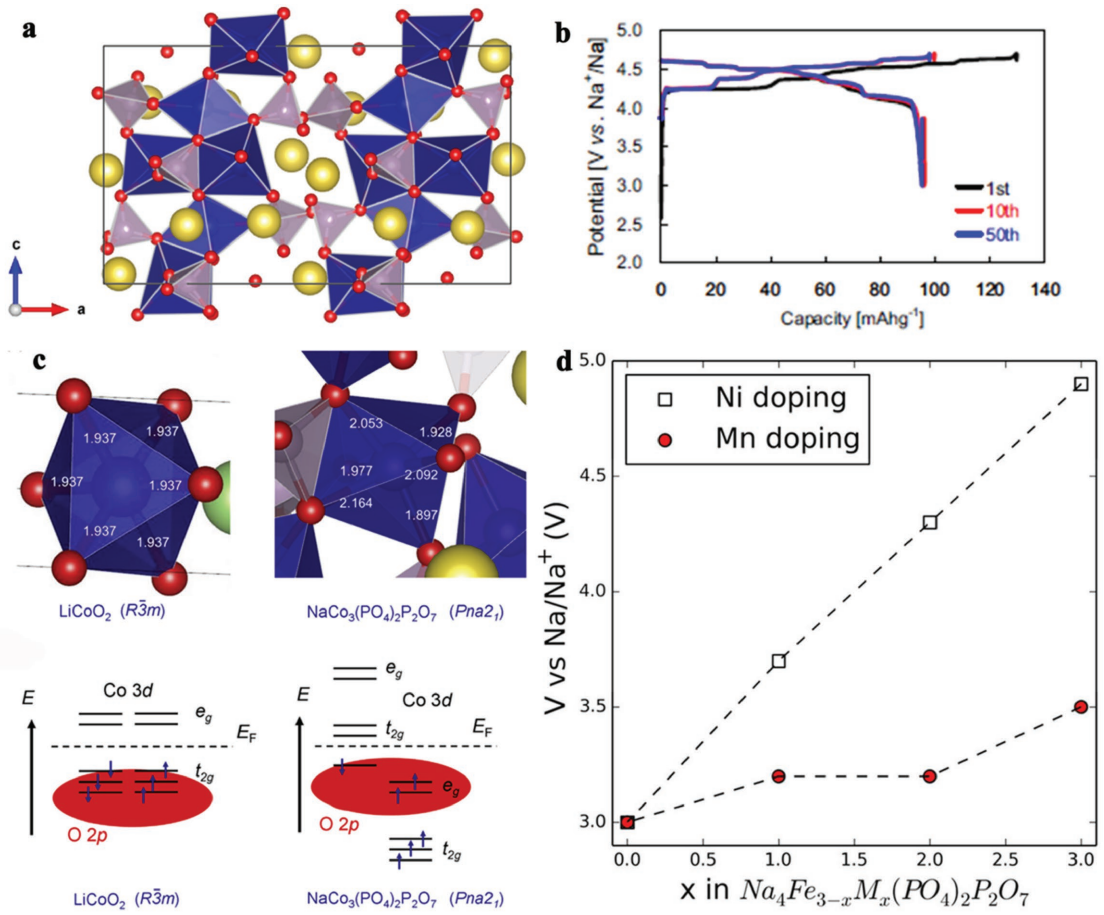

Figure 21. a) Crystal structure and b) typical voltage profiles of $Na_4Co_3(PO_4)_2P_2O_7$.[229] c) Local environments of Co ions in $LiCoO_2$ and $NaCo_3(PO_4)_2P_2O_7$ and Co 3d spin states (horizontal bars) relative to O 2p orbitals (filled ellipses) and the Fermi energy (E_F) for $LiCoO_2$ and $NaCo_3(PO_4)_2P_2O_7$.[230] d) Trends in cell voltage (vs Na^+/Na) as a function of increasing Mn and Ni concentrations on the Fe site in $NaFe_3(PO_4)_2P_2O_7$.[232] Panel (b) reproduced with permission.[229] Copyright 2013, Elsevier. Panel (c) reproduced with permission.[230] Copyright 2016, Elsevier. Panel (d) reproduced with permission.[232] Copyright 2015, American Chemical Society.

theoretical capcity (170 mA h g^{-1} based on 4 Na de-intercalation). Using DFT calculations, Moriwake et al. found that further removal of Na to give $Co_3(PO_4)_2P_2O_7$ requires oxidation of oxygen 2p orbitals in the P_2O_7 polyhedra instead of Co^{3+} oxidation to Co^{4+}.[230] The inability of Co^{3+} to be oxidized to Co^{4+} in $Na_4Co_3(PO_4)_2P_2O_7$ is in contrast to that in $LiCoO_2$ and $NaCoO_2$. This difference was ascribed to the local structures around Co ions and their spin states. In $Na_4Co_3(PO_4)_2P_2O_7$, Co^{3+} ions are located within large, distorted CoO_6 octahedra and are in a high spin state with a larger ionic radius; Whie in $LiCoO_2$, Co^{3+} ions sit within smaller, symmetrical CoO_6 octahedra (Co—O bond length ≈1.94 Å), and are in a low spin state (Figure 21c). Therefore, oxidizing Co^{3+} to Co^{4+} in the less densely packed phosphate structure would impose a large energy penalty, which explains why electrons are removed from 2p orbitals of O atoms in a P_2O_7 units instead of Co^{3+} cations during the last stage of sodium removal. Therefore, less than three-quarters of the theoretical capacity was attained.

$Na_4Fe_3(PO_4)_2P_2O_7$ has been studied by Kang et al. using combined experimental and calculational (DFT) techniques.[231] Its theoretical capacity of 129 mA h g^{-1} delivered at approximately 3.2 V (vs Na^+/Na) is competitive with that of other Na-ion cathodes. It has been shown that $Na_4Fe_3(PO_4)_2P_2O_7$ does not undergo a phase change upon Na^+ extraction, leading to good long-term cycle life. Furthermore, Islam and co-workers reported that Ni doping is predicted to deliver a significant increase in cell voltage, providing a high degree of voltage control by varying the doping concentration (Figure 21d).[232] Thus, Ni-doped $Na_4Fe_3(PO_4)_2P_2O_7$ with a relatively modest level of Ni would lead to a ≈25% enhancement in voltage; this is a significant increase in energy density, while Mn doping provides a relatively minor increase in cell voltage and energy density.

3. Anode Materials

3.1. Carbon-Based Anode Materials

3.1.1. Graphitic Carbon (Graphite Material)

Graphite is the anode choice in state-of-the-art LIBs considering its high gravimetric and volumetric capacity.[233] During the discharge process, Li^+ is intercalated between graphene layers to form lithium–graphite intercalation compounds (Li-GIC) with

different stage transformations,[234–236] and all graphite layers are fully filled by Li, forming LiC_6 at the end of the electrochemical reduction process.[237]

In the case of SIBs, the lattice mismatch between the graphite layers and Na^+ creates a large barrier for the insert of Na^+ into the graphite.[4,234] According to quantum calculations, the optimum formation energy for Na–graphite is reached when the graphite interlayer distance is expanded to 4.3 Å.[238] Hence, Wang and co-workers reported that expanded graphite (EG) can be used as a superior SIB anode material.[23] It was found that the interlayer spacing of EG can be manipulated by controlled oxidation and reduction processing. Na^+ can be reversibly inserted into and extracted from the EG, with an interlayer distance of 4.3 Å (**Figure 22**a,b). The sodiation/de-sodiation-induced microstructure changes of EG are dynamically captured during real-time imaging at the atomic scale using in situ HRTEM. Electrochemical tests show that the EG can deliver 284 mA h g^{-1} after 30 cycles at 20 mA g^{-1} (Figure 22c). It also shows long cycle stability up to 2000 cycles, with a capacity retention of 73.92%.

3.1.2. Nongraphitic Carbon

The soft and hard carbon materials such as nongraphitizable carbon are very attractive for SIBs because of the expanded graphene sheet spacing.[239] It was reported that soft carbon can present higher capacities than graphite when used as anode of LIBs.[240] However, large irreversible capacity was observed owing to aggravated electrolyte decomposition on the high specific surface soft carbon.[241]

The nongraphitizable materials were utilized as electrodes in commercial LIBs earlier than the graphite in the cells released by Sony Corporation in 1991. In particular, a hard-carbon electrode delivers comparable reversible capacity to graphite material.[240] In 2000, Stevens and Dahn first reported that hard carbon obtained by 1000 °C carbonization is able to host Na^+ at room temperature, which can attain a specific capacity of 300 mA h g^{-1}.[242] Recent efforts further enhanced the reversible capacity of hard carbon through structural investigation. Hasegawa et al. reported hard-carbon structure dependency on the synthesis conditions. They varied the carbonization temperature from 800 to 3000 °C to explore the relationship between various physical properties and electrochemical performance.[243] As shown in **Figure 23**a, the hard-carbon electrode carbonized at 1600–2500 °C and delivered the highest capacity within a narrow potential range as well as high initial Coulombic efficiency over 90%. Very recently, Kano et al. reported a high reversible capacity of 438 mA h g^{-1} for hard carbon by using the carbon sources including a pore-forming agent prepared by high temperature of 2100 °C.[244]

Extensive attempts have been made to investigate the Na storage mechanism of hard carbon. Different reaction models have been proposed. Stevens and Dahn were also the first to report the insertion mechanism of Na^+ ions into disordered hard carbon. The suggested mechanism was the "house of cards" for Na^+ ions storage, which is composed from two domains in a disordered hard carbon structure without staging transition.[245] In fact, Na^+ ions are inserted between parallel graphene sheets (in the sloping voltage region) upon increasing the interlayer space. Additionally, Na^+ ions fill the nanopores (in the plateau region) of the disordered carbon structure. Furthermore, Komaba et al. confirmed structural changes after sodiation of hard carbon via XRD and small-angle X-ray scattering measurements, indicating the reversible Na intercalation in disordered stack of graphene and insertion into micropore site.[246] Moreover, Simone et al. demonstrated the impact of the carbonization temperature on the structure of hard carbons made from cellulose pyrolysis.[247] Figure 23b shows a clear relationship of the irreversible, plateau, sloping region and the reversible capacities as a function of the pyrolysis temperature. Based on the "card house" model mechanism, the slope and flat region capacities are attributed to Na^+ intercalation between the graphene layers and Na^+ insertion into the micropores, respectively. While Bommier et al. proposed a distinct sodium storage mechanism from the card-house model in hard carbon, which indicated that the Na^+ storage is mainly based defect sites and pore-filling as shown in Figure 23c.[248] More recently, Stratford et al. provided a direct evidence of Na^+ ions insertion mechanism by using operando ^{23}Na solid-state NMR spectroscopy (Figure 23d) and PDF analysis.[249] They found that control of the pore design during synthesis could determine the size of

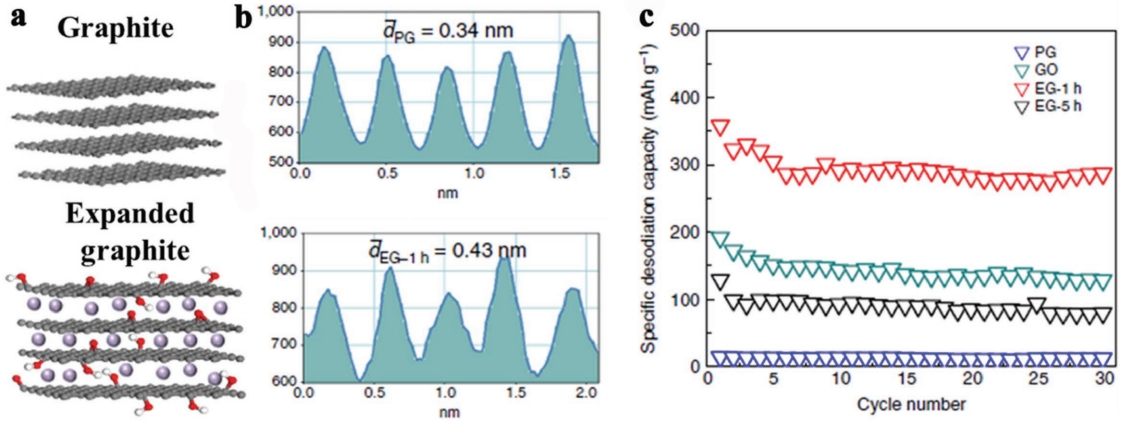

Figure 22. a) Schematic illustration and b) contrast profiles of pristine graphite (PG) and expanded graphite (EG). c) Short-term cycling stability test for PG, GO, EG-1 h, and EG-5 h at a current density of 20 mA g^{-1}. Panels (a–c) reproduced with permission.[23] Copyright 2014, Nature Publishing Group.

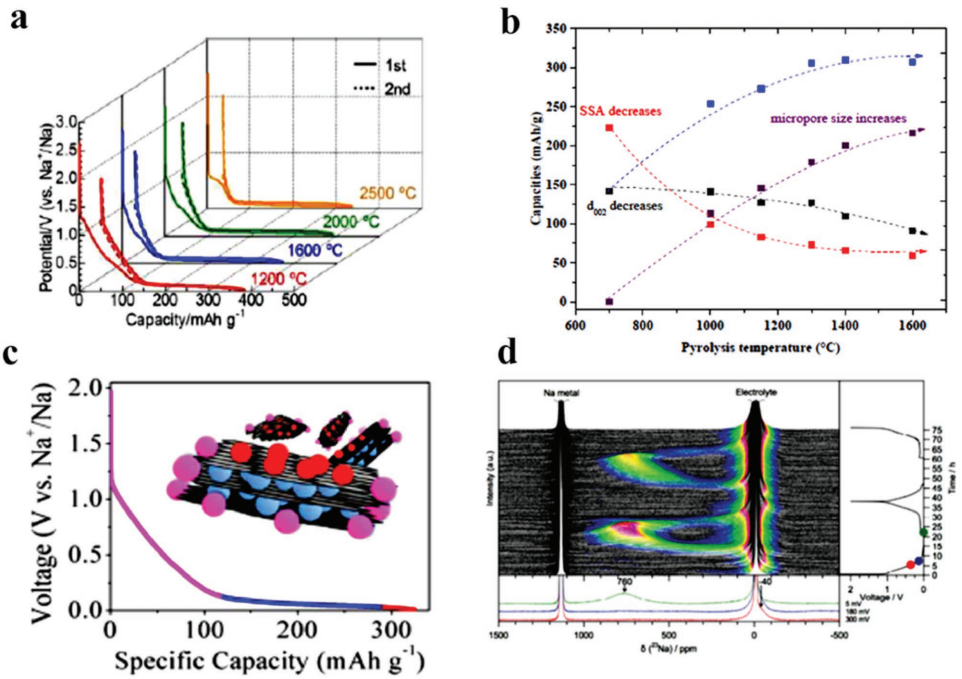

Figure 23. a) Charge/discharge curves of carbon electrodes treated at 1200–2500 °C and tested between 2.0 and 0.005 V at 20 mA g^{-1}.[243] b) Evolution of the irreversible, plateau, sloping region, and reversible capacities as a function of the pyrolysis temperature.[247] c) Potentiogram and schematic of proposed Na-ion three-part storage mechanism.[248] d) Operando ^{23}Na NMR spectra for an electrochemical cell with sodium metal and hard carbon electrodes and $NaPF_6$ electrolyte.[249] Panel (a) reproduced with permission.[243] Copyright 2015, Wiley-VCH. Panel (b) reproduced with permission.[247] Copyright 2016, Elsevier. Panel (c) reproduced with permission.[248] Copyright 2015, American Chemical Society. Panel (d) reproduced with permission.[249] Copyright 2016, Royal Society of Chemistry.

the sodium clusters formed and, thus, grant the ability to boost the relative capacities.

3.1.3. Biomass and Doped Hard Carbons

Hard carbon material is generally derived from petroleum products, while it can also be made from raw materials because of its abundance, low cost, and sustainability, e.g., apple-bio-waste,[250] corn cob,[251] harmful algal blooms,[252] sweet potato,[253] and peanut shell.[254] To synthesize high-capacity hard carbon materials for SIBs, numerous approaches have been developed by optimizing their physical structure and surface chemistry. Distinct hard carbon made from banana peels was reported by Lotfabad et al.[255] The banana peel materials are composed of pseudographitic arrays possessing dilated graphene spacing, leading to a large amount of Na^+ intercalation between the layers, which can deliver 342 mA h g^{-1} with 88% capacity retention over 290 cycles. Moreover, **Figure 24**a reveals the effect of carbonization temperature on the sloping-voltage region and flat plateau at potentials lower than 0.2 V. Lotfabad et al. attributed the long sloping high-voltage charge storage region to reversible binding of Na^+ ions at graphene divacancies and Stone–Wales defects.[255] Very recently, hard carbon materials were prepared from Argan bio-waste.[256] As shown in Figure 24a,b, it was found that large nanopores size is crucial to improve Na^+ ions storage into hard carbon for the plateau region below 0.15 V. Additionally, hard carbons derived from Argan with HCl pretreatment have a larger number of active sites available for electrochemical Na^+ ion storage. Therefore, the Argan electrode carbonized at 1200 °C and treated in HCl solution delivers the highest reversible capacity of 333 mA h g^{-1} among the samples prepared. Noteworthy is that doping of phosphorus oxide (PO_x) into local structures of hard carbon makes more defects in the hard carbon structure as well expands the interlayer distance of the turbostratic domains,[257] therefore increasing the reversible capacity from 283 to 359 mA h g^{-1} (Figure 24c). Recently, Zhang et al.[258] improved the reversibly of Na^+ ion intercalation by using nitrogen-doped carbon from a honey substance carbonized at 700 °C and treated in HF solution. The optimized honey-derived carbon delivers the highest reversible capacity (427 mA g^{-1}) among carbon materials derived from biomass (Figure 24d). However, the working voltage for hard carbon-based anode materials is too close to the sodium metal deposition potential, which would cause serious safety concerns.

3.2. Ti-Based Anode Materials

3.2.1. $Li_4Ti_5O_{12}$

Spinel $Li_4Ti_5O_{12}$ is well known for its excellent cycling performance in LIBs due to its minute volume change during lithiation/de-lithiation.[259] In 2012, Zhao and co-workers for the first time investigated its application as an anode in SIBs.[260] They illustrated that $Li_4Ti_5O_{12}$ exhibit 145 mA h g^{-1} with an average working voltage of ≈1 V, and that the Na storage mechanism

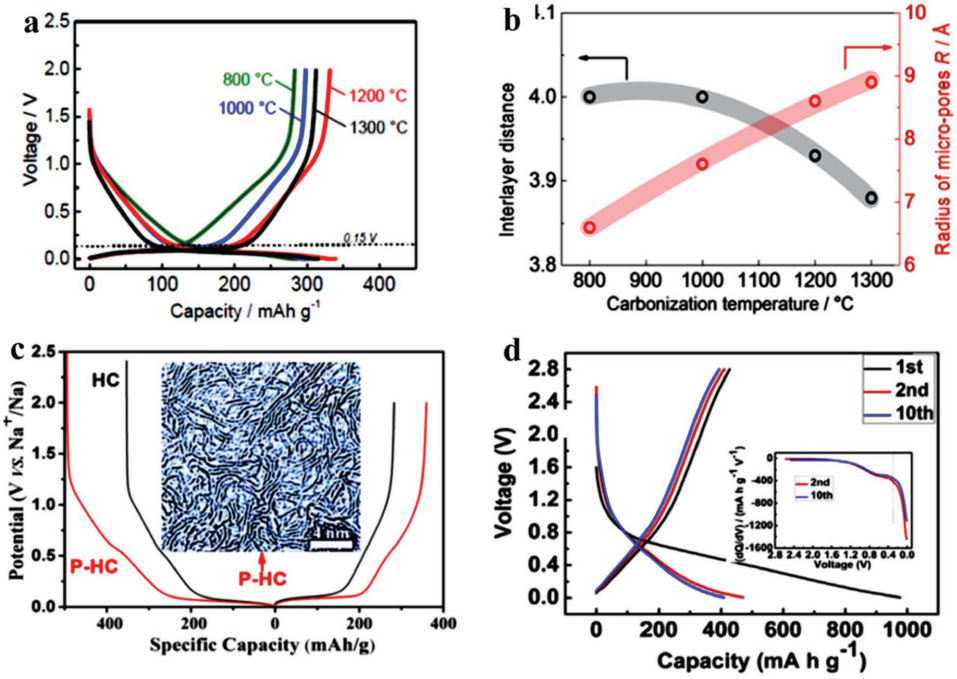

Figure 24. a) Second galvanostatic charge/discharge profiles of the Argan-800W, Argan-1000W, Argan-1200W, and Argan-1300W electrodes pretreated with HC.[256] b) Evolution of the interlayer distance d002 between the graphene sheets (black curve) and the micropore radius R (red curve) versus the carbonization temperatures of the Argan-based hard carbons.[256] c) Voltage profiles of HC and P-HC with the inset showing SEM image of P-HC.[257] d) Charge/discharge profiles of HMNC-700 at a current density of 100 mA g^{-1} with the inset showing the differential capacity versus cell voltage plots.[258] Panels (a,b) reproduced with permission.[256] Copyright 2017, Royal Society of Chemistry. Panel (c) reproduced with permission.[257] Copyright 2016, American Chemical Society. Panel (d) reproduced with permission.[258] Copyright 2016, Elsevier.

$Li_4Ti_5O_{12}$ is different from that of Li: it might be a mixture of $LiNa_6Ti_5O_{12}$ and $Li_7Ti_5O_{12}$ instead of a single-phase $Li_4Na_3Ti_5O_{12}$. Sun et al. demonstrated that the $Li_4Ti_5O_{12}$ can store Na in a different way from that of Li.[261] DFT calculation predicted that the insertion of Na into $Li_4Ti_5O_{12}$ occurs through a three-phase separation mechanism

$$2Li_4Ti_5O_{12} + 6Na^+ + 6e^- \rightarrow Li_7Ti_5O_{12} + Na_6LiTi_5O_{12} \quad (1)$$

which was further confirmed through in situ synchrotron XRD and advanced scanning transmission electron microscopy (STEM) imaging techniques (**Figure 25**a,b). Due to the large size of Na^+, it preferred to stay in *16c* octahedral sites to form $Na_6LiTi_5O_{12}$ phase rather than *8a* tetrahedral sites. Hence, Li[8a] ions are pushed to the nearest neighbor $Li_4Ti_5O_{12}$ phase, forming $Li_7Ti_5O_{12}$ phase.

Even though $Li_4Ti_5O_{12}$ seems to be a promising anode, its low ionic and electric conductivity significantly limited its electrochemical performance. Recently, various approaches such as carbon coating, element doping, and surface engineering have been carried out to obtain better electrochemical performance.[262–270] Sun's group investigated carbon-coated $Li_4Ti_5O_{12}$ nanowires, which exhibit a very good rate performance (Figure 25c).[271] Liu et al. recently reported some promising results using carbon-coated $Li_4Ti_5O_{12}$ nanoparticles.[272] They used a solid-state reaction coupled with chemical vapor deposition to synthesize carbon-coated $Li_4Ti_5O_{12}$ nanoparticles, which can still maintain 90 mA h g^{-1} after 500 cycles of charge/discharge (Figure 25d). In addition, a full cell was fabricated with carbon-coated $Na_3V_2(PO_4)_3$ as the positive electrode, which can deliver an initial capacity of 138.5 mA h g^{-1} with a capacity retention of ≈83% after 50 cycles at 0.05 A g^{-1}. These results indicate that $Li_4Ti_5O_{12}$ shows promising electrochemical performance as SIB anode materials.

3.2.2. $Na_2Ti_3O_7$

$Na_2Ti_3O_7$ is another attractive titanate based anodes for SIBs.[273–278] Senguttuvan et al. first reported that $Na_2Ti_3O_7$ can insert 2 Na^+, and could thus offer 200 mA h g^{-1} with an average working voltage of 0.3 V.[279] The charge/discharge profiles of $Na_2Ti_3O_7$/carbon black composite (red curve) and carbon black electrode (blue curve) are displayed in **Figure 26**a. The $Na_2Ti_3O_7$/carbon exhibits two plateaus: an irreversible reaction at 0.7 V, which corresponds to the carbon black additive redox reaction, and a reversible reaction at 0.3 V, which corresponds to the intercalation of two Na^+ ions in the structure. Xu et al. coupled DFT calculations with experimental results to explain the structural evolution and the low voltage behavior of $Na_2Ti_3O_7$.[280] The calculation suggested that the fully intercalated phase $Na_4Ti_3O_7$ forms upon the intercalation of two Na^+ ions in the $Na_2Ti_3O_7$ structure. Xu et al. attributed the lower voltage to structure instability, which is caused by the strong electrostatic repulsion in the fully discharged phase $Na_4Ti_3O_7$ that would tend to self-relax and gradually transform to $Na_2Ti_3O_7$ after a few days of storage.

Rudola et al. reported a new intermediate phase, $Na_{3-x}Ti_3O_7$, between $Na_2Ti_3O_7$ and $Na_4Ti_3O_7$, which resulted in very

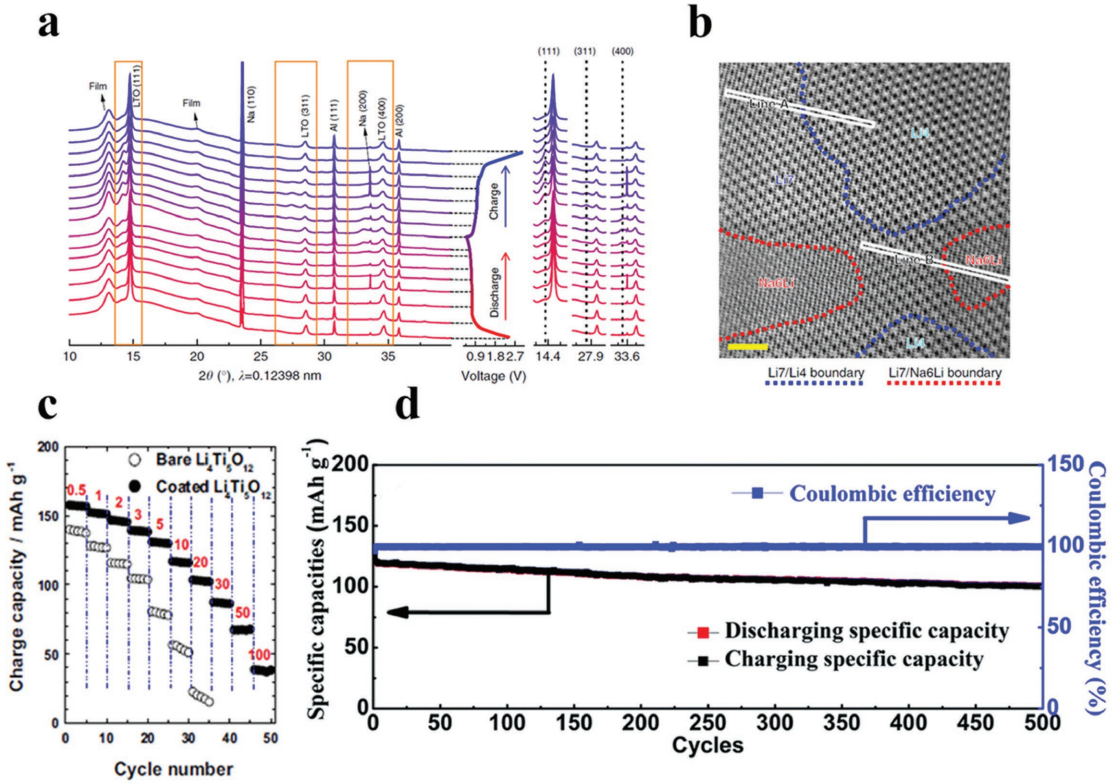

Figure 25. a) Operando XRD data recorded during the first cycle for the $Li_4Ti_5O_{12}$ electrode in SIB system. For the Li_4/Li_7 phases, the main peaks correspond to (111), (311), and (400) reflections. These regions are highlighted in the right column and peaks corresponding to the Na_6Li phase are marked by black dotted lines.[261] b) Annular bright field (ABF) image in the half electrochemically sodiated $Li_4Ti_5O_{12}$ nanoparticle. In ABF line profile, the contrast is inverted for convenient visualization. Scale bar, 2 nm.[261] c) Rate capability data of bare $Li_4Ti_5O_{12}$ and carbon-coated $Li_4Ti_5O_{12}$ from 0.5 C to 100 °C (17.5 A g^{-1}).[271] d) Cycle performance of N-LTO@C.[272] Panels (a,b) reproduced with permission.[261] Copyright 2014, Nature Publishing Group. Panel (c) reproduced with permission.[271] Copyright 2015, Elsevier. Panel (d) reproduced with permission.[272] Copyright 2017, Royal Society of Chemistry.

low charge plateau at 0.2 V with negligible polarization (Figure 26b).[281] The new phase was achieved by limiting the lower cut-off voltage to 0.155 V instead of 0.01 V. This resulted in a charging plateau at 0.22 V, corresponding to the reaction $Na_2Ti_3O_7 \leftrightharpoons Na_{3-x}Ti_3O_7$, compared to the 0.44 V plateau if the cell is allowed to discharge to 0.01 V, which corresponds to the formation of $Na_4Ti_3O_7$ instead. The new $Na_2Ti_3O_7 \leftrightharpoons Na_{3-x}Ti_3O_7$ pathway demonstrated a capacity of 86 mA h g^{-1} at the C/5 rate and very good capacity retention at high rates, e.g., ≈69% retention for 80 C (Figure 26c), in addition to a decent cycle life with minimal polarization increase.

Later, Ni et al. tried a surface engineering approach to improve the electrochemistry of $Na_2Ti_3O_7$.[282] They synthesized $Na_2Ti_3O_7$ (denoted as NTO) nanotube arrays using S-doped TiO_2 nanolayers. A schematic of their approach is given in Figure 26d. Initially, they grew NTO nanotube arrays on a Ti metal foil. Then, they used ALD to deposit a TiO_2 layer onto the nanoarrays (referred to as T-NTO). After that, they treated the T-NTO nanoarrays in sulfur vapor at an optimized temperature (400 °C) to improve the overall conductivity (referred to as ST-NTO). The SEM images of the ST-NTO confirm the growth of the T-NTO nanotubes on the surface of TiO_2 with a diameter of 30–40 nm (Figure 26e– 1). High-resolution TEM images confirmed the growth of a 5 nm nanotube with a layered structure (Figure 26e- 2 and e-3). The electrochemical performance of ST-NTO could deliver ≈221 mA h g^{-1} at C/5, which suggests that the ST-NTO structure could intercalate/de-intercalate ≈2.5 Na^+ ions per unit formula; in addition, the results indicate a stable cycle life up to 10 000 cycles at high rates of 10 C (Figure 26f,g). Ni et al. attributed the improved performance to the good mechanical adhesion and the electrical connection enabled by the nanoarrays grown on conductive Ti substrate, which lower the charge transfer resistance; in addition, the porous configuration provides a high surface area and facilitates the exposure of the nanotubes to the electrolyte, leading to enhanced interfacial kinetics. These kinetics can also have negative SEI layer effects, which could lead to lower the first cycle Coulombic efficiency up to 41%.[283]

Recently, Xie et al. explored $Na_2Ti_3O_7$ hollow spheres assembled from N-doped carbon-coated ultrathin $Na_2Ti_3O_7$ nanosheets as a stable anode for SIB. The synthesis route is displayed in Figure 26h.[284] They proposed that the hollow structure will enable better electrolyte access, increase the surface area, and reduce the diffusion pathway for both ions and electrons. The morphology of the hollow spheres composed of carbon-coated $Na_2Ti_3O_7$ ultrathin nanosheets (referred to as $Na_2Ti_3O_7$@C HHSs) was investigated by SEM and HRTEM. The SEM and TEM images (Figure 26i–1 and i-2) confirmed

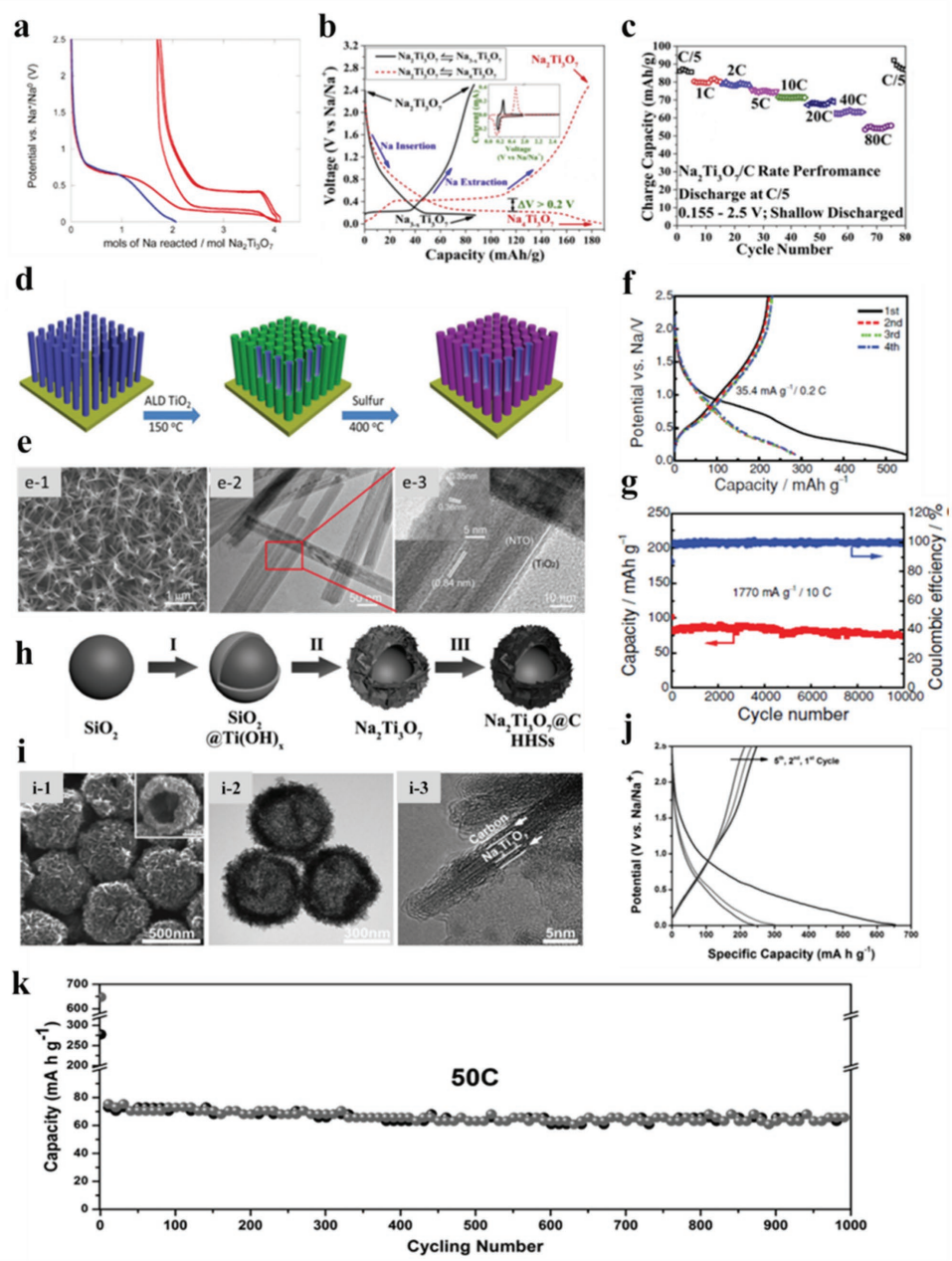

Figure 26. a) Voltage versus composition profile for the electrochemical reduction of a blank electrode containing only carbon black (blue curve) and a composite electrode containing $Na_2Ti_3O_7$ and 30% carbon black (red curve), where the reversible insertion of ≈2 mol of sodium ions per mol $Na_2Ti_3O_7$ is observed.[279] b) C/5 cycling (not the first cycle) of $Na_2Ti_3O_7 \leftrightharpoons Na_{3-x}Ti_3O_7$ and $Na_2Ti_3O_7 \leftrightharpoons Na_4Ti_3O_7$ pathways with corresponding cyclic voltammetry curves as inset.[281] c) Rate performance of $Na_2Ti_3O_7$/C $\leftrightharpoons$ $Na_{3-x}Ti_3O_7$ /C pathway.[281] d) Schematic illustration of the fabrication of surface-engineered $Na_2Ti_3O_7$ nanotube arrays grown on Ti foil.[282] e) e-1) SEM image of top-view of ST-NTO. e-2) TEM image of ST-NTO nanotubes. The lattice fringe spacing of 0.84 nm coincides with the (001) facet of monoclinic $Na_2Ti_3O_7$. The moiré fringes are present over two crossed nanotubes. Inset in (e-3) shows the lattice spacing of 0.35 nm for surface anatase and 0.36 nm for bulk, suggesting a possible epitaxial growth of TiO_2 along the (201) facet of $Na_2Ti_3O_7$.[282] f) Electrochemical Na-storage performance of $Na_2Ti_3O_7$ nanoarray and surface-engineered products. Comparison of cycling stability at a rate of 5 C.[282] g) Long-term cycling performance of ST-NTO at a rate of 10 C.[282] h) Illustration of the route for synthesis of $Na_2Ti_3O_7$@C hollow spheres. i) SEM h-1), TEM (h-2), and HRTEM (h-3) images of $Na_2Ti_3O_7$@C.[284] j) Initial discharge/charge voltage profiles of the first, second, and fifth cycles in the current density of 1 C of $Na_2Ti_3O_7$@C HHSs.[284] k) Cycling performance of $Na_2Ti_3O_7$@C HHSs under high current density of 50 C.[284] Panel (a) reproduced with permission.[279] Copyright 2011, American Chemical Society. Panels (b,c) reproduced with permission.[281] Copyright 2015, Elsevier. Panels (d–g) reproduced with permission.[282] Copyright 2016, Wiley-VCH. Panels (h–k) reproduced with permission.[284] Copyright 2017, Wiley-VCH.

the hollow structure of the $Na_2Ti_3O_7$@C HHSs composite with an estimated shell thickness of 40 nm. The HRTEM image in Figure 26i- 3 shows that this material consists of uniform 2D ultrathin $Na_2Ti_3O_7$ sheets with a thickness of 5 nm. The voltage profiles of the $Na_2Ti_3O_7$@C HHSs at 1 C are shown in Figure 26j. The first discharge and charge capacity of this

material are measured to 647 and 278 mA h g^{-1}, respectively, resulting in a low CE of 43%. The authors attributed this low efficiency to the degradation of electrolyte and the formation of an SEI layer. The rate performance of the $Na_2Ti_3O_7$@C HHSs was excellent, as it could retain 40% of the theoretical capacity at 50 C. Also, cycling at this high rate maintained good capacity retention 93.5% after 1000 cycles (Figure 26k) with a columbic efficiency over 90%.

In addition, Pan et al. reported the sodium storage mechanism of $Na_2Ti_3O_7$ by combination of first-principles calculations and electrochemical techniques. The Na storage behavior in $Na_2Ti_3O_7$ is investigated from both thermodynamic and kinetic aspects. It was found that the sodium storage behavior of $Na_2Ti_3O_7$ was greatly affected by the particle size. Moreover, three specific trajectories with fairly low activation energies of 0.186, 0.219, and 0.226 eV via the Na1 and Na2 vacancies alternatively between the TiO_6 octahedron layers according to a vacancy-hopping mechanism, forming a quasi-3D zigzag trajectory in $Na_2Ti_3O_7$.[285]

3.2.3. TiO_2

Titanium oxide materials have attracted serious interest as intercalation materials for LIBs because of their low cost, low toxicity, stability, and abundance.[286] Recently, several studies have been focusing on metal oxides such as anatase and rutile (TiO_2) in addition to alkali metal titanium oxides such as $Li_4Ti_5O_{12}$, $Na_4Ti_5O_{12}$, $Na_2Ti_3O_7$, and $Na_2Ti_6O_{13}$. Xiong et al. reported the first TiO_2-based anode for SIBs, which was fabricated by using a TiO_2 nanotube grown on a Ti substrate. This material demonstrated a gradually increasing reversible capacity of ≈150 mA h g^{-1} at 50 mA g^{-1}.[287] This work was critical in stimulating the investigation of TiO_2 with various polymorphs including amorphous, anatase, rutile, brookite, and bronze as the SIB anode.[288–308]

However, the detailed sodium insertion/extraction mechanism is not consistent, which impedes further improvement of the electrochemical performance of TiO_2-based anode materials. For example, Kim et al. reported that anatase TiO_2/C nanorods exhibit very stable cycling performance.[309] Based on ex situ XRD, HRTEM, and X-ray absorption near edge structure (XANES) k-edge spectra, they showed that the structure did not transform to an amorphous phase and the anatase TiO_2 nanorods retained their morphology. They concluded that the chemistry of the anatase TiO_2 nanorods support a Ti^{4+}/Ti^{3+} redox reaction based on a Na^+ intercalation process during electrochemical reaction. Yang and co-workers also found that graphene–TiO_2 nanospheres go through a reversible Na^+-intercalation mechanism without involving any conversion reactions (**Figure 27**a).[310] This was further confirmed by Cha et al., who reported a TiO_2/nitrogen-doped open pore channeled graphene (TNCG).[311] In this case, the improved performance is due to use of nitrogen-doped graphene, which promotes the e^- transfer in the electrochemical reaction. Also, the open pore channels in the 2D porous graphene might have contributed to the improvement in the storage characteristics of TiO_2 by facilitating the efficient access of electrolyte to the electrode and improve the intercalation of Na^+ ions.

Chen et al. demonstrated that TiO_2/graphene nanoparticles undergo a Na^+ pseudocapacitance intercalation, which can demonstrate a reversible capacity of ≈90 mA h g^{-1} at 36 C with more than 4000 cycles.[312] Further sodiation dynamics analysis based on first-principle calculations showed that the hybridization of graphene with TiO_2 nanocrystals provides a more feasible channel at the graphene–TiO_2 interface for sodium intercalation/de-intercalation with a much lower energy barrier (Figure 27b). Very recently, Le et al. proposed a sodium based energy storage system using a nanocomposite of TiO_2 mesocages anchored on graphene sheets which exhibits ultrahigh pseudocapacitive characteristics (Figure 27c).[313] The TiO_2 mesocage–graphene nanocomposite (designated as MWTOG) was synthesized by a microwave-assisted solvothermal method. Le et al. used oxygen-containing functional groups on graphene sheets as nucleation sites to start the growth of TiO_2 mesocages. The MWTOG electrode can still deliver 162 mA h g^{-1} after 7000 cycles at 5 C and 126 mA h g^{-1} after 18 000 cycles at 10 C. A full cell of sodium-ion capacitor with a carbon-based cathode successfully demonstrated an energy density of 64.2 Wh kg^{-1} at 56.3 W kg^{-1} and 25.8 Wh kg^{-1} at 1357 W kg^{-1}, as well as an ultralong lifespan of 10 000 cycles with over 90% of capacity retention.

In spite of their superior cycle stability and high rate capability, the initial CE of TiO_2-based anode materials for SIBs is usually lower than 50% (Figure 27d),[309] which dramatically hinders its practical application. Further study should focus on increasing the initial efficiency of this system.

3.3. Phosphorus-Based Anode Materials

Thanks to its low cost, chemical stability, abundance, and high theoretical capacity as it electrochemically reacts with Li and Na to form Li_3P and Na_3P, respectively, phosphorus has gained attention as a promising anode material for both LIBs and SIBs.[314–316] Phosphorus exists in three main allotropes, white, red, and black each with its own distinct properties.[317] The tetrahedral white phosphorus is toxic and chemically unstable at room temperature and therefore unsuitable for battery applications as it poses a safety hazard. The amorphous red phosphorus (RP) was found to reversibly alloy with Na. However, its poor electronic conductivity (≈10^{-14} S cm^{-1}), instability toward the electrolyte, and huge volume change (≈400%) during sodiation/de-sodiation severely affect the cycling and the rate performance. The orthorhombic black phosphorus (BP) is the most stable among all three allotropes. Its layered crystal structure, high electrical conductivity (≈300 S m^{-1}), and appearance resemble those of graphite, making it suitable for battery applications. However, these alloy-based anode materials undergo huge volume expansion during repeated charge/discharge, which will lead to pulverization of particles, continuous decomposition of electrolytes, isolation of active materials, and finally de-lamination of electrode, and thus lead to significant performance degradation of the battery.[318]

To address the huge volume expansion and the poor electrical conductivity of this system, several approaches have been explored. Most approaches focus on developing carbonaceous phosphorus composites, such as amorphous

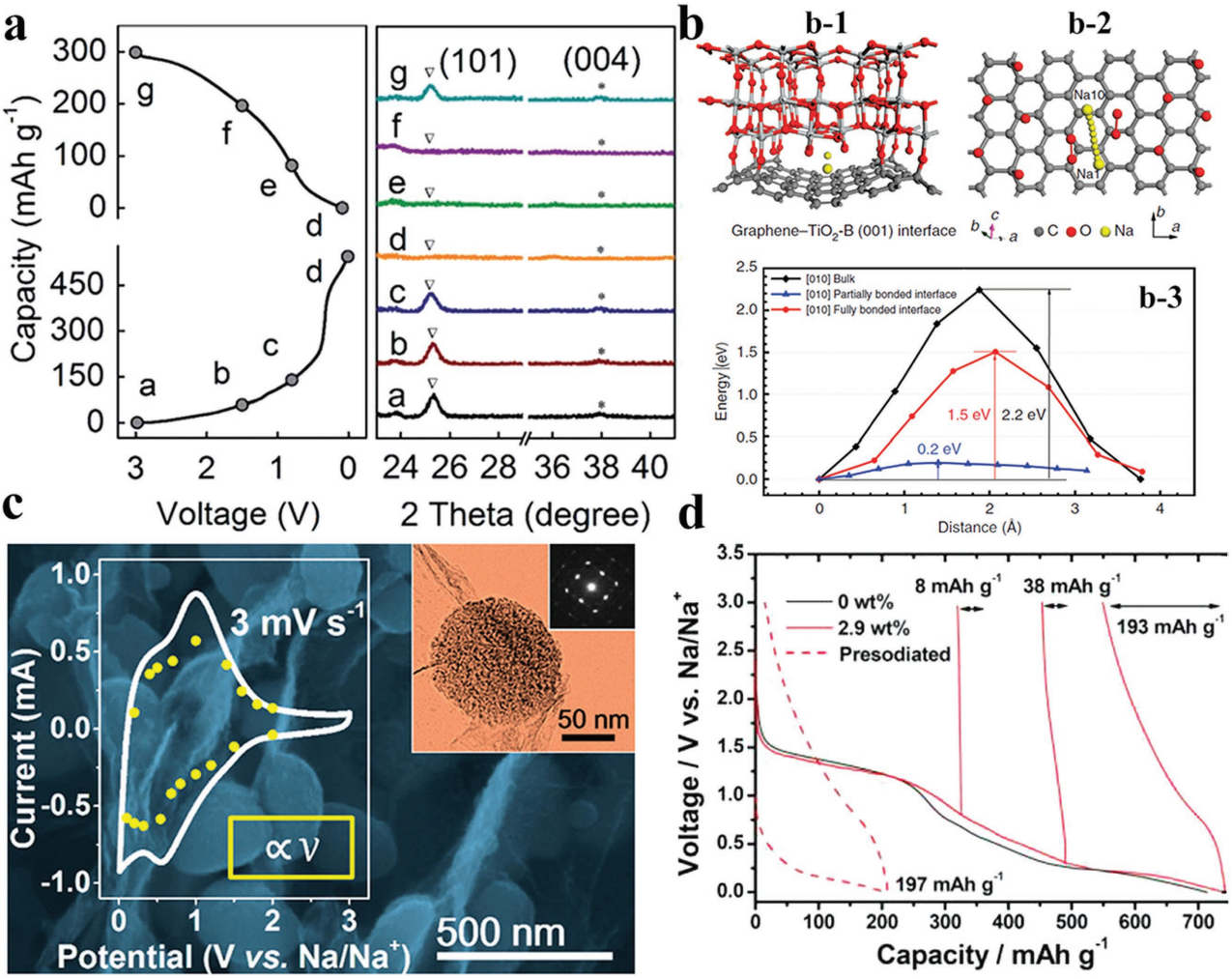

Figure 27. a) Left: a typical charge/discharge profile of the rGO–TiO_2 anode, where alphabetic characters on the curves denote the sampling positions; right: XRD patterns of the rGO–TiO_2 anode at different depths of charge and discharge.[310] b) b-1) Illustration of the partially bonded graphene–TiO_2-B (001) interface. b-2) Top-view of (b-1), illustrating the Na diffusion path along the [010] direction from Na1 to Na10 sites. b-3) Migration activation energy of the Na þ ion diffusing along the [010] direction in bulk TiO_2-B, as well as fully bonded and partially bonded graphene–TiO_2–B (001) interface, calculated with DFT.[312] c). SEM image of MWTOG with TEM image and cyclic voltammetry curves as inset.[313] d) First discharge curve of bare and 2.9 wt% carbon-coated anatase nanorod TiO_2 measured at 10 mA g^{-1}.[309] Panel (a) reproduced with permission.[310] Copyright 2016, Royal Society of Chemistry. Panel (b) reproduced with permission.[312] Copyright 2015, Nature Publishing Group. Panel (c) reproduced with permission.[313] Copyright 2017, American Chemical Society. Panel (d) reproduced with permission.[309] Copyright 2014, American Chemical Society.

RP/activated carbon, RP/Super-P, RP/graphene, phosphorene/graphene, amorphous P/N-doped graphene, and BP/ketjen-black carbon.[31,314–316,319–333]

3.3.1. Red Phosphorus

RP is considered as a potential anode of SIBs due to its high theoretical capacity of ≈2600 mA h g^{-1} (assuming Na_3P is formed) and safe operating potential (≈0.70 V vs Na^+/Na). However, its low electrical conductivity limits the utilization of the active material and increases the polarization. Also, the continuous volume expansion during sodium intercalation/de-intercalation has many drawbacks, such as the pulverization of the active material, which further worsens the electrical contact with the current collector and binder, and the formation of an unstable SEI, and thus hinders the kinetics and leads to low columbic efficiency. So far, advanced phosphorus anode materials can be synthesized by four different approaches: ball milling, vaporization–condensation, and carbothermic reduction and wet-chemical synthesis.

Kim et al. reported an amorphous RP/carbon composite with 70 wt% phosphorus loading by ball milling, which exhibit two sloping regions and one plateau in its voltage profiles (**Figure 28**a).[316] The cycle stability test in Figure 28b showed that this material have relatively stable cycle life in 30 cycles. This result has stimulated extensive research on phosphorus-based anode material for SIBs by optimizing the structures of host materials for phosphorus to increase the electronic conductivity and accommodate volume changes during charge and discharge.[319,323,324,327–329] Song et al. further reported a chemically bonded P-CNT hybrid

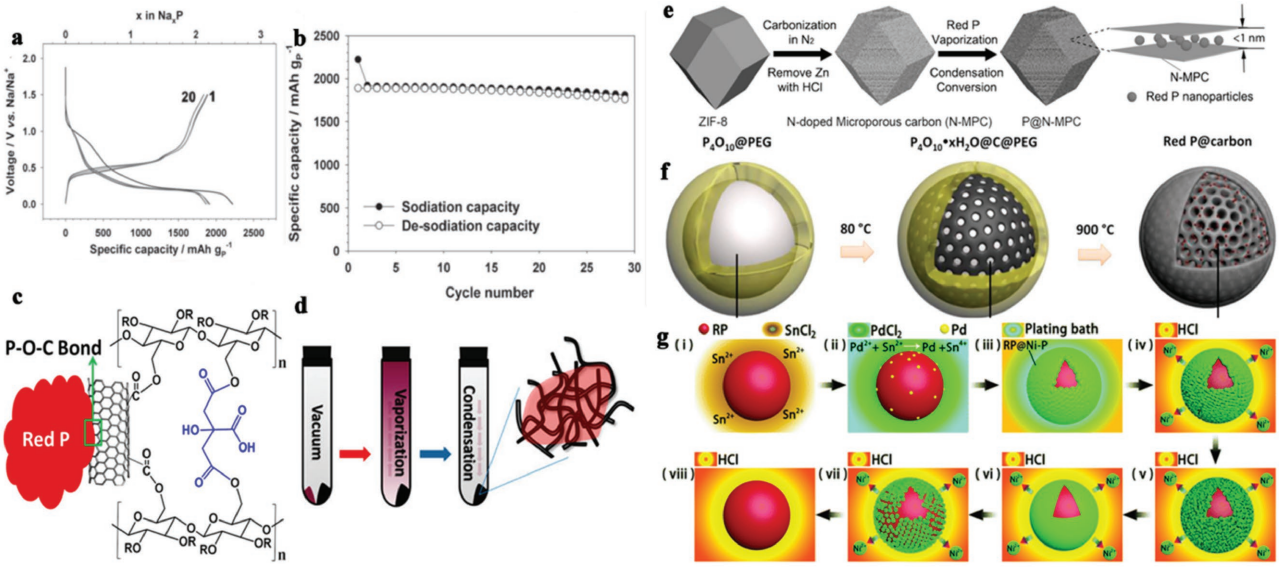

Figure 28. a) Voltage profiles and b) cycle performance of amorphous red P/C composite obtained with PAA binder.[316] c) Interaction between P-CNT hybrid and c-NaCMC-CA binder.[334] d) Schematic illustration of the synthesis process for red P-SWCNT composite.[324] e) Schematic illustration of the preparation process for P@N-MPC.[329] f) Schematic and digital photographs of the synthesis procedure for the ultrafine red P particles embedded in a 3D carbon framework (P/C composite).[335] g) Schematics of electroless deposition of Ni on the red P nanoparticle (i–iii) and the evolution of the red P@Ni-P core@shell nanostructure through chemical de-alloying (iv–viii).[330] Panels (a,b) reproduced with permission.[316] Copyright, 2013 Wiley-VCH. Panel (c) reproduced with permission.[334] Copyright 2015, American Chemical Society. Panel (d) reproduced with permission.[324] Copyright 2015, American Chemical Society. Panel (e) reproduced with permission.[329] Copyright 2017, Wiley-VCH. Panel (f) reproduced with permission.[335] Copyright 2016, Elsevier. Panel (g) reproduced with permission.[330] Copyright 2017, Royal Society of Chemistry.

(Figure 28c), which can deliver an initial capacity of ≈2100 mA h g^{-1} with a capacity retention of 75.5% after 100 cycles at 520 mA g^{-1}.[334]

Using a modified vaporization–condensation method different from ball milling, Zhu et al. synthesized a RP/single-walled carbon nanotube composite (red P-SWCNT) (Figure 28d).[324] The resulted RP/SWCNT electrode presents a stable cycle life up to 2000 cycles even charged/discharged at a high rate of 2 A g^{-1}. Liu et al. used physical vapor deposition to uniformly deposit red phosphorus nanodots on flexible reduced graphene oxide sheets (referred to as P@RGO).[331] The RGO acts as a mediator between RP and the external circuit, reduces the Na^+ diffusion path, and provides structure reinforcement during the sodiation/de-sodiation due to the free space between the RGO sheets. Thus, the electrochemical performance is enhanced compared to amorphous RP. Using a vaporization–condensation-conversion method, Yu and co-workers reported on a phosphorus-carbon composite synthesized by confining nanosized amorphous RP into a zeolitic imidazolate framework-8 (ZIF-8)-derived nitrogen-doped microporous carbon matrix (denoted as P@N-MPC) (Figure 28e).[329] When used as the anode for SIBs, the P@N-MPC composite demonstrated excellent rate performance and long cycle life, which can still maintain ≈450 mA h g^{-1} at 1 A g^{-1} after 1000 cycles. The superior sodium storage performance of the P@N-MPC is mainly attributed to the novel structure. The N-doped porous carbon with sub1 nm micropore facilitates the rapid diffusion of organic electrolyte ions and improves the conductivity of the encapsulated RP. Furthermore, the porous carbon matrix can buffer the volume change of RP during repeated sodiation/de-sodiation, keeping the structure intact after a long cycle life.

Sun et al. demonstrated a carbothermic reduction of P_4O_{10} into nanoporous RP particles (≈ nm) embedded in a 3D carbon framework (Figure 28f).[335] Enhanced imaging of the P/C composite confirmed its nanostructure and the presence of inner porous interchannels where carbon is uniformly dispersed and phosphorus is located along the channels. The P/C composite exhibits an initial specific capacity of 1027 A g^{-1} at C/5 with a columbic efficiency of 76%, along with a decent cycling performance of 88% retention after 160 cycles at 0.2 C. This performance improvement is due to the nanostructure of RP, which minimizes the diffusion path of Na^+ ions, and the role of the carbon framework, which enhances the electrical conductivity of RP due to the P—O—C bonds and provides a buffer space for the volumetric changes during the intercalation/de-intercalation of Na^+.

Recently, Zhou et al. developed a wet solvothermal method to synthesize hollow RP nanospheres (HPNs) with porous shells and proposed a possible gas-bubble mechanism that direct the formation of the hollow nanospheres.[336] They hypothesized that the P nuclei are produced at the surface of NaN_3 initially. Then, with the increase in the gas-bubble sizes, P nuclei are gradually assembled at the surface of the bubbles, and as they detach from the surface of NaN_3, they form hollow phosphorus nanospheres. The resulted HPNs with 60 wt% P loading exhibit a specific capacity of 969.8 mA h g^{-1} (based on P weight) after 600 cycles at 1 C, demonstrating excellent cycle stability at high rate of charge/discharge. Very recently, Liu et al. further reported RP@Ni-P core@shell nanostructure as an SIB anode via electroless disposition with

chemical alloying (Figure 28g).[330] The Ni_2P shell generated on the RP core particle facilitates intimate contact between RP and a mechanically strong amorphous Ni-P outer shell with a high electronic conductivity, which ensures strong electrode structural integrity, a stable solid electrolyte interphase, and ultrafast electronic transport. It was found that the de-alloying time of (RP)@Ni-P can vary with shell thickness and composition of the Ni_2P layer. The 8 h RP@Ni–P composite presents a super high capacity, superior rate capability, and unprecedented ultralong cycle life at high rates (409.1 mA h $g^{-1}_{composite}$ after 2000 cycles). This simple scalable synthesis approach provides a new strategy for the optimization of core@shell nanostructures, paving the way for mass production of high-performance electrodes for SIBs and other energy storage systems.

3.3.2. Black Phosphorus and Phosphorene

Black Phosphorus: After the accidental discovery of black phosphorus (BP) during the conversion of white phosphorus to red phosphorus under high pressure (1.2 GPa and 200 °C).[337] Several attempts have been made to synthesize it by different methods. The most common is the high-energy ball milling of the commercially available red phosphorus.[338] In 2007, Park and Sohn reported a BP anode for LIBs through high-energy mechanical milling (**Figure 29**a).[339] After that, BP received much attention as the anode material for LIBs.[314,315,332,340–343]

Use of BP as the SIB anode was reported by Yu et al. in 2013.[344] Using first-principles simulation, they investigated the lithiation and sodiation kinetic of BP. It was found that BP can facilitate the diffusion of Li^+ and Na^+ along *a* axis of the large tunnels that

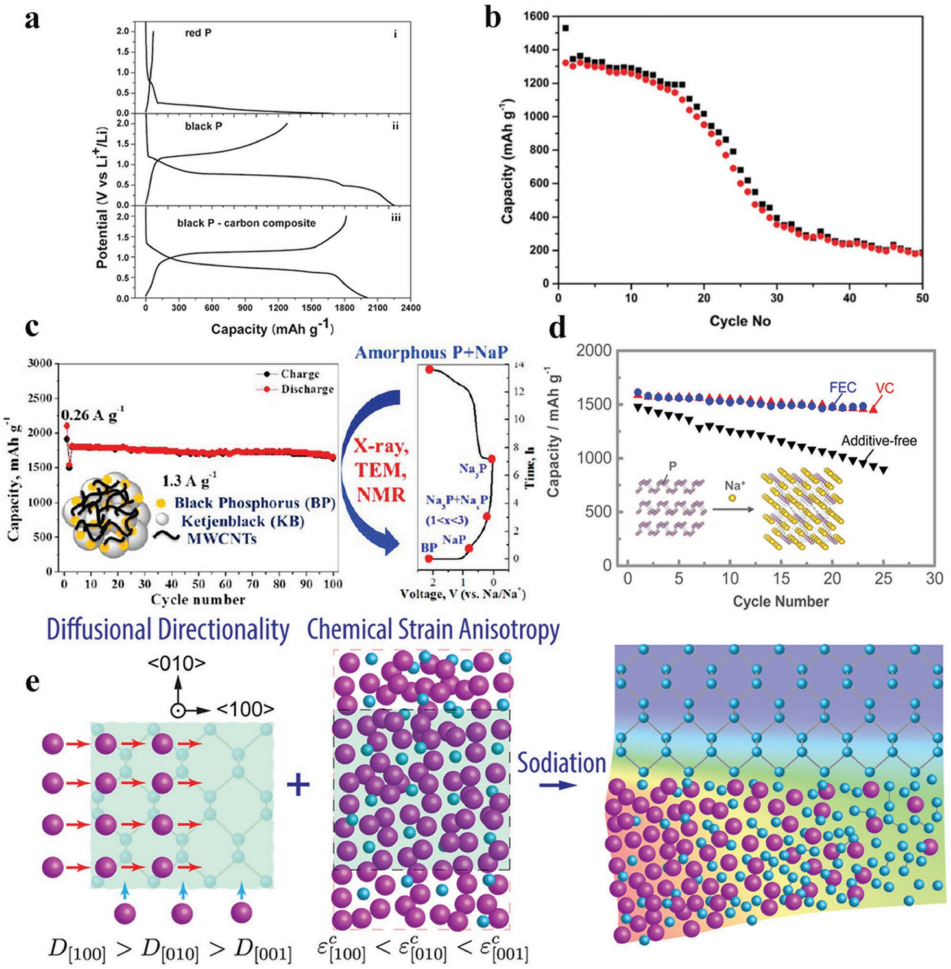

Figure 29. a) Electrochemical behaviors of various types of phosphorus: voltage profiles for first cycle of i) red phosphorus, ii) black phosphorus, and iii) black phosphorus–carbon composite.[339] b) Cycling performance of the phosphorus-carbon composites (C-1) in sodium half-cells within the potential window of 2.0–0.01 V (vs Na^+/Na) at a current rate of 100 mA g^{-1}.[345] c) Structure schematic and cycling performance of BPC composite at 1.3 A g^{-1} with voltage profile illustrating the phases at different states of charge.[31] d) Cycling performance of black P/PANa electrode in Na cells using additive-free electrolyte, electrolyte with FEC, and VC additive, with schematic illustrations of the crystal structures of black P and Na_3P as inset.[347] e) Illustration of the effect of diffusional directionality and chemical strain anisotropy on the morphological evolution in sodiated black phosphorus.[348] Panel (a) reproduced with permission.[339] Copyright 2007, Wiley-VCH. Panel (b) reproduced with permission.[345] Copyright 2015, Royal Society of Chemistry. Panel (c) reproduced with permission.[31] Copyright 2016, American Chemical Society. Panel (d) reproduced with permission.[347] Copyright 2016, American Chemical Society. Panel (e) reproduced with permission.[348] Copyright 2017, American Chemical Society.

formed during lithiation or sodiation. This finding showed that BP would be also an attractive anode material of SIBs. Ramireddy et al. demonstrated that, based on the use of a particular ball milling unit, a composite can be manufactured with nanoparticles of BP in a significantly disordered state (Figure 29b).[345] However, the reversible capacity of the as-prepared composite continuously decayed in 50 cycles, indicating the need for optimization on the structure and electrode/electrolyte interface of BP–host materials.

Therefore, Xu et al. synthesized a nanostructured BP/Ketjenblack-multiwalled carbon nanotubes composite (referred to as BPC).[31] The BPC composite was prepared by high-energy ball milling of phosphorous (70 wt%), ketjenblack, and multiwalled carbon nanotubes. The phosphorus nanoparticles interact with the highly conductive ketjenblack, forming secondary micro-sized particles. Introducing the multiwalled carbon nanotubes to the matrix forms a secondary conductive network and stabilizes the composite. The BPC composite delivered a high initial discharge capacity of 2011 mA h g^{-1} with an initial CE that exceeded 90%. It also attained a much-improved cycling performance and rate capability. Operando high-energy XRD coupled with ex situ ^{31}P NMR confirmed the formation of a crystalline Na_3P phase that starts at 0.3 V and gradually increases till the end of sodiation (0.2 V) in addition to an intermediate amorphous phase (NaP) at 0.8 V (Figure 29c). Recently, Ding et al. introduced an amorphous BP (αP) coupled with cubic boron nitrile (c-BN) and coated with nanoporous graphene (pGra).[346] The c-BN can act as a rigid skeleton that suppress volume expansion of the P during the sodiation process, while the pGra provides a tunnel for Na^+ ions by shortening the diffusion path and improves the electrical conductivity. The composite can exhibit initial discharge of 1220 mA h g^{-1} but with relatively lower columbic efficiency (≈64%) and slightly stable cycling for 100 cycles, maintaining a capacity of 947 mA h g^{-1} at 50 mA g^{-1}.

Besides, Dahbi et al. reported a composite electrode BP/AB with poly(sodium acrylate) (PANa) binder, which displays a specific capacity above 1600 mA h g^{-1} and stable cycle life with 91% capacity retention over 20 cycles.[347] It is found that both fluoroethylene carbonate (FEC) and vinylene carbonate (VC) is efficient electrolyte additives for the Na cells by forming an SEI with different surface stabilization mechanisms. The SEI surface layers modified by the FEC and VC attain longer cycle life and higher reversibility of the de-sodiation/sodiation of the black P electrode (Figure 29d). Chen et al. proposed a modeling approach combined with in situ TEM analysis to understand the morphological evolution and the stress generation in crystalline BP during the sodiation process (Figure 29e).[348] The model reveals that the morphological evolution and stress generation are controlled by two intrinsic anisotropies: sodium diffusional directionality and insertion strain anisotropy. During the first step of the sodiation (intercalation), sodium atoms favor diffusion along the [100] direction due to its significantly lower diffusion barriers compared to the [010] and [001] directions. As the layered structure of BP gradually transforms into an amorphous phase, the sodium diffusion becomes isotropic. However, the high cost of BP is the main challenge for its practical application. A mixture of BP and red P would be a solution to combine their advantages.[349]

Phosphorene: Similar to graphene as a single layer of graphite, phosphorene can be viewed as a single or few layers of black phosphorus. There are two main approaches to prepare phosphorene, including top-down and bottom-up.[350] The top-down approach relies on chemical (liquid phase/shear mixing) or mechanical (ball milling) exfoliation of bulk crystals into a few layers by weakening the interlayer interaction. The bottom-up approach relies on chemical synthesis.[351]

Using first principles calculation, Kulish et al. conducted a systematic study on a monolayer phosphorene to investigate its sodiation behaviour.[352] Kulish et al. found that Na diffusion on phosphorene is favorable and anisotropic, with a very small energy barrier of only 0.04 eV (**Figure 30**a). The phosphorene exhibits a high mechanical stability during the sodium insertion, and the Na–phosphorene tends to become more metallic as the Na ions intercalate in the structure, which increases the electronic conductivity. Therefore, because of the above advantages, monolayer phosphorene could an appealing anode of SIBs. Cui and co-workers, introduced for the first time a nanostructured phosphorene–graphene hybrid with 48.3% phosphorus that consists of phosphorene layers sandwiched between graphene sheets as displayed in Figure 30b.[353] This material can still maintain a reversible capacity of over 2000 mA h g^{-1} after 100 cycles at C/20. Cycling at moderate rates (3 C) and relatively high rates (10 C) showed similar trends (Figure 30c). This electrochemical improvement and cycle stability were attributed to the interaction between phosphorene and graphene. The graphene layers can accommodate the anisotropic volume expansion of phosphorene during the sodiation/de-sodiation and provides an electrical pathway that facilitates the electron transport, while the phosphorene layers offer a short diffusion path for Na^+ ions. Recently, Zhang et al. have reported functionalized few-layer phosphorene nanosheets decorated with PEDOT nanofibers, which can significantly improve the reaction kinetics and the surface wettability with the electrolytes. Therefore, it can demonstrate superior sodium/lithium storage performance with improved cycle life and rate capability.[354] However, one of the big concerns is the scalable synthesis of phosphorene for practical application, which requires novel approaches.

3.3.3. Tin Phosphide

Another promising SIB anode material is Sn_4P_3, which possesses a volumetric capacity of 6650 mA h cm^{-3}, a gravimetric capacity of 1132 mA h g^{-1}, and good electrical conductivity (30.7 S cm^{-1}). Qian et al. reported a synergistic Na-storage reaction in the Sn_4P_3 anode, where the Sn and P atoms react with Na to form $Na_{15}Sn_4$ and Na_3P, respectively. The resulting $Na_{15}Sn_4$ alloy acts as a conducting pathway to activate the reversible Na storage reaction of nonconductive Na_3P particles; meanwhile, the well-dispersed Na_3P phases provide a shielding matrix to prevent the aggregation of the $Na_{15}Sn_4$/Sn nanoparticles, thus improving the cycling stability of the Sn_4P_3 anode (**Figure 31**a).[355] The Sn_4P_3/C nanocomposite could deliver a reversible capacity of over 700 mA h g^{-1} after 150 cycles at 50 mA g^{-1} (Figure 31b), indicating its potential applicability as a new SIB anode host. Kim et al. reported that Sn_4P_3 with the presence of FEC additives exhibited no sign of capacity fading within 100 cycles in spite of its large (micrometer-sized)

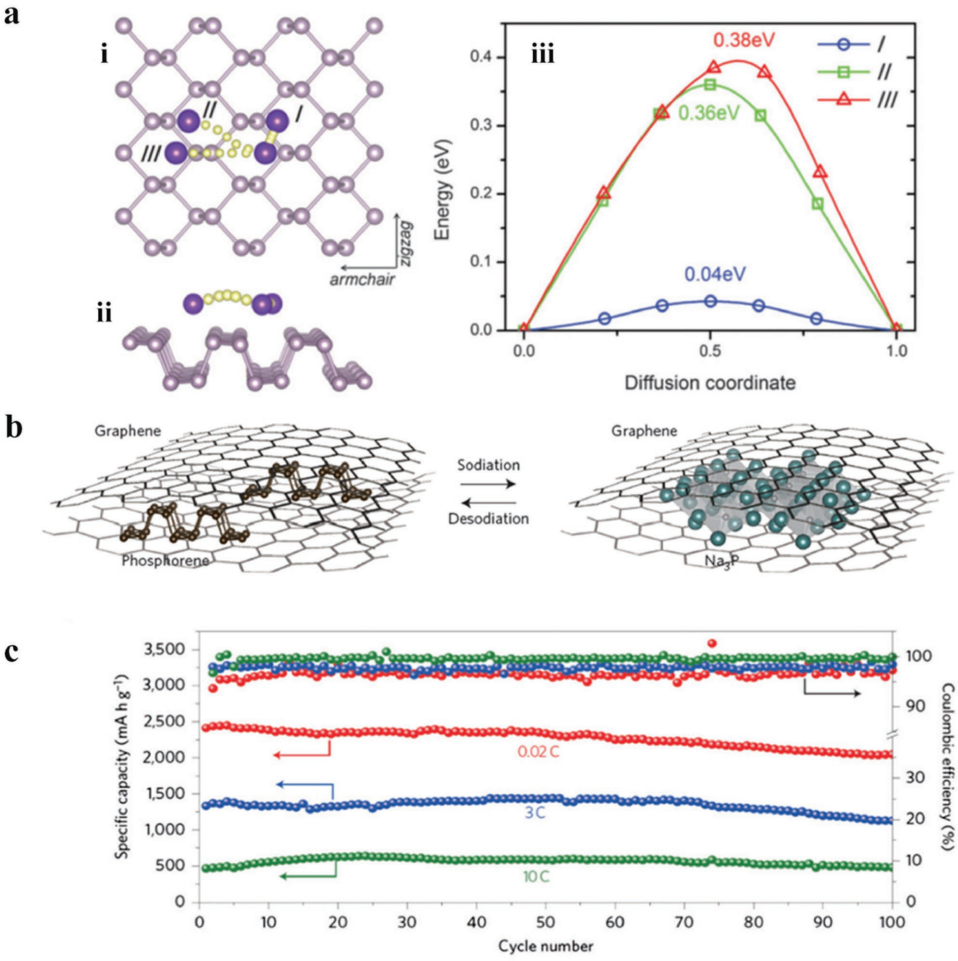

Figure 30. a) Sodium diffusion on monolayer phosphorene: (i) top and (ii) side views of Na diffusion pathways: (I) H-B-H, (II) H-B1-Hand (III)H-T-H. (iii) Corresponding energy barriers for Na diffusion on phosphorene.[352] b) Structural evolution of the sandwiched phosphorene–graphene structure during sodiation.[353] c) Reversible desodiation capacity and Coulombic efficiency for the first 100 galvanostatic cycles of the phosphorene/graphene (48.3 wt% P) anode tested under different currents.[353] Panel (a) reproduced with permission.[352] Copyright 2015, Royal Society of Chemistry. Panels (b,c) reproduced with permission.[353] Copyright 2015, Nature Publishing Group.

particles (Figure 31c).[356] Jang et al. reported that the combination of tris(trimethylsilyl)phosphite (TMSP) and FEC can further create a protective surface film on the Sn_4P_3 anode against unwanted electrolyte decomposition and prevent the formation of the $Na_{15}Sn_4$ phase, which will case a large volume expansion during the Na insertion (sodiation) process.[357]

Recently, Li et al. used a different method than conventional mechanical ball milling to synthesize Sn_4P_3/reduced graphene oxide nanohybrids with 89.6% Sn_4P_3.[358] They used low-temperature solution-based phosphorization reaction route from Sn/rGO (Figure 31d). The resulted Sn_4P_3/rGO electrode can deliver 656 mA h g^{-1} at 100 mA g^{-1} and still 391 mA h g^{-1} when increased the rate to 2.0 A g^{-1}. In addition, a longer cycling performance of 1500 cycles with a capacity of 362 mA h g^{-1} at a moderate rate of 1.0 A g^{-1} can be obtained. The porous structure, the rGO conductive host, and the strong interaction between Sn_4P_3 and rGO were assigned for its excellent electrochemical performance. While using a top-down phosphorization, Liu et al. reported uniform yolk–shell Sn_4P_3@C nanospheres (Figure 31e).[359] The rationally designed void space in between the shell and nanoparticles allows for the expansion of Sn_4P_3 without deforming the carbon shell or disrupting the SEI on the outside surface. Owing to these unique structural features, the as-obtained yolk–shell Sn_4P_3@C nanospheres exhibit high specific capacity of 790 mA h g^{-1} together with good cycle stability up to 400 cycles and good rate capability up to 3 C.

4. Electrolytes

4.1. Nonaqueous Organic Electrolytes

The electrolyte is an important component of battery system.[360] Its compatibility with sodium-based electrodes is an essential step toward development of advanced SIB technology.[14,40,361] Requirements for liquid electrolytes in SIBs are similar to those required for LIBs. The electrolyte challenges can be summarized as follows: (i) a big difference between the energy levels for the lowest unoccupied molecular orbital and highest occupied molecular orbital in the extended voltage window stability

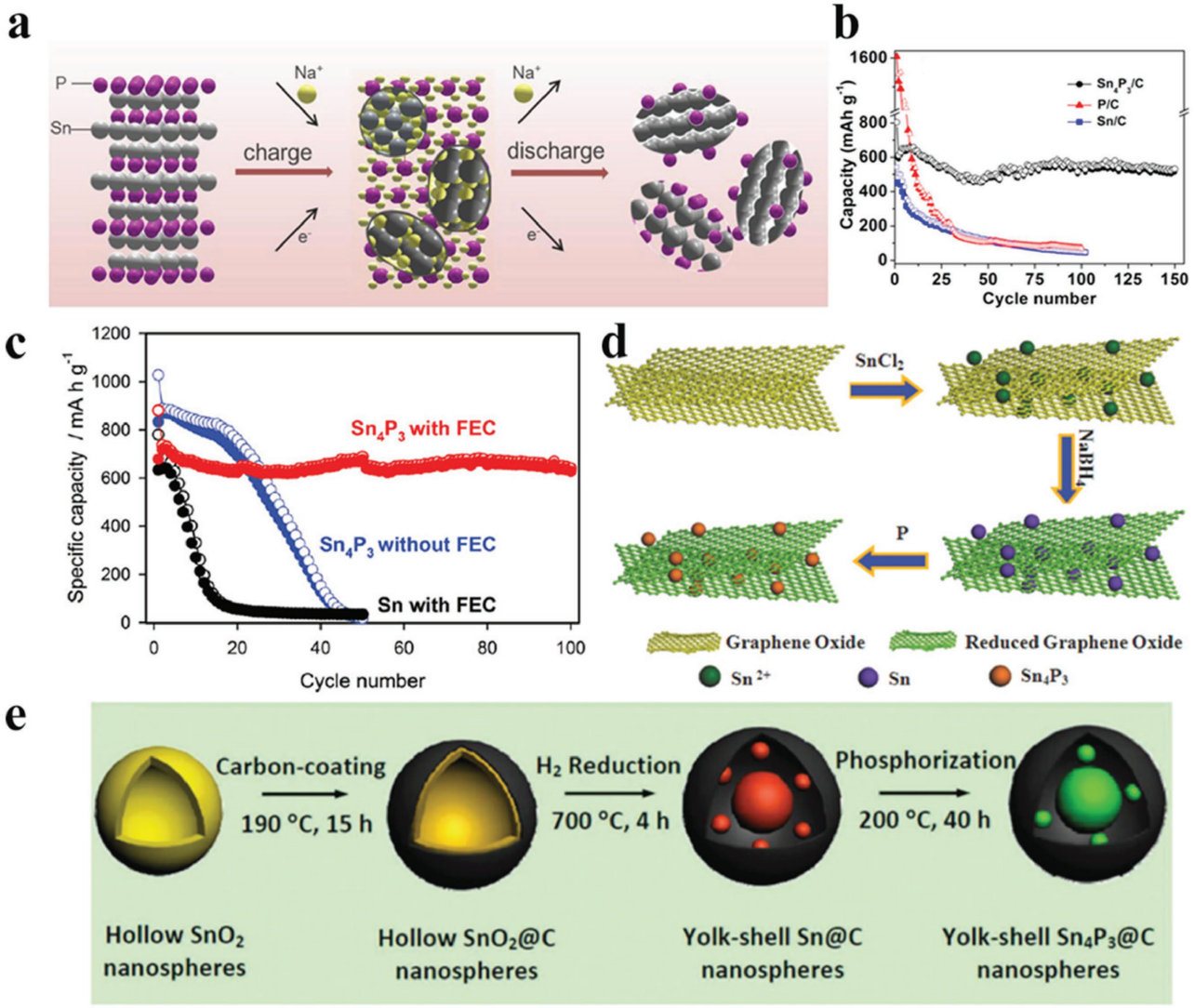

Figure 31. a) Schematic illustration of the Na-storage mechanism in Sn_4P_3 electrode.[355] b) Comparison of the reversible capacities of the Sn_4P_3/C, Sn/C, and P/C electrodes at a current rate of 100 mA g^{-1}. All the capacities were calculated on the basis of the mass of active materials, excluding the carbon.[355] c) Cycle performance of Sn_4P_3 and Sn electrodes obtained with or without an FEC additive.[356] d) Schematic illustration of the synthesis process of the Sn_4P_3/RGO hybrid sample.[358] e) Schematic illustration of the fabrication of uniform yolk–shell Sn_4P_3@C nanosphere anodes.[359] Panels (a,b) reproduced with permission.[355] Copyright 2014, American Chemical Society. Panel (c) reproduced with permission.[356] Copyright 2014, Wiley-VCH. Panel (d) reproduced with permission.[358] Copyright 2016, Wiley-VCH. Panel (e) reproduced with permission.[359] Copyright 2015, Royal Society of Chemistry.

of 0–5.5 V (vs Na), (ii) high ionic conductivity (>5 mS cm^{-1}) with low viscosity, iii) compatibility problems between sodium anode-based materials and sodium cathode materials, iv) thermal instability and degradation with cycling, and v) high cost.[40]

Electrolytes are known to react with electrode surfaces during battery cycling to form a SEI.[362] Stabilizing the SEI, especially on the anode electrode surface, was a key factor for the commercialization of LIBs and will also be so for SIBs in the rechargeable battery market. As is the case for LIBs, most electrolytes for SIBs are based on carbonate and ester solvents. For LIBs, the beneficial effect of ethylene carbonate (EC) in stabilizing the graphite surface under intercalation and de-intercalation of lithium was the origin of the commercialization of LIBs in 1991.[363] Unfortunately, in carbonate-based electrolyte, sodium cannot intercalate into the graphite sheet alone due to its large radius.[364] This problem eliminates graphite as an appropriate anode candidate for SIBs, and EC by itself was discarded as a solvent due to its high melting point. Propylene carbonate (PC) was used instead, in the presence of a sodium perchlorate salt ($NaClO_4$), which is less moisture sensitive than sodium hexafluorophosphate ($NaPF_6$) salt. To improve the cycling performance of SIBs and increase the ionic conductivity of the electrolyte, binary and ternary solvent mixtures have been studied. For example, EC was used as a co-solvent to form a stable SEI on a hard carbon anode in SIBs. An earlier study by Thomas et al. demonstrated, through TEM and electron energy loss spectroscopy, the formation of SEI on natural

graphite when it is cycled with sodium in the presence of 1.5 M $NaClO_4$ in EC.[365] The main composition of this SEI layer is Na_2CO_3 carbonate and sodium alkylcarbonates ($ROCO_2Na$). The authors proposed a mechanism for the SEI formation based on two steps. Above 0.8 V, the electrolyte decomposition forms Na_2CO_3 while below this potential, the electrolyte decomposition leads to the formation of sodium alkylcarbonates [$(-CH_2-OCO_2Na)_2$ and $(-CH_2-CH_2-OCO_2Na)_2$] with the formation of NaCl. This mechanism of decomposition of EC in SIBs is similar to that proposed for LIBs.[366] Later, Stevens and Dahn reported that hard carbon can deliver ≈300 mA h g^{-1} in an electrolyte compose of EC/diethyl carbonate (DEC) mixture with 1 M $NaClO_4$.[22] Alcántara et al. reported that hard carbon with a highly disordered structure and a low specific surface area can attain 285 mA h g^{-1} in an EC/dimethyl carbonate (DMC) based electrolyte.[367] Komaba et al. conducted a systematic study of a binary solvent by mixing EC, PC, butylene carbonate (BC), DMC, and DEC in various combinations.[368] They identified PC alone, EC alone, and EC:DEC as the best solvents in term of compatibility with a hard carbon anode. In half-cell tests, 1 M $NaClO_4$ in PC delivered 220 mA h g^{-1} with good Coulombic efficiency and stable cycle life (**Figure 32**a). The authors confirmed by XPS that the formation of thin SEI on the hard carbon is based on sodium carbonate (Na_2CO_3), alkyl carbonate ($ROCO_2Na$), ester linkage (−CO−O−), and alkane linkage ($-CH_2-$).

Ponrouch et al. conducted a systematic study on optimizing the electrolyte formulation to decrease the interfacial reactions and thus improve the electrochemical performance and abuse tolerance.[369] They found that the EC:PC solvent mixture was the best solvent formulation among various electrolytes, which has the largest electrochemical window (0–5 V vs Na) and best thermal stability (Figure 32b). Hard carbon was able to deliver 200 mA h g^{-1} with stable cycle life of over 180 cycles in 1 M $NaPF_6$/EC:PC or $NaClO_4$/EC:PC.[369] Moreover, sodiated hard carbon has the highest onset heat generation temperature and lowest enthalpy of reaction in $NaPF_6$/EC:PC as revealed by differential scanning calorimetry (DSC) (Figure 32c). Ponrouch et al. further explored a ternary solvent-based electrolyte composed of 0.45 (EC):0.45(PC):0.1(PC), in which the $Na_3V_2(PO_4)_2F_3$// hard carbon full cell presented stable voltage profiles, good capacity retention and Coulombic efficiency (Figure 32d).[370]

Ether-based electrolytes have been also studied in SIBs because of their low viscosity and melting point. It is worth

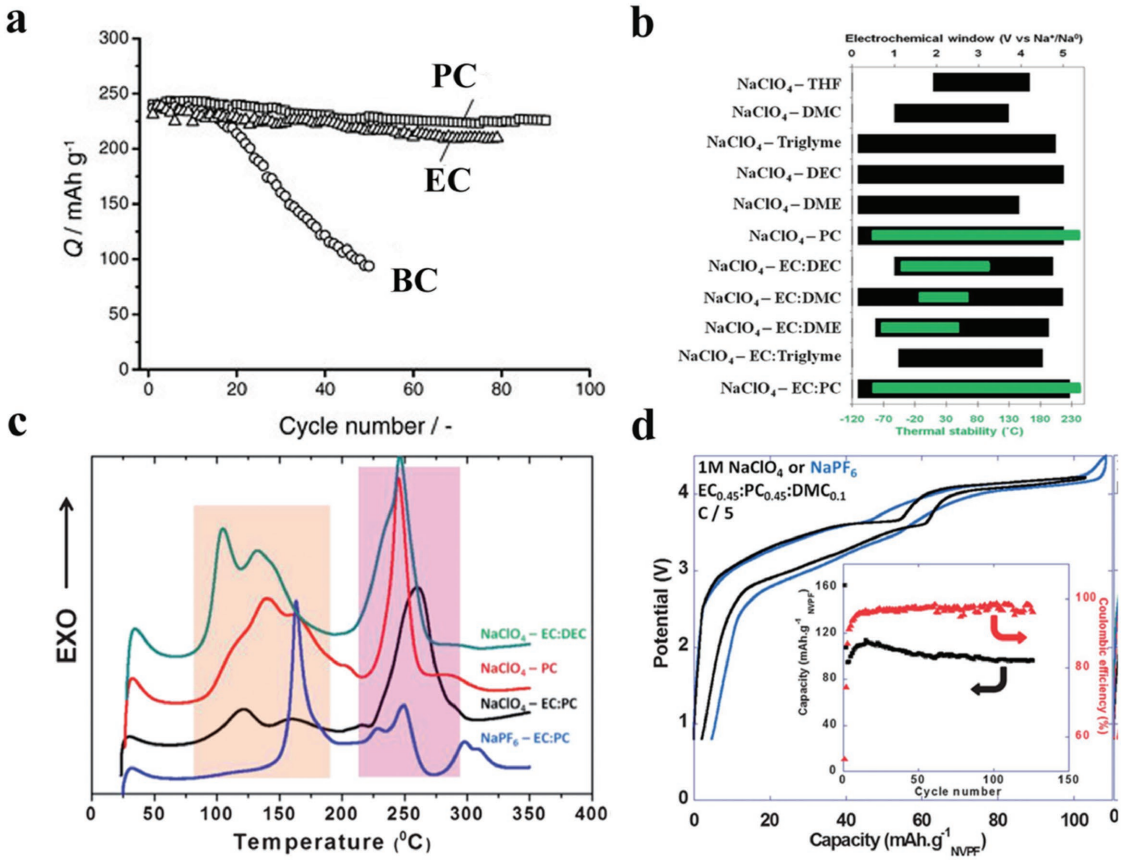

Figure 32. a) Variation in reversible capacities for hard-carbon electrodes in EC, PC, and BC solution containing 1 mol dm^{-3} $NaClO_4$ tested at 25 mA g^{-1} in beaker-type cells.[368] b) Electrochemical potential window stability (black bars and upper *y* axis) and thermal range (green bars and lower *y* axis) values of electrolytes based on 1 M $NaClO_4$ dissolved in various solvents and solvent mixtures and c) DSC heating curves of fully sodiated hard carbon in various electrolyte formulations.[369] d) Voltage versus capacity profiles for $Na_3V_2(PO_4)_2F_3$/HC full Na-ion cells cycled in 1 M $NaPF_6$ or 1 M $NaClO_4$ in $EC_{0.45}$:$PC_{0.45}$:$DMC_{0.1}$ recorded at C/5 (the inset displays the charge capacity and Coulombic efficiency versus cycle number (C/5; 1 M $NaClO_4$ in $EC_{0.45}$:$PC_{0.45}$:$DMC_{0.1}$).[370] Panel (a) reproduced with permission.[368] Copyright 2011, Wiley-VCH. Panels (b,c) reproduced with permission.[369] Copyright 2012, Royal Society of Chemistry. Panel (d) reproduced with permission.[370] Copyright 2013, Royal Society of Chemistry.

noting that these electrolytes are not commercially practical due to their high vapor pressure and narrow potential window. Recently, Jache et al. reported that graphite could be served as SIB anode by using ether-based electrolytes of 1 M NaOTf salt in diglyme (**Figure 33**a).[371] The sodium insertion into the graphite occurs via the formation of ternary graphite intercalation compounds (*t*-GIC) instead of binary GICs. In this electrolyte system, graphite could deliver 100 mA h g^{-1} for 1000 cycles at C/10 (Figure 33b). This result has stimulated the research of ether-based electrolytes in SIBs.[372–375] The proposed mechanism of sodium ether intercalation in diglyme was confirmed by Kim et al., who studied tetraethylene glycol dimethyl ether (TEGDME), diethylene glycol dimethyl ether (DEGDME), and DME containing 1 M $NaPF_6$ by in situ XRD and DFT calculations (Figure 33c).[372,373] The authors found that during Na intercalation, multi-stage reactions happen with Na/C atomic ratio between 1/28 and 1/21. Their DFT calculation indicated that Na ions and ether solvents are intercalated into the graphite in the form of $[Na–ether]^+$ complexes double stacked in parallel with graphene layers. Recently, impressive cycling performance was reported by Zhu et al. for graphite anode and 1 M $NaCF_3SO_3$/tetraglyme electrolyte.[374] More than 100 mA h g^{-1} as a reversible capacity was sustained after 6000 cycles under a 0.2 A g^{-1} current. The authors pointed out that the good electrochemical performance arises from the contribution of the capacitance in the total capacity, as revealed in cyclic voltammetry scans with graphite. This explanation was also proposed by Kim et al. during their investigation of Na insertion in hard carbon using $NaPF_6$ in ether-based electrolyte.[372] Jache et al. also conducted a systematic study on the insertion of sodium with different glymes and their derivatives containing 1 M sodium triflate into the graphite.[375] The redox potentials of this insertion shift depend on the ether chain length, which allows the tuning of the redox behavior by selecting and mixing appropriate ether solvents. The obtained capacity for monoglyme, diglyme, and tetraglyme solvent with the basic structural composition $CH_3–(O–CH_2)_n–O–CH_3$ with n = 1, 2, and 4 was about ≈80–100 mA h g^{-1}. The inferior behavior of triglyme, only 50 mA h g^{-1} reversible capacity, was attributed by the authors, in part, to the geometrically unfavorable coordination of the sodium ion by the solvent molecules. Sulfonate-based solvents were also explored for SIBs. For example, 1 M $NaClO_4$ in methyl ethyl methane sulfonate ($CH_3–SO_2–OC_2H_5$) with 2 vol% FEC shows higher electrochemical voltage stability than the same salt in PC containing the same amount of FEC additive (Figure 33d).[376] The cycling

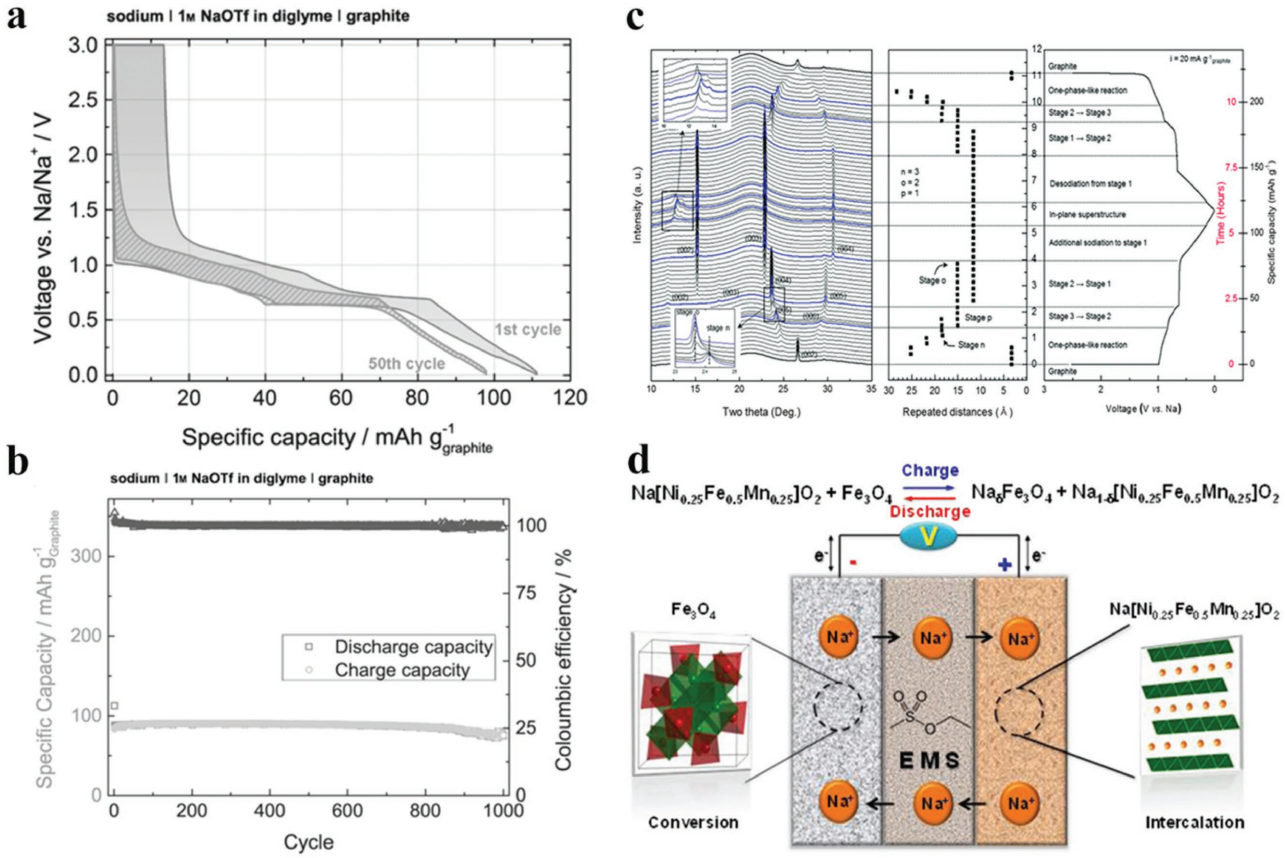

Figure 33. a) Specific capacities and charge/discharge characteristics of sodium/graphite cells cycled at i = 37.2 mA g^{-1} in 1 M $M^+(OTf)$ in diglyme and b) Coulombic efficiency of the sodium/graphite cell in 1 M NaOTf in diglyme over 1000 cycles at 0.1 C.[371] c) Operando synchrotron XRD analysis of the structural evolution of the ternary Na–ether–graphite system observed during electrochemical solvated-Na-ion intercalation and de-intercalation into/out of graphite in Na|1 M $NaPF_6$ in a DEGDME|graphite cell.[373] d) Schematic of C-Fe_3O_4/$NaClO_4$-EMS+2 vol% FEC/$Na[Ni_{0.25}Fe_{0.5}Mn_{0.25}]O_2$ full Na-ion battery, where EMS = ethyl methane sulfonate.[376] Panels (a,b) reproduced with permission.[371] Copyright 2014, Wiley-VCH. Panel (c) reproduced with permission.[373] Copyright 2015, Royal Society of Chemistry. Panel (d) reproduced with permission.[376] Copyright 2014, American Chemical Society.

performance of a $Na[Ni_{0.25}Fe_{0.5}Mn_{0.25}]O_2//Fe_3O_4$ full cell can deliver ≈100 mA h g^{-1} with an average working voltage of ≈2.4 V and stable cycle life up to 150 cycles at C/2.

Appropriate electrolyte salts stable toward oxidation/decomposition in SIBs are being sought. The conductivity of PC-based electrolytes with different salts are in an order of, $NaPF_6$ (7.98 mS cm^{-1}) > $NaClO_4$ (6.5 mS cm^{-1}) > NaTFSI (6.2 mS cm^{-1}), while the viscosities are basically the same (**Figure 34**a).[369] This conductivity dependence on anion are similar with that observed in LIBs, which was because the PF_6^- anion can suppress the salt dissociation and enhance ionic mobility.[377] Bhide et al. investigated the effect of salts on the electrochemical window and cathode cycling stability in SIBs.[378] They studied the suitability of $NaPF_6$, $NaClO_4$ and $NaCF_3SO_3$ in an EC/DMC mixture and found that the best ionic conductivity for a sodium electrolyte was obtained for 0.6 M $NaPF_6$ with ≈7 ms cm^{-1} and 1.0 M $NaClO_4$ with ≈5 ms cm^{-1} (Figure 34b,c). Of these mixtures, the $NaPF_6$-based electrolyte showed a better reversibility of the $Na_{0.7}CoO_2$ cathode material with less electrolyte decomposition. On the basis of impedance measurements, the authors concluded that a protective passivation layer with less resistivity is formed on the cathode material in the case of electrolyte containing $NaPF_6$ salt. In addition, Komaba et al. reported that better cycling performance in a hard carbon/$NaNi_{0.5}Mn_{0.5}O_2$ cell was obtained in $NaPF_6$-based electrolyte than $NaClO_4$- and NaTFSA-based electrolyte (Figure 34d).[368] Other salts such as sodium bis(fluorosulfonyl) imide (NaFSI), sodium bis[oxalate]-borate (NaBOB), and sodium-difluoro(oxalato)borate (NaDFOB) were explored for SIBs. For example, NaFSI in methyltetrahydrofuran (Me-THF) was found to exhibit the best electrochemical performance for imine-based anode materials containing Schiff bases and terephthalic groups.[379] The reported performance was attributed to better stability of organic anode materials and their low solubility in the NaFSI-(Me-THF) electrolyte.

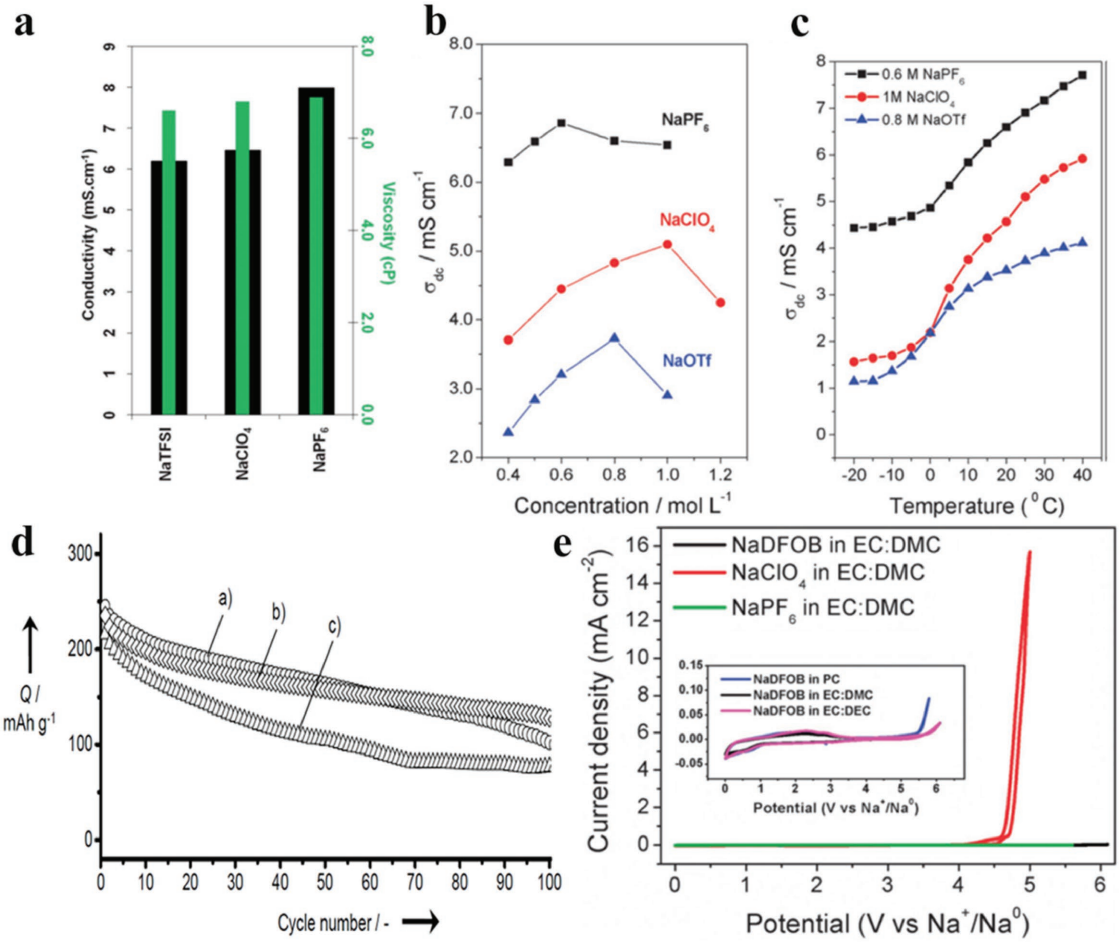

Figure 34. a) Conductivity (black bars) and viscosity (green bars) of PC-based electrolytes with 1 M of various Na salts.[369] b) Ionic conductivity of electrolytes containing $NaPF_6$, NaOTf, and $NaClO_4$ salts in EC:DMC (30:70 wt%) as a function of composition and c) ionic conductivity of liquid electrolytes with concentrations of 0.6 M $NaPF_6$, 0.8 M NaOTf, and 1 M $NaClO_4$ in EC:DMC as a function of temperature.[378] d) Variation in discharge capacities of hard-carbon/$NaNi_{0.5}Mn_{0.5}O_2$ cell galvanostatically tested at 300 mA ($g_{\text{of hard-carbon}}$)$^{-1}$ in PC solution containing 1 mol dm^{-3} (a) NaTFSA, (b) $NaPF_6$, and (c) $NaClO_4$.[368] e) Cyclic voltammograms of the cells with electrolytes of 1.0 M NaX (X = DFOB, ClO_4, and PF_6) in EC:DMC at room temperature at a scan rate of 1 mV s^{-1}. The inset shows the voltammograms of the cells with electrolytes of NaDFOB in PC, EC:DEC, and EC:DMC.[382] Panel (a) reproduced with permission.[369] Copyright 2012, Royal Society of Chemistry. Panels (b,c) reproduced with permission.[378] Copyright 2014, Royal Society of Chemistry. Panel (d) reproduced with permission.[368] Copyright 2011, Wiley-VCH. Panel (e) reproduced with permission.[382] Copyright 2015, Royal Society of Chemistry.

The good electrochemical performance could also result from the high resistivity of the Me-THF solvent to reduction. The same NaFSI salt also shows better electrochemical performance than $NaClO_4$ in the PC solvent when it is used in Na/$NaFe_{0.2}Ni_{0.4}Ti_{0.4}O_2$ and Na/$NaFe_{0.4}Ni_{0.3}Ti_{0.3}O_2$ half-cells.[380] The authors suggest that better compatibility between the electrolyte and the electrodes is responsible for the improved electrochemical performance. In addition, NaBOB shows better thermal stability with decomposition starting around ≈350 °C, as revealed by thermogravimetric analysis under nitrogen.[381] Unfortunately, this salt cannot be used alone in SIBs due to its poor solubility in carbonate solvents. To improve the Coulombic efficiency of the current SIBs, NaDFOB salt was tested with EC/DMC solvent.[382] The salt was prepared from the reaction of sodium oxalate ($Na_2C_2O_4$) with boron trifluoride diethyl etherate in acetonitrile. The NaDFOB in EC/DMC electrolyte provides a stable electrochemical window of 5.5 V and was tested in a Na/$Na_{0.44}MnO_2$ half-cell (Figure 34e). In this test, the NaDFOB-based electrolyte exhibited a high Coulombic efficiency (close to 100%) and long cycle life with low capacity fade. The reported performance was higher than that obtained by using $NaClO_4$- and $NaPF_6$-based electrolytes for the same system. This finding was explained as being due to the lower viscosities of the NaDFOB salt compared with the $NaClO_4$ and $NaPF_6$ salts.

Extending performance up to several thousand cycles in a full SIB is needed before possible deployment of this technology. This will require the use of electrolyte additives, as was the case for LIBs. The FEC additive is used to inhibit a continuous degradation of the SEI on the graphite anode for LIBs. So far, FEC has been the most common additive used in SIBs as shown by improved electrochemical performance with extended cycling.[383–385] The effect of the FEC additive is to form a stable SEI on the anode surface. This SEI should be thin in order to allow sodium-ion transport. A thick SEI could form, however, due to the continuous reaction of electrolyte with the electrode material surface. A systematic study was performed by Komaba et al. on the use of FEC, VC, trans-difluoroethylene carbonate (DFEC), and ethylene sulfite (ES) in the presence of 1 M $NaClO_4$ in a PC-based electrolyte (**Figure 35**a).[383,386] The results indicated that FEC is the only efficient electrolyte additive for both the cathode and the anode. Better cycling performance was obtained with 2 vol% FEC because of the formation of thin and stable organic-rich SEI. In addition, FEC was used by Wang et al. to extend the cycling life of a half-cell based on reduced graphene oxide.[387] In this work, the presence of 5% FEC in 1 M $NaClO_4$/EC+DEC electrolyte improved the capacity retention of reduced graphene oxide anode material by 20%. Choi and co-workers reported that a combination additive of FEC and tris(trimethylsilyl)phosphite (TMSP) could further

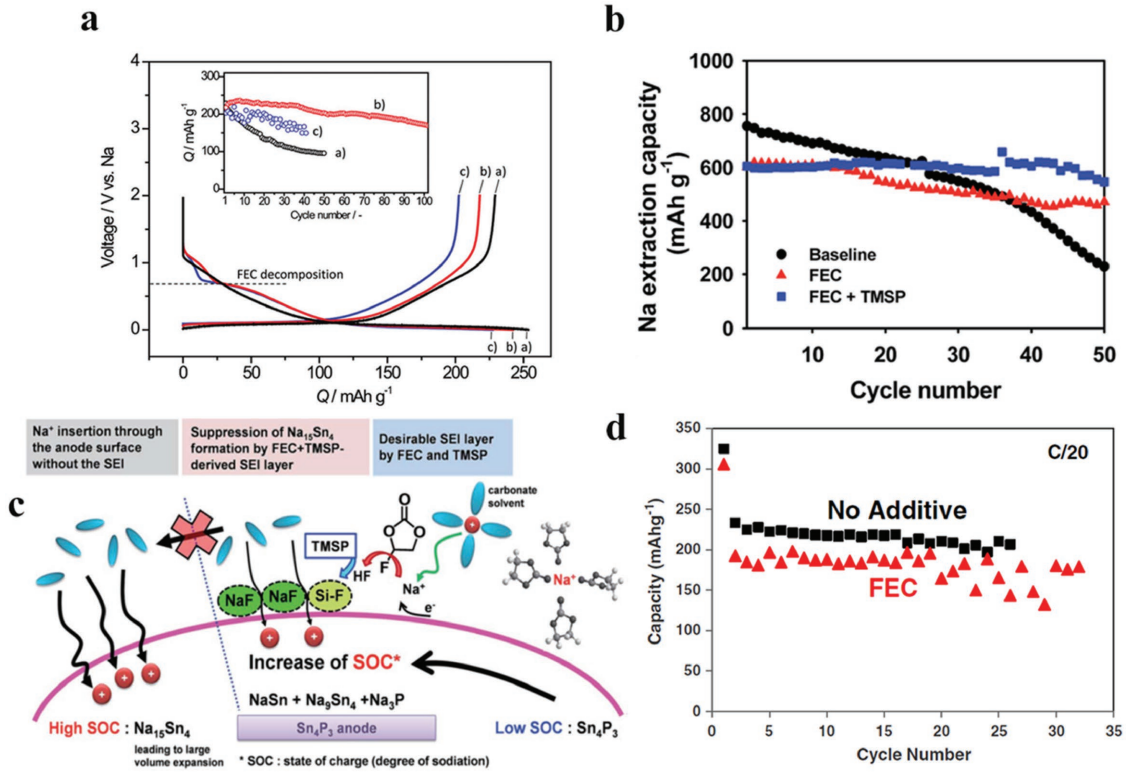

Figure 35. Initial reduction/oxidation curves for hard-carbon electrodes in 1 mol dm^{-3} $NaClO_4$ PC solution a) without and with b) 2 vol% and c) 10 vol% FEC at a rate of −25 and +25 mA g^{-1} in coin-type Na cells. Inset shows variation in reversible oxidative capacities for hard carbon during successive cycle tests.[383] b) Na extraction capacity of the Sn_4P_3 anodes at a rate of C/10 and c) schematic showing the function of the NaF-based SEI layer formed during sodiation.[388] d) Discharge capacity versus cycle number for hard carbon electrodes cycled (C/10) in 1 M $NaClO_4$ in EC:PC or without FEC addition.[389] Panel (a) reproduced with permission.[383] Copyright 2011, American chemical Society. Panels (b,c) reproduced with permission.[388] Copyright 2015, Royal Society of Chemistry. Panel (d) reproduced with permission.[389] Copyright 2013, Elsevier.

extend the cycle stability of Sn_4P_3 anode (Figure 35b).[388] This is possible because the hybrid SEI layer formed by the decomposition of the binary additive (FEC+TMSP) exhibited relatively high interfacial resistive NaF compared to a baseline electrolyte. As a result, the migration of Na ions into the anode was suppressed, which can prevent the formation of $Na_{15}Sn_4$ phase that would induce large volume expansion during sodiation (Figure 35c). However, a few studies report no improvement in hard carbon cycling when FEC is used in the half-cell configuration (Figure 35d).[389] This finding is attributed to an increased polarization during discharge and an inefficient plating or stripping at the sodium metal anode. Moreover, VC showed some electrochemical performance improvements on the cycling of a black phosphorus anode[390] and Na_2MnSiO_4 cathode materials.[391]

4.2. Solid-State Electrolytes

Compared to nonaqueous organic electrolytes, solid-state electrolytes have excellent mechanical properties, high thermal stability, a wide electrochemical window, and separator-free processes. These properties suggest that solid-state SIBs will probably become the ultimate choice for a higher energy and safer battery system.[361] For the solid-state electrolytes, inorganic solid materials such as glass–ceramic, solid polymers, and hybrids mixed with polymer and ceramic have been studied in SIBs, basically focusing on the room-temperature ionic conductivity and interfacial resistance.

Sulfide solid electrolyte has superionic conductivity ($\geq 10^{-4}$ S cm^{-1}) as well as excellent mechanical properties. A glass–ceramic Na_3PS_4 electrolyte was developed by Hayashi et al. through a high-temperature crystallization treatment (270 °C) after a planetary ball mill.[392] It has a high ambient-temperature conductivity of 2×10^{-4} S cm^{-1} (**Figure 36**a) and a wide electrochemical window of 5 V (Figure 36b) and was first used in a Na–Sn/Na_3PS_4/TiS_2 solid-state cell for room-temperature operation. The cell can maintain 90 mA h g^{-1} for 10 cycles. Later on, Hayaski et al. optimized the synthesis condition with high-purity crystalline Na_2S and increased the ionic conductivity of the Na_3PS_4 glass–ceramics to 4×10^{-4} S cm^{-1}.[393] Furthermore, they reported on a $(100 - x)Na_3PS_4 \cdot xNa_4SiS_4$ glass–ceramic electrolyte with even higher ionic conductivity. When increasing the amount of Na_4SiS_4 to 6 mol%, the conductivity reached 7.4×10^{-4} S cm^{-1} at room temperature.[394] The effect of aliovalent doping of M^{4+}, such as Si^{4+} for P^{5+} in cubic Na_3PO_4, being able to increase Na^+ conductivity was confirmed with the first-principles investigation of Ong and and co-workers.[395] Another sodium superionic conductor, Na_3SbS_4, with an ionic conductivity of 1.1×10^{-3} S cm^{-1} at 25 °C, was successfully demonstrated in the $NaCrO_2$/Na–Sn cell (Figure 36c–e).[396] In addition, this sulfide electrolyte was prepared by scalable solution processes using methanol or water to provide intimate ionic contact between $NaCrO_2$ and Na_3SbS_4. Besides the cation substitutions aforementioned, anion substitutions was also reported to improve the rate of ion diffusion.[397] The cubic Na_3PSe_4, in which S sites were substituted by the selenide (Se^{2-}), had a high ionic conductivity of 1.16×10^{-3} S cm^{-1}. The high ionic conductivity of Na_3PSe_4 was attributed to the large atomic radius of Se, which leads to lattice expansion and faster Na diffusion. Also, the high polarizability of Se^{2-} could lower the barrier between Na^+ and the anion framework.[398]

Another attractive Na^+ ionic conductor is based on the NASICON compounds. Using a solution-assisted solid-state reaction method, Guillon and co-workers synthesized a series of scandium-substituted $Na_3Zr_2(SiO_4)_2(PO_4)$ in the form of $Na_{3+x}Sc_xZr_{2-x}(SiO_4)_2(PO_4)(0 \leq x \leq 0.6)$.[399] In this case, when $x = 0.4$, an ionic conductivity of 4.0×10^{-3} S cm^{-1} at 25 °C was achieved with a high electrochemical stability window of up to 6 V (vs Na^+/Na). Recently, Hu and co-workers developed a new sodium composite electrolyte by introducing La^{3+} in the NASICON system, $Na_{3+x}La_xZr_{2-x}Si_2PO_{12}$. They obtained an ultrahigh ionic conductivity of 3.4×10^{-3} S cm^{-1} at 25 °C and 1.4×10^{-2} S cm^{-1} at 80 °C when x was 0.3.[400] They also assembled a solid-state cell based on $Na_3V_2(PO_4)_3$/IL/$Na_{3.3}La_{0.3}Zr_{1.7}Si_2PO_{12}$(SE)/Na (where IL is an ionic liquid, *N*-methyl-*N*-propyl-piperidinium-bis(fluorosulfonyl) imide) and found excellent cycling and rate performance, as shown in **Figure 37**. A novel NASICON material, $Na_{3+x}Sc_2(SiO_4)_x(PO_4)_3(0.05 \leq x \leq 0.8)$, was also investigated as a solid electrolyte for SIBs. Due to the ionic radius of Sc (0.745 Å), which is similar to Zr (0.72 Å), and the trivalence of Sc, $Na_{3.4}Sc_2(SiO_4)_{0.4}(PO_4)_3$ obtained a high ion conductivity (6.9×10^{-4} S cm^{-1}) at 25 °C.[401]

Although the inorganic solid electrolyte solves the safety issues, the high resistance at the solid–solid interface limits the electrochemical performance of these batteries. Moreover, the inorganic solid materials lack flexibility and are not easy to manufacture. To overcome these limitations, a highly flexible and light polymer electrolyte was introduced to form a hybrid solid electrolyte (HSE), which could combine both advantages of an inorganic (glass) ceramic and polymer. A homogeneous HSE based on NASICON ceramic powder ($Na_3Zr_2SiPO_{12}$), polyvinylidene fluoride-*co*-hexafluoropropene polymer, and ether-based electrolyte was designed by Kim et al. (**Figure 38**a)[402] This HSE displayed a high ionic conductivity of 3.6×10^{-4} S cm^{-1} at room temperature (Figure 38b) and a good compatibility with both hard carbon anode and $NaFePO_4$ cathode. Furthermore, a pouch, flexible solid-state SIB composed of hard carbon/HSE/$NaFePO_4$ exhibited good cycling performance and high specific capacity (Figure 38c). In addition, the HSE showed good thermal stability against shrinkage, whereas a commercial membrane experiences shrinkage at above 100 °C (Figure 38d). Similarly, Hu and co-workers studied a solvent-free hybrid solid electrolytes, and the best reported formula is 40 wt% $Na_{3.4}Zr_{1.8}Mg_{0.2}Si_2PO_{12}$ ceramic, polyethylene oxide (PEO_{12}) polymer, and NaFSI sodium salt (ratio of ester oxygen of PEO to Na^+ is 12:1).[403] This composite solid electrolyte showed high ionic conductivity of 2.4×10^{-3} S cm^{-1} at 80 °C and good thermal stability up to 150 °C and was successfully used in solid-state batteries composed of $Na_3V_2(PO_4)_3$/HSE/Na. Besides polymers, Goodenough and co-workers very recently developed a new method through introducing a plastic–crystal electrolyte interphase into the solid cathode particles ($Na_3V_2(PO_4)_3$) and solid electrolyte ($Na_3Zr_2(Si_2PO_{12})$) that effectively reduced the interfacial resistance (**Figure 39**).[404] Specifically, a plastic–crystal phase was obtained after 65 °C by heat treatment of a mixture of succinonitrile and $NaClO_4$ with a molar ratio of 20:1. With the

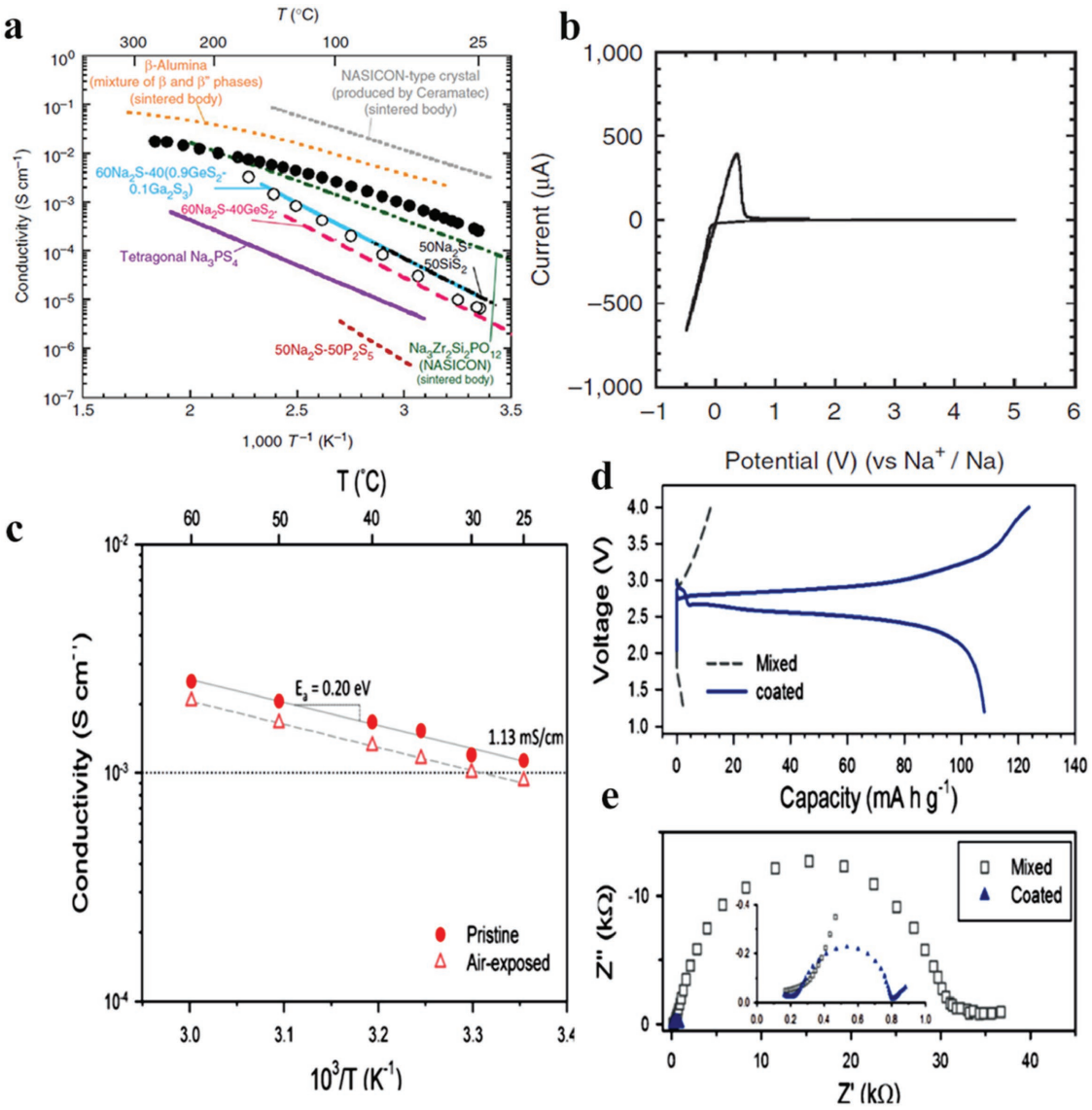

Figure 36. a) Conductivity of Na_3PS_4 glass and glass–ceramic electrolytes. Temperature dependences of the conductivities of the Na_3PS_4 glass (open circles) and the glass–ceramic prepared at 270 °C (solid circles). Conductivities of several Na^+ conductors reported so far are also shown as a comparison.[392] b) Cyclic voltammogram of the Na_3PS_4 glass–ceramic electrolyte. The glass–ceramic was prepared at 270 °C. A stainless-steel disk, as the working electrode, and a sodium foil, as the counter/reference electrode, were used. The potential sweep was performed with a scanning rate of 5 mV s^{-1} at 25 °C.[392] c) Conductivity of Na_3SbS_4 prepared by solid-state reaction at 550 °C. Data after exposure to dry air for 24 h are also compared. d) Initial charge/discharge voltage profiles (50 μA cm^{-2}, 30 °C).[396] e) Nyquist plots of NCO/Na-Sn all-solid-state cells. Results of the mixed electrode and the Na_3SbS_4-coated NCO electrode are compared. The cells were fabricated by pressing at 370 MPa. The NCO:Na_3SbS_4 weight ratio is 87:13.[396] Reproduced with permission.[392,396] Panels (a,b) reproduced with permission.[392] Copyright 2012, Nature Publishing Group. Panels (c–e) reproduced with permission.[396] Copyright 2016, Wiley-VCH.

addition of the plastic–crystal electrolyte, the discharge capacity of the cathode sharply increased from 8 to 112 mA h g^{-1}.

Solid polymer electrolytes (SPE) possess the general properties of the solid-state electrolyte and also have special characteristics such as flexibility, easy processability, and light weight, but still suffer from low ionic conductivity at room temperature (≤10^{-5} S cm^{-1}). The most promising polymer matrix, PEO, has been intensively studied in LIBs due to ether oxygen atoms with a strong donor character.[405] A PEO-based solid polymer electrolyte for SIB and the influence of the content of sodium salt and other inorganic nanopowders in SPE on ionic conductivity were investigated by Hwang and co-workers[406] They found that a polymer electrolyte with EO/$Na^+(NaClO_4)$ = 20 exhibits a maximum ionic conductivity of 1.35×10^{-4} S cm^{-1} and even higher value of 2.62×10^{-4} S cm^{-1} after addition of 5 wt% TiO_2 at 60 °C. This ionic conductivity increase was due to more defects and higher amorphicity in the PEO matrix. However, a $Na_{2/3}Co_{2/3}Mn_{1/3}O_2$ half-cell based on TiO_2-blended SPE had a first discharge capacity of only 49.2 mA h g^{-1} (0.1 C and 60 °C), which is much lower than that of the cell in a liquid electrolyte because of large polarization (high interfacial resistance).

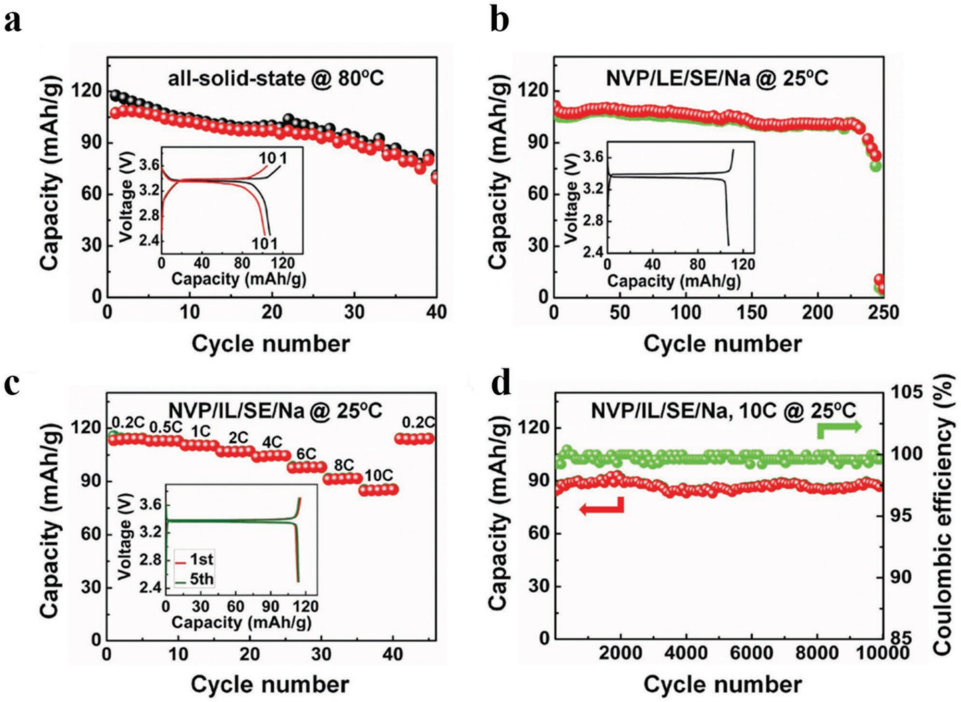

Figure 37. The electrochemical performance of solid-state batteries. a) The cycling performance of the NVP/SE/Na all-solid-state battery operated at 80 °C; the inset displays the charge/discharge curves of the 1st and 10th cycles at a current rate of 0.1 C. b) The cycling performance of the NVP/LE/SE/Na hybrid battery operated under a current of 0.2 C at room temperature; the inset shows the charge/discharge curve of the first cycle. c) Rate performance of the NVP/IL/SE/Na solid-state battery at room temperature with current rates of 0.2 C, 0.5 C, 1 C, 2 C, 4 C, 6 C, 8 C, 10 C; the inset exhibits the charge/discharge curves of the 1st and 10th cycle at a current rate of 0.2 C for the NVP/IL/SE/Na solid-state battery at room temperature. d) Cycling performance and Coulombic efficiency of the NVP/IL/SE/Na solid-state battery at room temperature with a current rate of 10 C for 10 000 cycles. Panels (a–d) reproduced with permission.[400] Copyright 2017, Wiley-VCH.

A cellulose-based hybrid polymer electrolyte is another effective method to optimize the electrolyte/electrode interface. Gerbaldi and co-workers explored this kind of SPE using sodium caroxymethyl cellulose (Na-CMC) which could not only improve the mechanical strength but also reduce the interfacial resistance.[407] Furthermore, biocompatibility, solubility in water, and low cost of Na-CMC are beneficial for large-scale application. The optimized electrolyte (PEO/$NaClO_4$/Na-CMC with 82/9/9 ratio) was studied in Na/SPE/TiO_2 and Na/SPE/$NaFePO_4$ cells at 60 °C. Both cells showed good cycling stability and well-defined voltage plateaus. The same research group introduced an ultraviolet-induced polymerization process in preparing polymer electrolytes for SIBs.[408] This preparation technology is efficient, ecofriendly, and economical for large-scale application. The photopolymer electrolyte with the best properties was synthesized by ultraviolet treatment using a mixture of bisphenol A ethoylate dimethacrylate (BEMA) and poly(ethylene glycol) methyl ether methacrylate (PEGMA) in a ratio of 35:65. The BEMA offered a 3D network, and the PEGMA co-monomer was used to reduce the glass transition temperature and enhance the mobility of Na^+. After swelling in $NaClO_4$/PC, the polymer electrolyte maintained the mechanical strength of SPE and was easy to manage. Also, the active photopolymer electrolyte showed a high ionic conductivity of about 5×10^{-3} S cm^{-1} at 20 °C, with an electrochemical window of up to 4.6 V and good thermal stability over 100 °C. Furthermore, favorable performance of the TiO_2/Na cell with photopolymer electrolyte led to more research on these membranes.

5. Operando Diagnostics

5.1. Operando Characterization on the Synthesis of SIBs Materials

Electrode materials are key components in rechargeable batteries. The crystal structures and morphologies of electrodes can significantly affect their reversible capacities, cycle stability, and rate capability. So far, numerous methods have been used to prepare battery electrodes, including high temperature calcination,[409] co-precipitation,[410] sol–gel,[411] hydrothermal reaction,[412] microwave reaction,[413] chemical vapor deposition,[414] electro-deposition,[415] electrospinning,[416] and ball milling.[417] In these methods, different starting materials, reaction temperature, time, and atmosphere can lead to completely different morphologies and phase structures. Operando real-time experiments enable direct observation of the sample under dynamic conditions showing the effects that normally are not discernible during ex situ post-synthesis measurements; thus, applying operando techniques is deemed indispensable to electrode synthesis improvement.

XRD is a primary technique for characterization of crystalline materials and has been widely used to analyze battery materials

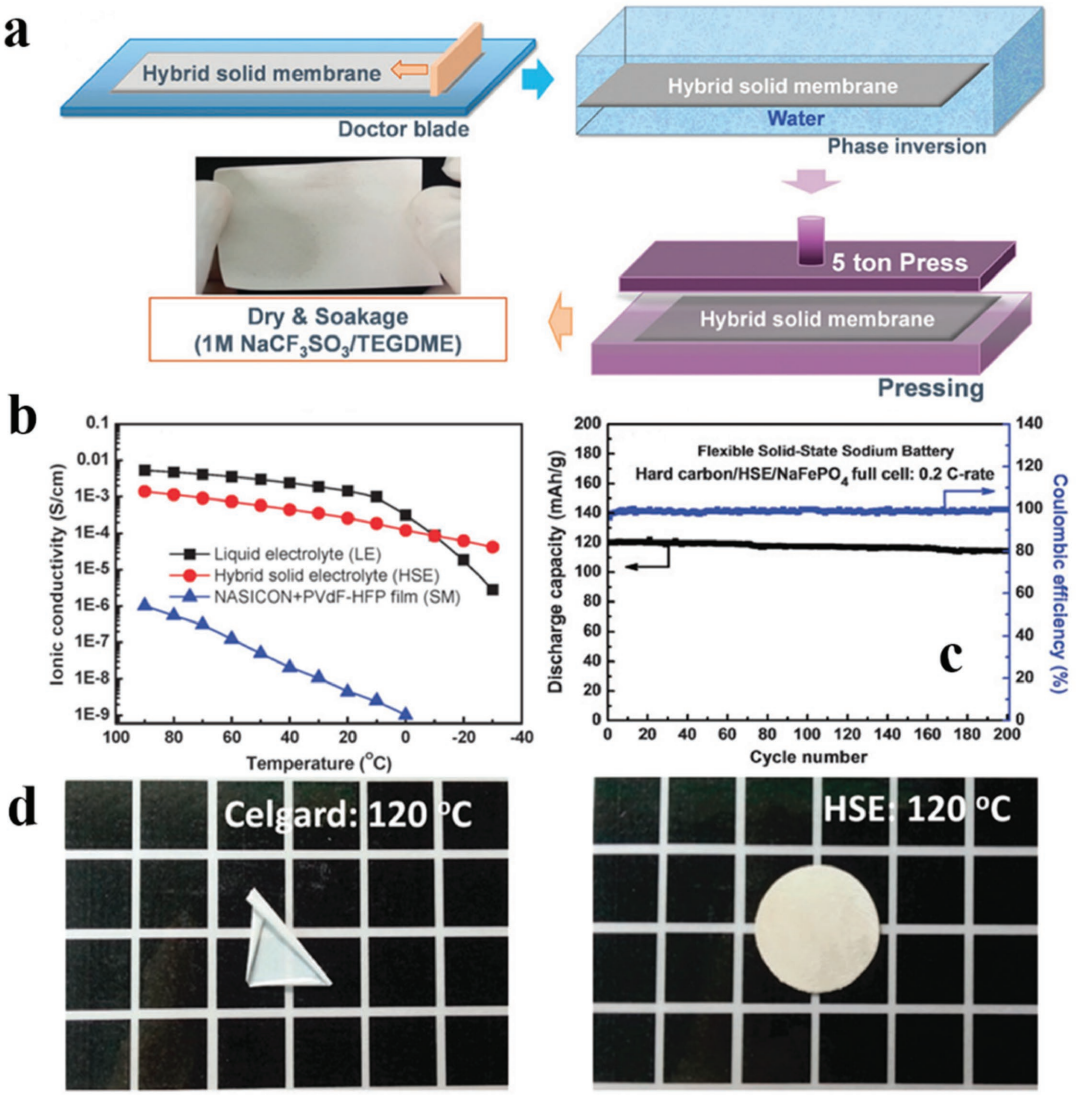

Figure 38. a) HSE hybrid preparation process involving NASICON powder, PVdF–HFP, and 1 M $NaCF_3SO_3$/TEGDME. b) Ionic conductivity versus temperature for composite solid film (SM), HSE, and ether-based liquid electrolyte (LE). c) Cycle performances and Coulombic efficiency of a flexible full cell for HC/HSE/$NaFePO_4$ batteries. d) Shrinkage of commercial membrane (Celgard) and HSE at 120 °C. Panels (a–d) reproduced with permission.[402] Copyright 2015, Royal Society of Chemistry.

for phase-identification studies.[418] Operando HEXRD has been extensively used to guide the synthesis of advanced electrode materials for LIBs. Chen et al. have investigated the phase evolution and crystal structure transition during solid-state synthesis of $LiFePO_4$.[33] They found that the solid state reaction forming $LiFePO_4$ started at a very low temperature, and $LiFePO_4$ was clearly observed when the reaction temperature was increased to above 173 °C. Several impurities including Li_3PO_4, Fe_2P, and Fe_3P that can improve the electrochemical performance of $LiFePO_4$ cathode material emerged when the reaction temperature was increased to above 400 °C. Chen and co-workers have further explored the development of full concentration gradient Ni-rich layered cathode for high energy LIBs.[419] By using in operando HEXRD, they found that both the pre-heating step and the sintering temperature play a critical role in controlling phase separation of the transition metal oxides and minimizing the content of Li_2CO_3 and NiO, both of which will deteriorate the electrochemical performance of the final material. In the case of SIBs, especially cathode materials, some crystal structures are actually metal-stable phases, while some are very sensitive to moisture.[82,116,420] Significant efforts have been devoted to study the synthetic condition to achieve optimal electrochemical performance.[122,421] However, most studies have applied trial-and-error approaches, which not only are time consuming but also may miss some critical information. Accordingly, operando techniques should provide a better understanding on the solid-state synthesis of SIBs cathode materials. Ma et al. employed operando synchrotron high-energy X-ray diffraction (HEXRD) to explore the formation of P2-type $Na_{2/3}MnO_2$.[422] To the best of our knowledge, this is the

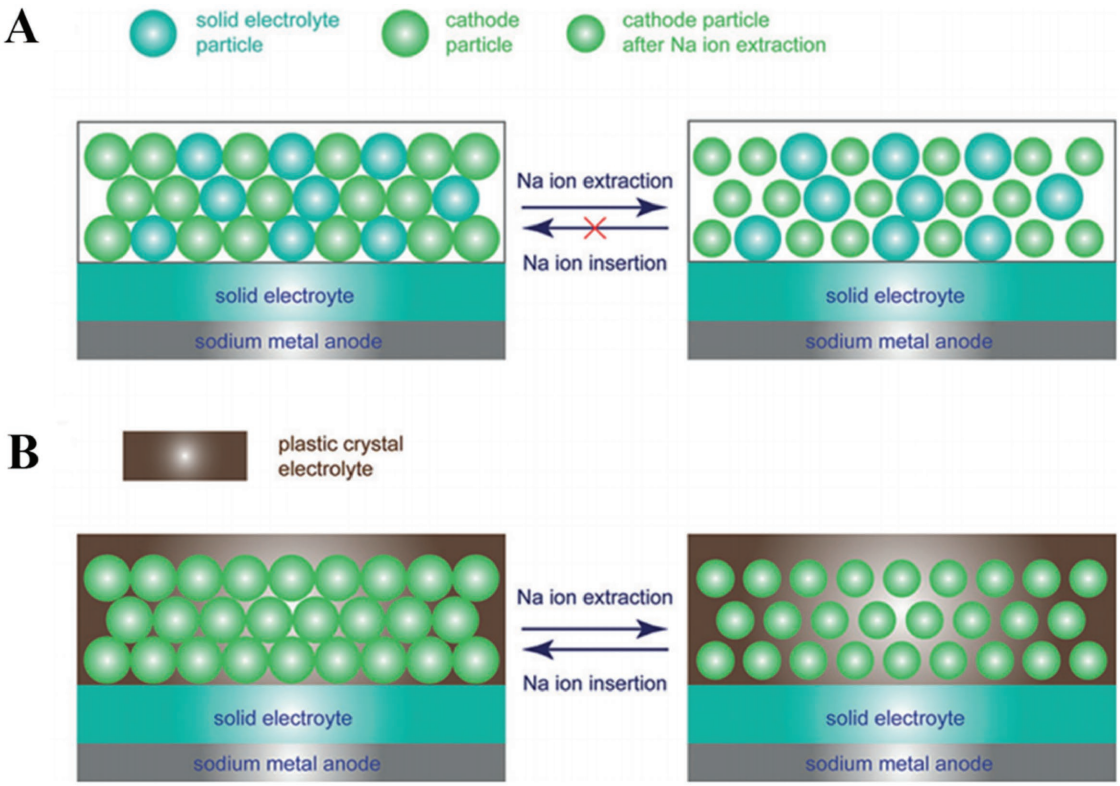

Figure 39. Illustrations of solid-state sodium batteries: a) Conventional solid-state sodium battery with solid electrolyte particles in the cathode. b) Solid-state sodium battery with plastic–crystal electrolyte in the cathode. Carbon black particles in the electrodes are omitted in the illustration for clarity. Panels (a,b) reproduced with permission.[404] Copyright 2017, Wiley-VCH.

first case using operando HEXRD to investigate the solid-state synthesis of cathode materials for SIBs. **Figure 40**a shows the contour plot of HEXRD patterns during the solid-state synthesis of P2-type $Na_{2/3}MnO_2$, in which the red means high intensity and blue represents low intensity. Covariance analysis[423] indicated that that the solid-state reaction mainly occurs at two temperature ranges: 270–300 °C and 550–710 °C. The representative HEXRD patterns in Figure 40b show the peak evolution of the starting material, intermediates, and final products. They indicate that a P3 type layered structure is formed at a relatively low temperature, 276 °C, and is then transformed into P3-type $Na_{2/3}MnO_2$ with an intermediated intergrown structure of P3 and P′3 at temperatures ranging from 559 to 596 °C. O′3 $NaMnO_2$ appears from 600 °C through 900 °C, while Na_3MnO_4 starts to form at about 704 °C. At 900 °C, a combination of Na_3MnO_4 and O′3 $NaMnO_2$ is obtained (Figure 40c). Based on this understanding, the composition of the products can be precisely controlled to systematically study the effect of different compositions. Xu et al. also investigated the solid-state synthesis of layered $NaNi_{1/3}Co_{1/3}Mn_{1/3}O_2$ cathode by using operando HEXRD.[123] They found that an intergrowth P2/O3/O1 structure formed at high temperature but disappeared during the cooling process, indicating that this structure needs to be obtained by a quenching process. Indeed, the intergrowth P2/O3/O1 structure showed significantly improved cycle performance compared with P2/O3 and P2/P3 structures during high-voltage cycling. Besides solid state synthesis, in operando HEXRD is also able to monitor the material synthesis by using microwave,[424] solvothermal,[425] hydrothermal,[426] and mechnochemical milling,[427] which can provide new insights and opportunities for the development of advanced battery materials.

XAS is a synchrotron-related characterization technique that includes XANES and EXAFS.[428] A significant difference between XRD and XAS is that XAS is sensitive to both crystalline and amorphous sample. In the X-ray absorption process, a core electron is excited to an empty state, and the X-ray probes the unoccupied part of the electronic structure of the system. The great power of XANES derives from its elemental specificity, so it can be used to determine the average oxidation state of an element in the sample, especially in the case of 3d-transition-metal compounds. EXAFS is a local probe for the unoccupied density of states around the ionization potential, and it is most often explained by scattering of photoelectrons at neighboring atoms revealing structural information.[429–432] To further understand the formation mechanism of Na_xMnO_2, Ma et al. used operando XAS to monitor changes in the chemical environment of Mn during solid-state synthesis.[422] As far as we know, this is the first use of operando XAS to study battery material synthesis. Figure 40d shows the contour plot of operando XANES spectra during the solid-state synthesis of P2-type $Na_{2/3}MnO_2$. As shown, from 271 to 305 °C, a significant edge shift occurs in the XANES spectra to higher energy compared with the Mn_2O_3 reference spectrum, suggesting that the valence of Mn in P3 Na_xMnO_2 is far more than 3+, yet not very close to 4+. As the temperature continuously increases to the

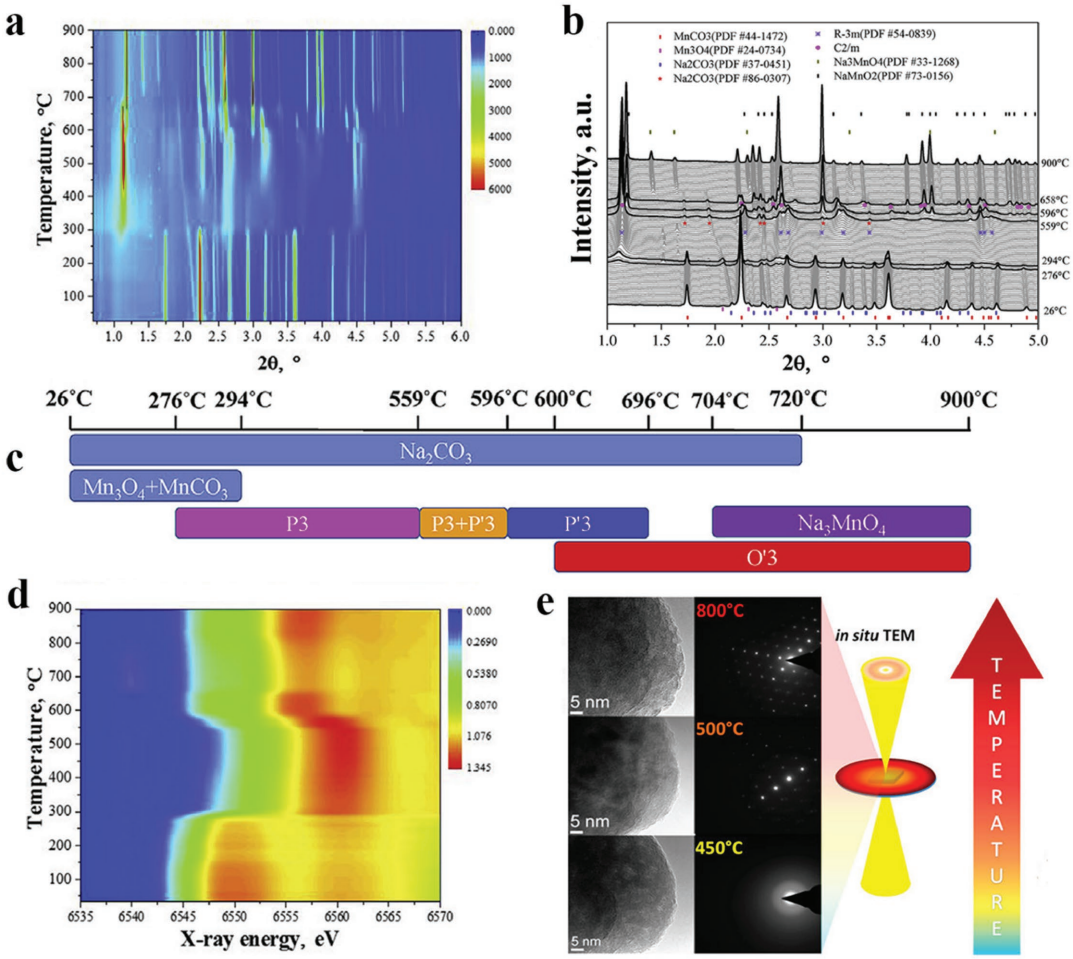

Figure 40. a) Contour plot of in situ HEXRD patterns.[422] b) In situ HEXRD patterns.[422] c) Phase evolution during the solid-state synthesis.[422] d) Contour plot of in situ Mn K-edge XANES spectrum collected during the solid-state synthesis.[422] e) Parallel in situ TEM and XRD heating experiments of $LiFePO_4$ precursors obtained by sol–gel method.[439] Panels (a–d) reproduced with permission.[422] Copyright 2017, Elsevier. Panel (e) reproduced with permission.[439] Copyright 2016, American Chemical Society.

point of the formation of intergrowth P3/P′3, the edge of the spectra shifted back to a lower energy. The decreased average valence for Mn is presumably a result of increasing the x value in Na_xMnO_2. As the Na insertion continues with rising temperature, the average valence of Mn further drops to almost 3+, presenting an edge position close to Mn_2O_3. Finally, the mean oxidative state of Mn does not change much as O′3 Na_xMnO_2 is formed and P′3 type Na_xMnO_2 disappears, indicating that the x value in this P′3 phase is very close to the actual x value in O′3 phase. These findings are consistent with the results obtained by operando HEXRD. Wang et al. has recently used in operando XAS to study the synthesis of nickel-rich layered transition metal oxides cathode, $LiNi_{0.7}Mn_{0.15}Co_{0.15}O_2$, during solid-state synthesis process.[433] Through synthetic control of the kinetic reaction pathway, a layered $LiNi_{0.7}Mn_{0.15}Co_{0.15}O_2$ with low cationic disordering and high reversible capacity is prepared in air. The findings may help to pave the way for designing high-Ni layered oxide cathodes for LIBs.

In addition to the crystal structure, the final shapes and sizes of crystals that govern their electrochemical performance are critically affected by the kinetic pathway of the phase transformation. The importance of in situ studies is that they can provide direct information on the structural and morphological evolution of the material during its synthesis, which, in turn, illustrates optimal synthesis conditions and improves the efficiency of the process. In situ TEM studies, where simultaneous imaging, spectroscopic, and diffraction measurements can be conducted with high spatial resolution, often at the nanoscale, are ideal tools for monitoring the time-dependent morphological and structural response of a material to the alteration of process conditions. So far, few research groups have investigated the crystallization of SIB materials using in situ TEM. However, in situ analysis of the annealing of $LiFePO_4$ using in situ TEM has been widely reported.[434–436] Chung et al. for the first time showed the presence of metastable transient phases at an atomic scale during the crystallization of an olivine-type metal phosphate.[437] They further found that the initial crystallites after nucleation during crystallization have a very high degree of ordering, significant local cation disordering is induced by rapid crystal growth in $LiFePO_4$

nanocrystals.[438] The findings indicated that in order to obtain a high degree of cation ordering, subsequent control of crystal growth during coarsening is very important. Ziolkowska et al. also used in situ TEM to investigate the growth of $LiFePO_4$.[439] As shown in Figure 40e, the precursor was fully amorphous at the beginning of the annealing process, and mesoporosity (with the average pore size of about 2 nm) was visible in the particles. During further annealing, these grains arranged into bigger crystals (at 800 °C) despite the randomness of their initial nucleation and the presence of polycrystallites at lower temperatures. Based on the TEM images, with increasing annealing temperature, the morphology of the particles became more porous, and their surfaces and shapes changed slightly. By using in situ TEM, Zaghib and co-workers further found that 700 °C is the optimum synthesis temperature for $LiFePO_4$, while $LiFePO_4$ tend to decompose at temperatures higher than 800 °C.[435] And the results also indicated that the homogeneous deposit of the carbon deposit at 700 °C is the result of the annealing that cures the disorder of the surface layer of bare $LiFePO_4$. Thus, in situ TEM is a very effective way to study the synthesis process and better understand the relationships between the structure and the electrochemical properties of electrode materials. These encouraging results will stimulate the study of SIB materials using in situ TEM and facilitate the design and synthesis of high-performance electrode materials.

5.2. Operando Characterization on Charging/Discharging of SIBs Materials

Battery operation is usually accompanied by numerous structural changes in the bulk electrode materials and at the electrode/electrolyte interfaces, and these changes are highly related to the material's electrochemical behavior.[16] Of key importance is the nature of the structure evolution such as phase transition and reaction kinetics as well as morphological changes, which can give valuable information for future design and optimization of the battery performance. However, such information cannot be obtained by ex situ characterizations as the batteries usually work in a well-sealed environment and the reaction intermediates/products are sensitive to air and moisture. Thus, applying operando characterization is indispensable to elucidate the evolution of the electrode structure and the complicated chemical processes within it during battery operation.

5.2.1. Operando Characterization on Morphology Changes during Cycling

Most of the cathode materials are based on Na^+ intercalation/de-intercalation, and they usually undergo many atomic structure changes rather than morphological changes during charging/discharging. However, many anode materials (especially high capacity alloy-based anodes such as Na metal and Sn- and P-based materials) undergo huge volume changes during sodiation/de-sodiation, which pose a great challenge for attaining stable cycle life.[13,20,39,440–442] Therefore, it is vital to visualize the detailed volume expansion/contraction process and understand the failure mechanism of the battery.

Optical microscopy has a relatively low resolution due to the diffraction limit of visible light, thus limiting the detection of nanostructures.[443] However, when combined with electrochemical devices, in situ optical microscopy may allow the observation of the microstructure evolution or color changes during charge/discharge processes.[444–448] Using in situ light microscopy, Nakamura and co-workers observed cross-sections of the surface of sodium electrodes during the electrochemical sodium deposition/dissolution process and obtained video of sodium growth for in situ observation.[449] **Figure 41**a,b shows in situ light microscopy images of electrochemical sodium deposition and dissolution on a sodium electrode with 1 M $NaPF_6$/PC electrolyte. Nakamura and co-workers found that the electrochemical sodium deposition and dissolution were almost independent from the type of electrode materials, such as sodium or copper. Granular sodium was deposited at pits on an electrode. Then, the sodium particles grew linearly from the electrode surface, becoming needle-like in shape, which is different from the Li deposition process. This result may be due to different ionic mobility at the interface of the electrode and electrolyte solution. At the same time, the sodium was dissolved near the base of the needles and became "dead sodium". This would cause low Coulombic efficiency with respect to sodium deposition/dissolution. Such a low irreversibility would cause large amounts of sodium to be stored in the electrochemical cell. Very recently, Rodriguez et al. have further used in situ optical imaging to study the effects of FEC on sodium deposition.[450] It was found that sodium deposition in EC, DEC, and PC generated large volumes of gas and fragile, porous dendrites, while the use of FEC greatly reduced gassing during deposition and thus illustrate superior cycling performance, impedance, and cycling efficiency when it was used as a cosolvent with DEC (1:1 vol); however, porous depositions persisted. Coupled with time of flight secondary-ion mass spectrometry, they further revealed that the solid–electrolyte interphase formed in FEC/DEC, in contrast with the EC/DEC electrolyte, is thicker, richer in NaF, and forms a less dense polymer organic layer. However, there are still very few reports on electrochemical sodium deposition/dissolution. It is important to understand factors such as shape change during cycling and its effect on electrochemical reversibility and Coulombic efficiency to advance the development of SIBs.

Since the inception of in situ TEM techniques for battery research in 2010,[451] they have been used to study the morphological structure changes during cycling for many sodium-ion battery systems, such as expanded graphite,[23] metal oxide,[452] alloying-based metals,[453] and phosphorene.[353] For example, Chevrier and Ceder have calculated that both silicon (Si) and germanium (Ge) should alloy with Na at room temperature to form NaSi and NaGe.[454] However, crystalline Si and Ge, which have been shown to be promising high energy density anodes for Li-ion batteries,[455,456] have not worked in Na-ion batteries, apparently because of a high diffusion barrier for Na ions in the Si and Ge lattices.[457] To gain better understanding on this phenomenon, Korgel and co-workers conducted real-time, in situ TEM studies of Ge nanowires undergoing sodiation and de-sodiation.[458] The in situ TEM experiments confirmed

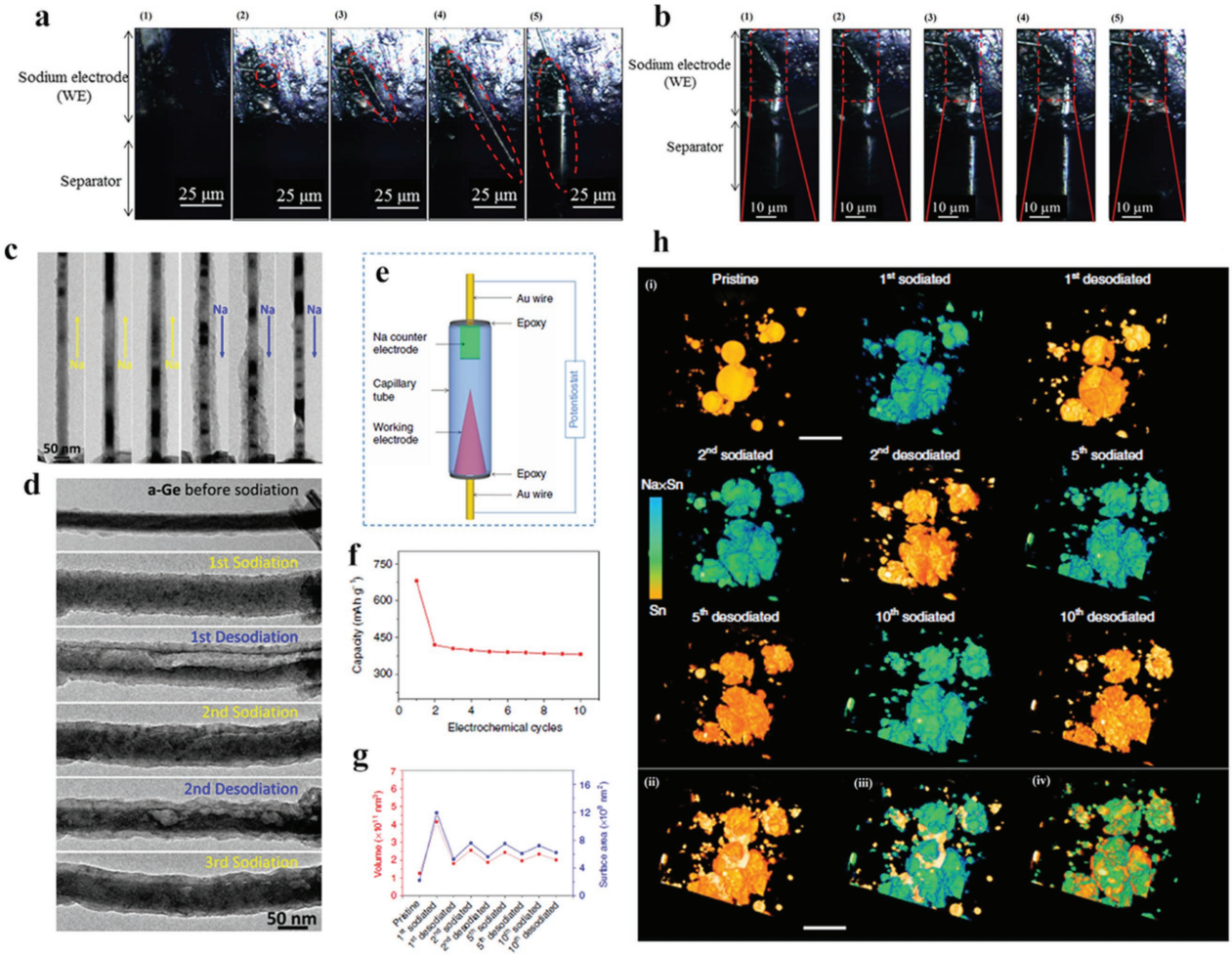

Figure 41. a) Light microscopy images of electrochemical sodium deposition on the sodium electrode in 1 M $NaPF_6$/PC. The images were taken at sodium deposition of (1) 44.17 μA h (at 53 min), (2) 100 μA h (at 120 min), (3) 137.5 μA h (at 165 min), (4) 187.5 μA h (at 225 min), and (5) 237.5 μA h (at 285 min).[449] b) Light microscopy images of electrochemical sodium dissolution on the sodium electrode in 1 M $NaPF_6$/PC. The images were taken at sodium dissolution of (1) 29.2 μA h (at 35 min), (2) 34.2 μA h (at 41 min), (3) 40.8 μA h (at 49 min), (4) 51.7 μAh (at 62 min), and (5) 59.2 μA h (at 71 min).[449] c) Sodium diffusion along the surface of a crystalline Ge nanowire. (Left) Sodium diffusion along the surface of crystalline Ge nanowires was observed when a voltage of −2 V was applied. The diameter and crystalline structure of the Ge nanowire do not change during this process. (Right) Application of a positive voltage bias led to the removal of sodium from the surface after a few minutes. The crystalline Ge nanowire was unaffected by the sodium diffusion along the surface of the nanowire.[458] d) Structural evolution during sodiation/desodiation cycles. (1) The de-lithiated/amorphorized Ge nanowire. (2) Sodiated Ge nanowire. (3) A huge pore was created by applying high desodiation bias. (4) Porous structure was recovered from second sodiation. (5) Small pores, instead of huge one, reformed during second desodiation upon milder desodiation. (6) Those small pores could also be recovered from sodiation.[458] e) Na-ion experimental cell and f) its electrochemical cycle performance and g) volume and surface area change during electrochemical cycles. h) 3D view of microstructural equilibrium in SIB: (i) Microstructural reversibility during 10 sodiation–desodiation cycles; the overlapped images of (ii) pristine/second de-sodiated, (iii) pristine/tenth sodiated, and (iv) second sodiated/tenth de-sodiated.[473] Panels (a,b) reproduced with permission.[449] Copyright 2016, Nature Publishing Group. Panels (c,d) reproduced with permission.[458] Copyright 2016, American Chemical Society. Panels (e–h) reproduced with permission.[473] Copyright 2015, Nature Publishing Group.

that crystalline Ge nanowires do not sodiate (Figure 41c). An applied potential can induce Na diffusion along the surface of the crystalline Ge nanowires, but Na insertion does not occur. Amorphization of the nanowires with an initial lithiation/de-lithiation cycle, however, makes them effective sodiation electrodes. The volume of amorphous Ge nanowires expands by more than 300%, which is significantly higher than expected based on a final sodiated phase of NaGe, and close to $Na_{1.6}Ge$ (Figure 41d). Such understanding is important for future design of high performance Ge-based anode materials for SIBs.

However, although the in situ TEM technique is a powerful tool for monitoring the morphology change of electrode materials during the electrochemical reaction, it still has some limitations.[459–461] A nonvolatile ionic liquid or Li_2O (Na_2O in the case of SIBs) is usually used in the high-vacuum TEM chamber, which makes the electrochemical process different from real batteries based on traditional organic liquid electrolytes. There are also some restrictions for the samples; nanostructures such as nanowires are preferred. Further technology innovation is still required to enable in situ TEM characterization on real

battery systems. Another challenge for battery materials study using TEM is the sample damage from high electron dose rates necessary for high resolution imaging. Over the past decades, the detailed nanostructure and crystallography of Li dendrite and chemical composition of SEI have not been explored on single-particle level. For the first time, Cui et al. used cryo-electron microscopy (EM) techniques to unravel the detailed structure of Li metal and its SEI,[462] showing that atomic-resolution imaging of individual lithium metal atoms and their interface with the SEI in their native state is possible at cryogenic conditions.[462] They found that lithium dendrites in carbonate-based electrolytes grow along the <111> (preferred), <110>, or <211> directions as faceted, single-crystalline nanowires.[462] These growth directions can change at kinks with no observable crystallographic defect.[462] This finding can lead to a more complete understanding of the failure mechanisms in high-energy batteries, and will stimulate numerous study of using cryo-TEM to investigate beam-senstive materials such as lithiated silicon or sulfur.

Synchrotron transmission X-ray microscopy has been extensively applied in the battery research as it is nondestructive, elementally sensitive, and highly penetrative.[463] The energy resolution of TXM can cover most of transition metals such as Fe, Co, Ni, Mn, etc., which, which is critical for batteries,[464] catalysts,[465,466] and other energy materials studies.[467–469] Wang's group at Brookhaven National Laboratory has recently made significant advances in use of in situ TXM to study the morphological changes of electrode materials during cycling.[470–472] In situ 2D TXM experiments can be performed in the typical coin cells with Kapton windows. However, the signal obtained in 2D TXM is usually spatially integrated along the depth direction. For these studies, Wang et al. reported a mini Na-ion battery that was fabricated in a quartz capillary (1 mm diameter) with two gold rods (0.5 mm diameter) connected with the two electrodes of the external potentiostat (Figure 41e), and applied a 3D full-field X-ray tomography technique to better monitor the sodiation/de-sodiation process of a Sn anode during the initial 10 electrochemical cycles (Figure 41f).[473] By employing a detailed 3D quantitative analysis and correlating it to discharge/charge performance, they found that unlike the conventional large volume expansion for Sn anode during lithiation, Sn has a better structural stability during the initial 10 sodiation/de-sodiation process (Figure 41g,h), which may make it a suitable anode of SIB.

Very recently, Hwang and co-workers have for the first time reported in situ visualization of lithium plating and stripping dynamics on Cu surface through a versatile and facile experimental cell by using in operando TXM.[474] This is a significant breakthrough for battery study using TXM since lithium is a very light element compared to other anode/cathode materials and gives a small contrast under X-ray imaging. It was found that the height of mossy lithium grows/shrinks more than its width during the plating/stripping process. They also observed a current density-dependence on the lithium shape, where mossy and dendritic lithium tend to grow under lower and higher current densities, respectively. And the growth of dendritic lithium under high current density contributes more than the mossy structure to form a dead lithium structure. The understanding of the growth mechanism from TXM can be beneficial for the development of safe lithium ion and lithium metal batteries.

5.2.2. Operando Characterization on Crystal Structures Evolution during Cycling

The HEXRD technique has been widely used to determine the phase composition of crystalline materials based on X-ray scattering. So far, many SIB materials have been studied by operando HEXRD, including layered NaT_MO_2 cathode family,[51,62,101,107,120,475] Polyanion cathode family,[476–478] Ti-based anodes,[261,479] and alloy-based anodes.[31,480] The capacity fading mechanism, doping effects, surface modification effects, and nanostructure effects on SIB electrode materials have been determined by this technique. For example, Wang et al. reported that Ti-substituted O3-type $NaNi_{0.5}Mn_{0.5-x}Ti_xO_2$ cathodes demonstrate much better cycling performance compared to Ti-free samples.[115] Operando HEXRD study revealed that the O3-type phase can transform reversibly into a P3-type phase upon Na^+ de-intercalation/intercalation. The substitution of Ti for Mn enlarges interslab distance and could restrain the unfavorable and irreversible multiphase transformation in the high voltage regions that is usually observed in O3-type $NaNi_{0.5}Mn_{0.5}O_2$, resulting in improved Na cell performance. Nevertheless, most of these studies have been focused on the phase transitions of electrode materials during battery cycling. Many electrode materials, especially cathode materials, are based on Na^+ ion intercalation compounds, and the structural instability from internal stresses is thought to be closely related to their electrochemical performance. Intergrowth structures were found to significantly improve the cycle performance, especially for high-voltage cycling, but the mechanism was not initially understood. Accordingly, in an operando HEXRD study, Xu et al. found that the intergrowth P2/O1/O3 undergo a highly reversible structure transformation during charge/discharge (**Figure 42**a).[123] They further conducted microstrain analysis and found that even at deep charged state, the interfacial microstrain existed in the electrode is not significantly increased, which confirms that the intergrowth structures can minimize the internal stress that may generated during the multiple phase transitions. Therefore, operando HEXRD characterization has provided clues on the mechanisms and related kinetics within SIBs. These clues will open new strategies for the design of electrode materials for high-energy-density SIBs. However, the phase changes within amorphous electrode materials cannot be determined by operando XRD techniques.

Battery materials, especially anode materials such as hard carbon, metals, metal oxides and so forth are commonly amorphous or nanocrystalline and cannot be characterized by conventional methods. Moreover, owing to the strong XRD signal from the necessary Cu current collector and Na metal in SIBs, it is difficult to obtain a good signal by operando HEXRD. Yet, since these materials have a complex or disordered structure, information on the local structure is critical in understanding their physical properties. One advanced technique for investigating these materials is PDF analysis. This technique uses Bragg scattering and diffuse scattering in parallel, meaning that while any long-range order that is present in the material

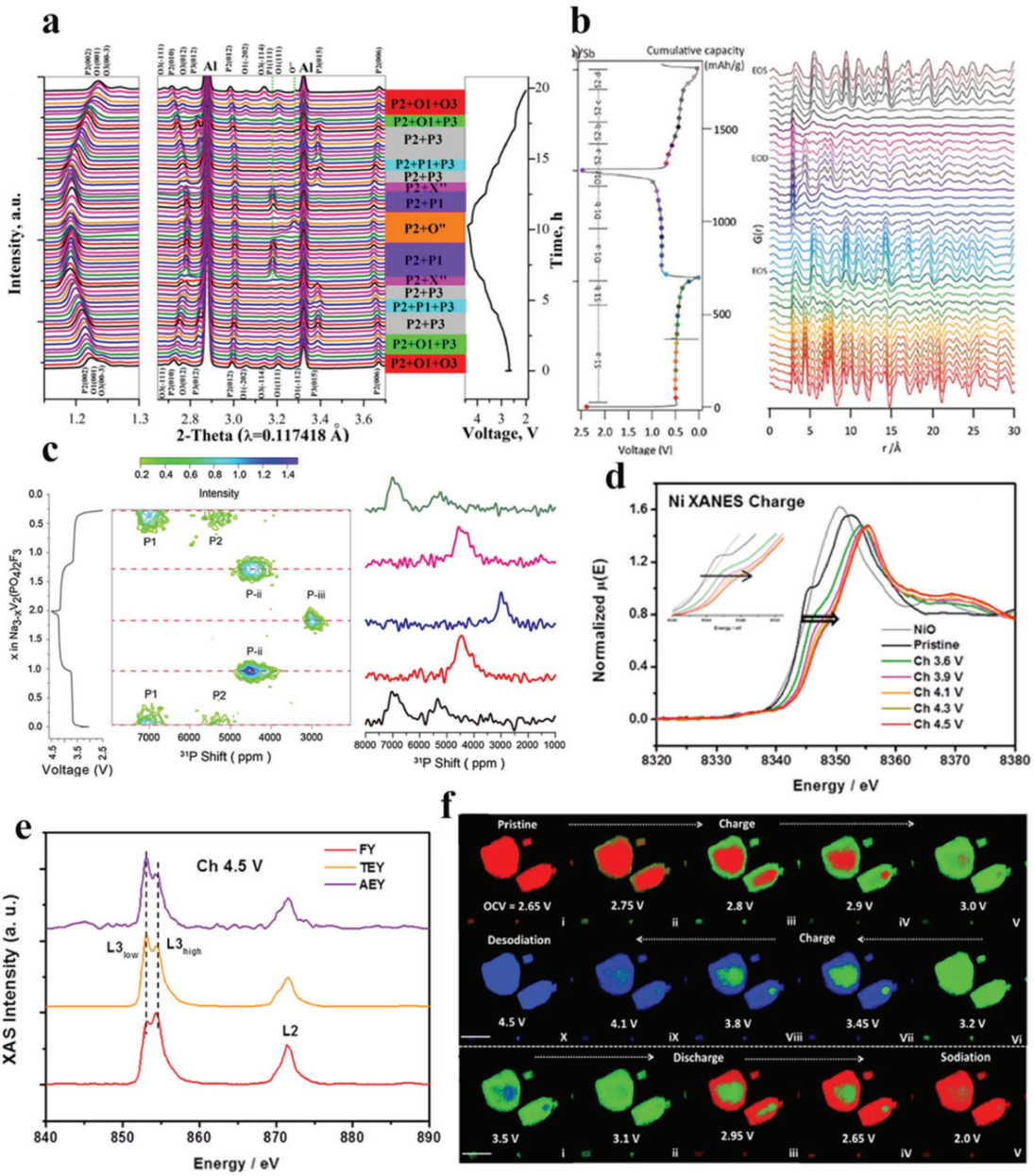

Figure 42. a) Operando synchrotron HEXRD patterns of the P2/O1/O3 cathode material during the first charge/discharge cycle within 2.0–4.4 V at 0.1 C.[123] b) Discharge/charge curves obtained for Sb during operando PDF measurements and selected PDFs obtained during the first discharge, first charge, and second discharge cycles by Fourier transforming the total scattering X-ray data.[483] c) Charge/discharge curve (left), ^{31}P in situ NMR spectra of $Na_3V_2(PO_4)_2F_3$/Na cell (middle), and slices of the 2D NMR contour plot at the horizontally marked (red dashed lines) states of charge at the right.[517] d) In situ XAS analysis of $Na_{0.78}Ni_{0.23}Mn_{0.69}O_2$ electrodes at different states of charge during the first electrochemical cycle: XANES spectra at Ni K-edge.[525] e) Ni XAS L-edge spectra of the fully charged electrode using AEY (purple), TEY (yellow), and FY (red) modes.[525] f) 2D chemical phase mapping during the first charge and discharge process. Scale bar: 10 μm.[93] Panel (a) reproduced with permission.[123] Copyright 2017, Royal Society of Chemistry. Panel (b) reproduced with permission.[483] Copyright 2016, American Chemical Society. Panel (c) reproduced with permission.[517] Copyright 2016, Elsevier. Panels (d,e) reproduced with permission.[525] Copyright 2017, American Chemical Society. Panel (f) reproduced with permission.[93] Copyright 2017, Elsevier.

is taken into account, it is also possible to characterize structures with deviations from long range order or phases that lack long-range order altogether.[481] The method has recently found application in characterization of battery electrodes both ex situ and operando.[482–487] Operando measurements, where scattering data are captured during battery operation, have particular advantages over ex situ analysis as they increase the consistency between data sets and circumvent issues of air contamination for most air-sensitive battery materials. In addition, operando measurements can capture the formation of metastable species that may form in the battery but may relax before postmortem analysis is carried out.[485] PDF data

can be obtained from powder diffraction data, synchrotron-based X-ray sources, and pulsed neutron sources, which allow both local and average structural information to be extracted. Using operando PDF analysis, Grey and co-workers studied the alloying mechanism of Sb anodes, and found that crystalline Sb was converted to crystalline Na_3Sb via a a-$Na_{3-x}Sb$ ($x \approx 0.4$–0.5) intermediate in the initial discharge process, while the main product at the end of initial charge process is composed of amorphous/crystalline Sb (Figure 42b).[483] Grey et al. showed that these connectivities react at distinct voltages via different sodiation pathways; the sequential manner of these transformations enhances the cyclability of the electrode by having an "inactive" component capable of buffering the strain associated with multiple phase transitions. Very recently, Clare et al. have further used operando PDF coupled with DFT and ex situ solid-state NMR to investigate the sodium storage mechanism of Sn anode.[488] They found the first electrochemical process of sodium insertion into tin results in the conversion of crystalline tin into a layered structure consisting of mixed Na/Sn occupancy sites intercalated between planar hexagonal layers of Sn atoms ($NaSn_3$).[488] After that, $NaSn_2$ that has similar hexagonal structure as $NaSn_3$ but without tin atoms between the layers formed.[488] Further reaction with sodium results in the formation of structures containing Sn–Sn dumbbells ($Na_{5-x}Sn_2$), which interconvert through a solid–solution mechanism.[488] The final product, $Na_{15}Sn_4$, can store additional sodium atoms as an off-stoichiometry compound ($Na_{15+x}Sn_4$). [488]

Nuclear magnetic resonance (NMR) spectroscopy can provide detailed structural information for a given material based on the corresponding responses of quadrupole moments and nuclear spins, as well as their resonances at characteristic frequencies.[34,489] The local structural and dynamics can be obtained through the interactions of the nuclear spin with its local environment, including chemical shift and dipolar and quadrupolar interactions.[490–493] Together with electrochemical devices, solid-state NMR spectroscopy can track dynamic processes for both crystalline and amorphous electrode materials during the electrochemical process.[485,494–512] Atoms with a nuclear spin $I \neq 0$ possess a magnetic moment and are, in principle, detectable by NMR spectroscopy. Although Na[23] NMR is usually conducted in SIBs systems, many other nuclei (e.g., $I = 1/2$ isotopes like ^1H, ^{13}C, ^{19}F, ^{29}Si, ^{31}P, and ^{119}Sn as well as quadrupolar nuclei with $I > 1/2$ like ^2H, ^{17}O,[25] Mg, ^{27}Al, ^{33}S, ^{39}K, ^{43}Ca, ^{51}V, and ^{67}Zn) can also provide useful insights.[513] In situ NMR experiments are of considerable interest because they enable monitoring of structural and electronic changes of the materials while the electrochemical processes are happening. The real-time investigations are highly beneficial since they minimize self-relaxation processes, offering a high chemical specificity to both crystalline and amorphous species, and enabling the monitoring of dynamic processes and the tracking of metastable and short-lived phases.[513]

Ex situ ^{23}Na measurements are often conducted in many electrode materials for SIBs.[47,514–516] However, there are only few in situ NMR studies on SIBs reported so far. Grey's group developed a new automatic tuning matching cycler (ATMC) in situ ^{31}P NMR probe to study the $Na_3V_2(PO_4)_2F_3$ cathode material for SIBs (Figure 42c).[517] They also applied ATMC ^{23}Na in situ NMR on symmetrical Na–Na cells during galvanostatic plating.[518] Although in situ NMR spectroscopy provides detailed information with respect to the phase evolution during battery operation, significantly different resonance frequencies, changing sample conditions, signal broadening, and interferences of the NMR and electrical conductivity circuit can impair the experiments. Besides, most measurements have been conducted with solid-state NMR, and that technique is time-consuming.[489,513,519] Thus, expanded applications of in situ NMR on SIBs materials are needed.

As introduced in the last section, synchrotron XAS (including hard and soft X-ray) is a powerful technique for probing the electronic and oxidation states changes of all the atoms of the target type in the bulk and surface of the samples, including crystalline and amorphous phases.[520–523] Thus, operando XAS is very suitable to analyze the electronic and structural dynamics of electrode materials during battery operation. Xu et al. employed operando hard XAS to perform a comparative study on the lithiation and sodiation kinetics of the Co_3O_4 anode.[524] Meng and co-workers recently used operando hard and soft XAS to explore the oxygen activity of P2-type $Na_{0.78}Ni_{0.23}Mn_{0.69}O_2$ cathode material for SIBs.[525] As shown in Figure 42d and the inset, they found that the main changes for Ni K-edge mainly occurred from open circuit voltage to 4.1 V, which has an energy shift of about 4 eV, indicating that the valence state of Ni is oxidized to Ni^{4+} from Ni^{2+}. However, in the voltage region of 4.1–4.5 V, the Ni K-edge has minimal energy shift. They indicated that the electrochemical reaction above 4.1 V may involve surface oxygen activity, which has been frequently reported in the case of Li-rich cathode materials. To confirm this hypothesis, Meng et al. further performed a soft XAS study to detect the surface depth chemical information using different acquisition mode. The depth resolution for Auger electron yield (AEY), total electron yield (TEY), and fluorescence yield (FY) are 1–2, 2–5, 5–50 nm, respectively.[520,526] This technique has been widely used to characterize LIBs cathode materials especially those with the participation of oxygen anions during high voltage charge.[527] As shown in Figure 42e, there is a Ni valence state gradient from bulk to the surface in the charged $Na_xNi_{0.23}Mn_{0.69}O_2$, which was attributed to the surface structure changes and redistribution of transition metal cations.[525] Coupled with O EELS spectra, they for the first time concluded that oxygen anions took place in the layered cathodes of SIBs. Using Mn L-edge soft XAS, Qiao et al. has investigated the impact of surface Mn^{2+} formation on the capacity fade of Mn-based cathode materials ($Na_{0.44}MnO_2$).[528] They have found that the amount of Mn^{2+} on the electrode surface increased after extended cycles, which is detrimental to the battery performance due to the dissolution and shuffling of Mn^{2+} in the electrolytes. The soft XAS further revealed that the formation of the detrimental surface Mn^{2+} could be suppressed by limiting the discharge cut-off voltage higher than 2.6 V, which could improve the battery capacity retention over extended cycles.

Combined with XANES spectroscopy, TXM can track the oxidation evolution and elemental distribution of electrode materials during charging/discharging. Wang et al. recently used operando TXM to unravel the origin of irreversible capacity loss in O3 $NaNiO_2$ for high-voltage SIBs.[93] The recorded TXM data were processed and fitted with the selected

standard reference spectra to obtain the chemical phase mapping during the charge and discharge process. As shown in Figure 42f, three consecutive phases from the de-intercalation of $NaNiO_2$ were investigated during the first charge. The results indicated that the phase transformation occurs at all directions, and a "core–shell" reaction mechanism is suggested by the operando quantitative chemical mapping. However, the phase mapping of the fully discharged particles after the first cycle is not the same as the one for pristine particles, exhibiting some mixed color pixels in the middle of the particles, which suggest an irreversible phase conversion in the first charge and discharge cycle. Therefore, the operando TXM–XANES experiment reveals that the partly irreversible phase transformation predominately occurs in the first charge and discharge process. By conducting further quantitative analysis, Wang et al. found that at high voltage of above 4.0 V, the XANES spectra exhibit a slight shape change with little absorption edge shift, a finding that is in agreement with the case of P2-$Na_xNi_{0.23}Mn_{0.69}O_2$ reported by Meng and co-workers.[525] However, they attributed this phenomenon to partial Ni migration from octahedral sites to the interslab space, which would lead to irreversible capacity loss when $NaNiO_2$ is charged to above 4.0 V. Therefore, the quantitative phase composition analysis by operando TXM clearly illustrates the "core–shell" reaction model and the origin of irreversible capacity loss during the intercalation and de-intercalation process. Xie et al. further used operando TXM to verify the presence of a nonequilibrium solid solution of $Na_{1-\delta}Ni_{1/3}Fe_{1/3}Mn_{1/3}O_2$ during charge.[529] The result clearly confirmed the existence of a substitutional solid solution of Na-poor $Na_{1-\delta}Ni_{1/3}Fe_{1/3}Mn_{1/3}O_2$, with compositions that span the entire composition between two thermodynamic phases, $NaNi_{1/3}Fe_{1/3}Mn_{1/3}O_2$ and $Ni_{1/3}Fe_{1/3}Mn_{1/3}O_2$. However, a limitation of this technique is that it can only provide chemical phase mapping information with the spatial resolution of sub-30 nm for 2D and sub-50 nm for 3D. In the case of operando battery cycling experiments, the spatial resolution should be hundreds of nanometers to micrometers for the purpose of a good signal.

5.3. Operando Characterization on Thermal Stability of SIBs Materials

The thermal stability of battery materials is related to the abuse tolerance of SIBs, which should be the first priority before commercialization of this technology.[530] The reactions between sodiated or de-sodiated electrodes and electrolytes could be used as indicator of thermal stability of battery materials.[531,532] In recent years, the thermal stability of de-sodiated cathodes such as P2-Na_xCoO_2,[533] O3-$NaCrO_2$[86,87,534], and O3-$NaNi_{0.6}Co_{0.05}Mn_{0.35}O_2$[91] has been reported. However, most of these efforts employed thermal analysis techniques such as differential scanning calorimetry (DSC), which are useful for determining the thermal effect of chemical or physical changes, but not as useful for understanding the chemical details of the reactions and morphological changes occurring inside the cell.[535] To overcome this technical barrier, novel characterization techniques are needed to unravel the detailed failure mechanism of overcharged SIBs.

Chang and co-workers used in situ TEM to investigate the thermal stability of P2-type Na_xCoO_2 cathode materials.[533] With an increase in temperature, the surface of Na_xCoO_2 became porous due to the thermal decomposition to Co_3O_4, CoO, and Co with the reduction of Co (**Figure 43**a,b). The degree of the thermal decomposition increased at higher cutoff voltages at the same temperature. At the harshest condition of 4.3 V cutoff voltage and 400 °C, significant changes were observed in the morphology as well as the crystallographic and the electronic structures as a result of the reduction of Co to the metallic state and the loss of oxygen, which are serious safety threats to the life of the battery system. This study demonstrated the instability of charged P2-type layered cathode materials at high temperatures. The thermal stability of electrode materials should be considerably improved to guarantee the safe operation of SIBs, and this work provides an excellent methodology to verify the thermal stability of newly developed cathode materials. Using the same technique, Sharifi-Asl et al. have investigated the thermal stability of $LiCoO_2$.[536] They found that oxygen release from Li_xCoO_2 cathode crystals is occurring at the surface of particles, and the oxygen release is highly dependent on Li_xCoO_2 facet orientation. The [001] facets are stable at 300 °C, and the oxygen release is observed from the [012] and [104] facets, where under-coordinated oxygen atoms from the delithiated structures can combine and eventually evolve as O_2.

Chen et al. developed operando HEXRD technique as an alternative to DSC and used it to investigate the chemical reactions between the electrode material and the electrolyte during thermal ramping.[33] The in situ heating setup and in situ DSC cell are shown in Figure 43c. A high energy X-ray source at about 0.1 A° was selected for its excellent penetration capability to detect structural changes in the bulk part of the sample. The high flux of the X-ray beam is a major advantage to carry out fast experiments at one spectrum per minute. Chen and co-workers used this technique to investigate the thermal stability of many Li—Ni—Co—Mn—O cathode materials.[423,530,537–544] Recently, they further investigated the thermal stability of the intergrowth P2/O1/O3 $NaNi_{1/3}Co_{1/3}Mn_{1/3}O_2$ cathode (Figure 43d).[123] The results suggest that a proper optimization of the electrolyte component can alter the decomposition pathway of de-sodiated cathodes, leading to improved safety of SIBs. And the intergrowth structure can also improve the thermal stability of layered cathode materials with an order of P2/O1/O3>P2/O3>P2/P3. The morphology effect on the thermal stability of layered cathode materials for sodium-ion battery has also been reported by Hwang et al. using in operando XRD technique.[91] They have found that both charged radially aligned hierarchical columnar (RAHC) $Na_{0.36}[Ni_{0.60}Co_{0.05}Mn_{0.35}]O_2$ and bulk $Na_{0.44}[Ni_{0.60}Co_{0.05}Mn_{0.35}]O_2$ show a monoclinic P3 phase at room temperature. However, in the case of charged RACH electrode, P3 structure is retained up to 400 °C and phase transformation to the spinel phase is completed at around 500 °C. In contrast, the advent of the spinel phase is observed at 240 °C for the bulk electrode, and the P3 phase has been drastically transformed to the spinel phase at 280 °C. Yu et al. further reported the effect of surface coating on the thermal stability of cathode materials for sodium-ion battery using the same technique.[87] They found that the carbon coating layer on the surface of $Na_{0.5}CrO_2$ can prevent the thermal damage of the crystal structure

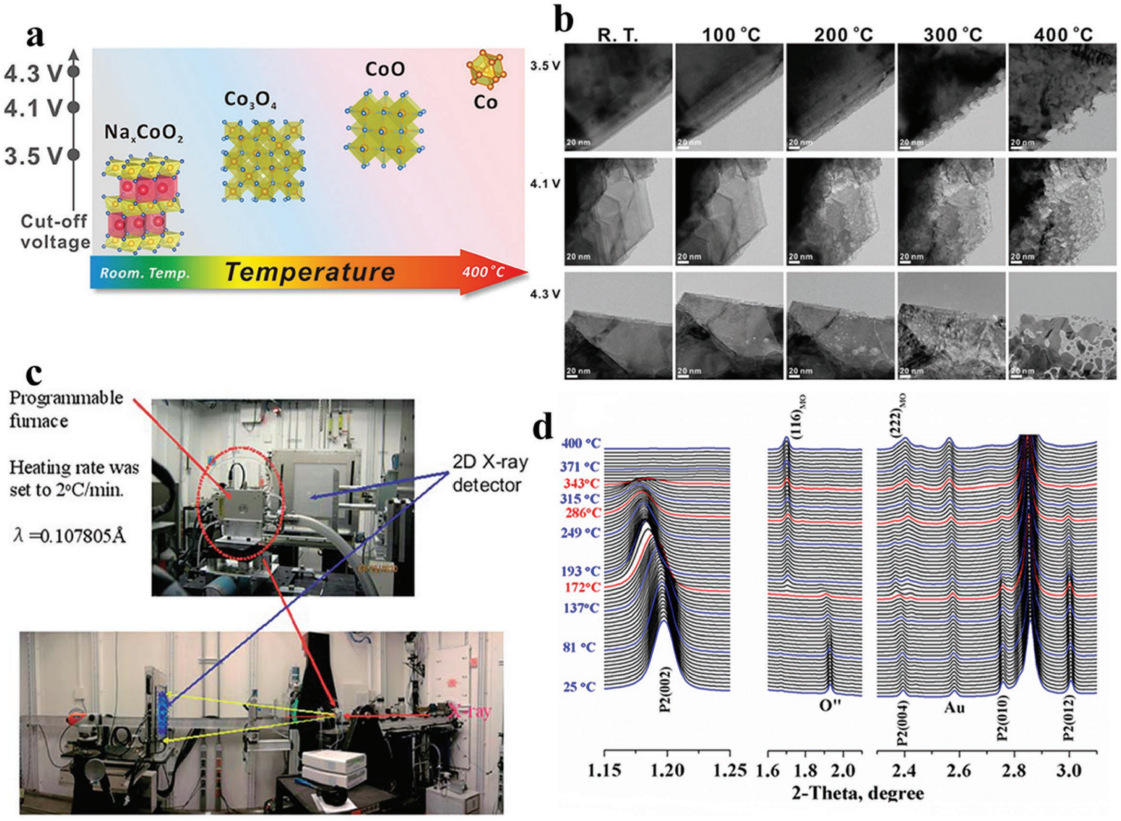

Figure 43. a) Schematic for the structure evolution for de-sodiated P2-Na$_x$CoO$_2$ cathode at different states of charge along with temperature.[533] b) Real-time bright-field images of the surface of NCO cathode materials charged up to (top) 3.5 V, (middle) 4.1 V, and (bottom) 4.3 V during heating.[533] c) Images of operando HEXRD experimental setup.[33] d) HEXRD patterns upon heating of de-sodiated P2/O1/O3 electrode with the presence of 2 µL electrolytes.[123] Panels (a,b) reproduced with permission.[533] Copyright 2017, American Chemical Society. Panel (c) reproduced with permission.[33] Copyright 2011, Royal Society of Chemistry. Panel (d) reproduced with permission.[123] Copyright 2017, Royal Society of Chemistry.

and thus retard the exothermic decomposition reaction at higher temperatures with less generation of heat. Therefore, in order to develop a safer sodium-ion battery, electrode composition, electrode structure, surface protection and electrolytes optimization are several critical issues need to be considered.

6. Sodium-Ion Full-Cell Systems

In 2014, Aquion Energy has announced a commercially available SIB with cost/kWh capacity similar to a lead acid battery for use as a backup power source for electricity microgrids. In 2015, a team of researchers in France have further reported a protype SIB in 18 650 cells. The reported SIB can achieve an energy density of ≈90 Wh kg^{-1} and a long cycle life span of over 2000 cycles, a performance comparable to lithium ion phosphate battery. In the past few years, because of the rapid development of SIB technology on the cathode, anode and electrolytes, the energy density of SIB has been dramatically increased. Deng et al. has recently reported a review article, in which they have discussed the design and development trends that are needed for SIBs to meet the requirements of practical application in large-scale energy storage.[545] They have identified the factors that are hindering the commercialization of SIB, and also evaluated the reported electrode materials and sodium-ion full-cell systems, including the aqueous full-cell system, nonaqueous symmetric full-cell system, and nonaqueous asymmetric full-cell system. Among them, aqueous full-cell systems can only offer an energy density of lower than 50 Wh kg^{-1}, which cannot meet the demand for large scale energy storage application. **Figure 44** has shown that most of the reported nonaqueous SIBs have an energy density of 90–260 Wh kg^{-1} depending on the cathode materials and anode materials utilized in the full cells. Various full cell systems have been reported, such as Sn-C//NaFePO$_4$ (150 Wh kg^{-1}), Fe$_3$O$_4$//Na$_2$FeP$_2$O$_7$ (203 Wh kg^{-1}), hard carbon//Na$_{0.9}$Cu$_{0.22}$Fe$_{0.30}$Mn$_{0.48}$O$_2$ (210 Wh kg^{-1}), hard carbon//NaNi$_{0.5}$Mn$_{0.5}$O$_2$ (240 Wh kg^{-1}), Sb/C//Na$_3$V$_2$(PO$_4$)$_3$@rGO (242 Wh kg^{-1}), and hard carbon//Na$_3$V$_2$(PO$_4$)$_3$ (258 Wh kg^{-1}). However, the energy densities of these cells are still far below than that of state-of-the-art lithium-ion battery. Therefore, in this report, we have pointed out the promising strategy from the materials selection to achieve a theoretical energy density of over 400 Wh kg^{-1} on the cell level for SIBs.

So far, phosphorus-based anode materials are the most promising anodes for high energy SIBs, which could deliver a reversible capacity up to 2000 mA h g^{-1} on the material level and an appropriate working voltage of 0.7 V (vs Na$^+$/Na). With significant material development in the past few years, the huge volume change during long-term cycling has

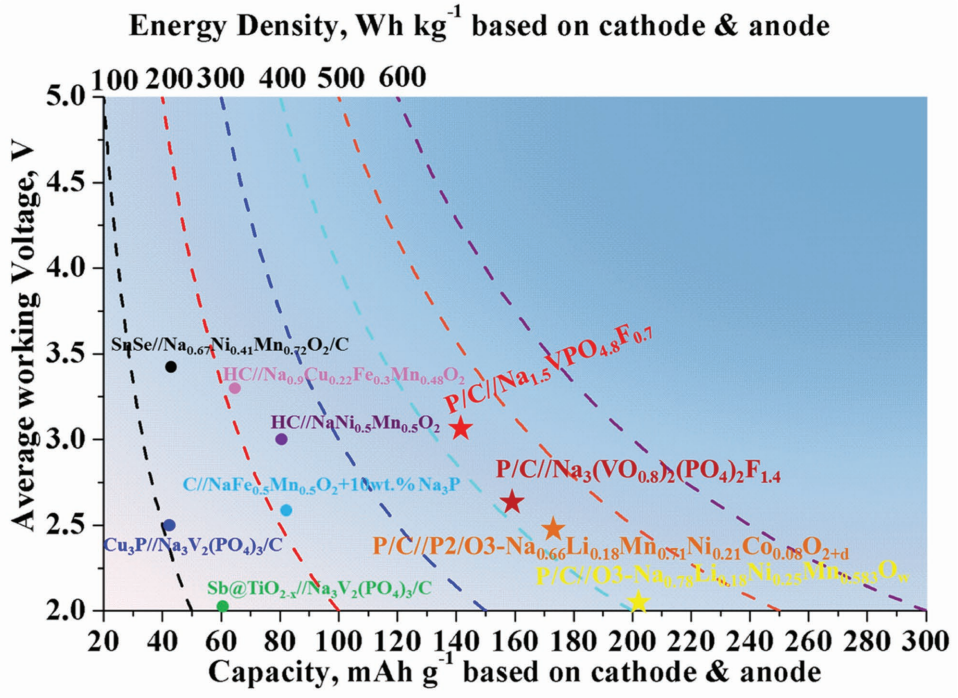

Figure 44. The energy density and average operating voltage of reported and projected sodium-ion battery. The data represented by circles are from ref. [545]. The energy density of full cells using phosphorus/carbon (P/C) composite as anode are calculated based on the mass of cathode and anode. The overall energy density and the average working voltage of P/C anode are estimated to be 1500 mA h g^{-1} and 0.7 V.

been remarkably mitigated through nanotechnology coupled with advanced binder; and high reversible capacity with thousands of cycles has been achieved. When coupled with the previous reported cathode materials with ultrahigh energy density including O3-$Na_{0.78}Li_{0.18}Ni_{0.25}Mn_{0.583}O_w$,[104] P2+O3 $Na_{0.66}Li_{0.18}Mn_{0.71}Ni_{0.21}Co_{0.08}O_{2+d}$,[475] $Na_3(VO_{0.8})_2(PO_4)_2F_{1.4}$[217], and $Na_{1.5}VPO_{4.8}F_{0.7}$,[219] the estimated energy densities for these cells can be over 400 Wh kg^{-1} on the cell level (see Figure 44). However, the stability of cathode materials in air atmosphere, cost of materials fabrication, environmental friendless, and industrial feasibility should be carefully considered. When replacing phosphorus/carbon anode with sodium metal anode, the energy density of SIBs can be further increased to over 500 Wh kg^{-1} on the cell level. However, research on room-temperature sodium metal battery remains sparse. The sodium dendrite problem is even more complicated than lithium dendrite as sodium metal is less stable with carbonate electrolytes than lithium metal and undergoes larger volume expansion during sodium plating/striping. Advanced electrolytes, efficient Na host materials and Na nucleation mechanism are one of the biggest challenges prior to really enable this technology to achieve high energy density.

7. Conclusions and Perspectives

This review summarizes the main achievements in the development of high-performance SIB materials and the advanced diagnostic techniques used to understand Na^+ intercalation chemistry.

In the cathode part of the paper, we reviewed recent research progress on layered transition metal oxide cathodes. We found that, although most of the cathode materials for SIBs are imitated or duplicated from their lithium analogues, there are distinctive differences in the intercalation chemistries between sodiation and lithiation. The electrochemical performance of layered cathode materials is very sensitive to their phase structures. O-type cathode materials usually present high capacities but low rate capability, while P-type cathode mateirals show lower capacities but better rate performance. This difference is owing to the amount of Na in the pristine material, the stability of each layer, and the kinetics being affected by the Na environment. Nevertheless, both individual P- and O-type cathode materials suffer from poor cycle stability when charged to high voltage. Oxygen activity, transition metal migration, stacking faults, and electrolyte decomposition are the main causes for the capacity fade. Fortunately, many smart structure design stratagies have been reported to overcome this issue. Foreign atom doping on transiton metal sites such as Li^+, Mg^{2+}, Cu^{2+}, Zn^{2+}, Al^{3+}, and Ti^{4+} have proven to improve the structure stability of P-type and O-type cathode materials during high voltage cycling. Moreover, formation of a P/O intergrowth structure by Li^+ substitution or controlled synthetic condition is another way to stabilize the cathode crystal structure and decrease the interfacial microstrain and thus enhance the electrochemical performance. Surface coating seems more related to prevent electrode/electrolyte side reaction than stabilizing the crystal structure.

We also reviewed recent progress of polyanion cathodes for SIBs, including $NaFePO_4$, $Na_3V_2(PO_4)_3$, $NaVPO_4F$,

$Na_3V_2(PO_4)_2F_3$, and $Na_4Co_3(PO_4)_2P_2O_7$, because of their structural stability and better safety. Low electronic conductivity is one of their main drawbacks in enabling long-term cycle stability. Foreign atom substitution and carbon modification such as coating, embedding, and supporting have been widely reported to increase the reversible capacity and extend the cycle life. It should be noted that oxygen doping on the F or P sites could enable additional Na^+ insertion/extraction for fluorophosphates cathodes. With these approaches, stable cycle life up to 1000 cycles and high energy density up to 600 Wh kg^{-1} can be achieved for polyanion cathodes.

In the anode part of the paper, we summarize recent development of carbon-, titanium-, and phosphorus-based anode materials. We found that graphite is not suitable for efficient Na^+ insertion/extraction due to the large radius of Na^+, while the low working voltage of hard carbon also brings huge challenge for practical application. Titanium-based anode materials, including $Li_4Ti_5O_{12}$, $Na_2Ti_3O_7$, and TiO_2, exhibit moderate working voltage, long-term cycle life up to tens of thousands cycles, and excellent rate capability, making them promising for use in high-power SIBs. However, the reversible capacities are generally limited to about 100–200 mA h g^{-1}, which dramatically decreases their energy densities. In addition, the low initial Coulombic efficiency in these materials is a concern. For alloy-based anode materials, black phosphorus and phosphorene show high electronic conductivity and very high reversible capacity. However, their cost makes them inappropriate for practical use in SIBs for larger-scale energy storage applications. Red phosphorus and metal phosphides are the most promising anode materials for the SIBs owing to their high reversible capacity of up to 2000 mA h g^{-1} and appropriate working voltage (0.7 V vs Na^+/Na). We also discuss various anode synthesis methods, including ball milling, vaporization–condensation, carbothermic reduction, and wet-chemical synthesis, and different structure design approaches to accommodate the huge volume expansion and increase in electronic conductivity. With these strategies, reasonable reversible capacity of ≈500 mA h g^{-1} with long cycle life up to 2000 cycles at high rate of charge/discharge (5 A g^{-1}) has been demonstrated, offering a great opportunity for commercialization of SIBs.

In the electrolytes part of the paper, we discuss the role of different salts and solvents in terms of ionic conductivity, viscosity, electrochemical window, and thermal stability, as well as electrode/electrolyte compatibility. Carbonate-based electrolytes, especially $NaPF_6$ in PC-based electrolytes, are mostly used in current SIB studies owing to their higher ionic conductivity and better thermal stability. Also discussed is the function of electrolyte additives such as FEC, VC, and TMSP, which are mainly used to stabilize the SEI layer. We also summarize recent achievements on solid-state electrolytes for SIBs owing to their excellent mechanical properties, high thermal stability, and wide electrochemical voltage window. The goal is to enable sodium metal batteries that can provide higher energy density. However, the ionic conductivity and interfacial resistance are two challenging problems in this system.

We also reported the application of operando and in situ diagnostic tools (including XRD, XAS, TEM, TXM, NMR, and PDF) in the exploration of high-performance battery materials for SIBs. These tools enable the investigation of the morphological and crystal structure evolution of battery materials during charging/discharging, which can provide an in-depth understanding on the interplay between electrodes, electrolytes, and interfaces and the relationship between structure and performance. We also cover the application of newly developed diagnostic tools to investigate the synthesis and thermal stability of battery materials, which can provide guidelines to design battery materials with better electrochemical performance and safety.

In spite of many achievements in the past few years, the energy density of SIBs still cannot compete with state-of-the-art LIBs. To develop competitive high-energy SIBs, there is a need of further development of advanced cathodes, anodes, and electrolytes. In addition, advanced diagnostic tools coupled with computational modeling are necessary. The following are some directions for advancing and enabling SIBs:

(1) *High Energy Cathodes*: Cathode materials largely determine the energy density of SIBs. Therefore, future studies on the cathode materials should focus on those systems with high theoretical or practical energy density. **Figure 45** shows the reported cathode systems with energy density higher than 600 Wh kg^{-1}, which is comparable to that of LIBs. For the layered cathode materials, Li doping and intergrowth structures should be the main focus to increase the energy density and enhance the cycle stability. Morphology optimization, such as full concentration gradient and core–shell structures, and the examination of different transition metal should be further explored to enable high voltage and thus high energy density. In addition, novel strategies to increase the structural stability of cathode materials toward moisture should be devised.
(2) *High Capacity Anodes*: High capacity anodes also play a critical role in the attainment of high-energy-density SIBs. More work should focus on mitigating the issue of large volume expansion and lesson learned from the Si anode in LIBs should be explored also with phosphorus and phosphides anode. In addition, we also need to explore advanced binders and carbon matrix use to prevent particle isolation and enable the use of a microsized phosphorous anode.
(3) *Advanced Electrolytes*: Functional electrolytes to prevent electrode/electrolyte side reactions and stabilize the electrode/electrolyte interface are critical and more work should focus on developing novel additives to enable long life SIBs. In particular, optimal electrolytes for high-voltage cathode materials of SIBs still need to be identified. Exploring fluorine or sulfone based electrolytes may help enable expending the voltage window in SIBs. A fundamental understanding of the SEI formation mechanism, structure, and component with organic electrolytes is still inadequate. Rational design of multifunctional groups (including solvent, salt, and additives) to improve the electrochemical performance is needed. Solid state electrolyte offers a great opportunity in extending life and improving safety of SIBs. However, the high interfacial contact resistance between solid-state electrolyte and electrode is a challenging barrier for their practical application. In addition, their low ionic conductivity and the instability toward Na metal are a concern, and little is known about the Na metal plating/stripping mechanism. Another alternative could be super high concentration electrolytes, which needed to be explored further.

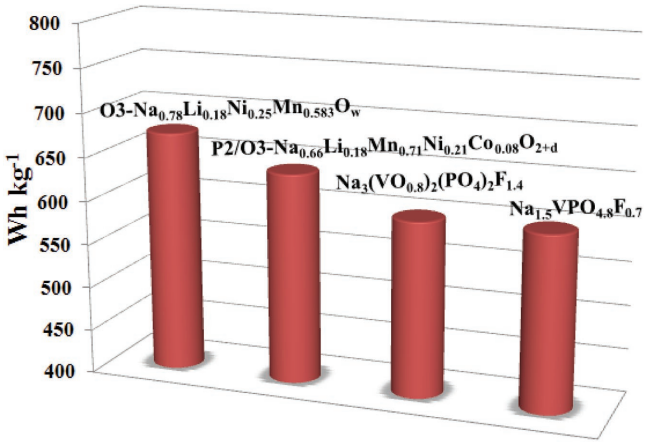

Figure 45. Energy density of reported cathode materials.

(4) *Diagnostics and Computational Modeling*: The application of in situ/operando diagnostic techniques has yielded insights into the fundamental dynamic processes during the operation of SIBs. These techniques have also helped to track phases, cation ordering, and interfacial microstrain development in the intermediate phases and thereby quantify the thermodynamic and kinetic parameters governing synthesis of SIB materials. Such information can help identify the reaction pathways for making electrode materials of desired phases and properties. These techniques can also monitor the thermal stability of electrode materials, providing guidelines to design safer SIBs. However, each technique has its limitation in terms of time resolution, spatial resolution, energy resolution, crystallinity and so forth. Thus, a combination of multiple techniques is necessary to advance the development of SIBs. In addition, computational modeling such as DFT-based first principles methods can predict relevant properties of battery materials, including voltage, structure stability, and electronic property, which can provide useful insights and understanding toward design and discovery of advanced SIBs.

Acknowledgements

The authors gratefully acknowledge the support from the U.S. Department of Energy (DOE), Vehicle Technologies Office. Argonne National Laboratory is operated by DOE Office of Science by UChicago Argonne, LLC, under contract number DE-AC02-06CH11357. The authors also thank the support from Clean Vehicles, US-China Clean Energy Research Center (CERC-CVC2). This article was published as part of the *Advanced Energy Materials* Excellence in Energy special series.

Conflict of Interest

The authors declare no conflict of interest.

Keywords

anodes, cathodes, diagnostics, electrolytes, sodium-ion batteries

Received: August 31, 2017
Revised: November 15, 2017
Published online: February 12, 2018

[1] M. Armand, J. M. Tarascon, *Nature* **2008**, *451*, 652.
[2] M. S. Whittingham, *Chem. Rev.* **2004**, *104*, 4271.
[3] G. L. Xu, Q. Wang, J. C. Fang, Y. F. Xu, L. Huang, S. G. Sun, *J. Mater. Chem. A* **2014**, *2*, 19941.
[4] N. Yabuuchi, K. Kubota, M. Dahbi, S. Komaba, *Chem. Rev.* **2014**, *114*, 11636.
[5] C. Grosjean, P. H. Miranda, M. Perrin, P. Poggi, *Renewable Sustainable Energy Rev.* **2012**, *16*, 1735.
[6] Z. Yang, J. Zhang, M. C. W. Kintner-Meyer, X. Lu, D. Choi, J. P. Lemmon, J. Liu, *Chem. Rev.* **2011**, *111*, 3577.
[7] M. S. Whittingham, *Science* **1976**, *192*, 1126.
[8] G. H. Newman, L. P. Klemann, *J. Electrochem. Soc.* **1980**, *127*, 2097.
[9] K. Kubota, S. Komaba, *J. Electrochem. Soc.* **2015**, *162*, A2538.
[10] H. Pan, Y.-S. Hu, L. Chen, *Energy Environ. Sci.* **2013**, *6*, 2338.
[11] C. Fang, Y. H. Huang, W. X. Zhang, J. T. Han, Z. Deng, Y. L. Cao, H. X. Yang, *Adv. Energy Mater.* **2016**, *6*, 1501727.
[12] X. Xiang, K. Zhang, J. Chen, *Adv. Mater.* **2015**, *27*, 5343.
[13] W. Luo, F. Shen, C. Bommier, H. Zhu, X. Ji, L. Hu, *Acc. Chem. Res.* **2016**, *49*, 231.
[14] H. Y. Che, S. L. Chen, Y. Y. Xie, H. Wang, K. Amine, X. Z. Liao, Z. F. Ma, *Energy Environ. Sci.* **2017**, *10*, 1075.
[15] C. Zhao, Y. Lu, Y. Li, L. Jiang, X. Rong, Y.-S. Hu, H. Li, L. Chen, *Small Methods* **2017**, *1*, 1600063.
[16] W. Huang, A. Marcelli, D. Xia, *Adv. Energy Mater.* **2017**, *7*, 1700460.
[17] M. H. Han, E. Gonzalo, G. Singh, T. Rojo, *Energy Environ. Sci.* **2015**, *8*, 81.
[18] S. Okada, Y. Takahashi, T. Kiyabu, T. Doi, J.-I. Yamaki, T. Nishida, *ECS Meet. Abstr.* **2006**, *2*, 201.
[19] A. R. Armstrong, D. W. Tee, F. La Mantia, P. Novák, P. G. Bruce, *J. Am. Chem. Soc.* **2008**, *130*, 3554.
[20] H. Kang, Y. Liu, K. Cao, Y. Zhao, L. Jiao, Y. Wang, H. Yuan, *J. Mater. Chem. A* **2015**, *3*, 17899.
[21] M.-S. Balogun, Y. Luo, W. Qiu, P. Liu, Y. Tong, *Carbon* **2016**, *98*, 162.
[22] D. Stevens, J. Dahn, *J. Electrochem. Soc.* **2000**, *147*, 1271.
[23] Y. Wen, K. He, Y. J. Zhu, F. D. Han, Y. H. Xu, I. Matsuda, Y. Ishii, J. Cumings, C. S. Wang, *Nat. Commun.* **2014**, *5*, 4033.
[24] A. Abouimrane, W. Weng, H. Eltayeb, Y. Cui, J. Niklas, O. Poluektov, K. Amine, *Energy Environ. Sci.* **2012**, *5*, 9632.
[25] M. M. Doeff, J. Cabana, M. Shirpour, *J. Inorg. Organomet. Polym. Mater.* **2014**, *24*, 5.
[26] K. Zhang, M. Park, L. Zhou, G.-H. Lee, W. Li, Y.-M. Kang, J. Chen, *Adv. Funct. Mater.* **2016**, *26*, 6729.
[27] C. B. Zhu, X. K. Mu, P. A. van Aken, Y. Yu, J. Maier, *Angew. Chem., Int. Ed.* **2014**, *53*, 2152.
[28] H. Kim, H. Kim, H. Kim, J. Kim, G. Yoon, K. Lim, W.-S. Yoon, K. Kang, *Adv. Funct. Mater.* **2016**, *26*, 5042.
[29] W. Sun, X. Rui, D. Yang, Z. Sun, B. Li, W. Zhang, Y. Zong, S. Madhavi, S. Dou, Q. Yan, *ACS Nano* **2015**, *9*, 11371.
[30] Y. Kim, K.-H. Ha, S. M. Oh, K. T. Lee, *Chem. Eur. J.* **2014**, *20*, 11980.
[31] G. L. Xu, Z. H. Chen, G. M. Zhong, Y. Z. Liu, Y. Yang, T. Y. Ma, Y. Ren, X. B. Zuo, X. H. Wu, X. Y. Zhang, K. Amine, *Nano Lett.* **2016**, *16*, 3955.
[32] Y. Yang, X. Liu, Z. Dai, F. Yuan, Y. Bando, D. Golberg, X. Wang, *Adv. Mater.* **2017**, *29*, 201606922.
[33] Z. H. Chen, Y. Ren, Y. Qin, H. M. Wu, S. Q. Ma, J. G. Ren, X. M. He, Y. K. Sun, K. Amine, *J. Mater. Chem.* **2011**, *21*, 5604.
[34] O. Pecher, J. Carretero-González, K. J. Griffith, C. P. Grey, *Chem. Mater.* **2017**, *29*, 213.
[35] D. Kundu, E. Talaie, V. Duffort, L. F. Nazar, *Angew. Chem., Int. Ed.* **2015**, *54*, 3431.
[36] J. Y. Hwang, S. T. Myung, Y. K. Sun, *Chem. Soc. Rev.* **2017**, *46*, 3529.
[37] V. Palomares, M. Casas-Cabanas, E. Castillo-Martinez, M. H. Han, T. Rojo, *Energy Environ. Sci.* **2013**, *6*, 2312.

[38] X. Xiang, K. Zhang, J. Chen, *Adv. Mater.* **2015**, *27*, 5343.
[39] Z. Li, J. Ding, D. Mitlin, *Acc. Chem. Res.* **2015**, *48*, 1657.
[40] A. Ponrouch, D. Monti, A. Boschin, B. Steen, P. Johansson, M. R. Palacin, *J. Mater. Chem. A* **2015**, *3*, 22.
[41] C. Delmas, C. Fouassier, P. Hagenmuller, *Phys. B+C* **1980**, *99*, 81.
[42] K. S. Kang, Y. S. Meng, J. Breger, C. P. Grey, G. Ceder, *Science* **2006**, *311*, 977.
[43] G. L. Xu, Y. Qin, Y. Ren, L. Cai, A. Ke, K. Amine, Z. H. Chen, *J. Mater. Chem. A* **2015**, *3*, 13031.
[44] C. Delmas, J. J. Braconnier, C. Fouassier, P. Hagenmuller, *Solid State Ionics* **1981**, *3–4*, 165.
[45] S. Kumakura, Y. Tahara, K. Kubota, K. Chihara, S. Komaba, *Angew. Chem., Int. Ed.* **2016**, *55*, 12760.
[46] K. Hemalatha, M. Jayakumar, P. Bera, A. S. Prakash, *J. Mater. Chem. A* **2015**, *3*, 20908.
[47] R. J. Clement, J. Billaud, A. R. Armstrong, G. Singh, T. Rojo, P. G. Bruce, C. P. Grey, *Energy Environ. Sci.* **2016**, *9*, 3240.
[48] N. Yabuuchi, M. Kajiyama, J. Iwatate, H. Nishikawa, S. Hitomi, R. Okuyama, R. Usui, Y. Yamada, S. Komaba, *Nat. Mater.* **2012**, *11*, 512.
[49] K. Park, D. Han, H. Kim, W. S. Chang, B. Choi, B. Anass, S. Lee, *RSC Adv.* **2014**, *4*, 22798.
[50] S. Kalluri, K. H. Seng, W. K. Pang, Z. Guo, Z. Chen, H.-K. Liu, S. X. Dou, *ACS Appl. Mater. Interfaces* **2014**, *6*, 8953.
[51] W. K. Pang, S. Kalluri, V. K. Peterson, N. Sharma, J. Kimpton, B. Johannessen, H. K. Liu, S. X. Dou, Z. P. Guo, *Chem. Mater.* **2015**, *27*, 3150.
[52] J. Xu, S.-L. Chou, J.-L. Wang, H.-K. Liu, S.-X. Dou, *Chemelectrochem* **2014**, *1*, 371.
[53] X. F. Wang, M. Tamaru, M. Okubo, A. Yamada, *J. Phys. Chem. C* **2013**, *117*, 15545.
[54] X. Xu, S. Ji, R. Gao, J. Liu, *RSC Adv.* **2015**, *5*, 51454.
[55] N. Bucher, S. Hartung, J. B. Franklin, A. M. Wise, L. Y. Lim, H. Y. Chen, J. N. Weker, M. F. Toney, M. Srinivasan, *Chem. Mater.* **2016**, *28*, 2041.
[56] X. Chen, X. Zhou, M. Hu, J. Liang, D. Wu, J. Wei, Z. Zhou, *J. Mater. Chem. A* **2015**, *3*, 20708.
[57] Y. Wen, B. Wang, G. Zeng, K. Nogita, D. Ye, L. Wang, *Chem. Asian J.* **2015**, *10*, 661.
[58] H. Wang, B. J. Yang, X. Z. Liao, J. Xu, D. Z. Yang, Y. S. He, Z. F. Ma, *Electrochim. Acta* **2013**, *113*, 200.
[59] W. Zhao, A. Tanaka, K. Momosaki, S. Yamamoto, F. Zhang, Q. Guo, H. Noguchi, *Electrochim. Acta* **2015**, *170*, 171.
[60] Y. H. Liu, X. Fang, A. Y. Zhang, C. F. Shen, Q. Z. Liu, H. A. Enaya, C. W. Zhou, *Nano Energy* **2016**, *27*, 27.
[61] X. H. Zhang, W. L. Pang, F. Wan, J. Z. Guo, H. Y. Lu, J. Y. Li, Y. M. Xing, J. P. Zhang, X. L. Wu, *ACS Appl. Mater. Interfaces* **2016**, *8*, 20650.
[62] L. Liu, X. Li, S.-H. Bo, Y. Wang, H. Chen, N. Twu, D. Wu, G. Ceder, *Adv. Energy Mater.* **2015**, *5*, 1500944.
[63] K. Wang, Z. G. Wu, T. Zhang, Y. P. Deng, J. T. Li, X. D. Guo, B. B. Xu, B. H. Zhong, *Electrochim. Acta* **2016**, *216*, 51.
[64] D. Buchholz, L. G. Chagas, C. Vaalma, L. Wu, S. Passerini, *J. Mater. Chem. A* **2014**, *2*, 13415.
[65] M. Sathiya, K. Hemalatha, K. Ramesha, J. M. Tarascon, A. S. Prakash, *Chem. Mater.* **2012**, *24*, 1846.
[66] Y. J. Fang, X. Y. Yu, X. W. Lou, *Angew. Chem. Int. Ed.* **2017**, *56*, 5801.
[67] X. H. Wu, G. L. Xu, G. M. Zhong, Z. L. Gong, M. J. McDonald, S. Y. Zheng, R. Q. Fu, Z. H. Chen, K. Amine, Y. Yang, *ACS Appl. Mater. Interfaces* **2016**, *8*, 22227.
[68] X. H. Wu, J. H. Guo, D. W. Wang, G. M. Zhong, M. J. McDonald, Y. Yang, *J. Power Sources* **2015**, *281*, 18.
[69] H. D. Hou, B. H. Gan, Y. D. Gong, N. Chen, C. W. Sun, *Inorg. Chem.* **2016**, *55*, 9033.
[70] J. J. Ding, Y. N. Zhou, Q. Sun, X. Q. Yu, X. Q. Yang, Z. W. Fu, *Electrochim. Acta* **2013**, *87*, 388.
[71] H. B. Wang, Y. Z. Xiao, C. Sun, C. Lai, X. P. Ai, *RSC Adv.* **2015**, *5*, 106519.
[72] B. Zhang, R. Dugas, G. Rousse, P. Rozier, A. M. Abakumov, J. M. Tarascon, *Nat. Commun.* **2016**, *7*, 10308.
[73] J. M. De Ilarduya, L. Otaegui, J. M. L. del Amo, M. Armand, G. Singh, *J. Power Sources* **2017**, *337*, 197.
[74] N. Yabuuchi, H. Yoshida, S. Komaba, *Electrochemistry* **2012**, *80*, 716.
[75] H. Yoshida, N. Yabuuchi, S. Komaba, *Electrochem. Commun.* **2013**, *34*, 60.
[76] B. M. de Boisse, J. H. Cheng, D. Carlier, M. Guignard, C. J. Pan, S. Bordere, D. Filimonov, C. Drathen, E. Suard, B. J. Hwang, A. Wattiaux, C. Delmas, *J. Mater. Chem. A* **2015**, *3*, 10976.
[77] N. Yabuuchi, M. Yano, H. Yoshida, S. Kuze, S. Komaba, *J. Electrochem. Soc.* **2013**, *160*, A3131.
[78] D. Kim, E. Lee, M. Slater, W. Lu, S. Rood, C. S. Johnson, *Electrochem. Commun.* **2012**, *18*, 66.
[79] P. Vassilaras, A. J. Toumar, G. Ceder, *Electrochem. Commun.* **2014**, *38*, 79.
[80] S.-M. Oh, S.-T. Myung, C. S. Yoon, J. Lu, J. Hassoun, B. Scrosati, K. Amine, Y.-K. Sun, *Nano Lett.* **2014**, *14*, 1620.
[81] J.-L. Yue, Y.-N. Zhou, X. Yu, S.-M. Bak, X.-Q. Yang, Z.-W. Fu, *J. Mater. Chem. A* **2015**, *3*, 23261.
[82] L. Mu, S. Xu, Y. Li, Y. S. Hu, H. Li, L. Chen, X. Huang, *Adv. Mater.* **2015**, *27*, 6755.
[83] E. Lee, D. E. Brown, E. E. Alp, Y. Ren, J. Lu, J. J. Woo, C. S. Johnson, *Chem. Mater.* **2015**, *27*, 6755.
[84] J. Braconnier, C. Delmas, P. Hagenmuller, *Mater. Res. Bull.* **1982**, *17*, 993.
[85] S. Komaba, C. Takei, T. Nakayama, A. Ogata, N. Yabuuchi, *Electrochem. Commun.* **2010**, *12*, 355.
[86] X. Xia, J. Dahn, *Electrochem. Solid-State Lett.* **2011**, *15*, A1.
[87] C. Y. Yu, J. S. Park, H. G. Jung, K. Y. Chung, D. Aurbach, Y. K. Sun, S. T. Myung, *Energy Environ. Sci.* **2015**, *8*, 2019.
[88] C. Y. Chen, K. Matsumoto, T. Nohira, R. Hagiwara, A. Fukunaga, S. Sakai, K. Nitta, S. Inazawa, *J. Power Sources* **2013**, *237*, 52.
[89] M. H. Cao, Y. Wang, Z. Shadike, J. L. Yue, E. Hu, S. M. Bak, Y. N. Zhou, X. Q. Yang, Z. W. Fu, *J. Mater. Chem. A* **2017**, *5*, 5442.
[90] J. Y. Hwang, C. S. Yoon, I. Belharouak, Y. K. Sun, *J. Mater. Chem. A* **2016**, *4*, 17952.
[91] J. Y. Hwang, S. M. Oh, S. T. Myung, K. Y. Chung, I. Belharouak, Y. K. Sun, *Nat. Commun.* **2015**, *6*, 6865.
[92] S. Komaba, N. Yabuuchi, T. Nakayama, A. Ogata, T. Ishikawa, I. Nakai, *Inorg. Chem.* **2012**, *51*, 6211.
[93] L. Wang, J. Wang, X. Zhang, Y. Ren, P. Zuo, G. Yin, J. Wang, *Nano Energy* **2017**, *34*, 215.
[94] C. Li, H. P. Zhang, L. J. Fu, H. Liu, Y. P. Wu, E. Ram, R. Holze, H. Q. Wu, *Electrochim. Acta* **2006**, *51*, 3872.
[95] S. T. Myung, K. Amine, Y. K. Sun, *J. Mater. Chem.* **2010**, *20*, 7074.
[96] K. Park, D. Han, J. Shon, S. G. Doo, S. Lee, *RSC Adv.* **2015**, *5*, 6340.
[97] X. Meng, X.-Q. Yang, X. Sun, *Adv. Mater.* **2012**, *24*, 3589.
[98] K. Kaliyappan, J. Liu, A. Lushington, R. Li, X. Sun, *ChemSusChem* **2015**, *8*, 2537.
[99] J. Alvarado, C. Ma, S. Wang, K. Nguyen, M. Kodur, Y. S. Meng, *ACS Appl. Mater. Interfaces* **2017**, *9*, 26518.
[100] D. Kim, S. H. Kang, M. Slater, S. Rood, J. T. Vaughey, N. Karan, M. Balasubramanian, C. S. Johnson, *Adv. Energy Mater.* **2011**, *1*, 333.
[101] J. Xu, D. H. Lee, R. J. Clément, X. Yu, M. Leskes, A. J. Pell, G. Pintacuda, X.-Q. Yang, C. P. Grey, Y. S. Meng, *Chem. Mater.* **2014**, *26*, 1260.
[102] J. Xu, H. Liu, Y. S. Meng, *Electrochem. Commun.* **2015**, *60*, 13.

[103] S. M. Oh, S. T. Myung, J. Y. Hwang, B. Scrosati, K. Amine, Y. K. Sun, *Chem. Mater.* **2014**, *26*, 6165.
[104] H. Liu, J. Xu, C. Ma, Y. S. Meng, *Chem. Commun.* **2015**, *51*, 4693.
[105] J. Billaud, G. Singh, A. R. Armstrong, E. Gonzalo, V. Roddatis, M. Armand, T. Rojob, P. G. Bruce, *Energy Environ. Sci.* **2014**, *7*, 1387.
[106] H. Li, X. Q. Yu, Y. Bai, F. Wu, C. Wu, L. Y. Liu, X. Q. Yang, *J. Mater. Chem. A* **2015**, *3*, 9578.
[107] P. F. Wang, Y. You, Y. X. Yin, Y. S. Wang, L. J. Wan, L. Gu, Y. G. Guo, *Angew. Chem., Int. Ed.* **2016**, *55*, 7445.
[108] J. Su, Y. Pei, Z. Yang, X. Wang, *RSC Adv.* **2015**, *5*, 27229.
[109] W. P. Kang, Z. Y. Zhang, P. K. Lee, T. W. Ng, W. Y. Li, Y. B. Tang, W. J. Zhang, C. S. Lee, D. Y. W. Yu, *J. Mater. Chem. A* **2015**, *3*, 22846.
[110] G. Ceder, Y. Chiang, D. Sadoway, M. Aydinol, *Nature* **1998**, *392*, 694.
[111] M. Dixit, B. Markovsky, D. Aurbach, D. T. Major, *J. Electrochem. Soc.* **2017**, *164*, A6359.
[112] D. D. Yuan, W. He, F. Pei, F. Y. Wu, Y. Wu, J. F. Qian, Y. L. Cao, X. P. Ai, H. X. Yang, *J. Mater. Chem. A* **2013**, *1*, 3895.
[113] I. Hasa, S. Passerini, J. Hassoun, *J. Mater. Chem. A* **2017**, *5*, 4467.
[114] H. Yoshida, N. Yabuuchi, K. Kubota, I. Ikeuchi, A. Garsuch, M. Schulz-Dobrick, S. Komaba, *Chem. Commun.* **2014**, *50*, 3677.
[115] P. F. Wang, H. R. Yao, X. Y. Liu, J. N. Zhang, L. Gu, X. Q. Yu, Y. X. Yin, Y. G. Guo, *Adv. Mater.* **2017**, *29*, 1700210.
[116] H. R. Yao, P. F. Wang, Y. Gong, J. Zhang, X. Yu, L. Gu, C. OuYang, Y. X. Yin, E. Hu, X. Q. Yang, E. Stavitski, Y. G. Guo, L. J. Wan, *J. Am. Chem. Soc.* **2017**, *139*, 8440.
[117] X. Sun, Y. Jin, C.-Y. Zhang, J.-W. Wen, Y. Shao, Y. Zang, C.-H. Chen, *J. Mater. Chem. A* **2014**, *2*, 17268.
[118] Z. Y. Li, R. Gao, L. M. Sun, Z. B. Hu, X. F. Liu, *Electrochim. Acta* **2017**, *223*, 92.
[119] Q. Zhang, Y. Huang, Y. Liu, S. Sun, K. Wang, Y. Li, X. Li, J. Han, Y. Huang, *Sci. China Mater.* **2017**, *60*, 629.
[120] E. Lee, J. Lu, Y. Ren, X. Luo, X. Zhang, J. Wen, D. Miller, A. DeWahl, S. Hackney, B. Key, D. Kim, M. D. Slater, C. S. Johnson, *Adv. Energy Mater.* **2014**, *4*, 1400458.
[121] S. Guo, P. Liu, H. Yu, Y. Zhu, M. Chen, M. Ishida, H. Zhou, *Angew. Chem., Int. Ed.* **2015**, *54*, 5894.
[122] M. Keller, D. Buchholz, S. Passerini, *Adv. Energy Mater.* **2016**, *6*, 1501555.
[123] G.-L. Xu, R. Amine, Y.-F. Xu, J. Liu, J. Gim, T. Ma, Y. Ren, C. Sun, Y. Liu, X. Zhang, S. Heald, A. Solhy, I. Saadoune, W. Mattis, S. G. Sun, Z. Chen, K. Amine, *Energy Environ. Sci.* **2017**, *10*, 1677.
[124] J. Zheng, P. Yan, W. H. Kan, C. Wang, A. Manthiram, *J. Electrochem. Soc.* **2016**, *163*, A584.
[125] Q. Ni, Y. Bai, F. Wu, C. Wu, *Adv. Sci.* **2017**, *4*, 1600275.
[126] H. Liu, F. C. Strobridge, O. J. Borkiewicz, K. M. Wiaderek, K. W. Chapman, P. J. Chupas, C. P. Grey, *Science* **2014**, *344*, 6191.
[127] A. Whiteside, C. A. J. Fisher, S. C. Parker, M. S. Islam, *Phys. Chem. Chem. Phys.* **2014**, *16*, 21788.
[128] M. Avdeev, Z. Mohamed, C. D. Ling, J. C. Lu, M. Tamaru, A. Yamada, P. Barpanda, *Inorg. Chem.* **2013**, *52*, 8685.
[129] J. Kim, D. H. Seo, H. Kim, I. Park, J. K. Yoo, S. K. Jung, Y. U. Park, W. A. Goddard, K. Kang, *Energy Environ. Sci.* **2015**, *8*, 540.
[130] C. Li, X. Miao, W. Chu, P. Wu, D. G. Tong, *J. Mater. Chem. A* **2015**, *3*, 8265.
[131] P. Moreau, D. Guyomard, J. Gaubicher, F. Boucher, *Chem. Mater.* **2010**, *22*, 4126.
[132] G. Ali, J. H. Lee, D. Susanto, S. W. Choi, B. W. Cho, K. W. Nam, K. Y. Chung, *ACS Appl. Mater. Interfaces* **2016**, *8*, 15422.
[133] Y. J. Fang, Q. Liu, L. F. Xiao, X. P. Ai, H. X. Yang, Y. L. Cao, *ACS Appl. Mater. Interfaces* **2015**, *7*, 17977.
[134] Y. J. Zhu, Y. H. Xu, Y. H. Liu, C. Luo, C. S. Wang, *Nanoscale* **2013**, *5*, 780.
[135] M. Galceran, D. Saurel, B. Acebedo, V. V. Roddatis, E. Martin, T. Rojo, M. Casas-Cabanas, *Phys. Chem. Chem. Phys.* **2014**, *16*, 8837.
[136] I. V. Zatovsky, *Acta Crystallogr., Sect. E: Struct. Rep. Online* **2010**, *66*, I12–194
[137] W. X. Song, H. S. Hou, X. B. Ji, *Acta Phys. Chim. Sin.* **2017**, *33*, 103.
[138] W. X. Song, X. B. Ji, Z. P. Wu, Y. R. Zhu, Y. C. Yang, J. Chen, M. J. Jing, F. Q. Li, C. E. Banks, *J. Mater. Chem. A* **2014**, *2*, 5358.
[139] R. Klee, M. J. Aragon, P. Lavela, R. Alcantara, J. L. Tirado, *ACS Appl. Mater. Interfaces* **2016**, *8*, 23151.
[140] X. H. Liang, X. Ou, F. H. Zheng, Q. C. Pan, X. H. Xiong, R. Z. Hu, C. H. Yang, M. L. Liu, *ACS Appl. Mater. Interfaces* **2017**, *9*, 13151.
[141] W. Shen, H. Li, Z. Y. Guo, C. Wang, Z. H. Li, Q. J. Xu, H. M. Liu, Y. G. Wang, Y. Y. Xia, *ACS Appl. Mater. Interfaces* **2016**, *8*, 15341.
[142] J. X. Zhang, Y. J. Fang, L. F. Xiao, J. F. Qian, Y. L. Cao, X. P. Ai, H. X. Yang, *ACS Appl. Mater. Interfaces* **2017**, *9*, 7177.
[143] Q. Y. An, F. Y. Xiong, Q. L. Wei, J. Z. Sheng, L. He, D. L. Ma, Y. Yao, L. Q. Mai, *Adv. Energy Mater.* **2015**, *5*, 1401963.
[144] Y. Jiang, Z. Z. Yang, W. H. Li, L. C. Zeng, F. S. Pan, M. Wang, X. Wei, G. T. Hu, L. Gu, Y. Yu, *Adv. Energy Mater.* **2015**, *5*, 1402104.
[145] Y. A. Xu, Q. L. Wei, C. Xu, Q. D. Li, Q. Y. An, P. F. Zhang, J. Z. Sheng, L. Zhou, L. Q. Mai, *Adv. Energy Mater.* **2016**, *6*, 1600389.
[146] Y. J. Fang, L. F. Xiao, X. P. Ai, Y. L. Cao, H. X. Yang, *Adv. Mater.* **2015**, *27*, 5895.
[147] S. Li, Y. F. Dong, L. Xu, X. Xu, L. He, L. Q. Mai, *Adv. Mater.* **2014**, *26*, 3545.
[148] X. H. Rui, W. P. Sun, C. Wu, Y. Yu, Q. Y. Yan, *Adv. Mater.* **2015**, *27*, 6670.
[149] H. Li, X. X. Bi, Y. Bai, Y. F. Yuan, R. Shahbazian-Yassar, C. Wu, F. Wu, J. Lu, K. Amine, *Adv. Mater. Interfaces* **2016**, *3*, 1500740.
[150] R. Rajagopalan, L. Zhang, S. X. Dou, H. K. Liu, *Adv. Mater. Interfaces* **2016**, *3*, 1600007.
[151] Z. Chu, C. Yue, *Ceram. Int.* **2016**, *42*, 820.
[152] J. Z. Guo, X. L. Wu, F. Wan, J. Wang, X. H. Zhang, R. S. Wang, *Chem. Eur. J.* **2015**, *21*, 17371.
[153] S. Kajiyama, J. Kikkawa, J. Hoshino, M. Okubo, E. Hosono, *Chem. Eur. J.* **2014**, *20*, 12636.
[154] Z. L. Jian, L. Zhao, H. L. Pan, Y. S. Hu, H. Li, W. Chen, L. Q. Chen, *Electrochem. Commun.* **2012**, *14*, 86.
[155] H. Wang, D. Jiang, Y. Zhang, G. Li, X. Lan, H. Zhong, Z. Zhang, Y. Jiang, *Electrochim. Acta* **2015**, *155*, 23.
[156] W. C. Duan, Z. Q. Zhu, H. Li, Z. Hu, K. Zhang, F. Y. Cheng, J. Chen, *J. Mater. Chem. A* **2014**, *2*, 8668.
[157] J. Q. Fang, S. Q. Wang, Z. T. Li, H. B. Chen, L. Xia, L. X. Ding, H. H. Wang, *J. Mater. Chem. A* **2016**, *4*, 1180.
[158] P. Y. Feng, W. Wang, K. L. Wang, S. J. Cheng, K. Jiang, *J. Mater. Chem. A* **2017**, *5*, 10261.
[159] Q. Hu, J. Y. Liao, B. K. Zou, H. Y. Wang, C. H. Chen, *J. Mater. Chem. A* **2016**, *4*, 16801.
[160] Y. H. Jung, C. H. Lim, D. K. Kim, *J. Mater. Chem. A* **2013**, *1*, 11350.
[161] J. F. Mao, C. Luo, T. Gao, X. L. Fan, C. S. Wang, *J. Mater. Chem. A* **2015**, *3*, 10378.
[162] W. H. Ren, Z. P. Zheng, C. Xu, C. J. Niu, Q. L. Wei, Q. Y. An, K. N. Zhao, M. Y. Yan, M. S. Qin, L. Q. Mai, *Nano Energy* **2016**, *25*, 145.
[163] Q. Zhang, W. Wang, Y. J. Wang, P. Y. Feng, K. L. Wang, S. J. Cheng, K. Jiang, *Nano Energy* **2016**, *20*, 11.
[164] C. B. Zhu, K. P. Song, P. A. van Aken, J. Maier, Y. Yu, *Nano Lett.* **2014**, *14*, 2175.
[165] Y. Jiang, H. C. Zhang, H. Yang, Z. Y. Qi, Y. Yu, *Nanoscale* **2017**, *9*, 6048.
[166] Z. L. Jian, W. Z. Han, X. Lu, H. X. Yang, Y. S. Hu, J. Zhou, Z. B. Zhou, J. Q. Li, W. Chen, D. F. Chen, L. Q. Chen, *Adv. Energy Mater.* **2013**, *3*, 156.

[167] K. Saravanan, C. W. Mason, A. Rudola, K. H. Wong, P. Balaya, *Adv. Energy Mater.* **2013**, *3*, 444.
[168] G. Y. Xu, G. G. Sun, *Ceram. Int.* **2016**, *42*, 14774.
[169] M. J. Aragon, P. Lavela, G. F. Ortiz, J. L. Tirado, *Chemelectrochem* **2015**, *2*, 995.
[170] F. Lalere, V. Seznec, M. Courty, R. David, J. N. Chotard, C. Masquelier, *J. Mater. Chem. A* **2015**, *3*, 16198.
[171] S. J. Lim, D. W. Han, D. H. Nam, K. S. Hong, J. Y. Eom, W. H. Ryu, H. S. Kwon, *J. Mater. Chem. A* **2014**, *2*, 19623.
[172] M. J. Aragon, P. Lavela, R. Alcantara, J. L. Tirado, *Electrochim. Acta* **2015**, *180*, 824.
[173] W. Shen, H. Li, Z. Y. Guo, Z. H. Li, Q. J. Xu, H. M. Liu, Y. G. Wang, *RSC Adv.* **2016**, *6*, 71581.
[174] P. Hu, X. Wang, T. Wang, L. Chen, J. Ma, Q. Kong, S. Shi, G. Cui, *Adv. Sci.* **2016**, *3*, 1600112.
[175] M. J. Aragon, P. Lavela, G. F. Ortiz, J. L. Tirado, *J. Electrochem. Soc.* **2015**, *162*, A3077.
[176] W. Zhang, Y. T. Liu, C. J. Chen, Z. Li, Y. H. Huang, X. L. Hu, *Small* **2015**, *11*, 3822.
[177] Y. Zhang, H. Y. Zhao, Y. P. Du, *J. Mater. Chem. A* **2016**, *4*, 7155.
[178] W. Wang, Q. J. Xu, H. M. Liu, Y. G. Wang, Y. Y. Xia, *J. Mater. Chem. A* **2017**, *5*, 8440.
[179] M. Bianchini, N. Brisset, F. Fauth, F. Weill, E. Elkaim, E. Suard, C. Masquelier, L. Croguennec, *Chem. Mater.* **2014**, *26*, 4238.
[180] M. Bianchini, F. Fauth, N. Brisset, F. Weill, E. Suard, C. Masquelier, L. Croguennec, *Chem. Mater.* **2015**, *27*, 3009.
[181] N. Eshraghi, S. Caes, A. Mahmoud, R. Cloots, B. Vertruyen, F. Boschini, *Electrochim. Acta* **2017**, *228*, 319.
[182] T. Jiang, G. Chen, A. Li, C. Z. Wang, Y. J. Wei, *J. Alloys Compd.* **2009**, *478*, 604.
[183] R. A. Shakoor, D. H. Seo, H. Kim, Y. U. Park, J. Kim, S. W. Kim, H. Gwon, S. Lee, K. Kang, *J. Mater. Chem.* **2012**, *22*, 20535.
[184] Q. Liu, D. X. Wang, X. Yang, N. Chen, C. Z. Wang, X. F. Bie, Y. J. Wei, G. Chen, F. Du, *J. Mater. Chem. A* **2015**, *3*, 21478.
[185] W. Q. Liu, H. M. Yi, Q. Zheng, X. F. Li, H. M. Zhang, *J. Mater. Chem. A* **2017**, *5*, 10928.
[186] R. Ling, S. Cai, S. B. Shen, X. D. Hu, D. L. Xie, F. Y. Zhang, X. H. Sun, N. Yu, F. W. Wang, *J. Alloys Compd.* **2017**, *704*, 631.
[187] N. V. Kosova, V. R. Podugolnikov, E. T. Devyatkina, A. B. Slobodyuk, *Mater. Res. Bull.* **2014**, *60*, 849.
[188] H. Zou, S. Li, X. Wu, M. J. McDonald, Y. Yang, *ECS Electrochem. Lett.* **2015**, *4*, A53.
[189] K. Kubota, K. Yokoh, N. Yabuuchi, S. Komaba, *Electrochemistry* **2014**, *82*, 909.
[190] B. Ellis, W. Makahnouk, Y. Makimura, K. Toghill, L. Nazar, *Nat. Mater.* **2007**, *6*, 749.
[191] M. Avdeev, C. D. Ling, T. T. Tan, S. Li, G. Oyama, A. Yamada, P. Barpanda, *Inorg. Chem.* **2013**, *53*, 682.
[192] A. Langrock, Y. Xu, Y. Liu, S. Ehrman, A. Manivannan, C. Wang, *J. Power Sources* **2013**, *223*, 62.
[193] D. L. Smiley, G. R. Goward, *Chem. Mater.* **2016**, *28*, 7645.
[194] X. Deng, W. Shi, J. Sunarso, M. Liu, Z. Shao, *ACS Appl. Mater. Interfaces* **2017**, *9*, 16280.
[195] Y. J. Zhong, Z. G. Wu, Y. Tang, W. Xiang, X. D. Guo, B. H. Zhong, *Mater. Lett.* **2015**, *145*, 269.
[196] Y. Zheng, P. Zhang, S. Wu, Y. Wen, Z. Zhu, Y. Yang, *J. Electrochem. Soc.* **2013**, *160*, A927.
[197] Y.-J. Zhong, J.-T. Li, Z.-G. Wu, B.-H. Zhong, X.-D. Guo, L. Huang, S.-G. Sun, *Acta Phys. Chim. Sin.* **2013**, *29*, 1989.
[198] M. W. Xu, C. J. Cheng, Q. Q. Sun, S. J. Bao, Y. B. Niu, H. He, Y. T. Li, J. Song, *RSC Adv.* **2015**, *5*, 56686.
[199] Y. Lu, S. Zhang, Y. Li, L. G. Xue, G. J. Xu, X. W. Zhang, *J. Power Sources* **2014**, *247*, 770.
[200] J. Q. Zhao, J. P. He, X. C. Ding, J. H. Zhou, Y. O. Ma, S. C. Wu, R. M. Huang, *J. Power Sources* **2010**, *195*, 6854.
[201] T. Jin, Y. Liu, Y. Li, K. Cao, X. Wang, L. Jiao, *Adv. Energy Mater.* **2017**, *54*, 1700087.
[202] M. W. Xu, C. J. Cheng, Q. Q. Sun, S. J. Bao, Y. B. Niu, H. He, Y. T. Li, J. Song, *RSC Adv.* **2015**, *5*, 40065.
[203] C.-X. Zhang, J.-P. He, G.-W. Zhao, J.-Q. Zhao, *Chin. J. Inorg. Chem.* **2007**, *23*, 649.
[204] J. Barker, M. Y. Saidi, J. L. Swoyer, *Electrochem. Solid-State Lett.* **2003**, *6*, A1.
[205] Y. Lu, S. Zhang, Y. Li, L. Xue, G. Xu, X. Zhang, *J. Power Sources* **2014**, *247*, 770.
[206] H. Zhuo, X. Wang, A. Tang, Z. Liu, S. Gamboa, P. Sebastian, *J. Power Sources* **2006**, *160*, 698.
[207] Y.-L. Ruan, K. Wang, S.-D. Song, X. Han, B.-W. Cheng, *Electrochim. Acta* **2015**, *160*, 330.
[208] J.-M. Le Meins, M.-P. Crosnier-Lopez, A. Hemon-Ribaud, G. Courbion, *J. Solid State Chem.* **1999**, *148*, 260.
[209] Z. G. Liu, Y. Y. Hu, M. T. Dunstan, H. Huo, X. G. Hao, H. Zou, G. M. Zhong, Y. Yang, C. P. Grey, *Chem. Mater.* **2014**, *26*, 2513.
[210] J. Barker, R. Gover, P. Burns, A. Bryan, *Electrochem. Solid-State Lett.* **2006**, *9*, A190.
[211] W. X. Song, X. B. Ji, Z. P. Wu, Y. R. Zhu, F. Q. Li, Y. P. Yao, C. E. Banks, *RSC Adv.* **2014**, *4*, 11375.
[212] Q. Liu, D. Wang, X. Yang, N. Chen, C. Wang, X. Bie, Y. Wei, G. Chen, F. Du, *J. Mater. Chem. A* **2015**, *3*, 21478.
[213] Q. Liu, X. Meng, Z. X. Wei, D. X. Wang, Y. Gao, Y. J. Wei, F. Du, G. Chen, *ACS Appl. Mater. Interfaces* **2016**, *8*, 31709.
[214] N. Pineda-Aguilar, V. J. Gallegos-Sanchez, E. M. Sanchez, L. C. Torres-Gonzalez, L. L. Garza-Tovar, *J. Sol-Gel Sci. Technol.* **2017**, *83*, 405.
[215] C. B. Zhu, C. Wu, C. C. Chen, P. Kopold, P. A. van Aken, J. Maier, Y. Yu, *Chem. Mater.* **2017**, *29*, 5207.
[216] P. Serras, V. Palomares, A. Goñi, I. G. de Muro, P. Kubiak, L. Lezama, T. Rojo, *J. Mater. Chem.* **2012**, *22*, 22301.
[217] M. Bianchini, P. Xiao, Y. Wang, G. Ceder, *Adv. Energy Mater.* **2017**, *7*, 1700514.
[218] Y. U. Park, D. H. Seo, H. Kim, J. Kim, S. Lee, B. Kim, K. Kang, *Adv. Funct. Mater.* **2014**, *24*, 4603.
[219] Y.-U. Park, D.-H. Seo, H.-S. Kwon, B. Kim, J. Kim, H. Kim, I. Kim, H.-I. Yoo, K. Kang, *J. Am. Chem. Soc.* **2013**, *135*, 13870.
[220] H. Kim, R. A. Shakoor, C. Park, S. Y. Lim, J. S. Kim, Y. N. Jo, W. Cho, K. Miyasaka, R. Kahraman, Y. Jung, J. W. Choi, *Adv. Funct. Mater.* **2013**, *23*, 1147.
[221] P. Barpanda, G. D. Liu, C. D. Ling, M. Tamaru, M. Avdeev, S. C. Chung, Y. Yamada, A. Yamada, *Chem. Mater.* **2013**, *25*, 3480.
[222] J. M. Clark, P. Barpanda, A. Yamada, M. S. Islam, *J. Mater. Chem. A* **2014**, *2*, 11807.
[223] G. Longoni, J. E. Wang, Y. H. Jung, D. K. Kim, C. M. Mari, R. Ruffo, *J. Power Sources* **2016**, *302*, 61.
[224] P. Barpanda, M. Avdeev, C. D. Ling, J. C. Lu, A. Yamada, *Inorg. Chem.* **2013**, *52*, 395.
[225] P. Barpanda, J. C. Lu, T. Ye, M. Kajiyama, S. C. Chung, N. Yabuuchi, S. Komaba, A. Yamada, *RSC Adv.* **2013**, *3*, 3857.
[226] P. Barpanda, T. Ye, M. Avdeev, S.-C. Chung, A. Yamada, *J. Mater. Chem. A* **2013**, *1*, 4194.
[227] C. S. Park, H. Kim, R. A. Shakoor, E. Yang, S. Y. Lim, R. Kahraman, Y. Jung, J. W. Choi, *J. Am. Chem. Soc.* **2013**, *135*, 2787.
[228] F. Sanz, C. Parada, U. Amador, M. Monge, C. R. Valero, *J. Solid State Chem.* **1996**, *123*, 129.
[229] M. Nose, H. Nakayama, K. Nobuhara, H. Yamaguchi, S. Nakanishi, H. Iba, *J. Power Sources* **2013**, *234*, 175.
[230] H. Moriwake, A. Kuwabara, C. A. J. Fisher, M. Nose, H. Nakayama, S. Nakanishi, H. Iba, Y. Ikuhara, *J. Power Sources* **2016**, *326*, 220.
[231] H. Kim, I. Park, S. Lee, H. Kim, K.-Y. Park, Y.-U. Park, H. Kim, J. Kim, H.-D. Lim, W.-S. Yoon, K. Kang, *Chem. Mater.* **2013**, *25*, 3614.

[232] S. M. Wood, C. Eames, E. Kendrick, M. S. Islam, *J. Phys. Chem. C* **2015**, *119*, 15935.
[233] D. Linden, T. B. Reddy, *Handbook of Batteries*, McGraw-Hill, New York **2002**.
[234] M. S. Dresselhaus, G. Dresselhaus, *Adv. Phys.* **1981**, *30*, 139.
[235] R. Yazami, P. Touzain, *J. Power Sources* **1983**, *9*, 365.
[236] T. Ohzuku, Y. Iwakoshi, K. Sawai, *J. Electrochem. Soc.* **1993**, *140*, 2490.
[237] S. Taminato, M. Yonemura, S. Shiotani, T. Kamiyama, S. Torii, M. Nagao, Y. Ishikawa, K. Mori, T. Fukunaga, Y. Onodera, T. Naka, M. Morishima, Y. Ukyo, D. S. Adipranoto, H. Arai, Y. Uchimoto, Z. Ogumi, K. Suzuki, M. Hirayama, R. Kanno, *Sci. Rep.* **2016**, *6*, 28843.
[238] Y. Liu, B. V. Merinov, W. A. Goddard, *Proc. Natl. Acad. Sci. USA* **2016**, *113*, 3735.
[239] M. Dahbi, N. Yabuuchi, K. Kubota, K. Tokiwa, S. Komaba, *Phys. Chem. Chem. Phys.* **2014**, *16*, 15007.
[240] J. R. Dahn, T. Zheng, Y. Liu, J. S. Xue, *Science* **1995**, *270*, 590.
[241] J. Collins, G. Gourdin, M. Foster, D. Qu, *Carbon* **2015**, *92*, 193.
[242] D. A. Stevens, J. R. Dahn, *J. Electrochem. Soc.* **2000**, *147*, 1271.
[243] G. Hasegawa, K. Kanamori, N. Kannari, J.-i. Ozaki, K. Nakanishi, T. Abe, *ChemElectroChem* **2015**, *2*, 1917.
[244] A. Kano, T. Okano, N. Hojo, S. Ito, M. Fujimoto, K. Nakura, *ECS Meet. Abstr.* **2016**, *02*, 668.
[245] E. Irisarri, A. Ponrouch, M. Palacin, *J. Electrochem. Soc.* **2015**, *162*, A2476.
[246] S. Komaba, W. Murata, T. Ishikawa, N. Yabuuchi, T. Ozeki, T. Nakayama, A. Ogata, K. Gotoh, K. Fujiwara, *Adv. Funct. Mater.* **2011**, *21*, 3859.
[247] V. Simone, A. Boulineau, A. de Geyer, D. Rouchon, L. Simonin, S. Martinet, *J. Energy Chem.* **2016**, *25*, 761.
[248] C. Bommier, T. W. Surta, M. Dolgos, X. Ji, *Nano Lett.* **2015**, *15*, 5888.
[249] J. M. Stratford, P. K. Allan, O. Pecher, P. A. Chater, C. P. Grey, *Chem. Commun.* **2016**, *52*, 12430.
[250] L. Wu, D. Buchholz, C. Vaalma, G. A. Giffin, S. Passerini, *ChemElectroChem* **2016**, *3*, 292.
[251] P. Liu, Y. Li, Y.-S. Hu, H. Li, L. Chen, X. Huang, *J. Mater. Chem. A* **2016**, *4*, 13046.
[252] X. Meng, P. E. Savage, D. Deng, *Environ. Sci. Technol.* **2015**, *49*, 12543.
[253] P. Zheng, T. Liu, J. Zhang, L. Zhang, Y. Liu, J. Huang, S. Guo, *RSC Adv.* **2015**, *5*, 40737.
[254] W. Lv, F. Wen, J. Xiang, J. Zhao, L. Li, L. Wang, Z. Liu, Y. Tian, *Electrochim. Acta* **2015**, *176*, 533.
[255] E. M. Lotfabad, J. Ding, K. Cui, A. Kohandehghan, W. P. Kalisvaart, M. Hazelton, D. Mitlin, *ACS Nano* **2014**, *8*, 7115.
[256] M. Dahbi, M. Kiso, K. Kubota, T. Horiba, T. Chafik, K. Hida, T. Matsuyama, S. Komaba, *J. Mater. Chem. A* **2017**, *5*, 9917.
[257] Z. Li, L. Ma, T. W. Surta, C. Bommier, Z. Jian, Z. Xing, W. F. Stickle, M. Dolgos, K. Amine, J. Lu, T. Wu, X. Ji, *ACS Energy Lett.* **2016**, *1*, 395.
[258] Y. Zhang, L. Chen, Y. Meng, J. Xie, Y. Guo, D. Xiao, *J. Power Sources* **2016**, *335*, 20.
[259] M. Kalbac, M. Zukalova, L. Kavan, *J. Solid State Electrochem.* **2003**, *8*, 2.
[260] L. Zhao, H. L. Pan, Y. S. Hu, H. Li, L. Q. Chen, *Chin. Phys. B* **2012**, *21*, 028201.
[261] Y. Sun, L. Zhao, H. Pan, X. Lu, L. Gu, Y.-S. Hu, H. Li, M. Armand, Y. Ikuhara, L. Chen, *Nat. Commun.* **2013**, *4*, 1870.
[262] Y. J. Sha, L. Li, S. Y. Wei, Z. P. Shao, *J. Alloys Compd.* **2017**, *705*, 164.
[263] Y. Tian, Z. L. Wu, G. B. Xu, L. W. Yang, J. X. Zhong, *RSC Adv.* **2017**, *7*, 3293.
[264] G. B. Xu, Y. Tian, X. L. Wei, L. W. Yang, P. K. Chu, *J. Power Sources* **2017**, *337*, 180.
[265] C. J. Chen, H. H. Xu, T. F. Zhou, Z. P. Guo, L. N. Chen, M. Y. Yan, L. Q. Mai, P. Hu, S. J. Cheng, Y. H. Huang, J. Xie, *Adv. Energy Mater.* **2016**, *6*, 1600322.
[266] X. Y. Feng, H. L. Zou, H. F. Xiang, X. Guo, T. P. Zhou, Y. C. Wu, W. Xu, P. F. Yan, C. M. Wang, J. G. Zhang, Y. Yu, *ACS Appl. Mater. Interfaces* **2016**, *8*, 16718.
[267] F. Zhao, P. Xue, H. H. Ge, L. Li, B. F. Wang, *J. Electrochem. Soc.* **2016**, *163*, A690.
[268] K. T. Kim, C. Y. Yu, C. S. Yoon, S. J. Kim, Y. K. Sun, S. T. Myung, *Nano Energy* **2015**, *12*, 725.
[269] L. Y. Yang, H. Z. Li, J. Liu, S. S. Tang, Y. K. Lu, S. T. Li, J. Min, N. Yan, M. Lei, *J. Mater. Chem. A* **2015**, *3*, 24446.
[270] Y. Q. Ge, H. Jiang, K. Fu, C. H. Zhang, J. D. Zhu, C. Chen, Y. Lu, Y. P. Qiu, X. W. Zhang, *J. Power Sources* **2014**, *272*, 860.
[271] K.-T. Kim, C.-Y. Yu, C. S. Yoon, S.-J. Kim, Y.-K. Sun, S.-T. Myung, *Nano Energy* **2015**, *12*, 725.
[272] Y. Liu, J. Liu, M. Hou, L. Fan, Y. Wang, Y. Xia, *J. Mater. Chem. A* **2017**, *5*, 8440.
[273] H. L. Pan, X. Lu, X. Q. Yu, Y. S. Hu, H. Li, X. Q. Yang, L. Q. Chen, *Adv. Energy Mater.* **2013**, *3*, 1186.
[274] S. Y. Dong, L. F. Shen, H. S. Li, G. Pang, H. Dou, X. G. Zhang, *Adv. Funct. Mater.* **2016**, *26*, 3703.
[275] Y. P. Zhang, L. Guo, S. H. Yang, *Chem. Commun.* **2014**, *50*, 14029.
[276] J. Z. Chen, X. Y. Zhou, C. T. Mei, J. L. Xu, C. P. Wong, *Electrochim. Acta* **2017**, *224*, 446.
[277] H. S. Li, L. L. Peng, Y. Zhu, D. H. Chen, X. G. Zhang, G. H. Yu, *Energy Environ. Sci.* **2016**, *9*, 3399.
[278] S. D. Fu, J. F. Ni, Y. Xu, Q. Zhang, L. Li, *Nano Lett.* **2016**, *16*, 4544.
[279] P. Senguttuvan, G. Rousse, V. Seznec, J. M. Tarascon, M. R. Palacin, *Chem. Mater.* **2011**, *23*, 4109.
[280] J. Xu, C. Z. Ma, M. Balasubramanian, Y. S. Meng, *Chem. Commun.* **2014**, *50*, 12564.
[281] A. Rudola, N. Sharma, P. Balaya, *Electrochem. Commun.* **2015**, *61*, 10.
[282] J. F. Ni, S. D. Fu, C. Wu, Y. Zhao, J. Maier, Y. Yu, L. Li, *Adv. Energy Mater.* **2016**, *6*, 1502568.
[283] Y. Xu, E. M. Lotfabad, H. Wang, B. Farbod, Z. Xu, A. Kohandehghan, D. Mitlin, *Chem. Commun.* **2013**, *49*, 8973.
[284] F. X. Xie, L. Zhang, D. W. Su, M. Jaroniec, S. Z. Qiao, *Adv. Mater.* **2017**, *29*, 1700989.
[285] H. Pan, X. Lu, X. Yu, Y. S. Hu, H. Li, X. Q. Yang, L. Chen, *Adv. Energy Mater.* **2013**, *3*, 1186.
[286] J. Wei, J. X. Liu, Y. C. Dang, K. Xu, Y. Zhou, *Adv. Mater. Res.* **2013**, *750–752*, 301.
[287] H. Xiong, M. D. Slater, M. Balasubramanian, C. S. Johnson, T. Rajh, *J. Phys. Chem. Lett.* **2011**, *2*, 2560.
[288] Z. H. Bi, M. P. Paranthaman, P. A. Menchhofer, R. R. Dehoff, C. A. Bridges, M. F. Chi, B. K. Guo, X. G. Sun, S. Dai, *J. Power Sources* **2013**, *222*, 461.
[289] J. P. Huang, D. D. Yuan, H. Z. Zhang, Y. L. Cao, G. R. Li, H. X. Yang, X. P. Gao, *RSC Adv.* **2013**, *3*, 12593.
[290] Y. Xu, E. M. Lotfabad, H. L. Wang, B. Farbod, Z. W. Xu, A. Kohandehghan, D. Mitlin, *Chem. Commun.* **2013**, *49*, 8973.
[291] J. C. Perez-Flores, C. Baehtz, A. Kuhn, F. Garcia-Alvarado, *J. Mater. Chem. A* **2014**, *2*, 1825.
[292] Y. Q. Ge, H. Jiang, J. D. Zhu, Y. Lu, C. Chen, Y. Hu, Y. P. Qiu, X. W. Zhang, *Electrochim. Acta* **2015**, *157*, 142.
[293] Y. Xu, M. Zhou, L. Y. Wen, C. L. Wang, H. P. Zhao, Y. Mi, L. Y. Liang, Q. Fu, M. H. Wu, Y. Lei, *Chem. Mater.* **2015**, *27*, 4274.
[294] D. Yan, C. Y. Yu, Y. Bai, W. F. Zhang, T. Q. Chen, B. W. Hu, Z. Sun, L. K. Pan, *Chem. Commun.* **2015**, *51*, 8261.
[295] X. M. Yang, C. Wang, Y. C. Yang, Y. Zhang, X. N. Jia, J. Chen, X. B. Ji, *J. Mater. Chem. A* **2015**, *3*, 8800

[296] Y. C. Yang, X. B. Ji, M. J. Jing, H. S. Hou, Y. R. Zhu, L. B. Fang, X. M. Yang, Q. Y. Chen, C. E. Banks, *J. Mater. Chem. A* **2015**, *3*, 5648.
[297] F. Zhao, B. F. Wang, Y. F. Tang, H. H. Ge, Z. G. Huang, H. K. Liu, *J. Mater. Chem. A* **2015**, *3*, 22969.
[298] S. A. Liu, Z. Y. Cai, J. Zhou, A. Q. Pan, S. Q. Liang, *J. Mater. Chem. A* **2016**, *4*, 18278.
[299] B. F. Wang, F. Zhao, G. D. Du, S. Porter, Y. Liu, P. Zhang, Z. X. Cheng, H. K. Liu, Z. G. Huang, *ACS Appl. Mater. Interfaces* **2016**, *8*, 16009.
[300] Z. Zhang, Y. L. An, X. Y. Xu, C. L. Dong, J. K. Feng, L. J. Ci, S. L. Xiong, *Chem. Commun.* **2016**, *52*, 12810.
[301] G. Q. Zou, H. S. Hou, Y. Zhang, Z. D. Huang, X. Q. Qiu, X. B. Ji, *J. Electrochem. Soc.* **2016**, *163*, A3117.
[302] T. B. Lan, T. Wang, W. F. Zhang, N. L. Wu, M. D. Wei, *J. Alloys Compd.* **2017**, *699*, 455.
[303] S. Qiu, L. F. Xiao, X. P. Ai, H. X. Yang, Y. L. Cao, *ACS Appl. Mater. Interfaces* **2017**, *9*, 345.
[304] Y. C. Yang, S. J. Liao, W. Shi, Y. D. Wu, R. H. Zhang, S. L. Leng, *RSC Adv.* **2017**, *7*, 10885.
[305] Q. Zhang, Y. Q. Wei, H. T. Yang, D. Su, Y. Ma, H. Q. Li, T. Y. Zhai, *ACS Appl. Mater. Interfaces* **2017**, *9*, 7009.
[306] X. J. Zhang, M. Wang, G. Zhu, D. S. Li, D. Yan, T. Lu, L. K. Pan, *Ceram. Int.* **2017**, *43*, 2398.
[307] Y. Zhao, S. D. Xu, D. Zhang, S. B. Liu, L. Chen, H. Q. Zhao, G. Q. Wei, *Int. J. Electrochem. Sci.* **2017**, *12*, 1929.
[308] M. Zhou, Y. Xu, C. L. Wang, Q. W. Li, J. X. Xiang, L. Y. Liang, M. H. Wu, H. P. Zhao, Y. Lei, *Nano Energy* **2017**, *31*, 514.
[309] K.-T. Kim, G. Ali, K. Y. Chung, C. S. Yoon, H. Yashiro, Y.-K. Sun, J. Lu, K. Amine, S.-T. Myung, *Nano Lett.* **2014**, *14*, 416.
[310] Y. Xiong, J. Qian, Y. Cao, X. Ai, H. Yang, *J. Mater. Chem. A* **2016**, *4*, 11351.
[311] H. A. Cha, H. M. Jeong, J. K. Kang, *J. Mater. Chem. A* **2014**, *2*, 5182.
[312] C. Chen, Y. Wen, X. Hu, X. Ji, M. Yan, L. Mai, P. Hu, B. Shan, Y. Huang, *Nat. Commun.* **2015**, *6*, 6929.
[313] Z. Le, F. Liu, P. Nie, X. Li, X. Liu, Z. Bian, G. Chen, H. B. Wu, Y. Lu, *ACS Nano* **2017**, *11*, 2952.
[314] L. Q. Sun, M. J. Li, K. Sun, S. H. Yu, R. S. Wang, H. M. Xie, *J. Phys. Chem. C* **2012**, *116*, 14772.
[315] L. Wang, X. M. He, J. J. Li, W. T. Sun, J. Gao, J. W. Guo, C. Y. Jiang, *Angew. Chem., Int. Ed.* **2012**, *51*, 9034.
[316] Y. Kim, Y. Park, A. Choi, N. S. Choi, J. Kim, J. Lee, J. H. Ryu, S. M. Oh, K. T. Lee, *Adv. Mater.* **2013**, *25*, 3045.
[317] J. Y. Li, L. Wang, X. M. He, *Prog. Chem.* **2016**, *28*, 193.
[318] M. Lao, Y. Zhang, W. Luo, Q. Yan, W. Sun, S. X. Dou, *Adv. Mater.* **2017**, *29*, 1700622.
[319] X. L. Ma, G. Q. Ning, C. L. Qi, C. G. Xu, J. S. Gao, *ACS Appl. Mater. Interfaces* **2014**, *6*, 14415.
[320] Q. F. Li, C. G. Duan, X. G. Wan, J. L. Kuo, *J. Phys. Chem. C* **2015**, *119*, 8662.
[321] W. W. Li, H. Q. Li, Z. J. Lu, L. Gan, L. B. Ke, T. Y. Zhai, H. S. Zhou, *Energy Environ. Sci.* **2015**, *8*, 3629.
[322] M. Walter, R. Erni, M. V. Kovalenko, *Sci. Rep.* **2015**, *5*, 8418.
[323] Y. L. Wang, L. Y. Tian, Z. H. Yao, F. Li, S. Li, S. H. Ye, *Electrochim. Acta* **2015**, *163*, 71.
[324] Y. J. Zhu, Y. Wen, X. L. Fan, T. Gao, F. D. Han, C. Luo, S. C. Liou, C. S. Wang, *ACS Nano* **2015**, *9*, 3254.
[325] L. Y. Wang, H. L. Guo, W. Wang, K. Y. Teng, Z. W. Xu, C. Chen, C. Y. Li, C. Y. Yang, C. S. Hu, *Electrochim. Acta* **2016**, *211*, 499.
[326] W. C. Chang, K. W. Tseng, H. Y. Tuan, *Nano Lett.* **2017**, *17*, 1240.
[327] G. H. Lee, M. R. Jo, K. Zhang, Y. M. Kang, *J. Mater. Chem. A* **2017**, *5*, 3683.
[328] M. Li, R. Carter, L. Oakes, A. Douglas, N. Muralidharan, C. L. Pint, *J. Mater. Chem. A* **2017**, *5*, 5266.
[329] W. H. Li, S. H. Hu, X. Y. Luo, Z. L. Li, X. Z. Sun, M. S. Li, F. F. Liu, Y. Yu, *Adv. Mater.* **2017**, *29*, 1605820.
[330] S. Liu, J. K. Feng, X. F. Bian, J. Liu, H. Xu, Y. L. An, *Energy Environ. Sci.* **2017**, *10*, 1222.
[331] Y. H. Liu, A. Y. Zhang, C. F. Shen, Q. Z. Liu, X. A. Cao, Y. Q. Ma, L. A. Chen, C. Lau, T. C. Chen, F. Wei, C. W. Zhou, *ACS Nano* **2017**, *11*, 5530.
[332] J. Sun, G. Y. Zheng, H. W. Lee, N. Liu, H. T. Wang, H. B. Yao, W. S. Yang, Y. Cui, *Nano Lett.* **2014**, *14*, 4573.
[333] W. Jin, Z. G. Wang, Y. Q. Fu, *J. Mater. Sci.* **2016**, *51*, 7355.
[334] J. X. Song, Z. X. Yu, M. L. Gordin, X. L. Li, H. S. Peng, D. H. Wang, *ACS Nano* **2015**, *9*, 11933.
[335] J. Sun, H. W. Lee, M. Pasta, Y. Sun, W. Liu, Y. Li, H. R. Lee, N. Liu, Y. Cui, *Energy Storage Mater.* **2016**, *4*, 130.
[336] J. Zhou, X. Liu, W. Cai, Y. Zhu, J. Liang, K. Zhang, Y. Lan, Z. Jiang, G. Wang, Y. Qian, *Adv. Mater.* **2017**, *29*, 1700214.
[337] P. Bridgman, *J. Am. Chem. Soc.* **1914**, *36*, 1344.
[338] J. N. Baillargeon, K. Y. Cheng, A. Y. Cho, S.-N. G. Chu, W.-Y. Hwang, *US 6110438 A*, **2000**.
[339] C. M. Park, H. J. Sohn, *Adv. Mater.* **2007**, *19*, 2465.
[340] L. Pan, X. D. Zhu, K. N. Sung, Y. T. Liu, X. M. Xie, X. Y. Ye, *Nano Energy* **2016**, *30*, 347.
[341] L. Chen, G. M. Zhou, Z. B. Liu, X. M. Ma, J. Chen, Z. Y. Zhang, X. L. Ma, F. Li, H. M. Cheng, W. C. Ren, *Adv. Mater.* **2016**, *28*, 510.
[342] M. Nagao, A. Hayashi, M. Tatsumisago, *J. Power Sources* **2011**, *196*, 6902.
[343] J. X. Song, Z. X. Yu, M. L. Gordin, S. Hu, R. Yi, D. H. Tang, T. Walter, M. Regula, D. Choi, X. L. Li, A. Maniyannan, D. H. Wang, *Nano Lett.* **2014**, *14*, 6329.
[344] X.-F. Yu, H. Ushiyama, K. Yamashita, *Chem. Lett.* **2014**, *43*, 1940.
[345] T. Ramireddy, T. Xing, M. M. Rahman, Y. Chen, Q. Dutercq, D. Gunzelmann, A. M. Glushenkov, *J. Mater. Chem. A* **2015**, *3*, 5572.
[346] X. Ding, Y. Huang, G. Li, Y. Tang, X. Li, Y. Huang, *Electrochim. Acta* **2017**, *235*, 150.
[347] M. Dahbi, N. Yabuuchi, M. Fukunishi, K. Kubota, K. Chihara, K. Tokiwa, X. F. Yu, H. Ushiyama, K. Yamashita, J. Y. Son, Y. T. Cui, H. Oji, S. Komaba, *Chem. Mater.* **2016**, *28*, 1625.
[348] T. W. Chen, P. Zhao, X. Guo, S. L. Zhang, *Nano Lett.* **2017**, *17*, 2299.
[349] G. Xu, Z. Chen, K. Amine, *US 20170214035 A1*, **2016**.
[350] M. Akhtar, G. Anderson, R. Zhao, A. Alruqi, J. E. Mroczkowska, G. Sumanasekera, J. B. Jasinski, *2D Mater. Appl.* **2017**, *1*, 5.
[351] M. Batmunkh, M. Bat-Erdene, J. G. Shapter, *Adv. Mater.* **2016**, *28*, 8586.
[352] V. V. Kulish, O. I. Malyi, C. Persson, P. Wu, *Phys. Chem. Chem. Phys.* **2015**, *17*, 13921.
[353] J. Sun, H.-W. Lee, M. Pasta, H. Yuan, G. Zheng, Y. Sun, Y. Li, Y. Cui, *Nat. Nanotechnol.* **2015**, *10*, 980.
[354] Y. Zhang, W. Sun, Z.-Z. Luo, Y. Zheng, Z. Yu, D. Zhang, J. Yang, H. T. Tan, J. Zhu, X. Wang, *Nano Energy* **2017**, *40*, 576.
[355] J. F. Qian, Y. Xiong, Y. L. Cao, X. P. Ai, H. X. Yang, *Nano Lett.* **2014**, *14*, 1865.
[356] Y. Kim, Y. Kim, A. Choi, S. Woo, D. Mok, N. S. Choi, Y. S. Jung, J. H. Ryu, S. M. Oh, K. T. Lee, *Adv. Mater.* **2014**, *26*, 4139.
[357] J. Y. Jang, Y. Lee, Y. Kim, J. Lee, S. M. Lee, K. T. Lee, N. S. Choi, *J. Mater. Chem. A* **2015**, *3*, 8332.
[358] Q. Li, Z. Li, Z. Zhang, C. Li, J. Ma, C. Wang, X. Ge, S. Dong, L. Yin, *Adv. Energy Mater.* **2016**, *6*, 1600376.
[359] J. Liu, P. Kopold, C. Wu, P. A. van Aken, J. Maier, Y. Yu, *Energy Environ. Sci.* **2015**, *8*, 3531.
[360] K. Xu, *Chem. Rev.* **2014**, *114*, 11503.
[361] K. Vignarooban, R. Kushagra, A. Elango, P. Badami, B. E. Mellander, X. Xu, T. G. Tucker, C. Nam, A. M. Kannan, *Int. J. Hydrogen Energy* **2016**, *41*, 2829.

[362] E. Peled, *J. Electrochem. Soc.* **1979**, *126*, 2047.
[363] R. Fong, U. Von Sacken, J. R. Dahn, *J. Electrochem. Soc.* **1990**, *137*, 2009.
[364] D. DiVincenzo, E. Mele, *Phys. Rev. B* **1985**, *32*, 2538.
[365] P. Thomas, J. Ghanbaja, D. Billaud, *Electrochim. Acta* **1999**, *45*, 423.
[366] J. Besenhard, M. Winter, J. Yang, W. Biberacher, *J. Power Sources* **1995**, *54*, 228.
[367] R. Alcántara, P. Lavela, G. F. Ortiz, J. L. Tirado, *Electrochem. Solid-State Lett.* **2005**, *8*, A222.
[368] S. Komaba, W. Murata, T. Ishikawa, N. Yabuuchi, T. Ozeki, T. Nakayama, A. Ogata, K. Gotoh, K. Fujiwara, *Adv. Funct. Mater.* **2011**, *21*, 3859.
[369] A. Ponrouch, E. Marchante, M. Courty, J. M. Tarascon, M. R. Palacin, *Energy Environ. Sci.* **2012**, *5*, 8572.
[370] A. Ponrouch, R. Dedryvere, D. Monti, A. E. Demet, J. M. A. Mba, L. Croguennec, C. Masquelier, P. Johansson, M. R. Palacin, *Energy Environ. Sci.* **2013**, *6*, 2361.
[371] B. Jache, P. Adelhelm, *Angew. Chem., Int. Ed.* **2014**, *53*, 10169.
[372] H. Kim, J. Hong, Y. U. Park, J. Kim, I. Hwang, K. Kang, *Adv. Funct. Mater.* **2015**, *25*, 534.
[373] H. Kim, J. Hong, G. Yoon, H. Kim, K.-Y. Park, M.-S. Park, W.-S. Yoon, K. Kang, *Energy Environ. Sci.* **2015**, *8*, 2963.
[374] Z. Zhu, F. Cheng, Z. Hu, Z. Niu, J. Chen, *J. Power Sources* **2015**, *293*, 626.
[375] B. Jache, J. O. Binder, T. Abe, P. Adelhelm, *Phys. Chem. Chem. Phys.* **2016**, *18*, 14299.
[376] S. M. Oh, S. T. Myung, C. S. Yoon, J. Lu, J. Hassoun, B. Scrosati, K. Amine, Y. K. Sun, *Nano Lett.* **2014**, *14*, 1620.
[377] J. Tarascon, D. Guyomard, *Solid State Ionics* **1994**, *69*, 293.
[378] A. Bhide, J. Hofmann, A. K. Dürr, J. Janek, P. Adelhelm, *Phys. Chem. Chem. Phys.* **2014**, *16*, 1987.
[379] E. C. Martínez, J. C. González, M. Armand, *Angew. Chem., Int. Ed.* **2014**, *53*, 5341.
[380] G. Singh, F. Aguesse, L. Otaegui, E. Goikolea, E. Gonzalo, J. Segalini, T. Rojo, *J. Power Sources* **2015**, *273*, 333.
[381] C. Ge, L. Wang, L. Xue, Z.-S. Wu, H. Li, Z. Gong, X.-D. Zhang, *J. Power Sources* **2014**, *248*, 77.
[382] J. Chen, Z. Huang, C. Wang, S. Porter, B. Wang, W. Lie, H. K. Liu, *Chem. Commun.* **2015**, *51*, 9809.
[383] S. Komaba, T. Ishikawa, N. Yabuuchi, W. Murata, A. Ito, Y. Ohsawa, *ACS Appl. Mater. Interfaces* **2011**, *3*, 4165.
[384] N. Takenaka, H. Sakai, Y. Suzuki, P. Uppula, M. Nagaoka, *J. Phys. Chem. C* **2015**, *119*, 18046.
[385] U. Purushotham, N. Takenaka, M. Nagaoka, *RSC Adv.* **2016**, *6*, 65232.
[386] M. Dahbi, T. Nakano, N. Yabuuchi, S. Fujimura, K. Chihara, K. Kubota, J. Y. Son, Y. T. Cui, H. Oji, S. Komaba, *ChemElectroChem* **2016**, *3*, 1856.
[387] Y. Wang, C. Wang, Y. Wang, H. Liu, Z. Huang, *ACS Appl. Mater. Interfaces* **2016**, *8*, 18860.
[388] J. Y. Jang, Y. Lee, Y. Kim, J. Lee, S.-M. Lee, K. T. Lee, N.-S. Choi, *J. Mater. Chem. A* **2015**, *3*, 8332.
[389] A. Ponrouch, A. R. Goni, M. R. Palacin, *Electrochem. Commun.* **2013**, *27*, 85.
[390] M. Dahbi, N. Yabuuchi, M. Fukunishi, K. Kubota, K. Chihara, K. Tokiwa, X. F. Yu, H. Ushiyama, K. Yamashita, J.-Y. Son, Y.-T. Cui, H. Oji, S. Komaba, *Chem. Mater.* **2016**, *28*, 1625.
[391] M. Law, V. Ramar, P. Balaya, *J. Power Sources* **2017**, *359*, 277.
[392] A. Hayashi, K. Noi, A. Sakuda, M. Tatsumisago, *Nat. Commun.* **2012**, *3*, 856.
[393] A. Hayashi, K. Noi, N. Tanibata, M. Nagao, M. Tatsumisago, *J. Power Sources* **2014**, *258*, 420.
[394] N. Tanibata, K. Noi, A. Hayashi, M. Tatsumisago, *RSC Adv.* **2014**, *4*, 17120.
[395] Z. Zhu, I.-H. Chu, Z. Deng, S. P. Ong, *Chem. Mater.* **2015**, *27*, 8318.
[396] A. Banerjee, K. H. Park, J. W. Heo, Y. J. Nam, C. K. Moon, S. M. Oh, S. T. Hong, Y. S. Jung, *Angew. Chem., Int. Ed.* **2016**, *128*, 9786.
[397] S. P. Ong, Y. Mo, W. D. Richards, L. Miara, H. S. Lee, G. Ceder, *Energy Environ. Sci.* **2013**, *6*, 148.
[398] L. Zhang, K. Yang, J. Mi, L. Lu, L. Zhao, L. Wang, Y. Li, H. Zeng, *Adv. Energy Mater.* **2015**, *5*, 1501294.
[399] Q. Ma, M. Guin, S. Naqash, C.-L. Tsai, F. Tietz, O. Guillon, *Chem. Mater.* **2016**, *28*, 4821.
[400] Z. Z. Zhang, Q. H. Zhang, J. A. Shi, Y. S. Chu, X. Q. Yu, K. Q. Xu, M. Y. Ge, H. F. Yan, W. J. Li, L. Gu, Y. S. Hu, H. Li, X. Q. Yang, L. Q. Chen, X. J. Huang, *Adv. Energy Mater.* **2017**, *7*, 1601196.
[401] M. Guin, F. Tietz, O. Guillon, *Solid State Ionics* **2016**, *293*, 18.
[402] J.-K. Kim, Y. J. Lim, H. Kim, G.-B. Cho, Y. Kim, *Energy Environ. Sci.* **2015**, *8*, 3589.
[403] Z. Zhang, Q. Zhang, C. Ren, F. Luo, Q. Ma, Y.-S. Hu, Z. Zhou, H. Li, X. Huang, L. Chen, *J. Mater. Chem. A* **2016**, *4*, 15823.
[404] H. Gao, L. Xue, S. Xin, K. Park, J. B. Goodenough, *Angew. Chem., Int. Ed.* **2017**, *129*, 5633.
[405] L. Long, S. Wang, M. Xiao, Y. Meng, *J. Mater. Chem. A* **2016**, *4*, 10038.
[406] Y. L. Ni'mah, M.-Y. Cheng, J. H. Cheng, J. Rick, B.-J. Hwang, *J. Power Sources* **2015**, *278*, 375.
[407] F. Colò, F. Bella, J. R. Nair, M. Destro, C. Gerbaldi, *Electrochim. Acta* **2015**, *174*, 185.
[408] F. Bella, F. Colò, J. R. Nair, C. Gerbaldi, *ChemSusChem* **2015**, *8*, 3668.
[409] D. Choi, D. Wang, I.-T. Bae, J. Xiao, Z. Nie, W. Wang, V. V. Viswanathan, Y. J. Lee, J.-G. Zhang, G. L. Graff, *Nano Lett.* **2010**, *10*, 2799.
[410] D. Wang, I. Belharouak, G. M. Koenig, G. Zhou, K. Amine, *J. Mater. Chem.* **2011**, *21*, 9290.
[411] Y. Hao, Q. Lai, Z. Xu, X. Liu, X. Ji, *Solid State Ionics* **2005**, *176*, 1201.
[412] H. Ma, S. Zhang, W. Ji, Z. Tao, J. Chen, *J. Am. Chem. Soc.* **2008**, *130*, 5361.
[413] J. Li, Y.-L. Jin, X.-G. Zhang, H. Yang, *Solid State Ionics* **2007**, *178*, 1590.
[414] Z.-J. Fan, J. Yan, T. Wei, G.-Q. Ning, L.-J. Zhi, J.-C. Liu, D.-X. Cao, G.-L. Wang, F. Wei, *ACS Nano* **2011**, *5*, 2787.
[415] P.-L. Taberna, S. Mitra, P. Poizot, P. Simon, J.-M. Tarascon, *Nat. Mater.* **2006**, *5*, 567.
[416] F. Croce, M. L. Focarete, J. Hassoun, I. Meschini, B. Scrosati, *Energy Environ. Sci.* **2011**, *4*, 921.
[417] J. Hassoun, G. Mulas, S. Panero, B. Scrosati, *Electrochem. Commun.* **2007**, *9*, 2075.
[418] M. Morcrette, Y. Chabre, G. Vaughan, G. Amatucci, J.-B. Leriche, S. Patoux, C. Masquelier, J. Tarascon, *Electrochim. Acta* **2002**, *47*, 3137.
[419] Y. Li, R. Xu, Y. Ren, J. Lu, H. Wu, L. Wang, D. J. Miller, Y.-K. Sun, K. Amine, Z. Chen, *Nano Energy* **2016**, *19*, 522.
[420] M. Hu, J. S. Jiang, *Mater. Res. Bull.* **2011**, *46*, 702.
[421] N. A. Nguyen, K. Kim, K. H. Choi, H. Jeon, K. Lee, M. H. Ryou, Y. M. Lee, *J. Electrochem. Soc.* **2017**, *164*, A6308.
[422] T. Ma, G.-L. Xu, X. Zeng, Y. Li, Y. Ren, C. Sun, S. M. Heald, J. Jorne, K. Amine, Z. Chen, *J. Power Sources* **2017**, *341*, 114.
[423] Y. Piao, Y. Qin, Y. Ren, S. M. Heald, C. J. Sun, D. H. Zhou, B. J. Polzin, S. E. Trask, K. Amine, Y. J. Wei, G. Chen, I. Bloom, Z. H. Chen, *Phys. Chem. Chem. Phys.* **2014**, *16*, 3254.
[424] Q. Liu, M.-R. Gao, Y. Liu, J. S. Okasinski, Y. Ren, Y. Sun, *Nano Lett.* **2015**, *16*, 715.
[425] J. Cravillon, C. A. Schröder, H. Bux, A. Rothkirch, J. Caro, M. Wiebcke, *CrystEngComm* **2012**, *14*, 492.

[426] J. Chen, J. Bai, H. Chen, J. Graetz, *J. Phys. Chem. Lett.* **2011**, *2*, 1874.
[427] T. Friščić, I. Halasz, P. J. Beldon, A. M. Belenguer, F. Adams, S. A. Kimber, V. Honkimäki, R. E. Dinnebier, *Nat. Chem.* **2013**, *5*, 66.
[428] J. Yano, V. K. Yachandra, *Photosynth. Res.* **2009**, *102*, 241.
[429] J. R. Croy, M. Balasubramanian, D. Kim, S.-H. Kang, M. M. Thackeray, *Chem. Mater.* **2011**, *23*, 5415.
[430] J. B. Metson, S. J. Hay, H. J. Trodahl, B. Ruck, Y. Hu, *Curr. Appl. Phys.* **2004**, *4*, 233.
[431] M. Balasubramanian, X. Sun, X. Q. Yang, J. McBreen, *J. Electrochem. Soc.* **2000**, *147*, 2903.
[432] O. Haas, A. Deb, E. J. Cairns, A. Wokaun, *J. Electrochem. Soc.* **2005**, *152*, A191.
[433] D. Wang, R. Kou, Y. Ren, C. J. Sun, H. Zhao, M. J. Zhang, Y. Li, A. Huq, J. Ko, F. Pan, Y. K. Sun, Y. Yang, K. Amine, J. M. Bai, Z. H. Chen, F. Wang, *Adv. Mater.* **2017**, *29*, 1606715.
[434] F. Krumeich, O. Waser, S. E. Pratsinis, *J. Solid State Chem.* **2016**, *242*, 96.
[435] M. L. Trudeau, D. Laul, R. Veillette, A. M. Serventi, A. Mauger, C. M. Julien, K. Zaghib, *J. Power Sources* **2011**, *196*, 7383.
[436] S. Y. Chung, Y. M. Kim, S. Y. Choi, J. G. Kim, *J. Am. Chem. Soc.* **2013**, *135*, 7811.
[437] S.-Y. Chung, Y.-M. Kim, J.-G. Kim, Y.-J. Kim, *Nat. Phys.* **2009**, *5*, 68.
[438] S.-Y. Chung, Y.-M. Kim, S. Lee, S. H. Oh, J.-G. Kim, S.-Y. Choi, Y.-J. Kim, S.-J. L. Kang, *Nano Lett.* **2012**, *12*, 3068.
[439] D. A. Ziolkowska, J. B. Jasinski, B. Hamankiewicz, K. P. Korona, S.-H. Wu, A. Czerwinski, *Cryst. Growth Des.* **2016**, *16*, 5006.
[440] C. Bommier, X. Ji, *Isr. J. Chem.* **2015**, *55*, 486.
[441] H. He, H. Wang, Y. Tang, Y. Liu, *Prog. Chem.* **2014**, *26*, 572.
[442] J. Li, L. Wang, X. He, *Prog. Chem.* **2016**, *28*, 193.
[443] E. Betzig, J. Trautman, *Science* **1991**, *251*, 1468.
[444] D. J. Miller, C. Proff, J. Wen, D. P. Abraham, J. Bareño, *Adv. Energy Mater.* **2013**, *3*, 1098.
[445] J. Lei, F. McLarnon, R. Kostecki, *J. Phys. Chem. B* **2005**, *109*, 952.
[446] D. Chen, S. Indris, M. Schulz, B. Gamer, R. Mönig, *J. Power Sources* **2011**, *196*, 6382.
[447] F. Orsini, A. Du Pasquier, B. Beaudoin, J. Tarascon, M. Trentin, N. Langenhuizen, E. De Beer, P. Notten, *J. Power Sources* **1998**, *76*, 19.
[448] T. Osaka, T. Momma, K. Nishimura, T. Tajima, *J. Electrochem. Soc.* **1993**, *140*, 2745.
[449] Y. Yui, M. Hayashi, J. Nakamura, *Sci. Rep.* **2016**, *6*, 22406.
[450] R. Rodriguez, K. E. Loeffler, S. S. Nathan, J. K. Sheavly, A. Dolocan, A. Heller, C. B. Mullins, *ACS Energy Lett.* **2017**, *2*, 2051.
[451] J. Y. Huang, L. Zhong, C. M. Wang, J. P. Sullivan, W. Xu, L. Q. Zhang, S. X. Mao, N. S. Hudak, X. H. Liu, A. Subramanian, *Science* **2010**, *330*, 1515.
[452] M. Gu, A. Kushima, Y. Shao, J.-G. Zhang, J. Liu, N. D. Browning, J. Li, C. Wang, *Nano Lett.* **2013**, *13*, 5203.
[453] Z. Li, X. Tan, P. Li, P. Kalisvaart, M. T. Janish, W. M. Mook, E. J. Luber, K. L. Jungjohann, C. B. Carter, D. Mitlin, *Nano Lett.* **2015**, *15*, 6339.
[454] V. Chevrier, G. Ceder, *J. Electrochem. Soc.* **2011**, *158*, A1011.
[455] H. Wu, Y. Cui, *Nano Today* **2012**, *7*, 414.
[456] M. H. Park, Y. Cho, K. Kim, J. Kim, M. Liu, J. Cho, *Angew. Chem., Int. Ed.* **2011**, *123*, 9821.
[457] F. Legrain, O. I. Malyi, S. Manzhos, *Solid State Ionics* **2013**, *253*, 157.
[458] X. Lu, E. R. Adkins, Y. He, L. Zhong, L. Luo, S. X. Mao, C.-M. Wang, B. A. Korgel, *Chem. Mater.* **2016**, *28*, 1236.
[459] X. H. Liu, J. Y. Huang, *Energy Environ. Sci.* **2011**, *4*, 3844.
[460] P. Harks, F. Mulder, P. Notten, *J. Power Sources* **2015**, *288*, 92.
[461] N. Hodnik, G. Dehm, K. J. Mayrhofer, *ACC. Chem. Res.* **2016**, *49*, 2015.
[462] Y. Li, Y. Li, A. Pei, K. Yan, Y. Sun, C.-L. Wu, L.-M. Joubert, R. Chin, A. L. Koh, Y. Yu, J. Perrino, B. Butz, S. Chu, Y. Cui, *Science* **2017**, *358*, 506.
[463] F. Meirer, J. Cabana, Y. Liu, A. Mehta, J. C. Andrews, P. Pianetta, *J. Synchrotron Radiat.* **2011**, *18*, 773.
[464] J. Nelson, S. Misra, Y. Yang, A. Jackson, Y. Liu, H. Wang, H. Dai, J. C. Andrews, Y. Cui, M. F. Toney, *J. Am. Chem. Soc.* **2012**, *134*, 6337
[465] E. de Smit, I. Swart, J. F. Creemer, G. H. Hoveling, M. K. Gilles, T. Tyliszczak, P. J. Kooyman, H. W. Zandbergen, C. Morin, B. M. Weckhuysen, *Nature* **2008**, *456*, 222.
[466] J.-D. Grunwaldt, C. G. Schroer, *Chem. Soc. Rev.* **2010**, *39*, 4741.
[467] J. H. Kinney, M. C. Nichols, *Annu. Rev. Mater. Sci.* **1992**, *22*, 121.
[468] A. Bosak, I. Snigireva, K. S. Napolskii, A. Snigirev, *Adv. Mater.* **2010**, *22*, 3256.
[469] Y.-T. Chen, T.-N. Lo, Y. S. Chu, J. Yi, C.-J. Liu, J.-Y. Wang, C.-L. Wang, C.-W. Chiu, T.-E. Hua, Y. Hwu, *Nanotechnolgy* **2008**, *19*, 395302.
[470] J. Wang, Y.-C. K. Chen-Wiegart, C. Eng, Q. Shen, J. Wang, *Nat. Commun.* **2016**, *7*, 12372.
[471] J. Wang, Y. C. K. Chen-Wiegart, J. Wang, *Nat. Commun.* **2014**, *5*, 4570.
[472] J. Wang, Y. C. K. Chen-Wiegart, J. Wang, *Angew. Chem., Int. Ed.* **2014**, *53*, 4460.
[473] J. Wang, C. Eng, Y.-c. K. Chen-Wiegart, J. Wang, *Nat. Commun.* **2015**, *6*, 7496.
[474] J.-H. Cheng, A. A. Assegie, C.-J. Huang, M.-H. Lin, A. M. Tripathi, C.-C. Wang, M.-T. Tang, Y.-F. Song, W.-N. Su, B. J. Hwang, *J. Phys. Chem. C* **2017**, *121*, 7761.
[475] S. H. Guo, P. Liu, H. J. Yu, Y. B. Zhu, M. W. Chen, M. Ishida, H. S. Zhou, *Angew. Chem., Int. Ed.* **2015**, *54*, 5894.
[476] M. Galceran, D. Saurel, B. Acebedo, V. V. Roddatis, E. Martin, T. Rojo, M. Casas-Cabanas, *Phys. Chem. Chem. Phys.* **2014**, *16*, 8837.
[477] Z. Jian, W. Han, X. Lu, H. Yang, Y. S. Hu, J. Zhou, Z. Zhou, J. Li, W. Chen, D. Chen, *Adv. Energy Mater.* **2013**, *3*, 156.
[478] J. Z. Guo, P. F. Wang, X. L. Wu, X. H. Zhang, Q. Yan, H. Chen, J. P. Zhang, Y. G. Guo, *Adv. Mater.* **2017**, *29*, 1701968.
[479] Y. Wang, X. Yu, S. Xu, J. Bai, R. Xiao, Y.-S. Hu, H. Li, X.-Q. Yang, L. Chen, X. Huang, *Nat. Commun.* **2013**, *4*, 2365
[480] A. Darwiche, C. Marino, M. T. Sougrati, B. Fraisse, L. Stievano, L. Monconduit, *J. Am. Chem. Soc.* **2012**, *134*, 20805.
[481] J. P. Perdew, Y. Wang, *Phys. Rev. B* **1992**, *46*, 12947.
[482] J. M. Stratford, M. Mayo, P. K. Allan, O. Pecher, O. J. Borkiewicz, K. M. Wiaderek, K. W. Chapman, C. J. Pickard, A. J. Morris, C. P. Grey, *J. Am. Chem. Soc.* **2017**, *139*, 7273.
[483] P. K. Allan, J. M. Griffin, A. Darwiche, O. J. Borkiewicz, K. M. Wiaderek, K. W. Chapman, A. J. Morris, P. J. Chupas, L. Monconduit, C. P. Grey, *J. Am. Chem. Soc.* **2016**, *138*, 2352.
[484] D. Dambournet, K. W. Chapman, M. V. Koudriachova, P. J. Chupas, I. Belharouak, K. Amine, *Inorg. Chem.* **2011**, *50*, 5855.
[485] B. Key, M. Morcrette, J. M. Tarascon, C. P. Grey, *J. Am. Chem. Soc.* **2011**, *133*, 503.
[486] M. Moriya, M. Miyahara, M. Hokazono, H. Sasaki, A. Nemoto, S. Katayama, Y. Akimoto, S. Hirano, Y. Ren, *J. Power Sources* **2014**, *263*, 7.
[487] D. L. Zeng, J. Cabana, J. L. Breger, W. S. Yoon, C. P. Grey, *Chem. Mater.* **2007**, *19*, 6277.
[488] J. M. Stratford, M. Mayo, P. K. Allan, O. Pecher, O. J. Borkiewicz, K. M. Wiaderek, K. W. Chapman, C. J. Pickard, A. J. Morris, C. P. Grey, *J. Am. Chem. Soc.* **2017**, *139*, 7273.
[489] F. Blanc, M. Leskes, C. P. Grey, *Acc. Chem. Res.* **2013**, *46*, 1952.
[490] J. Arai, R. Nakahigashi, T. Sugiyama, *J. Electrochem. Soc.* **2016**, *163*, A1064.
[491] K. Gotoh, M. Izuka, J. Arai, Y. Okada, T. Sugiyama, K. Takeda, H. Ishida, *Carbon* **2014**, *79*, 380.
[492] H. Fujimoto, A. Mabuchi, K. Tokumitsu, N. Chinnasamy, T. Kasuh, *J. Power Sources* **2011**, *196*, 1365.

[493] C. P. Grey, S. G. Greenbaum, *MRS Bull.* **2002**, *27*, 613.
[494] M. Leskes, N. E. Drewett, L. J. Hardwick, P. G. Bruce, G. R. Goward, C. P. Grey, *Angew. Chem., Int. Ed.* **2012**, *51*, 8560.
[495] L. N. Zhou, M. Leskes, T. Liu, C. P. Grey, *Angew. Chem., Int. Ed.* **2015**, *54*, 14782.
[496] C. P. Grey, N. Dupre, *Chem. Rev.* **2004**, *104*, 4493.
[497] R. J. Clement, D. S. Middlemiss, I. D. Seymour, A. J. Ilott, C. P. Grey, *Chem. Mater.* **2016**, *28*, 8228.
[498] K. J. Harris, J. M. Foster, M. Z. Tessaro, M. Jiang, X. Y. Yang, Y. Wu, B. Protas, G. R. Goward, *Chem. Mater.* **2017**, *29*, 5550.
[499] K. J. Harris, Z. E. M. Reeve, D. N. Wang, X. F. Li, X. L. Sun, G. R. Goward, *Chem. Mater.* **2015**, *27*, 3299.
[500] K. E. Johnston, M. T. Sougrati, L. Stievano, A. Darwiche, N. Dupre, C. P. Grey, L. Monconduit, *Chem. Mater.* **2016**, *28*, 4032.
[501] R. J. Messinger, M. Menetrier, E. Salager, A. Boulineau, M. Duttine, D. Carlier, J. M. A. Mba, L. Croguennec, C. Masquelier, D. Massiot, M. Deschamps, *Chem. Mater.* **2015**, *27*, 5212.
[502] F. Poli, A. Wong, J. S. Kshetrimayum, L. Monconduit, M. Letellier, *Chem. Mater.* **2016**, *28*, 1787.
[503] E. Salager, V. Sarou-Kanian, M. Sathiya, M. X. Tang, J. B. Leriche, P. Melin, Z. L. Wang, H. Vezin, C. Bessada, M. Deschamps, J. M. Tarascon, *Chem. Mater.* **2014**, *26*, 7009.
[504] B. Key, R. Bhattacharyya, M. Morcrette, V. Seznec, J. M. Tarascon, C. P. Grey, *J. Am. Chem. Soc.* **2009**, *131*, 9239.
[505] M. Klett, M. Giesecke, A. Nyman, F. Hallberg, R. W. Lindstrom, G. Lindbergh, I. Furo, *J. Am. Chem. Soc.* **2012**, *134*, 14654.
[506] Y. Paik, J. P. Osegovic, F. Wang, W. Bowden, C. P. Grey, *J. Am. Chem. Soc.* **2001**, *123*, 9367.
[507] K. A. See, M. Leskes, J. M. Griffin, S. Britto, P. D. Matthews, A. Emly, A. Van der Ven, D. S. Wright, A. J. Morris, C. P. Grey, R. Seshadri, *J. Am. Chem. Soc.* **2014**, *136*, 16368.
[508] I. D. Seymour, D. S. Middlemiss, D. M. Halat, N. M. Trease, A. J. Pell, C. P. Grey, *J. Am. Chem. Soc.* **2016**, *138*, 9405.
[509] M. C. Tucker, M. M. Doeff, T. J. Richardson, R. Finones, E. J. Cairns, J. A. Reimer, *J. Am. Chem. Soc.* **2002**, *124*, 3832.
[510] N. Yamakawa, M. Jiang, B. Key, C. P. Grey, *J. Am. Chem. Soc.* **2009**, *131*, 10525.
[511] K. Ogata, E. Salager, C. J. Kerr, A. E. Fraser, C. Ducati, A. J. Morris, S. Hofmann, C. P. Grey, *Nat. Commun.* **2014**, *5*, 3217.
[512] R. Bhattacharyya, B. Key, H. L. Chen, A. S. Best, A. F. Hollenkamp, C. P. Grey, *Nat. Mater.* **2010**, *9*, 504.
[513] O. Pecher, J. Carretero-Gonzalez, K. J. Griffith, C. P. Grey, *Chem. Mater.* **2017**, *29*, 213.
[514] K. Gotoh, T. Ishikawa, S. Shimadzu, N. Yabuuchi, S. Komaba, K. Takeda, A. Goto, K. Deguchi, S. Ohki, K. Hashi, T. Shimizu, H. Ishida, *J. Power Sources* **2013**, *225*, 137.
[515] D. Yuan, X. Liang, L. Wu, Y. Cao, X. Ai, J. Feng, H. Yang, *Adv. Mater.* **2014**, *26*, 6301.
[516] J. Billaud, R. J. Clément, A. R. Armstrong, J. Canales-Vázquez, P. Rozier, C. P. Grey, P. G. Bruce, *J. Am. Chem. Soc.* **2014**, *136*, 17243.
[517] O. Pecher, P. M. Bayley, H. Liu, Z. Liu, N. M. Trease, C. P. Grey, *J. Magn. Reson.* **2016**, *265*, 200.
[518] P. M. Bayley, N. M. Trease, C. P. Grey, *J. Am. Chem. Soc.* **2016**, *138*, 1955.
[519] Z. R. Zhang, Y. Yang, H. S. Liu, *Prog. Chem.* **2003**, *15*, 18.
[520] J. Zhong, H. Zhang, X. H. Sun, S. T. Lee, *Adv. Mater.* **2014**, *26*, 7786.
[521] Y. J. Cui, A. Abouimrane, J. Lu, T. Bolin, Y. Ren, W. Weng, C. J. Sun, V. A. Maroni, S. M. Heald, K. Amine, *J. Am. Chem. Soc.* **2013**, *135*, 8047.
[522] J. Purans, S. Benazeth, C. Souleau, *NATO Sci. Ser. II* **2003**, *117*, 231.
[523] X. S. Liu, T. C. Weng, *MRS Bull.* **2016**, *41*, 466.
[524] G.-L. Xu, T. Sheng, L. Chong, T. Ma, C.-J. Sun, X. Zuo, D.-J. Liu, Y. Ren, X. Zhang, Y. Liu, *Nano Lett.* **2017**, *17*, 953.
[525] C. Ma, J. Alvarado, J. Xu, R. J. Clément, M. Kodur, W. Tong, C. P. Grey, Y. S. Meng, *J. Am. Chem. Soc.* **2017**, *139*, 4835.
[526] A. Hanafusa, Y. Muramatsu, Y. Kaburagi, A. Yoshida, Y. Hishiyama, W. L. Yang, J. D. Denlinger, E. M. Gullikson, *J. Appl. Phys.* **2011**, *110*, 053504.
[527] F. Lin, I. M. Markus, D. Nordlund, T.-C. Weng, M. D. Asta, H. L. Xin, M. M. Doeff, *Nat. Commun.* **2014**, *5*, 3529.
[528] R. Qiao, Y. Wang, P. Olalde-Velasco, H. Li, Y.-S. Hu, W. Yang, *J. Power Sources* **2015**, *273*, 1120.
[529] Y. Xie, H. Wang, G. Xu, J. Wang, H. Sheng, Z. Chen, Y. Ren, C. J. Sun, J. Wen, J. Wang, D. J. Miller, J. Lu, K. Amine, Z. F. Ma, *Adv. Energy Mater.* **2016**, *6*, 1601306.
[530] Z. H. Chen, Y. Ren, E. Lee, C. Johnson, Y. Qin, K. Amine, *Adv. Energy Mater.* **2013**, *3*, 729.
[531] Y. Huang, Y. C. Lin, D. M. Jenkins, N. A. Chernova, Y. Chung, B. Radhakrishnan, I. H. Chu, J. Fang, Q. Wang, F. Omenya, S. P. Ong, M. S. Whittingham, *ACS Appl. Mater. Interfaces* **2016**, *8*, 7013.
[532] D. Choi, J. Xiao, Y. J. Choi, J. S. Hardy, M. Vijayakumar, M. S. Bhuvaneswari, J. Liu, W. Xu, W. Wang, Z. G. Yang, G. L. Graff, J. G. Zhang, *Energy Environ. Sci.* **2011**, *4*, 4560.
[533] S. Hwang, Y. Lee, E. Jo, K. Y. Chung, W. Choi, S. M. Kim, W. Chang, *ACS Appl. Mater. Interfaces* **2017**, *9*, 18883.
[534] N. Yabuuchi, I. Ikeuchi, K. Kubota, S. Komaba, *ACS Appl. Mater. Interfaces* **2016**, *8*, 32292.
[535] Z. Chen, Y. Ren, E. Lee, C. Johnson, Y. Qin, K. Amine, *Adv. Energy Mater.* **2013**, *3*, 729.
[536] S. Sharifi-Asl, F. A. Soto, A. Nie, Y. Yuan, H. Asayesh-Ardakani, T. Foroozan, V. Yurkiv, B. Song, F. Mashayek, R. F. Klie, *Nano Lett.* **2017**, *17*, 2165.
[537] C. K. Lin, Y. Piao, Y. C. Kan, J. Bareno, I. Bloom, Y. Ren, K. Amine, Z. H. Chen, *ACS Appl. Mater. Interfaces* **2014**, *6*, 12692.
[538] J. Q. Zhao, W. Zhang, A. Huq, S. T. Misture, B. L. Zhang, S. M. Guo, L. J. Wu, Y. M. Zhu, Z. H. Chen, K. Amine, F. Pan, J. M. Bai, F. Wang, *Adv. Energy Mater.* **2017**, *7*, 1601266.
[539] G. L. Xu, Y. Qin, Y. Ren, L. Cai, K. An, K. Amine, Z. H. Chen, *J. Mater. Chem. A* **2015**, *3*, 13031.
[540] Y. C. Kan, Y. Hu, Y. Ren, J. Bareno, I. Bloom, Y. K. Sun, K. Amine, Z. H. Chen, *J. Power Sources* **2014**, *271*, 97.
[541] C. K. Lin, Y. Ren, K. Amine, Y. Qin, Z. H. Chen, *J. Power Sources* **2013**, *230*, 32.
[542] J. X. Zheng, T. C. Liu, Z. X. Hu, Y. Wei, X. H. Song, Y. Ren, W. D. Wang, M. M. Rao, Y. Lin, Z. H. Chen, J. Lu, C. M. Wang, K. Amine, F. Pan, *J. Am. Chem. Soc.* **2016**, *138*, 13326.
[543] Y. K. Sun, Z. H. Chen, H. J. Noh, D. J. Lee, H. G. Jung, Y. Ren, S. Wang, C. S. Yoon, S. T. Myung, K. Amine, *Nat. Mater.* **2012**, *11*, 942.
[544] Y. C. Kan, Y. Hu, C. K. Lin, Y. Ren, Y. K. Sun, K. Amine, Z. H. Chen, *Phys. Chem. Chem. Phys.* **2014**, *16*, 20697.
[545] J. Deng, W. B. Luo, S. L. Chou, H. K. Liu, S. X. Dou, *Adv. Energy Mater.* **2017**, *7*, 1701428.